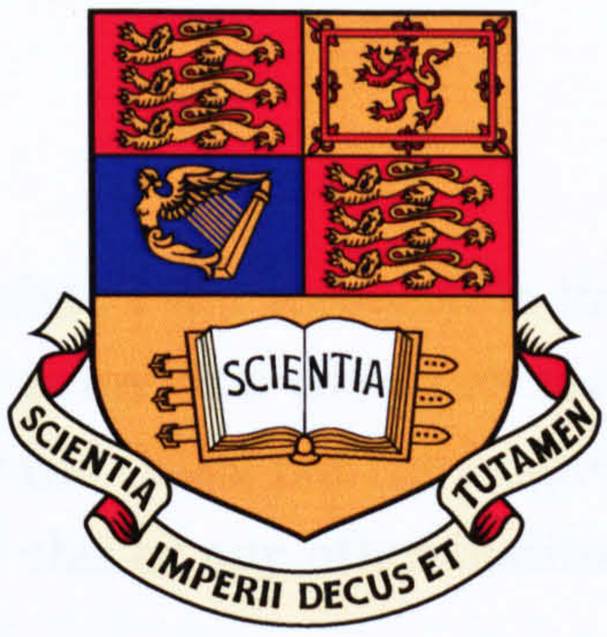


Imperial College of Science, Technology and Medicine

Department of Mechanical Engineering
Energy Technology for Sustainable Development Group

Axial Flux Permanent Magnet Synchronous Electric Machines for Hybrid Electric Vehicle Powertrains

Alan Walker
January 2006

Thesis submitted for the degree of Doctor of Philosophy
of the University of London

IBL
LONDON
UNIV

Declaration of Originality

By this statement, I certify that I am responsible for the work submitted in this thesis, that the original work is my own except as specified in acknowledgement or in reference, and that neither the thesis nor the original work contained therein has been previously submitted to this or any other institution for a higher degree.

..... signed

..... date

Abstract

The Axial Flux Permanent Magnet Machine is a synchronous electric machine, which compares favourably with the more common Radial Flux version in applications where the space envelope has a large diameter and short length. Road vehicle traction is such an application, but surprisingly this machine type has not been employed here to a significant degree.

With the increase in road transport due to our improving quality of life, the reduction in finite fossil fuel reserves and the dangers posed by excessive carbon emissions, there is strong motivation to reduce the energy consumption by transport. Bi-directional electric drives, as employed in Hybrid Electric Vehicles, offer technical advantages in this direction.

The thesis presents a combination of analytical, numerical and practical work on Surface-Mounted Axial Flux Permanent Magnet electric machines to be employed in Hybrid Electric Vehicles and design studies on these machines.

A series of analytical models are provided, which can be used as design support tools depending on complexity and the calculation in hand. The advanced models to evaluate the electromagnetic circuit can provide useful data to assess loss components or thermal modelling. These are important for predicting and improving overall powertrain performance.

Axial Flux machines feature a large number of design parameters, more so than Radial Flux machines, making the achievement of a high efficiency design a complex task. Studies on magnet profiling, conductor sizing and coil design relating to Axial Flux machines are presented, which are of particular interest to Synchronous Permanent Magnet machine designers, as they can result in high efficiency machines. Specific new designs of a double airgap slotted core Integrated Motor Generator and a multi airgap slotless core Generator are developed through this work. As new designs, the practical investigation provided of their manufacture is important.

Acknowledgements

My thanks go to my academic supervisors Dr Keith Pullen and Dr Shahram Etemad, and to my technical colleagues Mr Phil Wilson and Mr Dave Tomlin, who between them ensured I came to the point of writing this thesis.

The following academics gave invaluable assistance to a conventional automotive engineer grappling with electrical engineering problems: Prof Dave Rodger and Dr Phil Coles from University of Bath, Prof Chandur Sadarangani and Prof Sture Erikson from KTH-Royal Institute of Technology Stockholm, and Prof Ernie Freeman and Dr Carlos Hernandez-Aramburo from Imperial College London.

Of particular value has been an industrial perspective provided by the following people: Dr Hassan Mansir from Turbo Genset Co., Mr Tony Lakin from I-Power, Mr Ian Machell from Spicer Driveshaft and Mr Ken Moore from Iveco Ltd.

I gratefully acknowledge the financial support of the EPSRC and UK Department for Transport through the LINK ForesightVehicle Programme. I also thank Haldex AB, and Mr Sverker Stomrud, for financial involvement in early work on regenerative braking.

I am fortunate to have shared many discussions about problems, and a few beers, with my fellow researchers: Mr Peethamparam Anpalahan, Mr Sejul Shah, Mr Sebastian Tsakok, Mr Steven Wilkins, Miss Hamideh Razavi, Mr Sebastian Fernandez, Mr Stephan Meister, Dr Michael Lamperth my former supervisor, and Dr Niall McGlashan from Imperial College London, Prof Xuexun Guo from Wuhan Technical University, and Dr Erik Nordlund and Dr Freddy Magnussen, previously at KTH-Royal Institute of Technology Stockholm and now with ABB.

To my family, my parents and in particular my wife Andrea and our son Pascal, all my love and gratitude for your immense support and understanding during the years of this project.

Contents

1 Introduction **18**
- 1.1 Motivation for Energy-efficient Transport 18
- 1.2 More-electric Vehicles 21
- 1.3 Electric Machines in HEV Powertrains 25
- 1.4 Selected Machine Applications in HEV Powertrains 29
- 1.5 Types of Electric Machines 32
- 1.6 Types of Stator Windings 34
- 1.7 Electric Machine Topologies 35
- 1.8 Permanent Magnet Synchronous Machine Efficiency 38
- 1.9 Research Description 42
- 1.10 Thesis Layout 43

2 Hybrid Electric Powertrain Analysis **45**
- 2.1 Modelling for Selected Machine Applications in HEV Powertrains . . 45
- 2.2 Component Modelling 45
- 2.3 7.5 tonne Commercial Vehicle Powertrain for Urban Deliveries 51
- 2.4 70-seater Bus Powertrain 59
- 2.5 Summary 62

3 Review of Axial Flux Machines and Analytical Electromagnetic Models **63**
- 3.1 Categories of Axial Flux Machine 63
- 3.2 Single Airgap Machines 63
- 3.3 Through Flux Double Airgap Machines 66
- 3.4 Multiple Airgap Machines 71
- 3.5 An Introduction to Analytical Electromagnetic Modelling Methods . 72
- 3.6 Lumped Parameter Model 73
- 3.7 Surface Point Charge Representation 75
- 3.8 Regional Field Solution Model 75
- 3.9 Airgap Field Co-energy 76
- 3.10 Equivalent Magnetic Circuit Model 76
- 3.11 Summary 80

4 Cored Axial Flux Permanent Magnet Synchronous Machine Theory **81**
- 4.1 Electromagnetic Operation of the Permanent Magnet Synchronous Machine 82

4.2 Inductance 91
4.3 Supply Waveform 95
4.4 Motor Constant 97
4.5 Design Optimisation 98
4.6 Axial Flux Machine Parameter Calculation Program 101
4.7 Parametric Analyses 102
4.8 AFMPC Program Use in Initial Machine Design 105
4.9 Summary 107

5 3D Equivalent Magnetic Circuit Model for a Double Airgap, Airgap Winding Machine 108
5.1 Leakage and Fringing 108
5.2 Solution 108
5.3 Verification with Lorentz Law Calculation 110
5.4 Verification with FEM 111
5.5 Summary 113

6 Permanent Magnet Excitation Field Study 114
6.1 Field Waveforms 114
6.2 Peak Airgap Flux Density 116
6.3 Single-piece Poles 119
6.4 Multi-piece Poles 122
6.5 Summary 125

7 Conductor and Coil Geometry for Airgap Winding Study 126
7.1 Current and Copper Losses 126
7.2 No-load Losses 129
7.3 Optimal Conductor Geometry 131
7.4 Coil Design 135
7.5 Summary 144

8 Experimental Machines 145
8.1 IMG Manufacture 145
8.2 Test Results 151
8.3 Generator Active Parts Manufacture 153
8.4 Summary 154

9 Slotted Core Stator and Winding Study 157
9.1 Salient Stator Structure and Slot Leakage 157
9.2 Airgap Permeance Function 162
9.3 Losses 164
9.4 Integrated Teeth Winding 166
9.5 Summary 168

10 Conclusions and Future Work 170
10.1 Relative to Research Objectives 170
10.2 Further Work 172

Bibliography **174**

A Theoretical Relations for Axial Flux Machines **189**
A.1 Radial and Axial Machine Torque 189
A.2 Y−connected BLDC Torque Calculation 191
A.3 PMSM Back emf Calculation 191
A.4 Motor Constant Calculation 192
A.5 Concentrated Coil Winding Dimensions 192
A.6 Skew 193

B Equivalent Magnetic Circuit Model Terms **197**
B.1 Reluctances and Fluxes 197
B.2 Solution Matrices 197
B.3 3D Equivalent Magnetic Circuit Model 200
B.4 Stator Leakage Paths 203

C Test Rig & Manufacturing Jigs **205**
C.1 Airgap Conductor Test Rig 205
C.2 Excitation Field Measurement 205
C.3 Coil Winding Jigs 205
C.4 Iron Core Jigs 205

List of Figures

1.1 Transport energy consumption in UK. 19
1.2 UK road transport. 19
1.3 Projected CO2 emissions in UK. 20
1.4 Grid charged EV configuration. 21
1.5 Energy density of fuels and ESD types. 22
1.6 Series configuration HEV. 22
1.7 Parallel configuration HEV. 23
1.8 Turbocharged diesel engine BSFC map, with constant power lines at % of maximum power. Lowest and highest effiency regions marked. . 24
1.9 New operating point on Optimum Operating Line. 24
1.10 Cutaway of the Toyota Hybrid System. 25
1.11 IC generator configuration. 26
1.12 Honda 12kW LPG engine and GenSmart S22AA-002 generator. . . . 26
1.13 Wheel motor configuration. 27
1.14 Axle-mounted traction motor. 27
1.15 In-wheel motor of the Ion scooter. 28
1.16 Integrated Motor Generator configuration. 28
1.17 Cutaway of engine-transmission interface, exposing an Induction ISA in the Parallel Hybrid Truck. 28
1.18 ISA armature for a CV engine viewed from the engine side. 29
1.19 Heavy Goods Vehicle chassis used for HEV project. 30
1.20 Parallel hybrid powertrain configuration for Motor-Generator machine application. 30
1.21 Typical 70-seater Bus as used for HEV project. 31
1.22 Series hybrid powertrain configuration for Generator machine application. 32
1.23 Categorisation of types of synchronous electric machines. 33
1.24 Radial and Axial Flux electric machine topologies. 36

2.1 Schematic of frequency inverter layout. 48
2.2 Schematic of voltage converter layout. 48
2.3 Combined EC drive cycle with four urban (ECE15) and 1 extra-urban (EUDC) cycles. 52
2.4 Real world urban delivery CV drive cycle. 52
2.5 IMG duty plot for vehicle operating the drive cycle in Figure 2.4. . . 53
2.6 Power curves for *Iveco* CIDI ICE. 54
2.7 Schematic of battery layout. 55

2.8 Powertrain assembly in lab. 56
2.9 Power loss components for operating points of interest. (Data given in Table 2.3.) 58
2.10 Radial Flux PM generator and geardrive to ICE, manufactured by *Siemens*. 60
2.11 Real world bus drive cycles. 60
2.12 Power curves for selected CIDI ICE V8s and V10. 61

3.1 A single coil mounted on a slotless and a slotted stator. 64
3.2 Torus electromagnetic operation. 66
3.3 Double airgap rotor–stator configurations. 70
3.4 Lumped parameter circuit for non-salient pole (SM PMSM) machine. 74
3.5 Lumped parameter circuits for salient pole machine. 74
3.6 Permanent Magnet representation by surface point charges. 75
3.7 Rectilinear slice at a constant radial position. 77
3.8 2D equivalent magnetic circuit of main flux path of airgap winding. . 77
3.9 2D equivalent magnetic circuit for main flux path and leakage paths of airgap winding. 78
3.10 Equivalent magnetic circuit for inductance calculation. 79
3.11 Stacked 2D model of double airgap, internal rotor machine. 80

4.1 Flux, current and force vectors (B, i, F) for Axial Flux machine compared with Radial Flux. 82
4.2 Torque according to torque angle for salient pole PM machine. 83
4.3 Square wave of magnet flux density and ideal sinusoidal wave of airgap flux density, $B_g = \hat{B}_g \sin\theta$. 84
4.4 Fractional pitch poles with the pole pitch angle marked. 85
4.5 Axial Flux multi-pole array shapes. 86
4.6 Fractional pitch coils with the coil pitch and pole pitch angles marked. 87
4.7 Torque and specific torque for ratio of active area radial dimensions for an 8 pole Axial Flux machine. 88
4.8 Current loading S_1 and airgap flux density B_g out of phase by $(90° - \vartheta)$. 90
4.9 The flux from current in the $d-$ and $q-$axes. 92
4.10 Shaft and active volume dimensions. 98
4.11 AFMPC program user interface for initial machine design. 101
4.12 Calculation process for AFMPC program shown in Figure 4.11. . . . 102
4.13 Optimised design process with parametric and FEM calculations. . . 103
4.14 Torque from optimum designs with defined outside radius r_o. 103
4.15 Specific torque for optimum designs with required torque. 104
4.16 Torque density for optimum designs with required torque. 104
4.17 Copper losses for optimum designs with required torque. 105
4.18 Iron losses for optimum designs with required torque. 105
4.19 Efficiency for optimum designs with required torque. 106

5.1 Double airgap, airgap winding for 3D equivalent circuit model. 109
5.2 Elevation and plan of double airgap, airgap winding model fringing and leakage reluctances. 109

5.3 Calculation process to resolve the equivalent circuit model. 110
5.4 Rms terminal voltage values from equivalent magnetic circuit model, Lorentz *Blu* and FEM calculations, for the geometry given in Table 5.1. 111
5.5 FEM model for on-load verification of equivalent magnetic circuit model terminal voltage. 112

6.1 Peak flux density for pole aspect ratio (h_m/τ_m) and pole pitch ratio k_{ppitch}. 116
6.2 Harmonic components according to k_{ppitch}. Points are individual FEM models and lines are analytical relations. 117
6.3 Neighbouring poles without stator showing pole separation, height and leak paths. 118
6.4 Variation in k_{ppitch} with radial position. 118
6.5 1 rotor with 8 pole array. 119
6.6 Field vector plot at $z = g/5$. 120
6.7 Measurement of airgap field B_z. 121
6.8 Measurement of airgap field at $z = g/5$. 121
6.9 Geometric parameters of chamfered Surface Mounted Permanent Magnet poles, and individual chamfered pole. 122
6.10 2-piece poles. 122
6.11 A Halbach array with 8 pieces/pole. 123
6.12 Airgap excitation waveform for 8 piece/pole Halbach array. 123
6.13 Airgap excitation harmonics for 8 piece/pole Halbach array. 124
6.14 Harmonics in airgap excitation waveform for 4 piece/pole Halbach array with respect to volume of PM material. 124

7.1 Current loading for an Axial Flux stator. 128
7.2 Skin effect due to alternating current. 129
7.3 Eddy currents in airgap winding conductors. 130
7.4 Conductor geometries, showing copper and enamel 132
7.5 Array of selected conductors in a polymer holder. 132
7.6 Testrig torque measurements and calculated P_{EC}^{loss} 133
7.7 Calculated P_{c_ec} from reaction torque measurements and FEM at 200 Hz for selected arrays of conductors (Nxb_cxd_c). 133
7.8 MEGA model of the 80x1.5x0.2 conductor array and rotors. 134
7.9 Constant c for Equation (7.9) from measurements. 135
7.10 Comparison of eddy current calculations with measurements for the 80x1.5x0.2 conductor array, shown in Figure 7.7. 136
7.11 Axial Flux machines with airgap windings. 137
7.12 Patented *Segmented Array* concentrated coils. 137
7.13 Rhomboidal concentrated coils. 138
7.14 14-turn concentrated coil of flat wire conductor for coreless airgap winding and coils nested. 138
7.15 14-turn concentrated coil of flat wire conductor for cored airgap winding and coils nested. 139

7.16 Ideal stator *mmf* for proposed nested concentrated coil. 142
7.17 B_s waveform for proposed nested concentrated coil at $z = 1$ mm and $z = 3.5$ mm airgap positions. 142
7.18 Individual coil eddy current power loss calculated for each harmonic, with fundamental electrical frequency 400 Hz. 143

8.1 9-slot stator design. 146
8.2 9-slot stator design. 147
8.3 Internal stator rotor assembly with skewed poles. 148
8.4 Sector bonded NdFeB poles. 148
8.5 Coils for concentrated windings. 149
8.6 18-slot internal stator core section of compacted iron powder. 149
8.7 18-slot core with mounted coil(s). 150
8.8 Assembled 18-slot internal stator. 150
8.9 Open circuit voltage waveform and harmonics for one coil. 151
8.10 Open circuit voltage waveform for 12 parallel coils in phase. 152
8.11 Difference between open circuit voltages of parallel coils in phase, driving recirculating currents. 152
8.12 Internal rotor IMG design. 154
8.13 Interleaved concentrated airgap winding. 155
8.14 Interleaved concentrated airgap winding coils. 156
8.15 Wound core for airgap winding. 156

9.1 Teeth cross section and slot areas for constant $w_s(r)$ or $w_t(r)$, with 2 coils/slot concentrated coils. 160
9.2 Useful and leakage coil flux paths, and slot magnetic field. 160
9.3 Useful and leakage paths for PM flux. 161
9.4 Airgap flux density pulse due to a slot. 163
9.5 Conductor eddy currents from slot leakage. 164
9.6 2D view of integrated teeth. 167
9.7 B_s waveform for integrated teeth winding at $z = 1$ mm and $z = 3.5$ mm airgap positions. 168
9.8 B_s waveform for integrated teeth winding with 0.1 mm slot closure at $z = 1$ mm and $z = 3.5$ mm airgap positions. 168
9.9 B_s waveform for integrated teeth winding with 0.5 mm slot closure at $z = 1$ mm and $z = 3.5$ mm airgap positions. 169
9.10 B_s waveform for integrated teeth winding with 1.0 mm slot closure at $z = 1$ mm and $z = 3.5$ mm airgap positions. 169

A.1 Radial and Axial Flux machine topologies. 190
A.2 End turn geometry for concentrated coils. 193
A.3 Force vectors for skew angle between rotor and stator. 194
A.4 geometry of skewed slot 195

B.1 Flux by current in windings for 3D model. 198

C.1 Test rig 206

C.2 9-slot concentrated coil winding jigs. 206
C.3 Airgap winding manufacture jigs. 207
C.4 Slitting jig for laminated airgap winding core. 207

List of Tables

1.1 Summary of Axial and Radial Flux characteristics for non-integrated motors in traction applications. 36
1.2 Power loss mechanisms in electric machine. 39

2.1 Important operating points for electric traction machine operation. . 54
2.2 SAE J617C engine flywheel housings. 57
2.3 Power loss components and system efficiency calculated for important operating points (battery SOC = 0.7). 58
2.4 *Siemens* ELFA PM generators and Induction motor. 59
2.5 Fuel economy figures from modelling both case study powertrains. . . 62

3.1 Axial Flux machine configurations. (A: airgap, R: rotor, S: stator) . . 64
3.2 Torus and Internal stator double airgap machine comparison 69
3.3 Internal rotor and internal stator features. 71
3.4 Normalised characteristics of Axial Flux BLDC machines. 71
3.5 Comparison of selected reported Axial Flux machines. 71
3.6 Comparison of analytical modelling method characteristics. 74

4.1 Alternative design optimisation objectives. 100

5.1 Typical geometric dimensions and operating conditions selected for model verification. 111

6.1 Optimum pole (chamfered and Halbach) with respect to the standard sector pole 125

7.1 Properties of concentrated coil airgap windings. 139
7.2 Copper fill factor for flat wire for proposed coil and equivalent round wire. 140
7.3 Geometric dimensions and operating conditions for evaluating eddy currents in proposed coil. 143

9.1 Open and closed slot dimensions. Slot bottoms may be rounded rather than square. 158

A.1 Airgap magnetic shear stress values for selected machines. 191

Nomenclature

Symbols

A_{Cu}, V_{Cu}	Cross-sectional Area and Volume of Copper	mm^2 and mm^3
$A_{g,m}$	Airgap or Magnet Area	mm^2
A_s	Slot Area	mm^2
B	Magnetic Flux Density	T or Wb/m^2
B_g	Airgap Flux Density	T
B_m	Magnet Flux Density	T
B_r	Remnant Flux Density	T
B_s	Airgap Flux Density from Stator Current	T
C	Electrical Capacitance	C
e	Instantaneous emf	V
f	Frequency	Hz
F	Force	N
H	Magnetic Field Strength	A/m
H_c	Magnet Coercivity	A/m
i	Instantaneous Current	A
I	rms Current	A
J_c	Conductor Current Density	A/m^2
$K_{E,T}$	Back emf or Torque Constant	V/radM/sec or Nm/A
K_M	Motor Constant	Nm/W
$L_{\phi,g,slot,end}$	Phase, Airgap, Slot or Endwinding Inductance	H
M	Mass	kg
P	Real Power, Apparent Power	W, VA
$P_{input,output}$	Input or Output Power	W
$P^{loss}_{cond,EC}$	Conductor (Ohmic) or Eddy Current Power Loss	W
$P^{loss}_{Cu_s}$	Conductor Power Loss per Slot	W
R	Electrical Resistance	Ω
$\mathcal{R}$	Reluctance	
$\mathcal{R}_{m,mg}$	Magnet Reluctance, Magnet/Airgap Reluctance	
radE	electrical radians	
radM	mechanical radians	
S_1	Stator Current Loading	A/m
t	Time	sec
T	Torque	Nm

T_0	Ambient Temperature	°C
$T_{align,cog,rel}$	Alignment, Cogging or Reluctance Torque	Nm
u	Longitudinal Speed	m/sec
V_{DC}	DC Voltage	V
δ	Torque Angle	radE
η	Efficiency	%
θ	Angular Position	radE
Λ	Airgap Permeance Function	
$\mu_{r,0}$	Relative or Free Space Permeability	H/m
ρ_{Cu}	Electrical Resistivity of Copper	Ω m
σ_{elec}	Electrical Conductivity	Siemens/m
σ_g	Airgap Magnetic Shear Stress	N/mm^2
$\tau_{m,p,c,s}$	Magnet, Pole, Coil or Slot Pitch	radE
ϕ_g	Airgap Magnetic Flux	Wb
ψ	Flux Linkage	Wb
ω	Angular frequency	rad/sec
$\omega_{mech,elec}$	Mechanical or Electrical Angular Speed	radM/sec or radE/sec

Dimensionless Group

C_m	Windage Loss Torque Coefficient
d, q	Direct and Quadrature Axes
d	Switch Duty
G	Gain
k_l	Leakage Coefficient
$k_{ppitch,cpitch,spitch}$	Pole, Coil or Slot Pitch Factor
$k_{w,sk,p,b}$	Winding, Skew, Pitch or Breadth Factor
m	Number of Phases
n	Harmonic Number
N	Number of Turns
n_s	Number of Conductors in Slot
p	Number of Pole Pairs
P_c	Permeance Coefficient
q	Number of Slots per Pole per Phase
Q	Number of Slots
w	Weighting Function
Y,Δ	Star and Delta Connection
$z_{1,2,3,4...}$	Axial Plane
τ_{Vol}	Volume Ratio
ϕ	Phase

Geometric Group [mm]

b_c	Conductor Width

b'_c	Reduced Conductor Height
d_c	Conductor Thickness
$d_{s,so,st}$	Slot, Slot Opening or Slot Taper Depth
g	Airgap Length
g'	Modified Airgap Length (by Carter Coefficient)
$h_{Fe,s}$	Back Iron Thickness or Slot Depth
h_{Fer}	Rotor Back Iron Thickness
h_m	Pole height
l	Length
l_{end}	Endwinding Length
r	Radial Position
r_c	Conductor Radius
$r_{i,o,mean}$	Inner, Outer or Mean Radius
w_f	Inter-pole Gap
$w_{m,p}$	Magnet or Pole Width
$w_{s,so,t}$	Slot, Slot Opening or Tooth Width
z	Axial Position
δ_p	Skin Depth
$\varnothing$	Diameter

Acronyms

AC	Alternating Current
AFMPC	Axial Flux Machine Parameter Calculation
APU	Auxiliary Power Unit
BEM	Boundary Element Method
BLDC	Brushless DC
BPM DC	Brushed PM DC
BSFC	Brake Specific Fuel Consumption
CV	Commercial Vehicle
DC	Direct Current
emf	Electro-Motive Force
ESD	Energy Storage Device
EV	Electric Vehicle
FEM	Finite Element Methods
H2	Hydrogen
HEV	Hybrid Electric Vehicle
ICE	Internal Combustion Engine
IGBT	Insulated Gate Bipolar Transistor
IMG	Integrated Motor Generator
IPM	Interior PM
ISA	Integrated Starter Alternator
LPG	Liquified Petroleum Gas
mmf	Magneto-Motive Force
NdFeB	Neodymium Iron Boron

NiMH	Nickel Metal Hydride
OOL	Optimum Operating Line
PM	Permanent Magnet
PMSM	Permanent Magnet Synchronous Machine
PMU	Prime Mover Unit
PWM	Pulse Width Modulation
SAE	Society of Automotive Engineers
SV	Space Vector

Chapter 1

Introduction

1.1 Motivation for Energy-efficient Transport

The energy consumed by the transport sector comes from the earth's finite resource of fossil fuels. As these are combusted, carbon emissions, which contribute to accelerated climate change as the cause of global warming, and pollutants, which cause dimming and deteriorate air quality, are released [MacKenzie and Walsh, 1990; Weart, 2003]. Between 1970 and 2004, the combined energy consumption of all types of transport in the UK approximately doubled. These levels, shown in Figure 1.1, illustrate that all road transport accounts for approximately three-quarters of transport energy consumption.

1.1.1 Transport Demand

The increase in energy consumption by transport reflects increased transport by both passenger and freight during the period 1970 - 2004, as shown in Figure 1.2, and a greater increase in road transport than rail. These are increases of 85 % and 89 % during this period, while the UK population only increased by around 5 %, from 56m to 59m [U.K. DTI National Statistics, 2004*a*]. This disproportionate increase is in line with quality of life improvements.

Considering future trends, the number of vehicles globally is set to increase from 800 million to 1.2 billion by 2020. In the UK, new registrations of Commercial Vehicles (CV), for both freight and passenger transport, are predicted to rise by around 10 % between 2005 and 2010 [Automotive World, 2004]. Even this rise may be conservative as there was a 9.5 % increase from 2003 to 2004 [Dickeson, 2005]. Clearly, the growth of road-based transport is a trend that will continue and, in order to control a similar increase in energy consumption by transport and the related

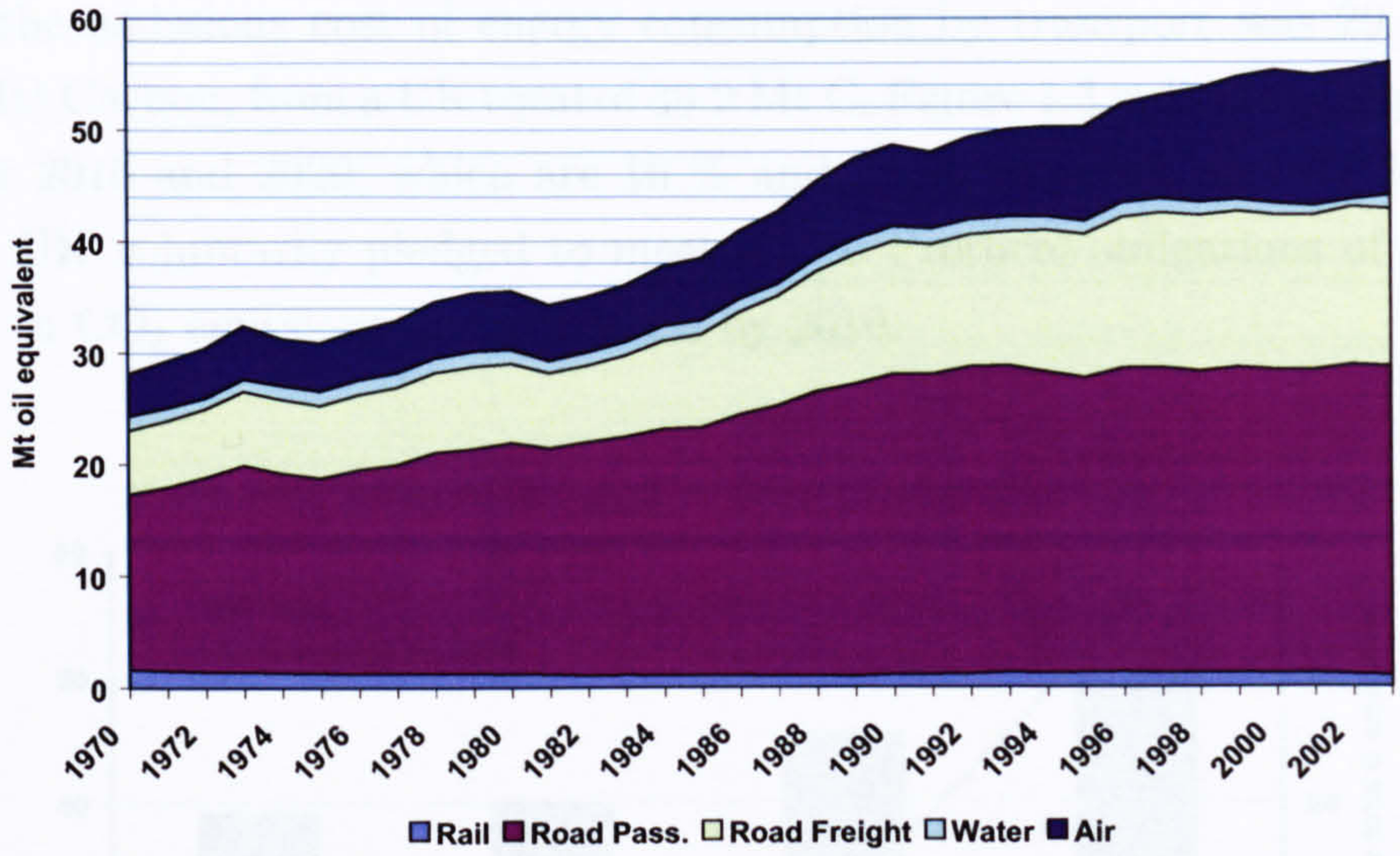
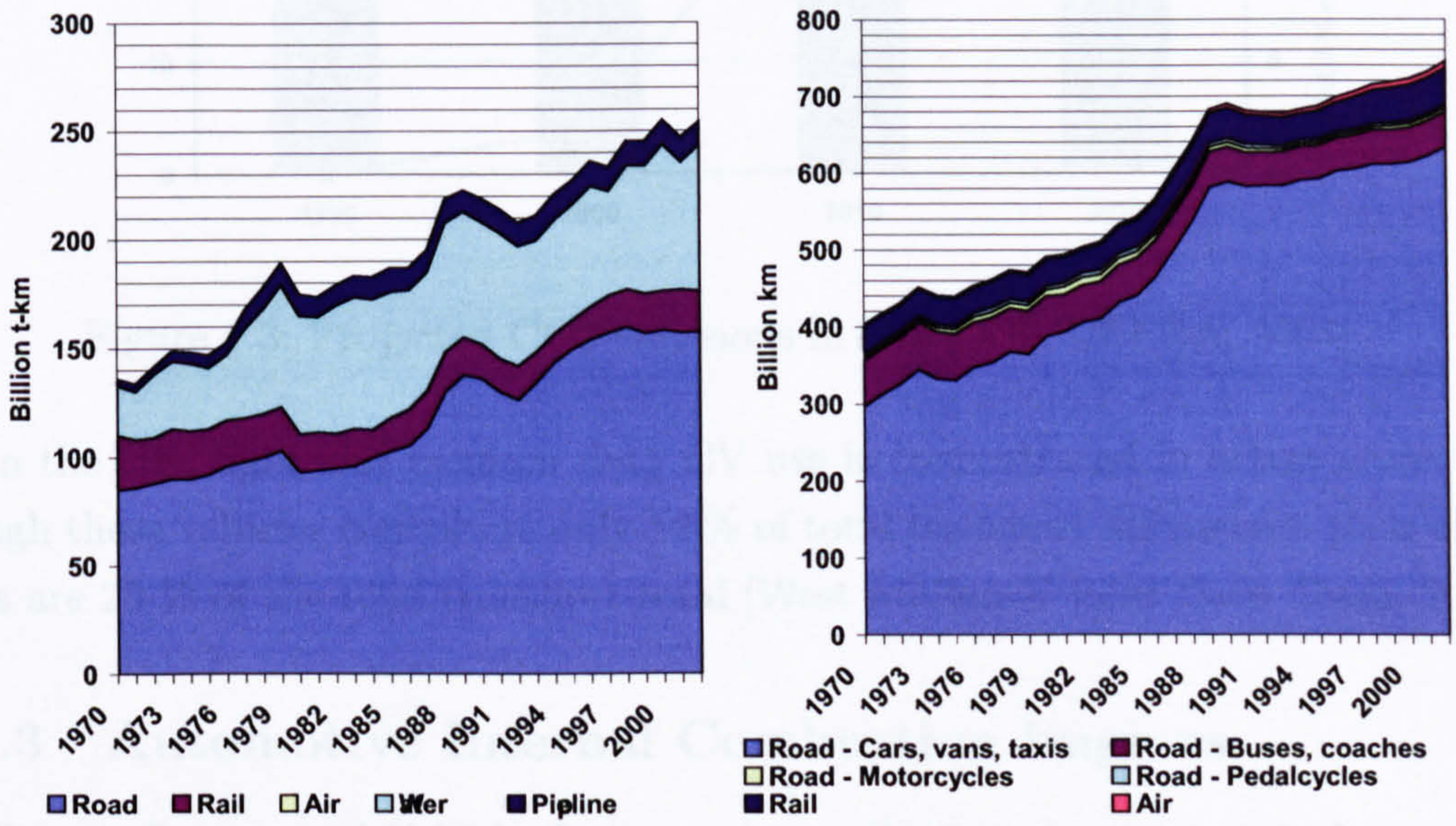


Figure 1.1: Transport energy consumption in UK [U.K. DTI National Statistics, 2004*b*].



(a) Goods tonne-km

(b) Passenger km

Figure 1.2: UK road transport [U.K. DTI National Statistics, 2004*b*].

costs, technical solutions must be found. These will not be solutions previously seen; the 1908 Ford Model T achieved fuel consumption figures of 9.4 - 11.8 litres per 100km (l/100km), yet the figures for the 2005 Ford Focus were 7.6 - 10.7 l/100km [U.S. DoE, 2005], an improvement of only 10 % in 97 years.

1.1.2 Carbon Emissions Levels

In 1990, the emissions cost of energy consumption by transport was 29.4 million tonnes (Mt) Carbon, from a UK total of 39.2 Mt C. Figure 1.3 indicates the projected figures for 2010 and 2020, which are 16 % and 28 % increases on 1990 levels. In 1997, the UK voluntarily pledged to meet Kyoto Protocol obligations of a 12.5 % reduction in CO_2 emissions on 1990 levels by 2010.

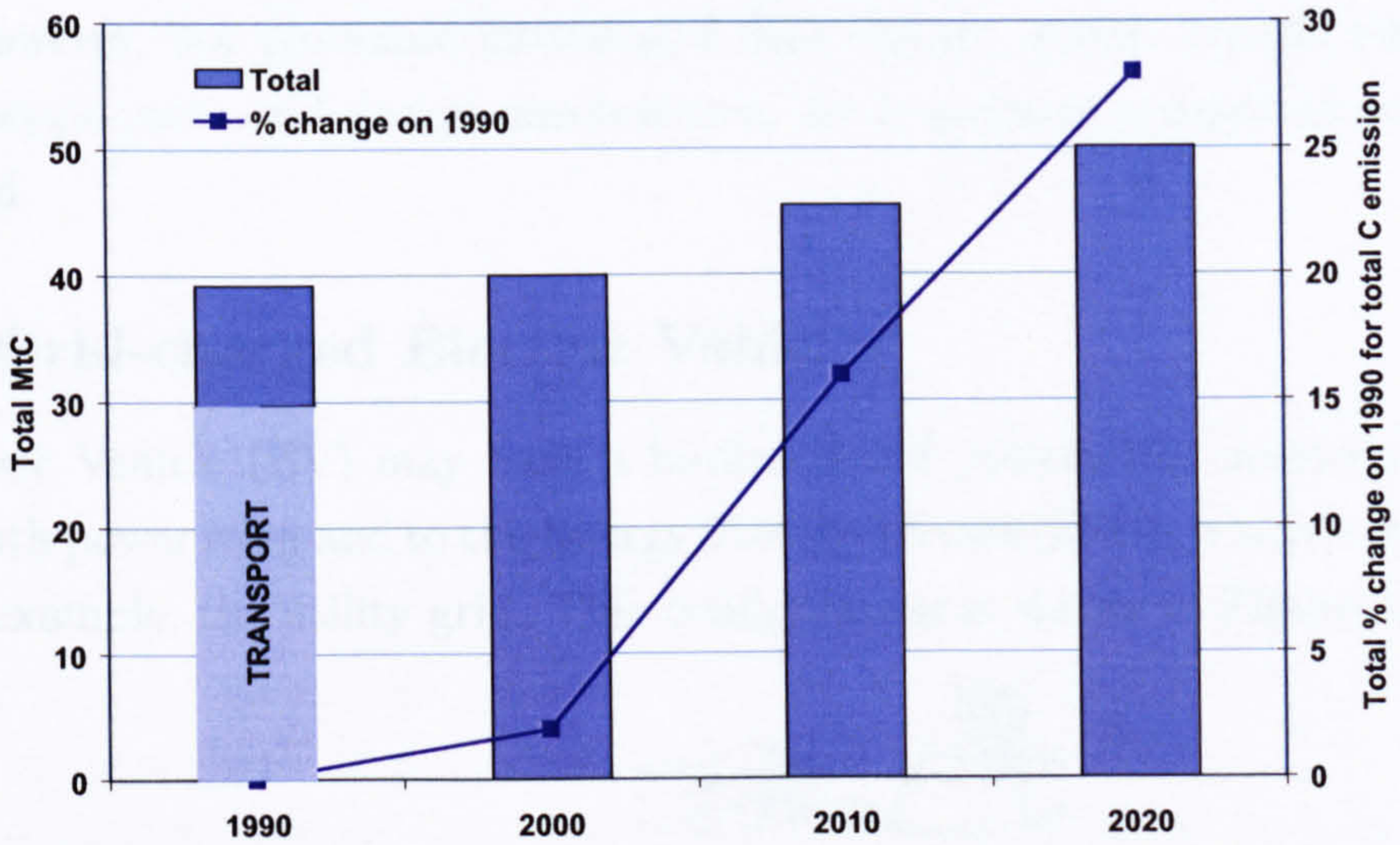


Figure 1.3: Projected CO2 emissions in UK [U.K. DEFRA, 2001].

In the UK, light and medium duty CV use is concentrated in urban areas. Although these vehicles contribute only 12 % of total transport kilometres, their emissions are 25 % of the road transport total [West Midlands Joint Data Team, 2001].

1.1.3 Automotive Internal Combustion Engines

Until now, Commercial Vehicles have employed diesel engines due to fuel economy, high torque and robustness, so market acceptance is good. Advanced automotive diesel engines using high pressure direct injection and turbocharger technology, are now widely available in Europe. Although Natural Gas engines have made inroads in the light Commercial Vehicle market, modern diesel engines are generally favoured over alternative fuel engines or alternative combustion technologies. Illustrative power curves for a modern Commercial Vehicle diesel engine, and a selection of diesel engines from German automotive manufacturers, are used in Chapter 8.

1.2 More-electric Vehicles

In order to control the energy consumption and related carbon emissions in line with Kyoto Protocol obligations and beyond, without reducing the number of passenger kilometres or freight tonne-kilometres travelled, the energy efficiency of vehicle powertrains must be improved. Technical options to achieve such improvements are varied, but characteristics such as emission-free at point of use, good operational performance and bi-directional operation for kinetic energy retention when decelerating have pushed development efforts towards the use of electric traction drives. However, the economic interests of fleet owners, which include regulatory issues, lifecycle costs and design obsolescence, are important considerations yet to be resolved.

1.2.1 Grid-charged Electric Vehicles

The Electric Vehicle (EV) may have a bi-directional powertrain, accelerating and braking with power from and to the Energy Storage Device (ESD), which is recharged from, for example, the utility grid. This configuration is shown in Figure 1.4.

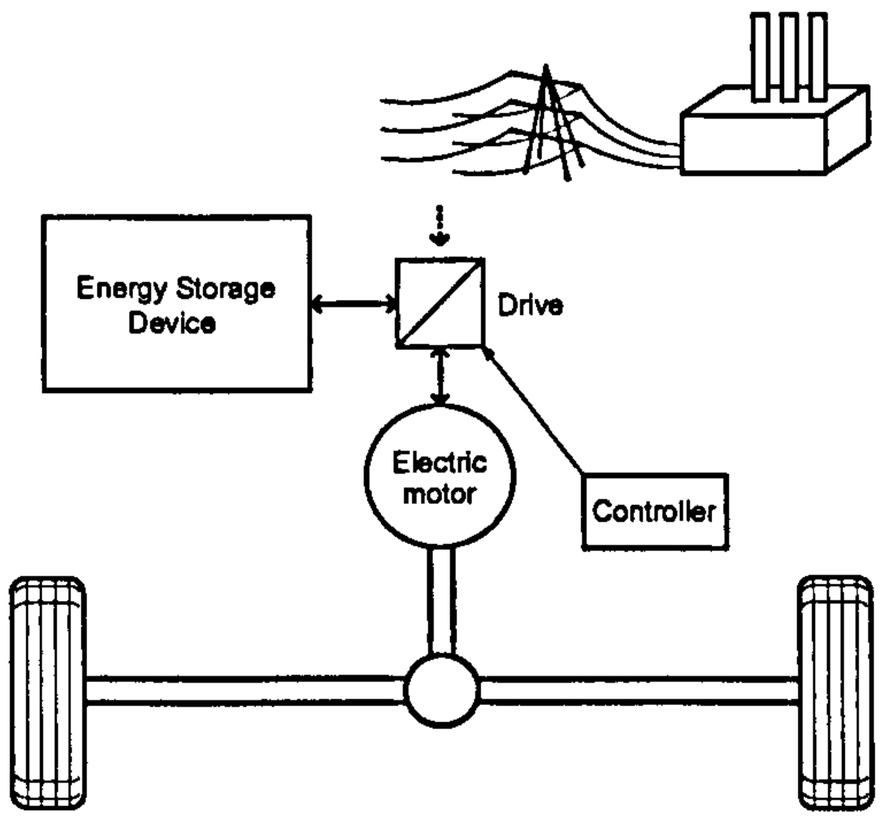


Figure 1.4: Grid charged EV configuration.

Efficiency of the EV powertrain is measured in a "well-to-wheel" analysis, which includes all energy transformation stages. The most readily available ESD is the electrochemical battery, which typically has the lowest turnaround efficiency.

Energy density for the ESD determines the energy storage capacity and therefore the vehicle range between recharging actions. Figure 1.5 illustrates the attractiveness of fossil fuels in this area. In order to increase the EV range, a larger (and heavier) ESD must be employed, which regardless of the unit cost requires more energy to move, thus reducing the cargo capacity or overall range.

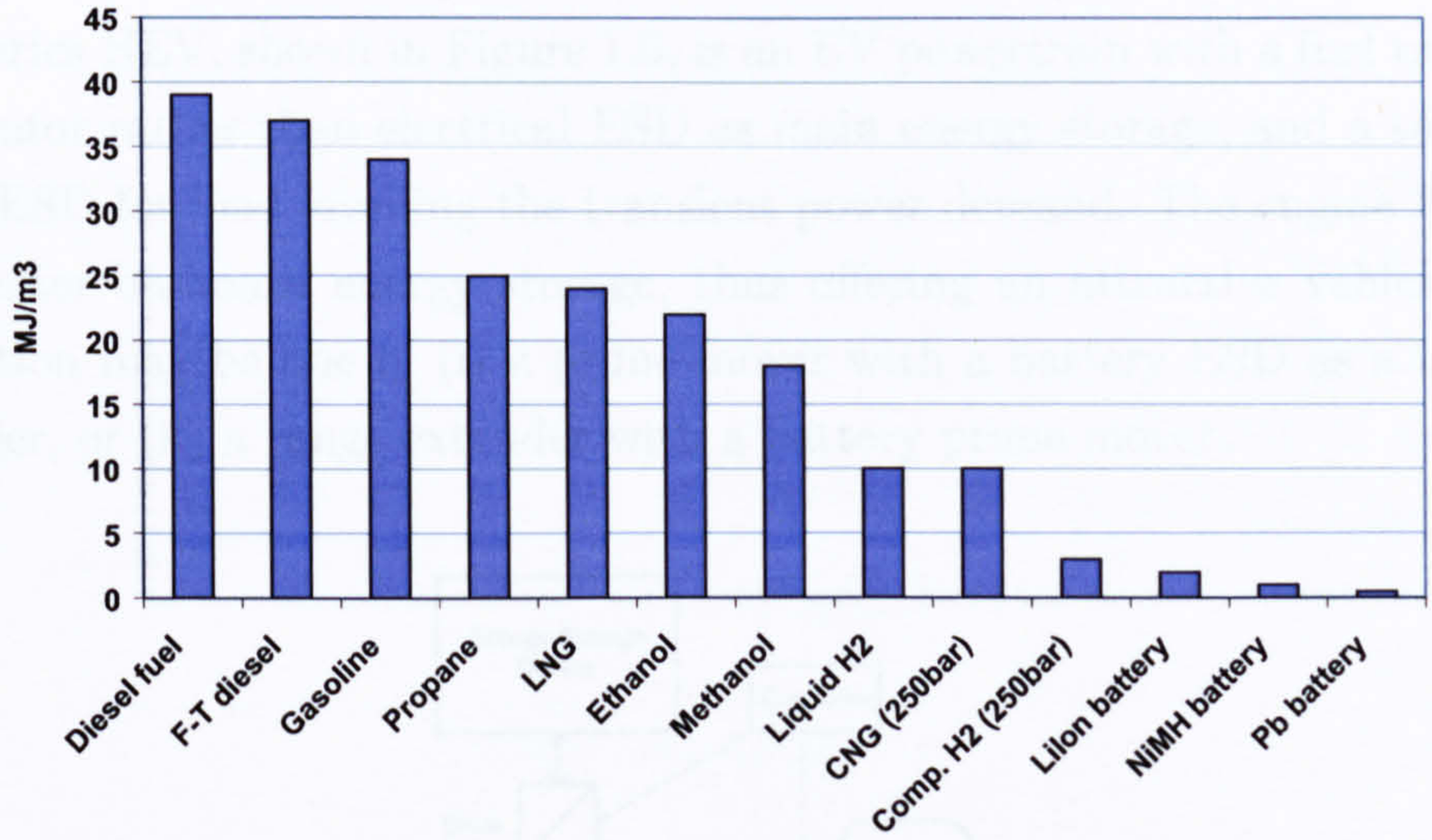


Figure 1.5: Energy density of fuels and ESD types [Husain, 2003].

1.2.2 Hybrid Electric Vehicles

The attractive operational characteristics of the EV and conventional powertrains are quite different, and by combining both in one Hybrid Electric Vehicle (HEV) powertrain, their advantages become complimentary while disadvantages are negated. However, a new hindrance becomes technical complexity and the unit cost of two powertrains in one vehicle.

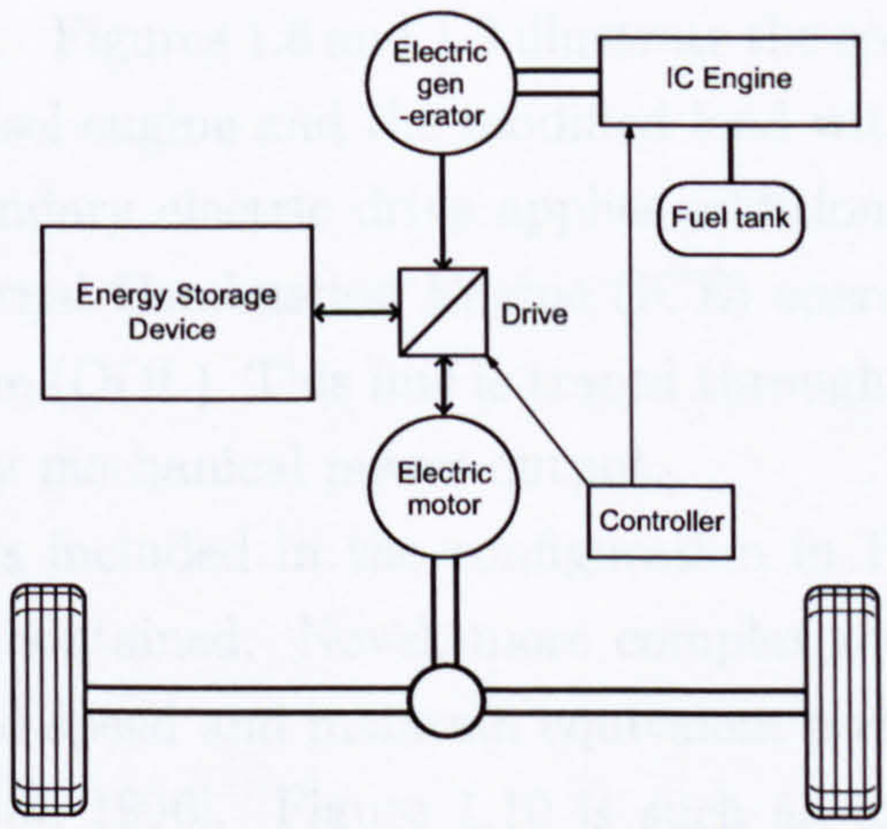


Figure 1.6: Series configuration HEV.

The "charge depleting strategy" of HEV powertrain design and control resembles the EV powertrain, where the range is extended by a Prime Mover Unit (PMU).

Alternatively, the "charge sustaining strategy" involves more integrated design and control of the powertrain components.

The Series HEV, shown in Figure 1.6, is an EV powertrain with a fuel tank, ICE and generator rather than electrical ESD as main energy storage, and a secondary electrical ESD for load levelling the transient power demand. The engine fuel tank allows greater on-board energy storage, thus offering an attractive vehicle range. This function may be one of (i) a prime mover with a battery ESD as a transient load leveller, or (ii) a range extender with a battery prime mover.

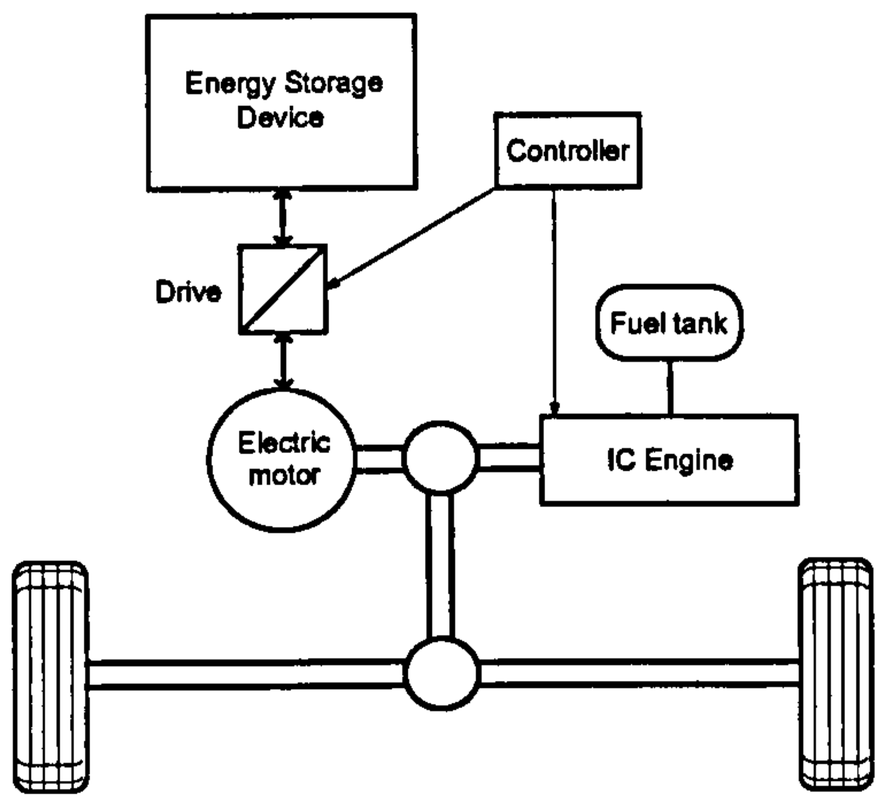


Figure 1.7: Parallel configuration HEV.

The Parallel HEV, shown in Figure 1.7, is a conventional powertrain with engine and mechanical drive, enhanced with a secondary electric drive for load levelling the transient power demand. Figures 1.8 and 1.9 illustrate the specific fuel consumption map of a typical CV diesel engine and the modified load with use of the secondary electric drive. The secondary electric drive applies additional positive or negative torque to move the Internal Combustion Engine (ICE) operating point load to the Optimum Operating Line (OOL). This line is traced through all points of minimum fuel consumption for any mechanical power output.

No further gearing is included in the configuration in Figure 1.7 so the same engine speed must be maintained. Novel, more complex mechanical designs exist to modify the torque and speed and maintain equivalent power for gasoline engines [Toyota, 2004; Bäckström, 1996]. Figure 1.10 is such an example consisting of a generator, planetary gear set, torque belt and a motor.

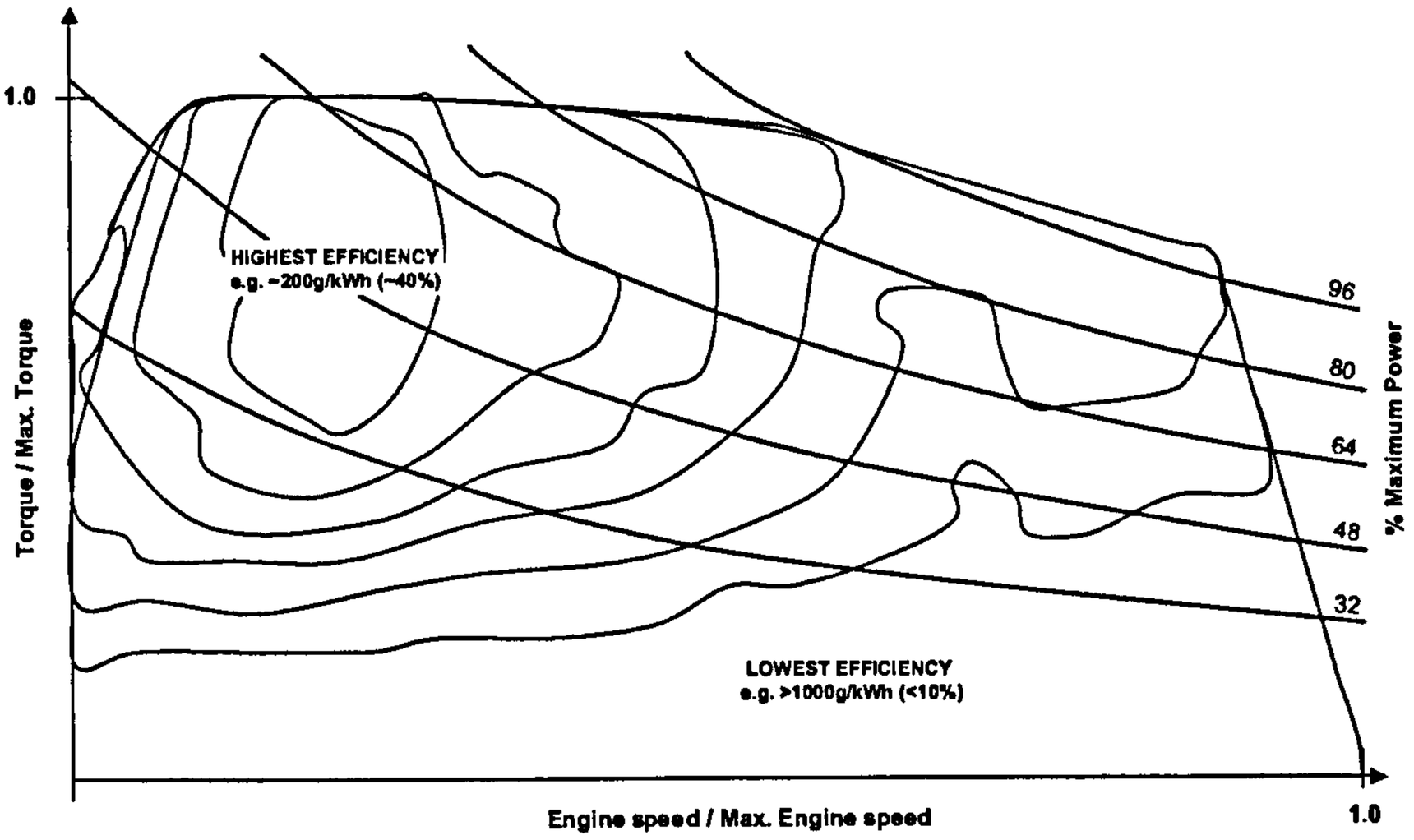


Figure 1.8: Turbocharged diesel engine BSFC map, with constant power lines at % of maximum power. Lowest and highest effiency regions marked.

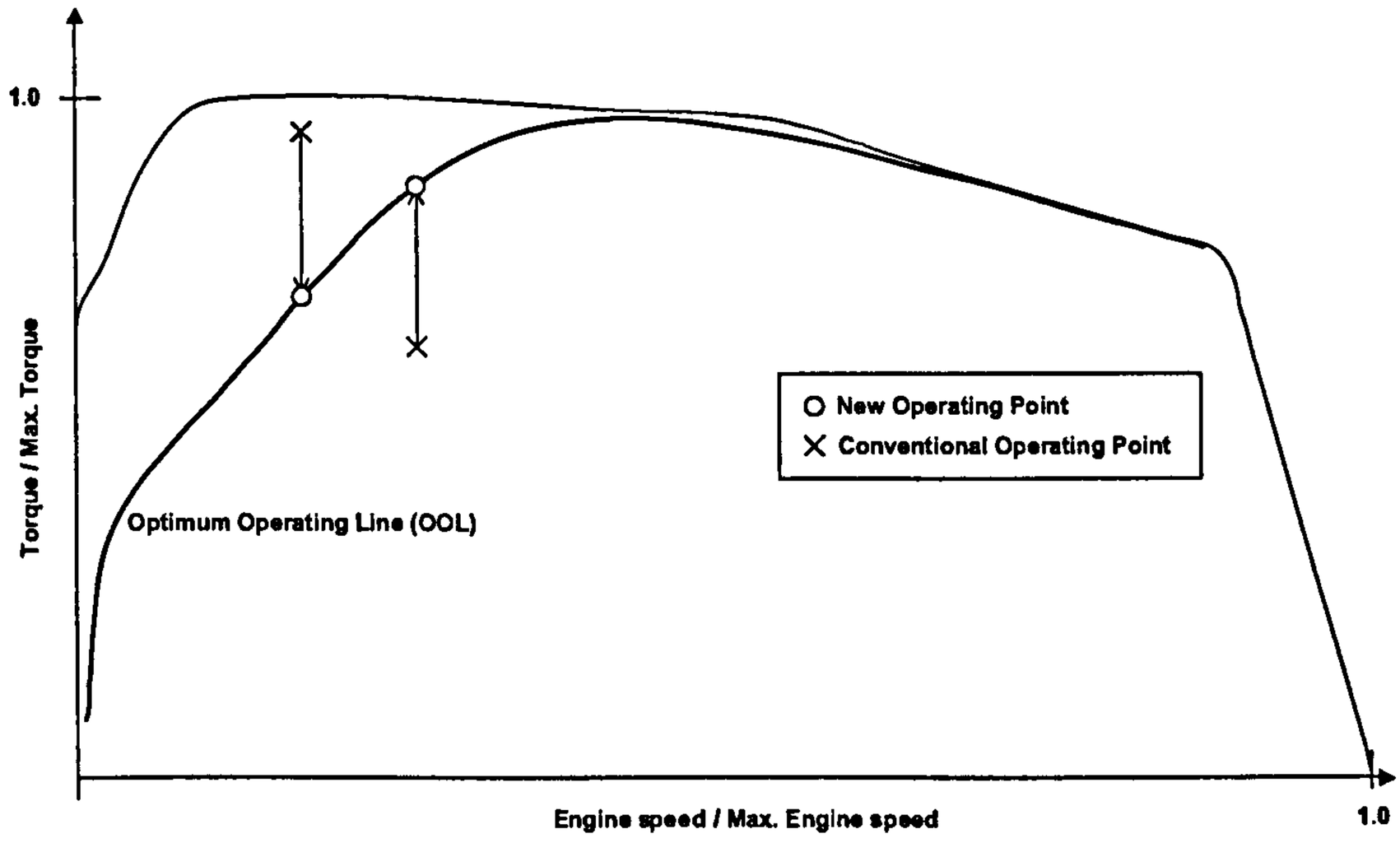


Figure 1.9: New operating point on Optimum Operating Line.

1.2.3 Duty Cycle

The suitability of these various HEV powertrains to particular applications is different in each case. Existing applications of EVs are milk floats and airport or golf buggies, where range and performance are not essential characteristics.

The majority of light and medium duty CVs are part of easily-identified fleets of delivery vehicles and passenger transit buses. Significantly, monitoring the duty cycle is straight forward using a digital tachometer. Ideal duty cycles for HEV powertrains include significant transient operation, such as frequent stops and starts,

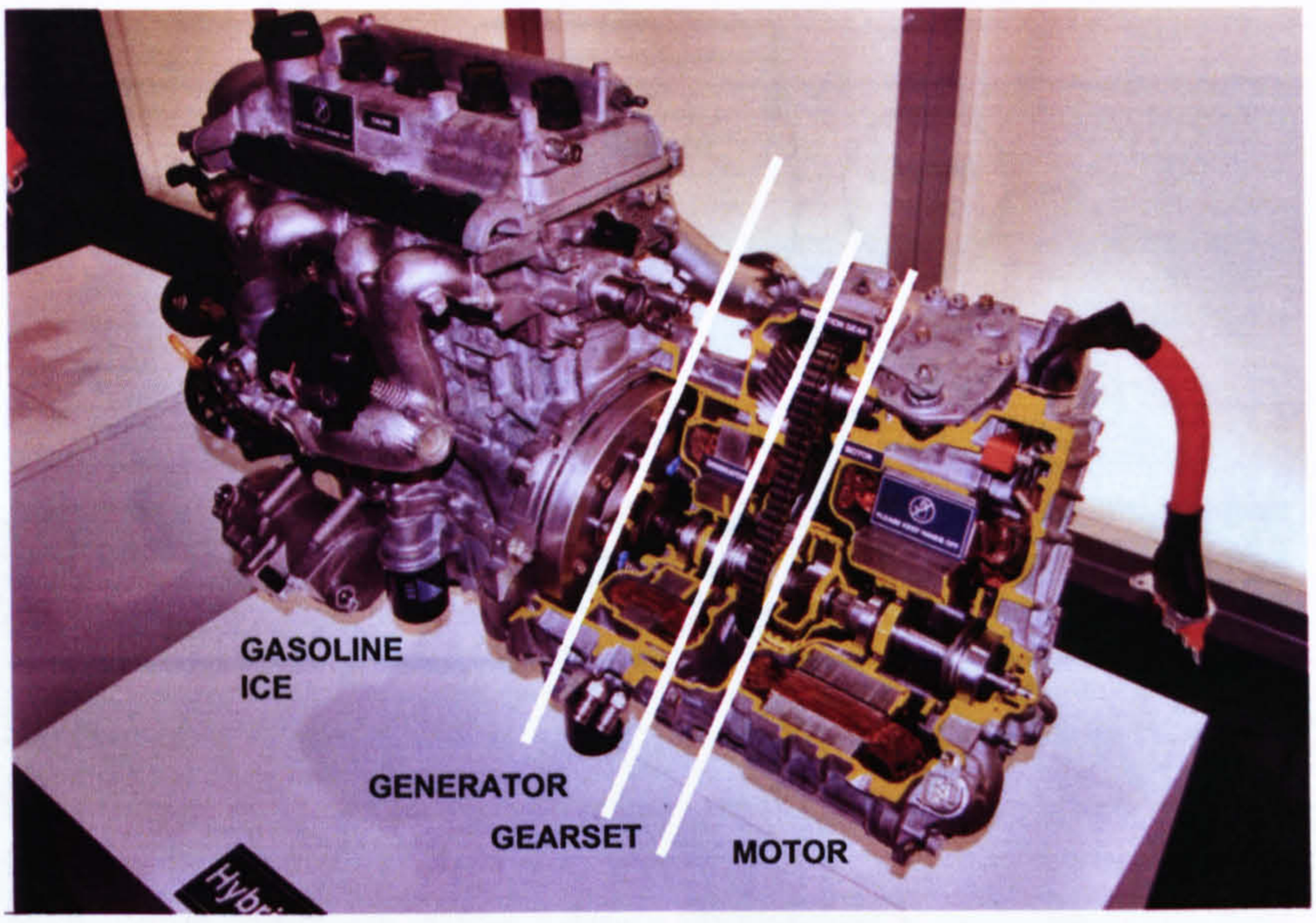


Figure 1.10: Cutaway of the Toyota Hybrid System.

for regenerative energy braking. The Series HEV is well suited to a passenger transit bus or refuse collection vehicle (a New York bus makes 8 scheduled stops per km, plus stops for traffic lights and congestion).

The Parallel HEV is well suited to a freight delivery vehicle because the duty cycle requires more flexibility. For motorway driving, the conventional mechanical drive is efficient in steady-state operation.

1.3 Electric Machines in HEV Powertrains

Three electric machine applications are major components of these HEV powertrains. The Generator and Traction Motor (direct drive or geared) are part of the Series HEV. An Integrated Motor Generator is part of the Parallel HEV powertrain.

1.3.1 Generator

The generator is sized to match the rated power of the engine and, without gearing, the speed range of the engine for a Series HEV. The engine-generator package, or Prime Mover Unit (PMU), shown in Figure 1.11 closely resembles an engine generating set (genset) with modified enclosure and power conversion. The generator should meet variable speed operation in order to operate at different positions on the engine OOL, according to power demand, although there are constant power versions for range extension. Figure 1.12 illustrates the typical volume relationship between ICE and generator for an APU.

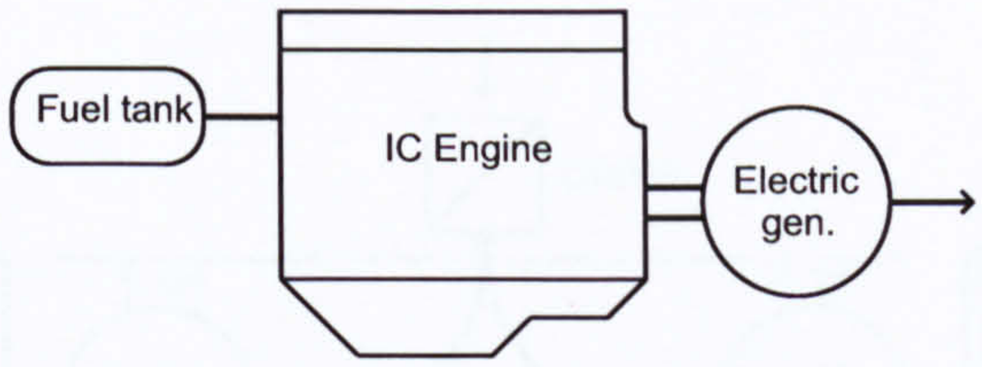


Figure 1.11: IC generator configuration.

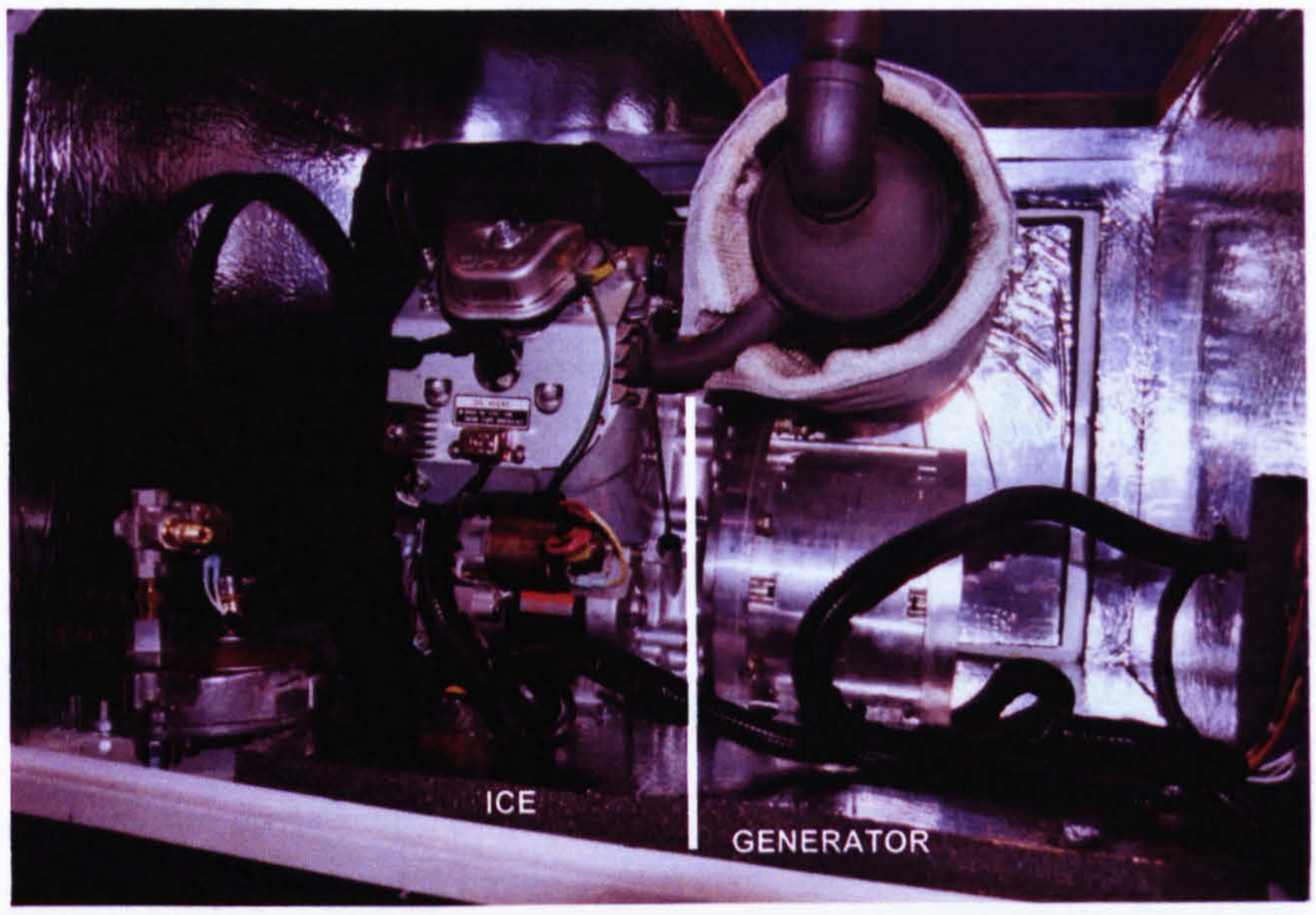


Figure 1.12: Honda 12kW LPG engine and GenSmart S22AA-002 generator [Light Engineering Inc., 2003].

1.3.2 Traction Motor

Figure 1.13 illustrates a "hub-mounted" motor, similar to the "in-wheel" motor. Direct drive or geared axle drive are alternative motor mountings, as shown in Figure 1.14 including gearing. The motor and drive must also operate in generator mode to provide regenerative braking, and be capable of field weakening, if the speed range should be extended. The rotor inertia should be low to minimise unsprung mass for vehicle drivability and ride comfort [Benoudjit et al., 2000]. Figure 1.15 illustrates an external rotor motor in an application where total mass is important.

1.3.3 Integrated Motor Generator

The Integrated Motor Generator (IMG) is also referred to as the Integrated Starter Alternator (ISA) and other combinations of these names, plus "Damper". The function is to load-level the powertrain demand in transient operation. As the single

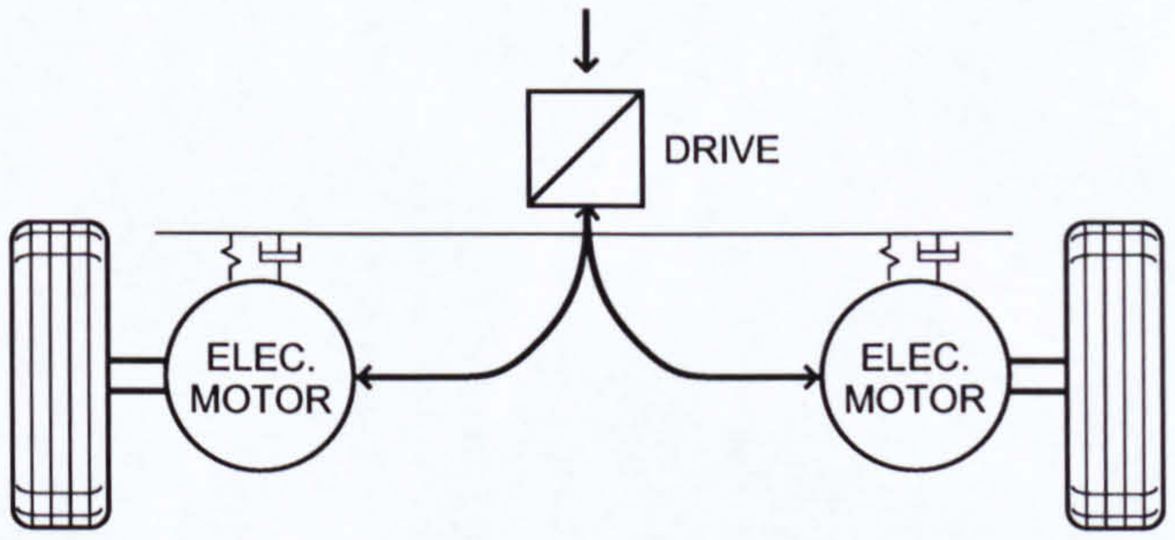


Figure 1.13: Wheel motor configuration.

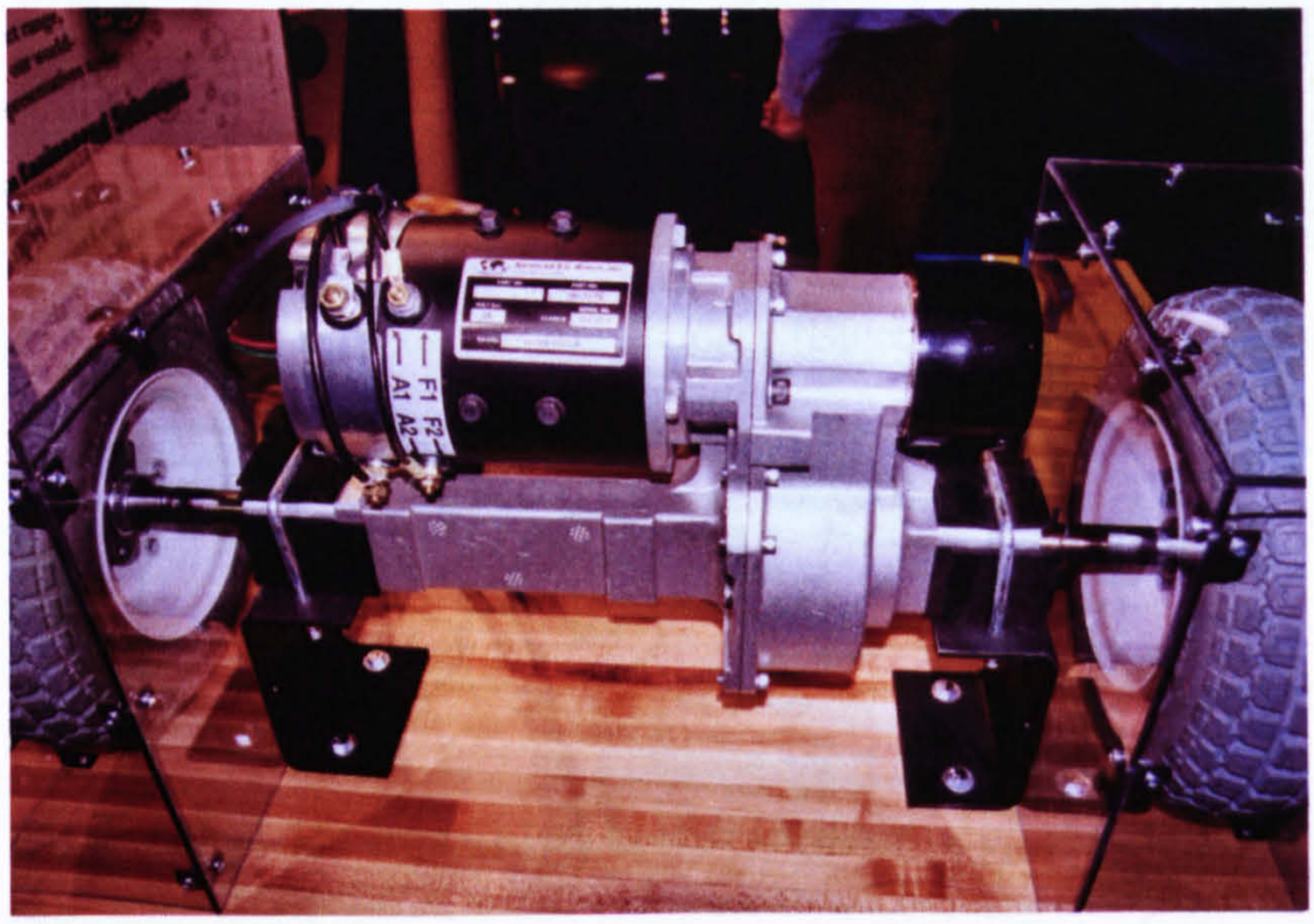


Figure 1.14: Axle-mounted traction motor [Advanced DC Motors Inc., 2004].

electric machine, it also starts the engine and services the auxiliary electrics and so operates in both motoring and generating modes. Figures 1.16 and 1.17 illustrate "crankshaft-mounted" or "in-line" IMGs. Other positions, such as belt-mounted in the conventional alternator position, or integrated with clutch(es) and transmission are also possible. Figure 1.18 illustrates the housing and armature of a crankshaft mounted ISA for a CV engine, which mates with the ICE flywheel housing.

The integration of electric machines into the powertrain requires consideration of the size and shape, the housing mate, thermal aspects, dynamic aspects such as vibration and acoustic noise and the mechanical structure. The machines shown in Figures 1.10 and 1.14 illustrate the high and low levels of integration.



Figure 1.15: In-wheel motor of the Ion scooter [Electric Vehicle Technologies, 2004].

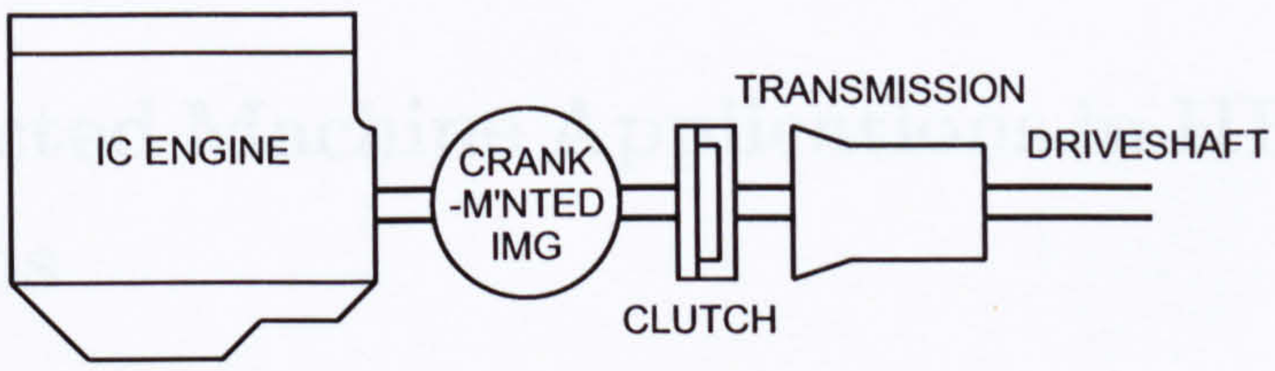


Figure 1.16: Integrated Motor Generator configuration.

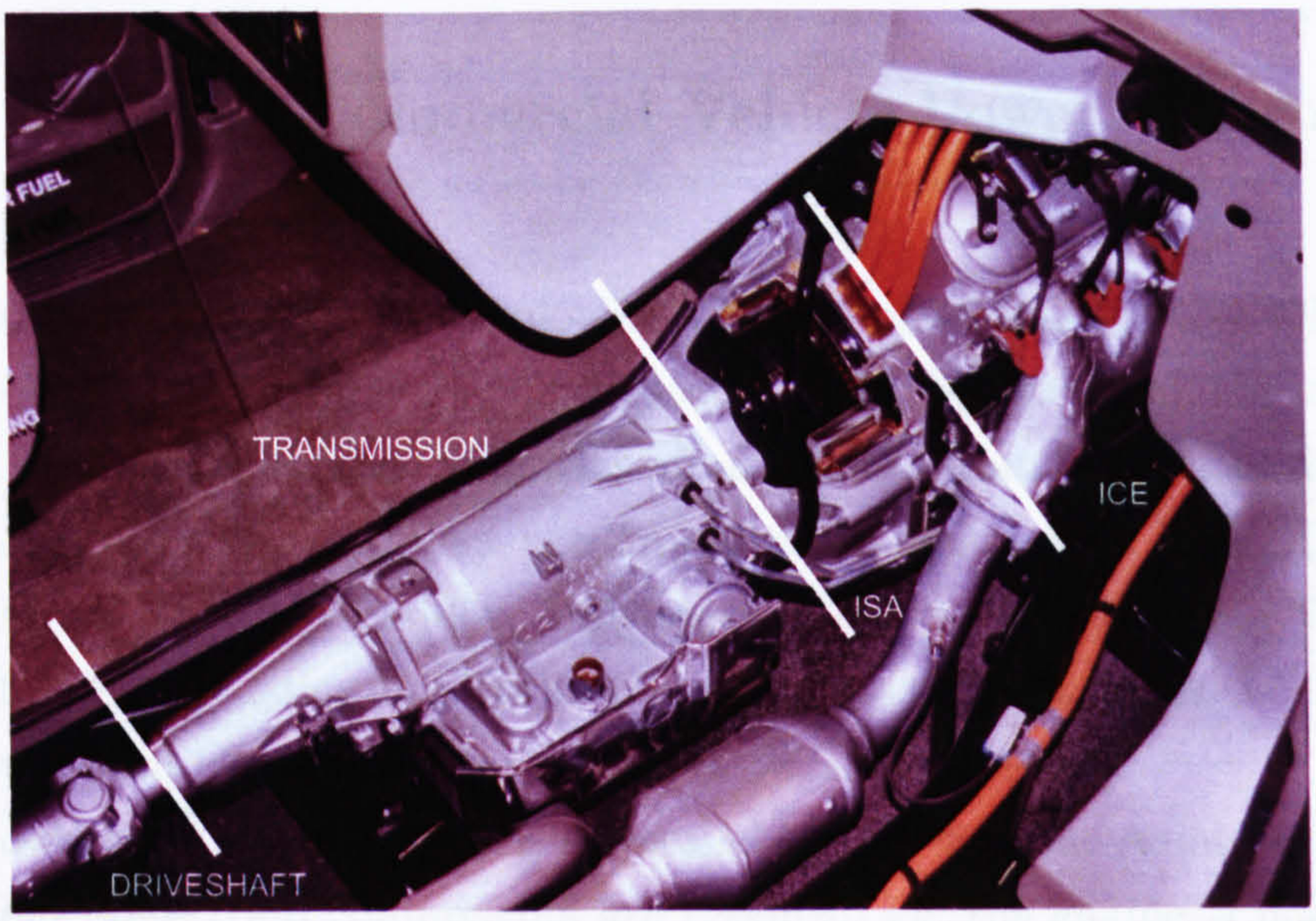


Figure 1.17: Cutaway of engine-transmission interface, exposing an Induction ISA in the Parallel Hybrid Truck [General Motors, 2004].

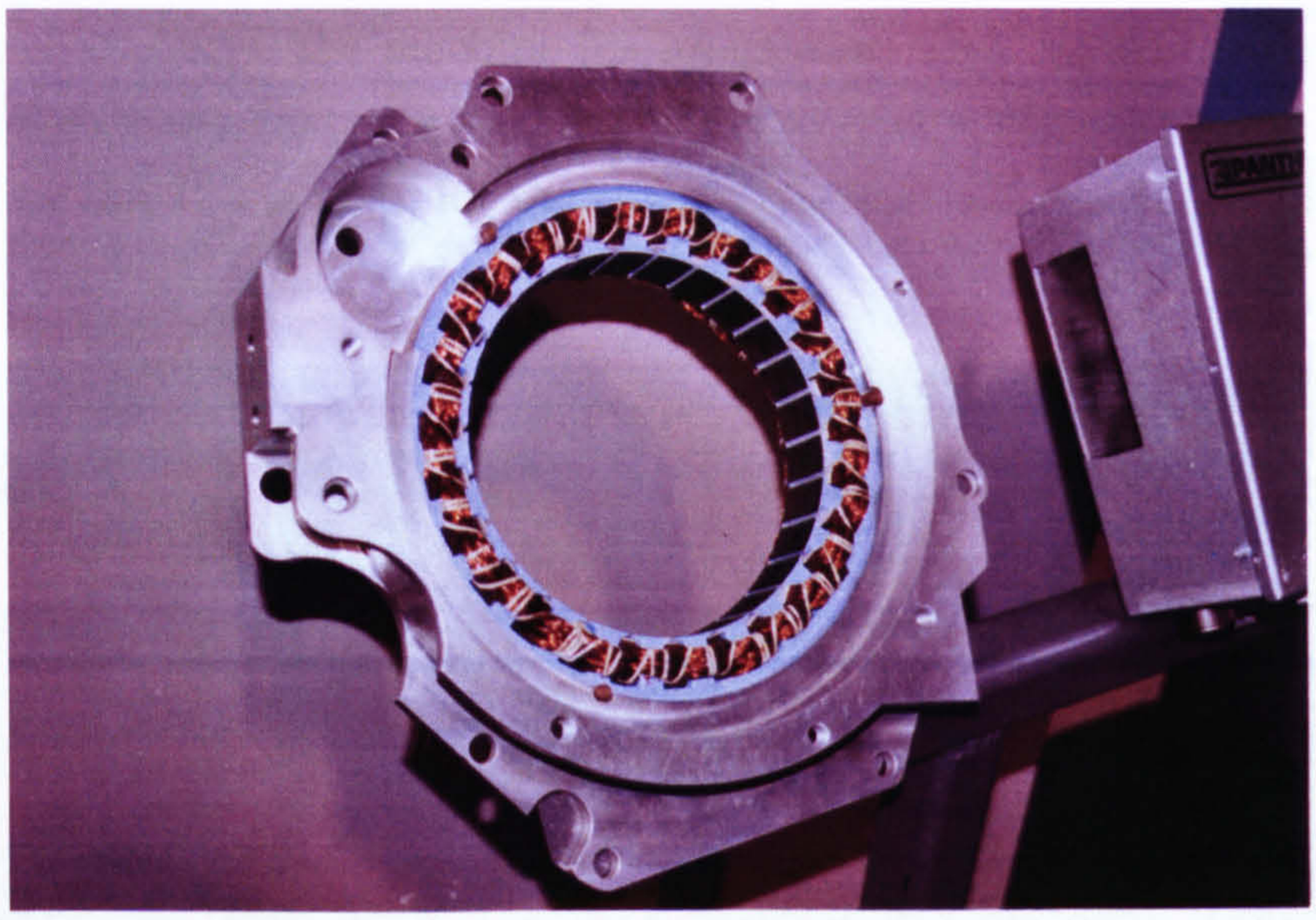


Figure 1.18: ISA armature for a CV engine viewed from the engine side [Enova Systems, 2004].

1.4 Selected Machine Applications in HEV Powertrains

Two of the machine applications described in Section 1.3 provide case studies for the application of Axial Flux machines, for which design work has been undertaken.

1.4.1 7.5 tonne Commercial Vehicle Powertrain for Urban Deliveries

There is strong motivation for employing a hybrid powertrain in this vehicle application. The vehicle operation is concentrated in urban areas where the traffic flow is congested with frequent stops. Vehicles often operate from depots, so the operation is well known, allowing confident prediction of the demand. A DTI LINK project, between Imperial College London, University of Bath, I-Power, Iveco Truck, Spicer Driveshaft, TNT Logistics and Turbo Genset partners, undertakes the development of this powertrain [*ForesightVehicle Project: MIHPOW*, 2005].

The powertrain configuration is a Parallel hybrid with an Axial Flux IMG. The conventional powertrain components are retained, i.e. the engine is not downsized, and the electric drive is incorporated between the engine and existing transmission with an additional clutch, as shown in Figure 1.20. The task here is to determine the required electric drive power rating according to the modes of operation and typical

loading, and to design the machine for integration with engine and transmission. The performance requirements are high efficiency over a wide operating range, i.e. a large area on the $T - \omega$ map, for the complete electric drive including inverter and battery.



Figure 1.19: Heavy Goods Vehicle chassis used for HEV project.

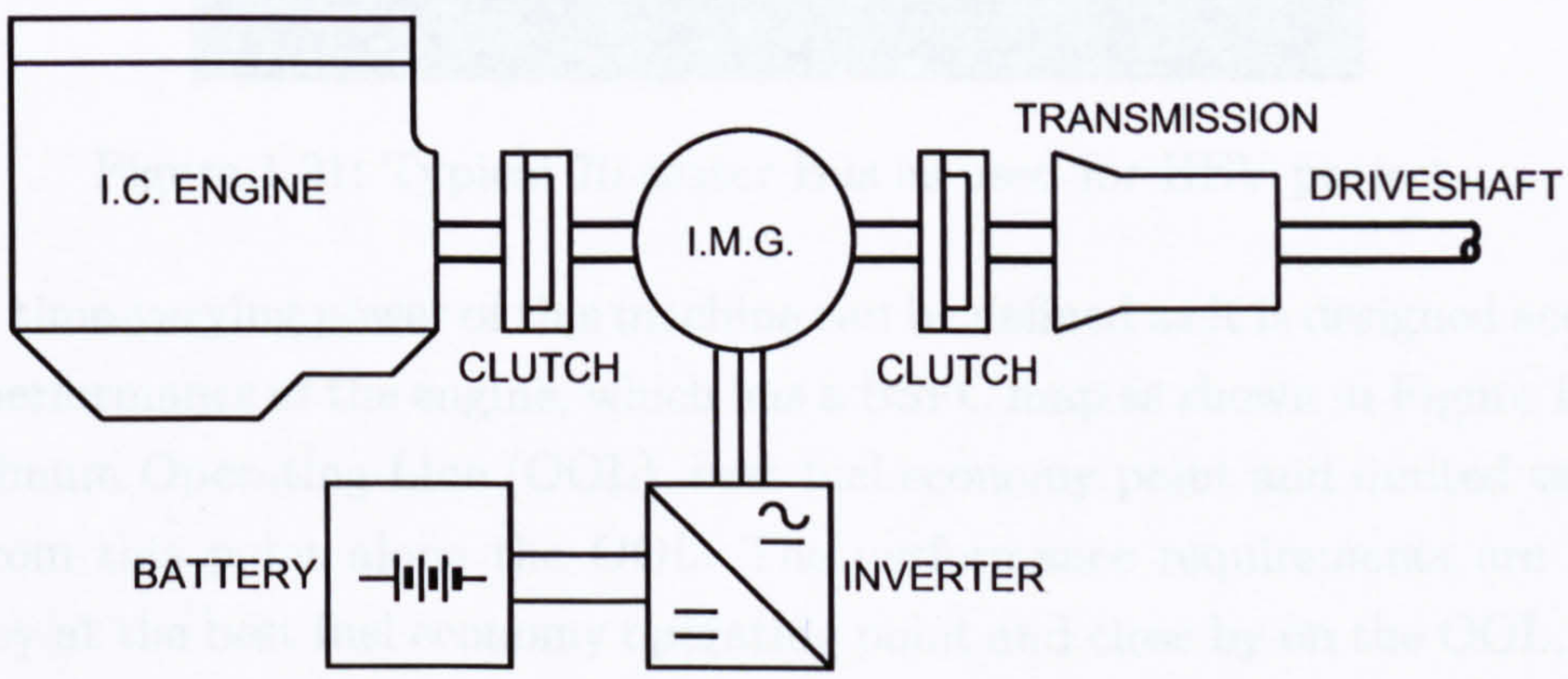


Figure 1.20: Parallel hybrid powertrain configuration for Motor-Generator machine application.

1.4.2 70-seater Bus Powertrain

This vehicle is around 10.5m in length, as shown in Figure 1.21, and typically the maximum number of passengers is around 90, with 70 seated [Wrightbus, 2004]. There is strong motivation for employing a hybrid powertrain in this vehicle application. The generally low speed operation, with frequent stops, provides good opportunity to capture kinetic energy through regenerative braking and store to reuse for traction. The Series hybrid configuration is favoured because it avoids the mechanical losses of employing a transmission, which improves the electric powertrain efficiency. Furthermore, the electric powertrain technology has matured for pure electric buses, although the limitations with battery energy storage have limited their market penetration. The engine–generator prime mover unit (PMU) provides conversion for the large stored energy in the fuel, thus significantly extending the vehicle's range. The battery ESD capacity for EV operation is considered as the PMU serves as this range extender and so operates over extended periods.



Figure 1.21: Typical 70-seater Bus as used for HEV project.

The time-varying power of this machine can be defined as it is designed according to the performance of the engine, which has a BSFC map as shown in Figure 1.8 with an Optimum Operating Line (OOL), best fuel economy point and limited variation away from this point along the OOL. The performance requirements are highest efficiency at the best fuel economy operating point and close by on the OOL, for the electric machine and rectifier.

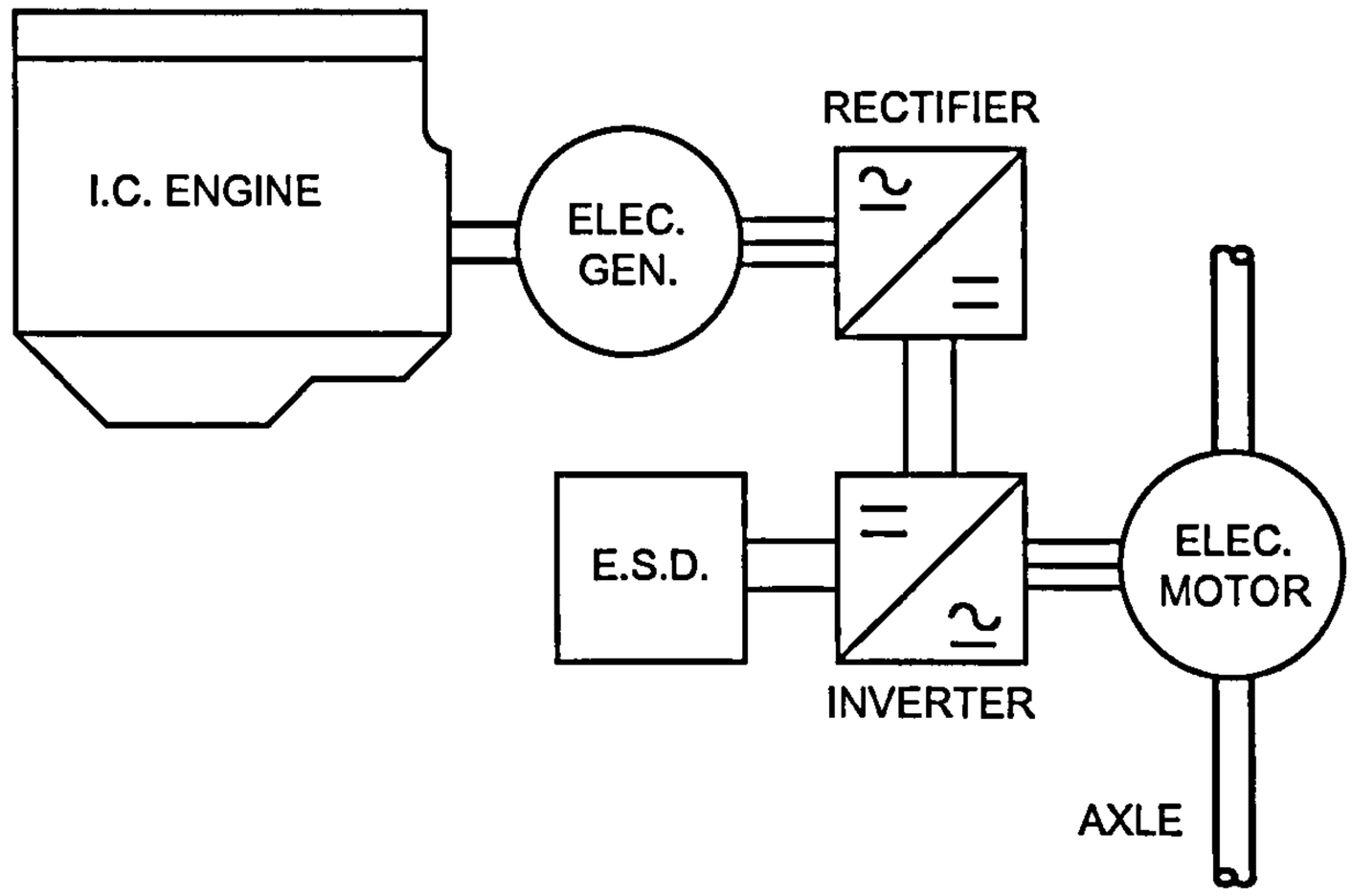


Figure 1.22: Series hybrid powertrain configuration for Generator machine application.

1.5 Types of Electric Machines

The main types of electric machines that are considered for HEV powertrain applications are Direct Current, Asynchronous (Induction), Synchronous Reluctance and Alternating Current Permanent Magnet.

1.5.1 Categorised by Supply Voltage

Direct Current or Alternating Current describe the machine supply voltage. Direct Current (DC) machines are a common traction machine in EVs [Campbell, 1974]. The popularity of DC machines grew due to simple variable voltage control. However, efficiency loss in voltage converters and the advances in high frequency switching, which easily facilitate an Alternating Current (AC) supply, mean this advantage no longer exists.

The static field of DC machines is either wound (in series or parallel with the armature) or Permanent Magnet (PM). Advances in PM materials offered high power density, which made Brushed Permanent Magnet (BPM) machines popular. DC machines are commutated by a brush unit, which requires maintenance. As brushes wear, the sparking may become a concern. As an example, during bench testing of two Axial Flux BPM motors [Lynch Motor Co. Ltd., 2001; Perm Motor GmbH, 2003] for a small regenerative braking study on a 10 kW Series HEV powertrain, brush units on both machines required replacing within 500 hours transient operation.

1.5.2 Categorised by Speed of Stator Field and Rotor

The AC machine excitation field and rotor may rotate synchronously or asynchronously, whereby a slip speed defines the difference. Asynchronous (Induction) machines, typically used for industrial application, have inferior torque density and efficiency. Advances in high frequency switching have made control of the machine supply simple, making Synchronous machines attractive. The Wound Rotor Synchronous machines, such as those used in large scale power generation, offer certain advantages, but torque density is not one of them, so Permanent Magnet Synchronous machines (PMSMs) are preferred for traction applications. The types of synchronous electric machines are illustrated in Figure 1.23.

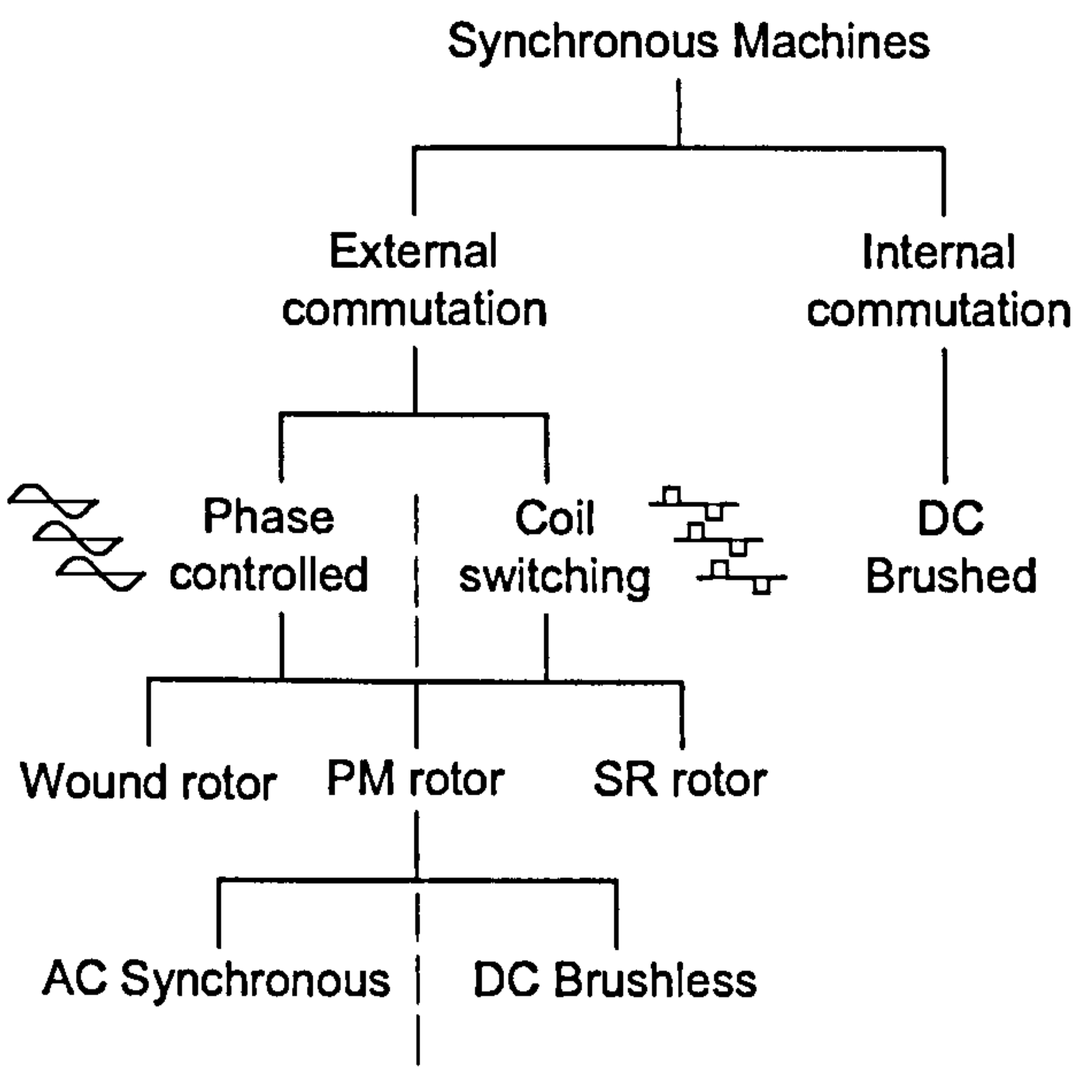


Figure 1.23: Categorisation of types of synchronous electric machines.

1.5.3 Categorised by Source of Rotor Field

The AC Synchronous machine may have a rotor field winding with a separate supply, as in the case of the Wound Rotor machine, an array of Permanent Magnet (PM) rotor poles, or no rotor excitation as in the case of a Synchronous Reluctance machine.

The BPM DC machine described above has a static PM field with a rotating armature. The Brushless DC machine is the reverse of this; a rotor with a PM array and stationary stator windings, which does not require a brush unit. This reduces maintenance requirements and improves efficiency.

Differentiation between the PM AC Synchronous (PMSM) and the PM Brushless DC (BLDC) machines is based on the supply waveform and the induced emf. The BLDC machine is excited by coil switching (i.e. almost rectangular current waveforms with respect to time) and is sometimes referred to as a "switched PM" machine. The PMSM is fed with sinusoidal currents.

The Transverse Flux machine (TFM), which offers a very high torque density, is sometimes described as another type of PM machine. This machine is predominantly a type of reluctance machine as the ratio of reluctance torque to total torque is high. Although the current flow direction within the machine is different to the Axial and Radial Flux topologies, the airgap and similarly the flux crossing it is either Radial or Axial to the shaft.

1.5.3.1 Permanent Magnet Materials

Permanent Magnets (PMs) are manufactured with rare earth materials. These have a high coercivity, which ensures they are not permanently demagnetised by strong opposing fields within their operating temperature range. Neodymium-based PMs offer the highest energy product, i.e. strength of field, but do not operate at high temperatures. Samarium-based PMs are weaker but can operate at a higher temperature.

1.6 Types of Stator Windings

The stator windings of most multi-phase AC machine types are similar. There are several design parameters, but these are generally not machine type-specific.

1.6.1 Slotted Core Windings

The vast majority of machines feature coils inserted into core slots. The endwindings are the coil turns at each end of the slots, whose length depends on the coil throw. The slot fill factor is the proportion of slot cross sectional area filled with copper. Smaller diameter wire allows a higher slot fill factor. The core slots result in a non-constant airgap permeance function, and variation in the torque output is due to the cogging torque.

Slots may contain conductors belonging to one or two coils in different phases. Two coils per slot is more common, but one coil per slot offers greater protection against phase-to-phase shorts. Coils at different slot depth positions belong to multi-layer windings.

Coils which occupy several slots are part of a distributed winding. This has overlapping endturns of different phases, increasing the risk of phase-to-phase shorts. The labour of winding this can be intensive. Coils which occupy only two slots are part of a concentrated winding. If these slots are either side of a single tooth (i.e. with a coil throw of one slot), the winding is often referred to as modular. This has less risk of phase-to-phase shorts and has less labour involved in the winding.

1.6.2 Airgap Windings

There are a small number of machines with coils not placed in slots. These are usually placed in front of a slotless core providing the flux return and, as such, the magnetic airgap length is much longer. The airgap flux has no preferential path through the winding, as there is no variation in the permeance [Chen et al., 1999]. Therefore, the winding conductors experience the full flux variation.

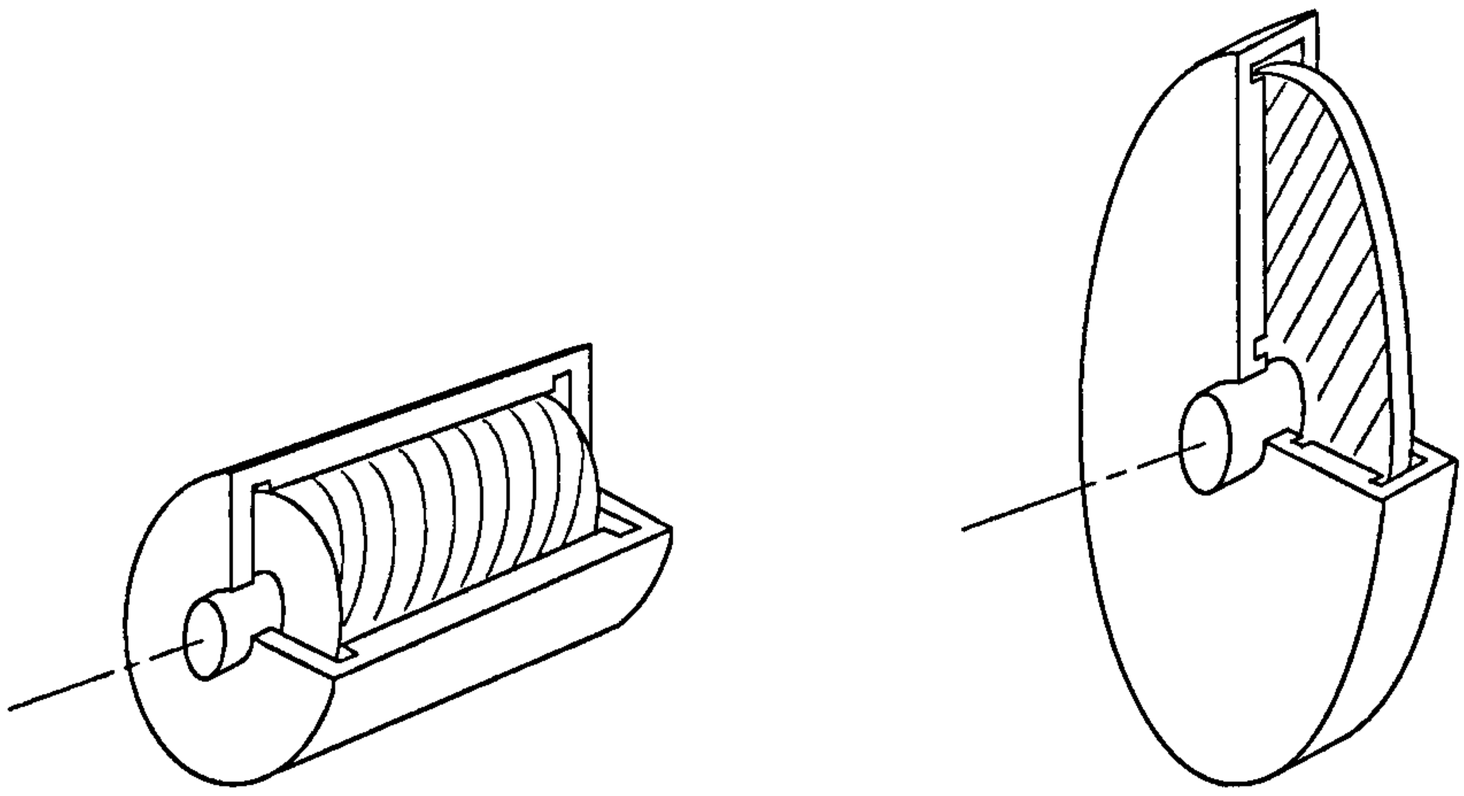
1.7 Electric Machine Topologies

The electric machine selection with a view to integrating with other powertrain components (ICE, clutch, transmission, etc.) must consider the mechanical aspects of machine envelope, sensitivity to heat and rotating inertia.

The Radial Flux topology is well established. The Axial Flux topology is relatively uncommon. The names "Radial" and "Axial" Flux refer to the airgap and electromagnetic arrangement. The airgap areas, over which electromagnetic torque is developed for these topologies, are illustrated in Figure 1.24. The Radial Flux has an open-ended cylindrical airgap area, while the Axial Flux has a holed-disc airgap area.

In automotive traction applications, the space envelope is the first criteria. HEV passenger cars in production all use Radial Flux machines with a short axial length [Toyota, 2004; Honda, 2001; Ford, 2005], mainly because the experience among machine designers lies in Radial Flux machines.

Publications comparing Radial Flux and Axial Flux machine topologies do not differentiate between topology related characteristics, such as aspect ratio, and those that are design-dependent, such as pole number of cooling regime. The comparisons are collated here and summarised in Table 1.1.



(a) Radial Flux topology: $\theta - z$ plane airgap

(b) Axial Flux topology: $r - \theta$ plane airgap

Figure 1.24: Radial and Axial Flux electric machine topologies.

Table 1.1: Summary of Axial and Radial Flux characteristics for non-integrated motors in traction applications.

Characteristic	Axial Flux	Radial Flux
Machine designer experience	Limited	Extensive
Airgap	Constant axial position	Constant radial position
Axial length	Short	Typically longer
Diameter	Typically larger	Standard
Desirable aspect ratio ($l/\varnothing$)	$\leqslant 0.3$	> 0.5
Specific torque (avoiding hollow volume)	Higher (min. hollow vol.)	Lower (more hollow vol.)
Dynamic response (low rotor inertia)	Higher (low)	Lower (higher)
For desired pole number	> 12	< 12
Efficiency	= (design dependent)	= (design dependent)
Cooling	Air & liquid	Typically liquid
Cooling Surface 1	Airgap	Outside stator
Cooling Surface 2	Stator	-
Rotor retainment (high speed)	not in magnetic airgap	in magnetic airgap

1.7.1 Aspect Ratio Comparison

The machine envelope is important in HEV powertrain applications as it must be integrated with the balance of the powertrain.

Cavagnino et al. [2002] and Caricchi, Crescimbini, Honorati, Di Napoli and Santini [1996] identified $\lesssim 0.3$ as the aspect ratio ($l/\varnothing$) for which the Axial Flux topology is advantageous. The proportion of a Radial Flux machine's length occupied by end turns increases as the active length reduces. A higher pole or coil number, with shorter coil pitch, shortens the area occupied by end turns, but incurs the penalty of lower efficiency due to losses arising from operating at a higher

electromagnetic frequency, such as iron losses.

The Radial Flux topology has a constant cross-section, allowing variable length and a flexible aspect ratio, but retains some hollow internal volume, which the Axial Flux machine utilises [Patterson, 1996; Millner, 1994]. Cavagnino et al. [2002] favoured the Axial Flux topology for better use of the machine envelope, comparing 12-pole machine designs.

1.7.2 Rotor Inertia and Specific Torque Comparison

The rotor inertia determines the machine's dynamic performance. With equivalent electromagnetic properties, Sitapati and Krishnan [2001] found the Axial Flux machine's rotor inertia is less than the Radial Flux machine. The mass of active material is also less, giving a higher specific torque. A *Kaman* Axial Flux machine with a 530 mm diameter rotor is the largest found in literature, having an inertia of 0.9 kg/m^2 and delivering 1350 Nm torque [Millner, 1994].

The specific torque of the Axial Flux machine increases with the pole number as the length reduces. The Radial Flux machine torque also increases, but is limited to four times the 2-pole machine torque, half that of the Axial Flux machine, as the diameter only reduces towards the airgap diameter [Şimşir and Ertan, 1999].

1.7.3 Torque Density Comparison

With equivalent electromagnetic properties, the machine torque is a function of the airgap area and the radial moment arm. The torque of the Axial and Radial Flux topologies varies with r^3 and r^2 respectively [Millner, 1994].

Examination of 10 kW machines with equivalent outer diameter found the Axial Flux machine has half the mass of active material of the Radial Flux machine, offering $5-8$ times higher torque density [Sitapati and Krishnan, 2001]. Qu et al. [2003] compared active volumes of double airgap machines, with approximately equal torque densities for $12-14$ poles. The radial moment arm of the Axial Flux topology, however, is smaller between similar size machines. For higher than 14 poles, the Axial Flux topology torque density is superior [Millner, 1994].

1.7.4 Efficiency Comparison

Power loss comparisons normalise flux densities in the airgap, teeth and core, and electrical frequency to ensure like-for-like electromagnetics. Cavagnino et al. [2001] and [2002] report no unique Axial Flux machine losses. A comparison by Sitapati

and Krishnan [2001] of active material volumes (copper, iron, permanent magnet) found only design-dependent parameters, rather than topology, determine losses.

Qu et al. [2003] differentiates between power losses of machine topologies based on electrical frequency, i.e. pole number. As with torque density, the Axial Flux is favoured for more than 12 poles.

1.7.5 Thermal and Integration Comparison

Power is limited by insulation for dielectric strength and thermal constraints. The thermal arrangement of the Axial Flux topology allows the housing for heat convection, if the stator is mounted to it. Otherwise, the peripheral mounting area for thermal conduction is limited. However, the rotor surface area to volume is large, allowing high thermal coefficients. The proximity of other powertrain components can prohibit heat convection via the housing. Radial Flux machines in HEVs in production employ liquid cooling around the outside of the stator, which is independent of integration. In the case of Axial Flux machines, some novel cooling arrangements include totally enclosed air cooling or liquid cooling with integrated heat exchanger [Sitapati and Krishnan, 2001].

1.7.6 Mechanical Considerations Comparison

High speed applications have a peripheral speed $u_{tip} \leqslant 250$ m/sec. The centrifugal loading of the rotor requires a retainment ring, typically made of carbon fibre. For the Radial Flux topology, the ring sits in the magnetic airgap, requiring a change in electromagnetic design [Millner, 1994]. The airgap of the Axial Flux topology is unaffected by a retainment ring [Turbo Genset Co., 2002], and the shorter magnetic airgap length leads to a higher airgap flux density.

1.8 Permanent Magnet Synchronous Machine Efficiency

For PMSM machines in HEV powertrains, the powertrain efficiency must be maximised. The mechanical and electrical power loss sources in these electric machines are shown in Table 1.2.

Table 1.2: Power loss mechanisms in electric machine.

	ELECTROMAGNETIC	MECHANICAL
Primary Torque dependence	On-load: Conductor Ohmic resistance (I^2R), On-load: Magnetic flux leakage and stray	Coolant pumping, Heat exchanger fan,
Secondary Torque dependence	On-load: Conductor eddy current (conductive material loss due to stator/amp-turn field), On-load: Iron eddy currents in rotor, PM eddy currents (magnetic material loss due to stator/amp-turn field),	
Primary Speed dependence	No-load: Stator conductor eddy currents, Stator iron eddy currents (conductive material loss due to excitation magnetic field), No-load: Iron hysteresis (magnetic material loss due to rotor excitation magnetic field)	Shaft friction (bearing, static and dynamic friction), Rotational aerodynamic drag (windage),

1.8.1 Evaluating Machine Efficiency

Phillips [2004] describes two methods of determining AC motor efficiency (IEC 34-2) as being the summation of the individual losses or the measurement of the total instantaneous losses. Although these methods are designed to provide the plated efficiency of industrial motors (typically running at constant speed) they highlight the need to assess individual loss components.

By summation, each constant and load loss is measured. Further unidentifiable losses are assumed to equate to 0.5 %. Therefore, $\eta_{sum_losses}[\%] = (P_{input} - \sum \text{Losses})/P_{input} \times 100\%$, whereas the total losses measurement requires an instantaneous measurement of the total input and output powers, with $\eta_{meas_total}[\%] = P_{input}/P_{output} \times 100\%$. Calorimeter tests can also be employed for total losses measurement.

Although the total loss measurement is quicker, an error in power measurement can result in summation of the error in the efficiency value. (Over-measurement of P_{input} and under-measurement of P_{output} renders larger percentage error in the efficiency value calculated.) By determining the separate losses, which takes longer to achieve, a better understanding of the loss sources and, therefore, areas for design improvement are found. Therefore, the loss components are detailed individually. As stated in the comparison of Radial and Axial Flux machine efficiencies in Section 1.7, loss components can be compared between machines based on design-dependent

parameters, rather than based on topology alone.

1.8.2 Mechanical Losses

With the electromagnetic torque at the airgap differentiating between electrical and mechanical power, in motoring operation, the mechanical losses are the airgap power less the shaft power.

1.8.2.1 Rotational Loss

The mechanical losses associated with rotation of the rotor are aerodynamic drag, or "windage", and bearing friction. These are no-load losses as they are present irrespective of torque. The windage is defined for spinning discs in an enclosed volume, according to a Taylor number for laminar flow with vortices. The bearing friction is described by empirical expressions, but variations in manufacture, such as a misaligned rotor or over-greased bearings, mean that accurate values for both windage and bearing friction are best achieved by testing. Typically, these tests are "run-down" tests using non-magnetised poles [Lovat et al., 1998]. The windage losses for a Radial Flux machine are proportional to the cube of the diameter, while the mechanical stress limitations of the rotor materials employed means that the limit on maximum speed varies with the square of the diameter. For an Axial Flux machine, the windage loss element arising from the disc surface is more pronounced than that from the drum surface. The disc surface loss is proportional to the diameter to the fifth power and the cube of the speed. However, Pullen [1991] illustrated that the windage loss torque coefficient C_m is a function of the diameter and speed, resulting in the disc surface loss being proportional to the diameter to the power 4.5 and the speed to the power 2.75.

1.8.2.2 Cooling Pumping and Resistance

The mechanical losses dependent on torque output, i.e. on-load losses, are windage due to coolant flow and power for coolant pumping. For airgap cooling, the increase in airgap flow for greater cooling requirement with larger electric load results in greater windage losses. A turbulent airgap flow offers improved thermal behaviour, but also produces more aerodynamic drag. Therefore, airgap cooling is commonly employed at a lower pressure, reducing windage, by connecting the air passage to the inlet of the fan. A fan with an optimum operating point is acceptable for shaft-mounting in a constant speed application, but transient operation does not suit a shaft-mounted fan. The majority of machines in transient applications are

liquid cooled, with a separate pump and heat exchanger. Load tests evaluate these conditions and the temperature rise, but the motor's operating temperature with respect to ambient temperature is where the efficiency must be measured.

Therefore, the mechanical losses of Axial Flux machines can be lowered through reducing the cooling demand and pumping, and minimising the rotor inertia.

1.8.3 Electrical Losses

With the electromagnetic torque at the airgap differentiating between electrical and mechanical power, in motoring operation, the electrical losses are difference between the input power the power given by torque at the airgap.

The constant electrical losses exist at constant speed operation. These are examined in studies reported in Chapters 6, 7 and 9.

1.8.3.1 Iron Hysteresis, Eddy Currents, Anomalous

Iron core losses are initially no-load losses because the PM field exists irrespective of torque. The flux density in the iron is changed by the stator reactive field, according to inductance. Iron losses are determined by flux density and electrical frequency. The inverter-fed motor supply may have time harmonics, which introduces iron loss components at higher frequencies.

1.8.3.2 Conductor Eddy Currents and Joule Effect

The constant electric losses in conductors are eddy currents arising from the PM field in all load conditions. Again these are determined by flux density and electrical frequency. These are related to the level of flux passing through the conductor, which is low in a slotted core machine, but high in an airgap winding machine.

1.8.4 Inter-relationship of Losses

The load loss mechanisms are related. Reducing the electrical load losses renders less demand for the cooling, thus reducing the mechanical load losses. Alternatively, improved effectiveness of the machine cooling reduces the conductor temperature, and electrical resistance, reducing electrical load losses. These are machine design considerations [Petro et al., 2005].

The no-load losses are also related, but may be treated individually. Harmonic components are a significant source of much of these losses. Harmonic distortion of the supply means a motor draws more current to deliver the same torque, increasing

winding losses, generating extra heat and increasing the winding's electrical resistance.

1.8.5 Harmonics Power Loss

Harmonics exist as spatial harmonics arising from the machine's electromagnetic design, and time harmonics arising from switching operations of the inverter-fed supply. The spatial harmonics arise in the airgap permeance function, due to stator or rotor saliency, and the rotor and stator mmfs, due to the magnet width and phase belt [Bolton et al., 1986]. The impact of lower order spatial harmonics (i.e. $n < 20$) is evaluated by considering the machine's individual power loss sources, but "harmonic", "distortion" and "torque derating" factors account for lower machine efficiency due to time harmonics [Phillips, 2004; Yang et al., 2002; Sadarangani, 2000].

1.9 Research Description

1.9.1 Problems

Several industry experts have commented on the suitability of, but lack of interest in, Axial Flux PMSM machines.

> "[The Axial Flux topology has been] ignored many times because the tooling and manufacturing processes needed for its construction are not readily available... [yet it] offers superior performance in those applications where the allowable radial dimension is sufficiently large." [Hanselman, 2003]
>
> "With a change in customer perception, we could easily expand our range of Axial Flux machine products." [Swindel, M. (Brook Compton), 2003]
>
> "As hybrid vehicles become "electric motor dominant", they require a motor that can deliver more power and torque at a lower cost and with more reliability... The [axial flux motor] technology is ideal for many applications including integrated hybrid motors, integrated starter generators, and is scalable for a wide range of sizes from small scooters to the large heavy vehicles and generators." [Dwyer, W. (Raser Technologies), 2003]

> "[Axial Flux machines] offer several advantages over Radial Flux machines, it only requires a change in the attitude of the machine designer to exploit the advantages." [Clarke, D. (Microcore), 2004]

Based on these observations, development and demonstration of Axial Flux PMSM machines in HEV applications will have an impact on industry practice.

1.9.2 Research Aim

The primary advantages of the Axial Flux PMSM machine are an attractive space envelope and high torque density for many HEV powertrain applications. The efficiency of the PMSM depends on the electromagnetic design. This research, therefore, explores the Axial Flux Permanent Magnet machine in HEV powertrains and considers design aspects which offer high efficiency yet maintain power density.

1.9.3 Research Objectives

- The Axial Flux machine is less familiar to electric machine designers than the Radial Flux machine. Derivation of design equations and manipulation into a program for Axial Flux machine sizing.
- Analytical model of airgap fields and machine performance for sizing.
- The limited previous research on Axial Flux machines means there has been a need for further work to understand the power loss mechanisms, in particular electrical losses. Consideration of individual power loss sources according to electromagnetic design aspects. Harmonics are an important focus to this.
- In order to achieve high powertrain efficiency, maximum efficiency of individual components should be attained. Analytical and empirical model of HEV electric powertrain including energy changes from battery to machine mechanical output to evaluate efficiency.
- Demonstrate superior performance of Axial Flux machines, and work with the industrial collaborators to realise Axial Flux machines in powertrain applications.

1.10 Thesis Layout

Parts of this introduction were presented in a review paper [Walker, 2003*b*].

Chapter 2 describes the analysis of an electric drive, including battery, for an HEV powertrain.

Chapter 3 is a review of published literature on Axial Flux machines and a review of analytical electromagnetic models used for analysis and design, plus specification of existing Radial Flux machines currently employed in HEV powertrain applications.

Chapter 4 is an outline of the theory of the electromagnetic operation of Axial Flux PM machines. Versions of this theory for Radial Flux machines is widely available in textbooks on electric machines, but not for Axial Flux machines. The theory is used to size the machines for the selected applications. Hanselman [2003] introduced many relations, and these are reconfigured specifically for machines in HEV applications.

Chapter 5 describes the analytical model used for some of the current research.

Chapters 6, 7 and 9 present results and a discussion of studies on PM excitation fields, airgap windings and slotted cored stators, respectively.

Chapter 8 describes the manufacture of demonstration machines for the HEV powertrain case studies.

Chapter 10 draws conclusions and proposes future work.

The Appendices include details of derived theory, geometric descriptions, analytical models, and test rigs and manufacturing jigs.

Chapter 2

Hybrid Electric Powertrain Analysis

2.1 Modelling for Selected Machine Applications in HEV Powertrains

Computer-based modelling has been used to simulate the performance of the powertrains with selected components. Various types of component models were used; analytical relations, empirical descriptions, measured data with look up tables, etc. and drive cycles describing the vehicle's dynamic operation with respect to time. The extended modelling undertaken for the 7.5 tonne CV powertrain is reported by Wilkins [2002] and similar modelling has been undertaken for the engine–generator operation in the 70-seater bus powertrain. The modelling provides the duty cycling of the electric drive, which is required to determine the nominal and peak torque and power ratings.

2.2 Component Modelling

2.2.1 Total Power Loss

Total system power loss (P_{total}^{loss}) is a summation of the power loss of each individual system component; integrated motor generator, frequency inverter, voltage converter, DC link and battery.

An approach for estimating the time-averaged power loss is presented for each component, comprising the individual component loss mechanisms.

2.2.2 Electric Machine Power Loss

The IMG losses are those described earlier in Section 1.8. The electrical losses are described in detail in Chapter 7, but approximations are given here for the system power loss calculations.

2.2.2.1 Copper Loss

The power loss due to stator winding current uses the phase current I_{ϕ_rms} allowing for the AC harmonic components. The skin depth δ_p is detailed in Section 7.1, regarding conductor size selection. It is sensitive to high frequency harmonics, so must be considered for the selected switching frequency.

The fundamental and switching frequencies render skin depths of $\delta_{p_fund} = 4.61$ mm and $\delta_{p_SW} = 0.461$ mm. As this Axial Flux machine has negligible tangential direction flux in the airgap, the conductor width is employed (dimension b) which for this machine is 1.63mm, and the skin effect correction factor κ_n gives the actual conductor resistance.

The stator total conduction loss is then a sum of all current frequencies and corresponding AC resistances ($P_{Cu}^{loss} = \sum_n I_n^2 R_n$ for all n current frequency components). The DC resistance according to temperature compensation is $R = 2.28\text{x}10^{-8}\Omega\text{m}^{-1}$ operating at the stator temperature of 70°C.

2.2.2.2 Mechanical Loss

Mechanical power losses are bearing friction P_{fric}^{bear}, aerodynamic windage P_{areo}^{rot}, and fan pumping P_{pump}^{fan}. Linear approximation is generally accepted for rolling friction of the bearing ($P_{fric}^{bear} = k_{fric}\omega_{mech}$) having overcome the static friction [Penton, 2005].

Aerodynamic windage on the rotor faces ($P_{areo}^{rot} = T_{wind}\omega_{mech}$) is based on:

$$T_{wind} = \frac{1}{2} C_m \rho_{air} \omega_{mech}^2 r_o^5 \tag{2.1}$$

The expression for windage coefficient C_m considers laminar or turbulent flow, dictated by the rotating Reynolds number Re_ω. In this analysis, general turbulent

flow gives [Romero-Hernandez, 2001]:

$$C_m = \begin{cases} \dfrac{2\pi}{\left(\dfrac{g}{r_o}\right)\mathrm{Re}_\omega} & \forall\ \mathrm{Re}_\omega \sim 10^4 \\ \dfrac{0.1\left(\dfrac{g}{r_o}\right)^{0.1}}{\mathrm{Re}_\omega^{0.2}} & \forall\ \mathrm{Re}_\omega \sim 10^6 \end{cases} \tag{2.2}$$

A quadratic approximation, based on mass flow rate $\dot{m}$ and fan size defines the fan pumping, which operates based on current loading ($P_{pump}^{fan} = k_{pump} I_{\phi_rms}^2$).

2.2.2.3 Machine Iron Loss

Iron losses, in the form of core hysteresis P_{hyst}^{Fe} and eddy currents P_{eddy}^{Fe} are approximated assuming a homogeneous material:

$$P_{hyst}^{Fe} = k_{hyst1} f_{fund,SW} \hat{B}_{Fe_hyst}^2 \tag{2.3}$$

The peak flux density $\hat{B}_{Fe}$ is 1.20 T and the lamination thickness δ is 0.5 mm, giving:

$$P_{eddy}^{Fe} = \frac{\sigma\delta^2}{12}\frac{1}{T}\int_T \left(\frac{\partial B_{Fe}}{\partial t}\right)^2 dt \tag{2.4}$$

2.2.3 Frequency Inverter

Figure 2.1 indicates the Frequency Inverter switching devices, which suffer operational power losses detracting from the system performance. A Voltage source inverter is employed, controlled with Space-Vector Pulse Width Modulation (SV PWM), with a reference wave Modulation index (Mi) of 0.9. This gives a peak phase voltage of $\hat{V}_\phi = \frac{V_{DC}}{\sqrt{3}}\mathrm{Mi}$. The advantage offered by SV PWM is fewer harmonics in the current waveform for maximum Mi, and lower Mi when employing field weakening for voltage control (with $V = Bf$). The power switching devices, Q1-Q6 in Figure 2.1, are combined IGBT and diode modules, selected on the bases of power rating, voltage, switching frequency and unit cost.

2.2.4 Voltage Converter

Figure 2.2 indicates the Voltage Converter switching devices, which suffer operational power losses detracting from the system performance. The battery terminal

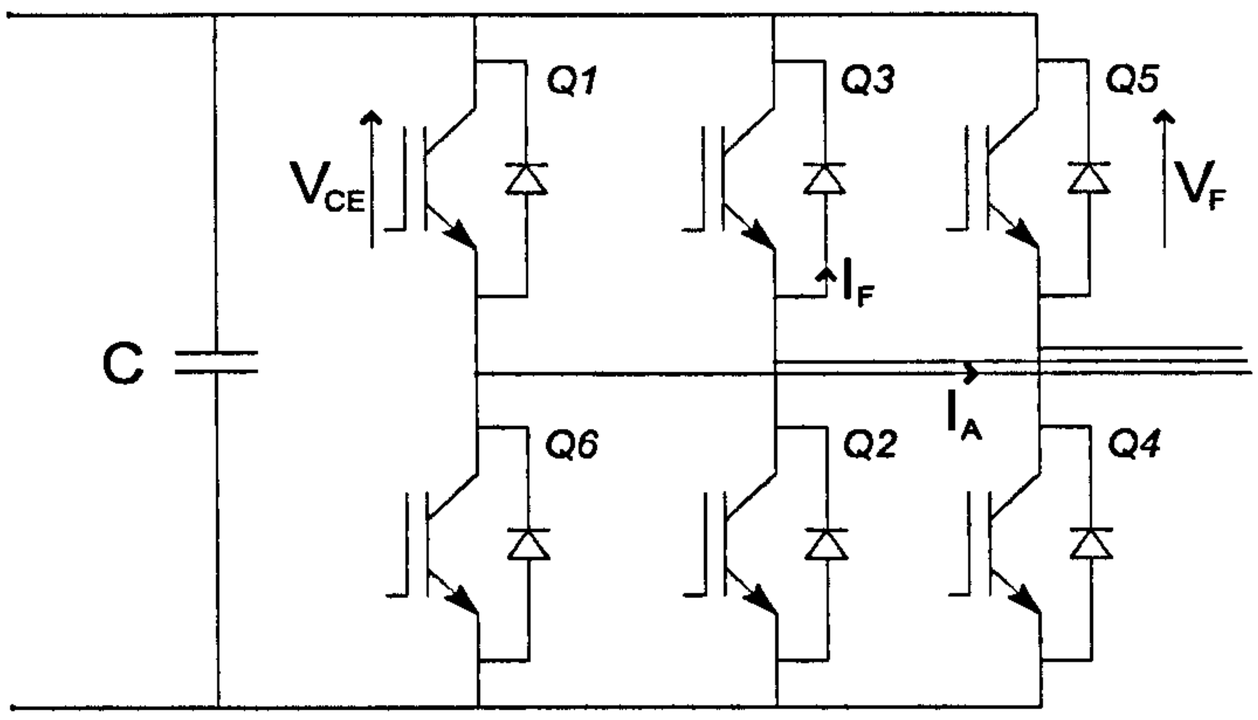


Figure 2.1: Schematic of frequency inverter layout.

voltage can vary below that required by the frequency inverter. Therefore, a voltage buck-boost converter is employed, giving a variable voltage output according to the Gain. At steady state, the current in the inductor is equivalent but opposite for the switch open and closed, giving a Gain of $G = \frac{V_{\text{out}}}{V_{\text{in}}} = \frac{-d}{1-d}$, where d is duty of the switch $(0-1)$.

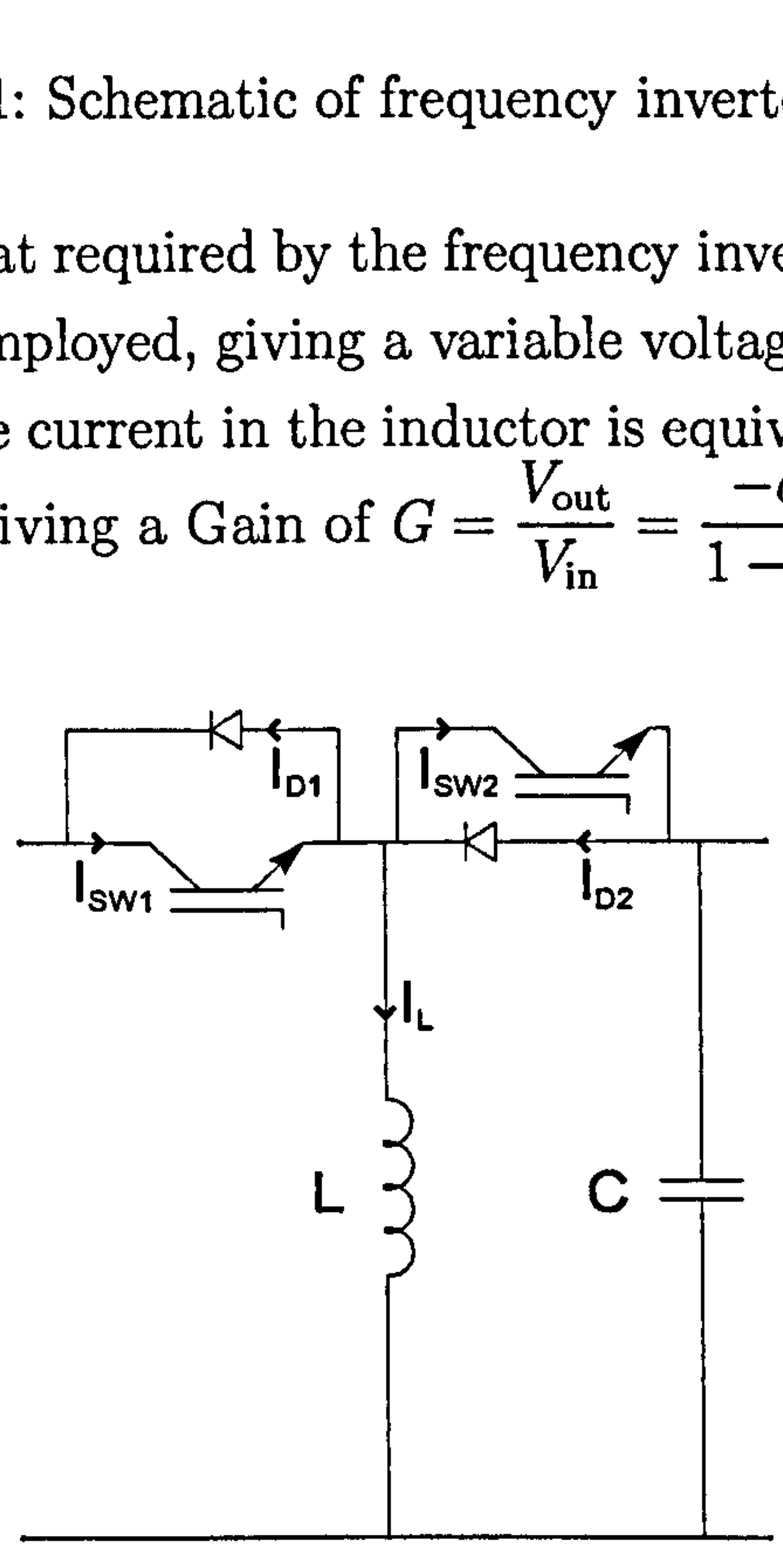


Figure 2.2: Schematic of voltage converter layout.

2.2.5 Frequency Inverter Power Loss

Inverter power losses arise from current in the power devices, with conduction $P_{cond}^{D,Q}$, switching $P_{SWon,SWoff}^{Q}$ and current recovery P_{rr}^{leg}. The small power consumption for the control logic is neglected.

The method of analysis employed here assesses the current in components when activated (such as when the switch is on, or when the diode allows current). The period T is discretised into portions determined by the duty d, and time-averaged values are found for those portions.

2.2.5.1 Inverter Conduction Loss

The conduction power loss in both the power devices in each inverter leg is found from summing the product of current and voltage drops while the components are active [Hernandez-Aramburo, 2003]:

$$P_{cond}^{D} = \frac{1}{T}\sum_{k=1}^{N_{SW}} V_{F_k} I_{F_k} (1-d)_k \tag{2.5}$$

$$P_{cond}^{Q} = \frac{1}{T}\sum_{k=1}^{N_{SW}} V_{CEsat_k} I_{C_k} d_k \tag{2.6}$$

where N_{SW} is the number of switching events during a fundamental cycle with period T, and k indexes each of these switching events due to the time-varying nature. $V_F = k_{F1} I_F + k_{F2}$ and $V_{CEsat} = k_{CE1} I_C + k_{CE2}$ are defined in the manufacturer's data sheet [Toshiba, 1997].

2.2.5.2 Inverter Switching Loss

The switching power loss for each leg over the period T is:

$$P_{SWon,SWoff}^{Q} = \frac{1}{T}\sum_{k=1}^{N_{SW}} k_{SWon,SWoff} I_{C_k} \tag{2.7}$$

where $k_{SWon,SWoff}$ are defined in the manufacturer's data sheet.

2.2.5.3 Inverter Reverse Recovery Loss

The loss from the reverse recovery current effect for each inverter leg is given by a polynomial fit provided by Toshiba [1997]:

$$P_{rr}^{leg} = 2\sum_{k=1}^{N_{SW}} \left(k_{rr1} I_{F_k}^2 + k_{rr2} I_{F_k} + k_{rr3}\right) \tag{2.8}$$

where the constant coefficient k_{rr2} is 2.211e+5 while k_{rr1} is -4e-8, indicating a near linear relationship.

2.2.6 V-Converter and DC Link Power Loss

Converter and link power losses arise from current in the power devices, with conduction $P_{cond}^{D,Q}$ and switching $P_{SWon,SWoff}^{Q}$, and conduction in the cabling P_{cond}^{link}.



2.2.6.1 V-Converter Conduction Loss

The average diode current I_D is equivalent to the output current I_{out}. The inductor current I_L is the sum of the diode and switch currents $I_D + I_{SW}$, which derives the conduction loss in terms of the duty d:

$$P_{cond}^{leg} = \frac{1}{T} V_{CE,D} I_{SW,D} \tag{2.9}$$

$V_{CE} = k_{CE1} I_{SW} + k_{CE2}$ and $V_D = k_{D1} I_{out} + k_{D2}$ are defined by the manufacturer, with $I_L = \frac{I_{out}}{1-d}$, and $I_{SW} = \frac{d}{1-d} I_{out}$, while the capacitor has an equivalent series resistance $P_{cond}^{C} = R_{ESR} I_{Cap}^2$.

2.2.6.2 V-Converter Switching Loss

Noting that the switching power loss is independent of the duty d, it is determined by:

$$P_{SWon,SWoff}^{Q} = k_{SWon,SWoff} f_{SW} I_{SW} \tag{2.10}$$

2.2.6.3 DC Link Conduction Loss

Conduction loss in the cabling is based on I^2R, using I_{SW}, with a total cabling length of 20 m.

2.2.7 Battery Pack Power Loss

Battery power losses arise from current conduction P_{cond}^{bat}, arising from the internal resistance R_{int}, and the pumping power used by the cooling and management system P_{cool}^{bat}. Assuming an approximately linear terminal voltage, internal resistance does not vary within the state-of-charge (SOC) limits, from which the current conduction loss is found.

Via "Dynamic Lumped Parameter Battery Modeling" [Powell et al., 1998], the instantaneous terminal voltage e_{tb} for a steady-state current is found, and used to determine the required V-converter Gain.

2.2.7.1 Battery Conduction Loss

The battery model employs:

$$v_{OC} = k_{b1}(k_{b2} + k_{b3} SOC) \tag{2.11}$$

$$R_{int}C_p\frac{de_{pc}}{dt} = v_{OC} + \frac{R_{int}}{R_b e_{tb}} - \frac{R_b + R_{int}}{R_b e_{pc}} \tag{2.12}$$

$$R_b C_i \frac{de_{tb}}{dt} = e_{pc} - R_b i_{tb} - e_{tb} \tag{2.13}$$

where C_p is polarization capacitance, e_{pc} is voltage drop from C_p, v_{OC} is open circuit voltage, R_b is terminal resistance, C_i is incipient terminal capacitance, and i_{tb} is terminal current. The battery capacity, in Ampere-hours, varies with temperature $C_t = C_{T_{ref}}(1 - \alpha(T_{ref} - T))$ where α is a temperature-based quadratic function from the manufacturer's data sheet.

2.3 7.5 tonne Commercial Vehicle Powertrain for Urban Deliveries

The hybrid-electric powertrain is for the 7.5 tonne delivery Commercial Vehicle introduced in Section 1.4.

2.3.1 Duty Cycle

Artificial and real world drive cycles are used in simulation to approximate the power demand with respect to time and rate the electric drive. The cycle illustrated in Figure 2.4 is a real world cycle for the 7.5t Commercial Vehicle making deliveries. The urban/suburban nature of the duty cycle requires operation by electric-only driving in urban areas, which are the subject of GreenZones, and conventional driving with electric-assist elsewhere.

The combined New European Driving Cycle (NEDC) for light duty vehicles, shown in Figure 2.3, is an artificial drive cycle. This is used to compare fuel economy of all new vehicles, but as it is unrepresentative of real world driving, it is not appropriate for this task. However, it is useful for initial determination of the power requirement for powertrain components.

Figure 2.4 illustrates a real world drive cycle obtained from operation of a 7.5 t CV providing urban deliveries in London. This is similar to bus operation but with longer stops [Marquis, 2004]. This cycle can be repeated to account for one complete day of vehicle operation.

Using this urban delivery duty cycle in Figure 2.4, the powertrain operation was modelled using the conventional transmission and simple gear selection based on vehicle speed. The torque–speed requirement of the IMG was derived in terms of operating points on the map shown in Figure 2.5, with a peak mechanical power of

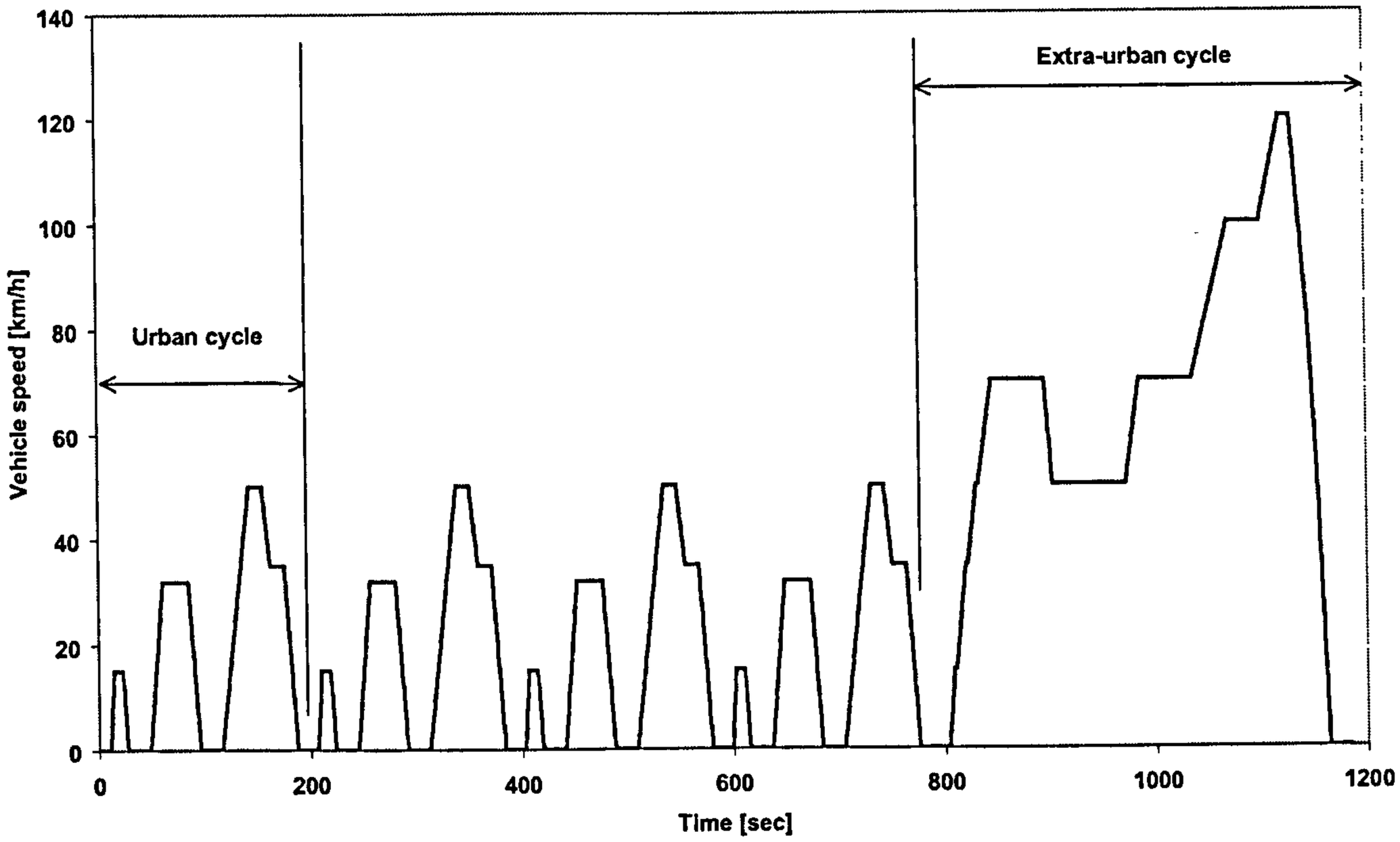


Figure 2.3: Combined EC drive cycle with four urban (ECE15) and 1 extra-urban (EUDC) cycles.

Figure 2.4: Real world urban delivery CV drive cycle.

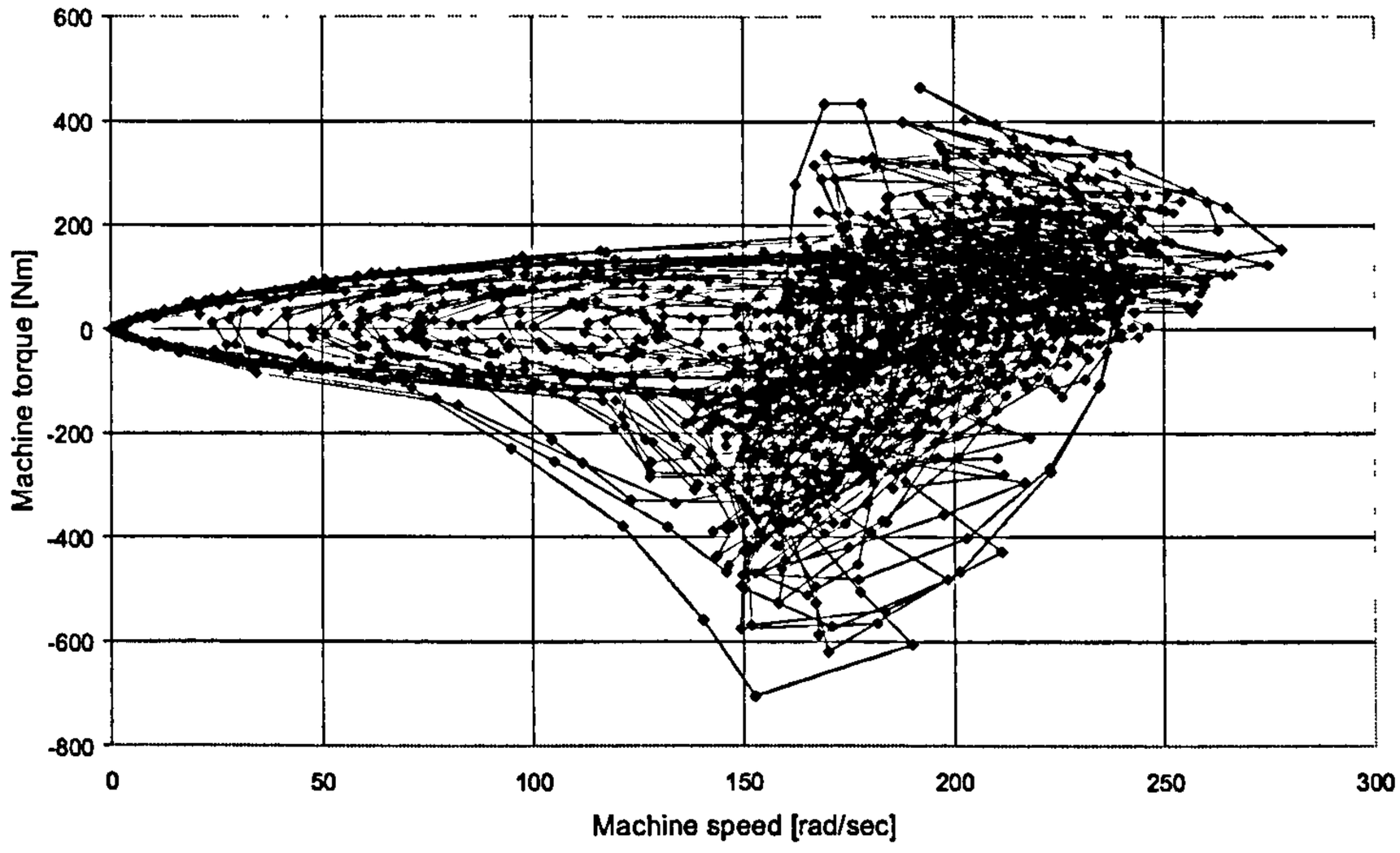


Figure 2.5: IMG duty plot for vehicle operating the drive cycle in Figure 2.4.

approximately 80 kW, and a high density of operation at 40 kW power. The map illustrates that using this simple gear selection results in higher torque requirement between $150 - 250$ rad/sec than between $0 - 150$ rad/sec. However, it is recognised that driver reaction results in the gear selection based on powertrain torque rather than vehicle speed, so this torque could be expected at lower speed.

Figure 2.6 illustrates the power curve for the *Iveco* ICE used in this CV application.

2.3.2 Duty Cycle on Electric Traction System

Delivery operations of the vehicle in London show that in the urban duty cycle the vehicle speed approaches 50 km/h, as illustrated in Figure 2.4, and driving slower than a predefined speed can be powered by electric only operation [Walker et al., n.d.]. Computer modelling of this operation provided the speed and torque operating points illustrated in Figure 2.5. 90% of the traction operation during the duty cycle is below 150 Nm and between 1250 and 2000 rpm. Therefore, this region is where highest efficiency is desirable. The power losses giving component efficiencies, and system efficiency, have been evaluated for the selected operating points, given in Table 2.1. It should be considered that the vehicle has dynamic time constants of seconds, making quasi-steady state operation acceptable. It is noted that in Figure 2.5, there is no torque at stand still. To emulate conventional vehicle operation with a clutch and manual gearbox, the machine is already rotating at pull away.

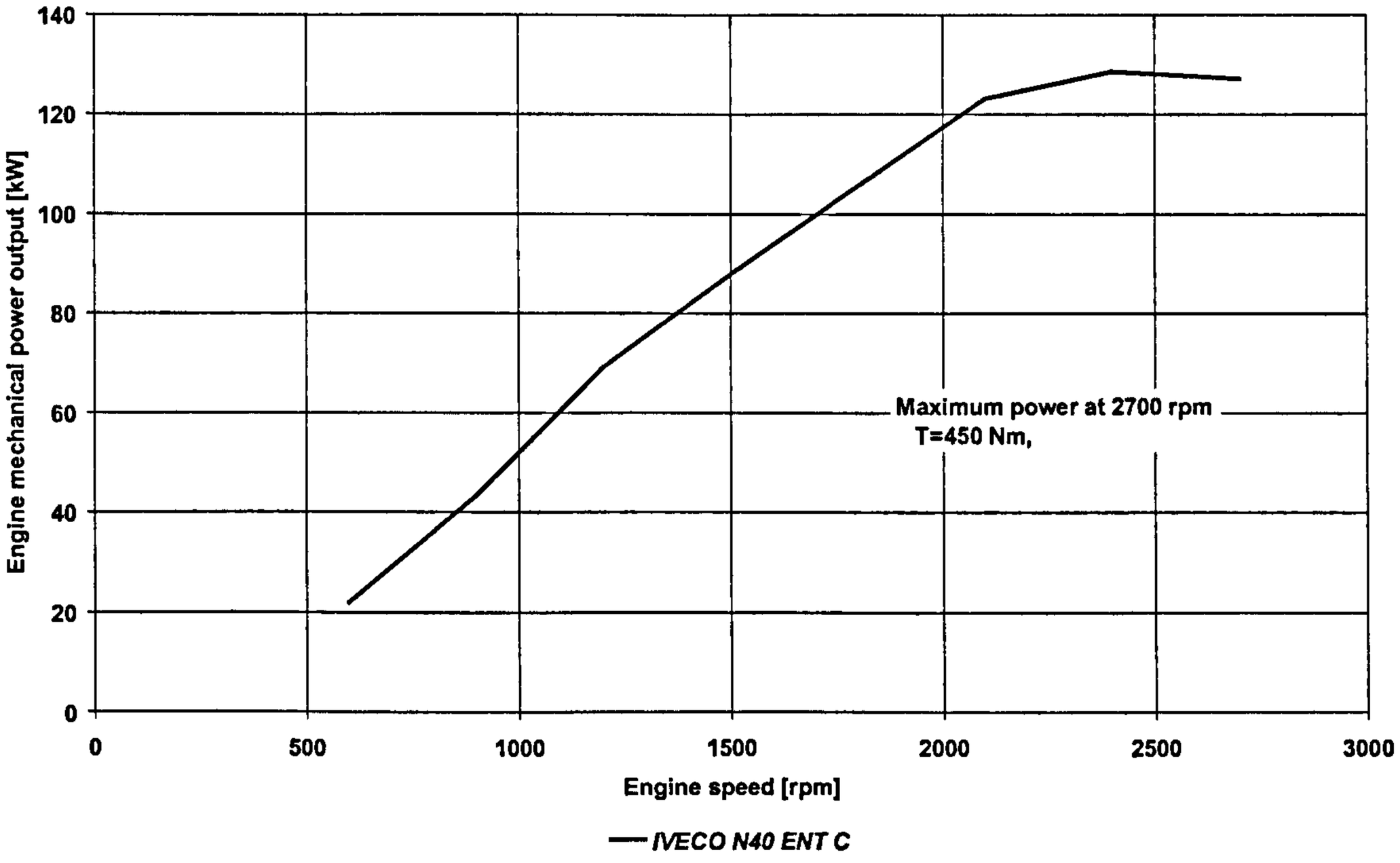


Figure 2.6: Power curves for *Iveco* CIDI ICE [Iveco, 2003].

Table 2.1: Important operating points for electric traction machine operation.

Operation	Speed [rpm]	Torque [Nm]	Power [kW]
Peak power	2005	160	33.6
Common region - high speed	2005	50	10.5
Common region - high Torque	1241	150	19.5
Peak torque	1337	200	28.0

2.3.3 Specified Rating

For the input to the transmission under conventional powertrain operation, Figure 2.5 plots the machine duty defined by torque and speed points per second. Constant power curves allow the rating for continuous operation, and peak ratings according to length of demand, i.e. 5-minute operation, 1-minute operation, 10-sec operation.

An estimation of the required power if acceleration is performed in EV operation using vehicle inertia validates the ratings. For the 7.5 t CV to accelerate from 0 to 25 km/h in 6 seconds requires a powertrain output of 30 kW.

Similar vehicles with similar powertrains employ Radial Flux machines. The *Navistar* 4700 Series 7.5 t truck includes a 49 kW IMG DC machine. The *Eaton* Class 4 truck (6.35 - 7.25 t) includes a 44 kW *Hitachi* PM Synchronous water-cooled IMG. This has a 350 mm stator outside diameter, between the automatic clutch and the transmission, delivering a maximum torque of 420 Nm at 1000 rpm, and 170

Nm at 2600 rpm.

Slightly smaller vehicles include the *Mitsubishi* Canter (5.5 t) Parallel HEV truck employing a 35 kW PM Synchronous IMG, and the 3 t *Iveco* Daily van HEV powertrain with a 35 kW rated (60 kW peak) IMG.

2.3.4 ESD Capacity & Rating

The battery pack provides a load levelling function in parallel hybrid mode, and full traction energy in EV operation. In order to meet the duty cycle energy requirements, the ESD capacity must be 50 kWh at 288 V Shah et al. [2004]. However, this capacity is larger than usual for a HEV powertrain with this configuration, demanded by the extended EV operation, and the weight penalty is too high for a cargo-carrying vehicle. Therefore, the EV operation range is modified to an ESD capacity of 26 kWh, for which a Nickel Metal Hydride (NiMH) pack is employed. Maximum battery life can only be achieved by cycling management, which determines the maximum charging and discharging currents according to the power demand. The operation is primarily for highest efficiency of the ESD. The maximum current values have been used to assess the system efficiency, from battery to motor-generator.

Figure 2.7 indicates the Battery layout, comprising three parallel chains of Saft NiMH cells, providing a pack voltage of 288 V and total capacity of 26 kWh [Saft, 2003]. The battery management system, required to prevent recirculating current between parallel chains of battery cells, is omitted from this idealised analysis.

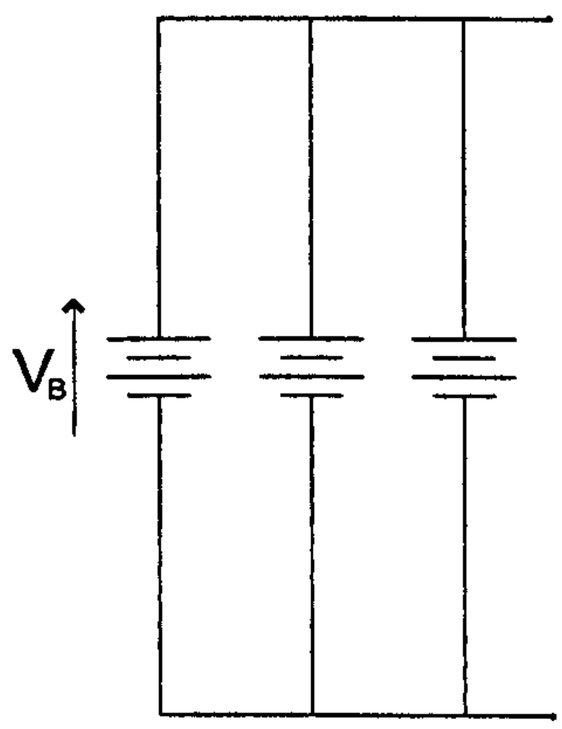


Figure 2.7: Schematic of battery layout.

2.3.5 Integrated Motor Generator Power Loss

The phase current waveform is assumed to be sinusoidal, i.e. is not approximated, defined by $i_\phi = 150 \sin\left(\frac{t}{4.6} 2\pi + \phi_\phi\right)$, where t is given in ms.

2.3.6 Powertrain Integration

The Parallel HEV configuration outlined in Figure 1.20 includes a second conventional clutch. The conventional engine and transmission for this powertrain are shown in Figure 2.8 mounted on a powertrain dynamometer testbed. The existing clutch is retained to operate the manual transmission, while the second clutch connects the ICE and allows the IMG to start the ICE.

In order to achieve integration with the ICE, the machine shaft and housing are mated with the ICE crankshaft and the flywheel housing.

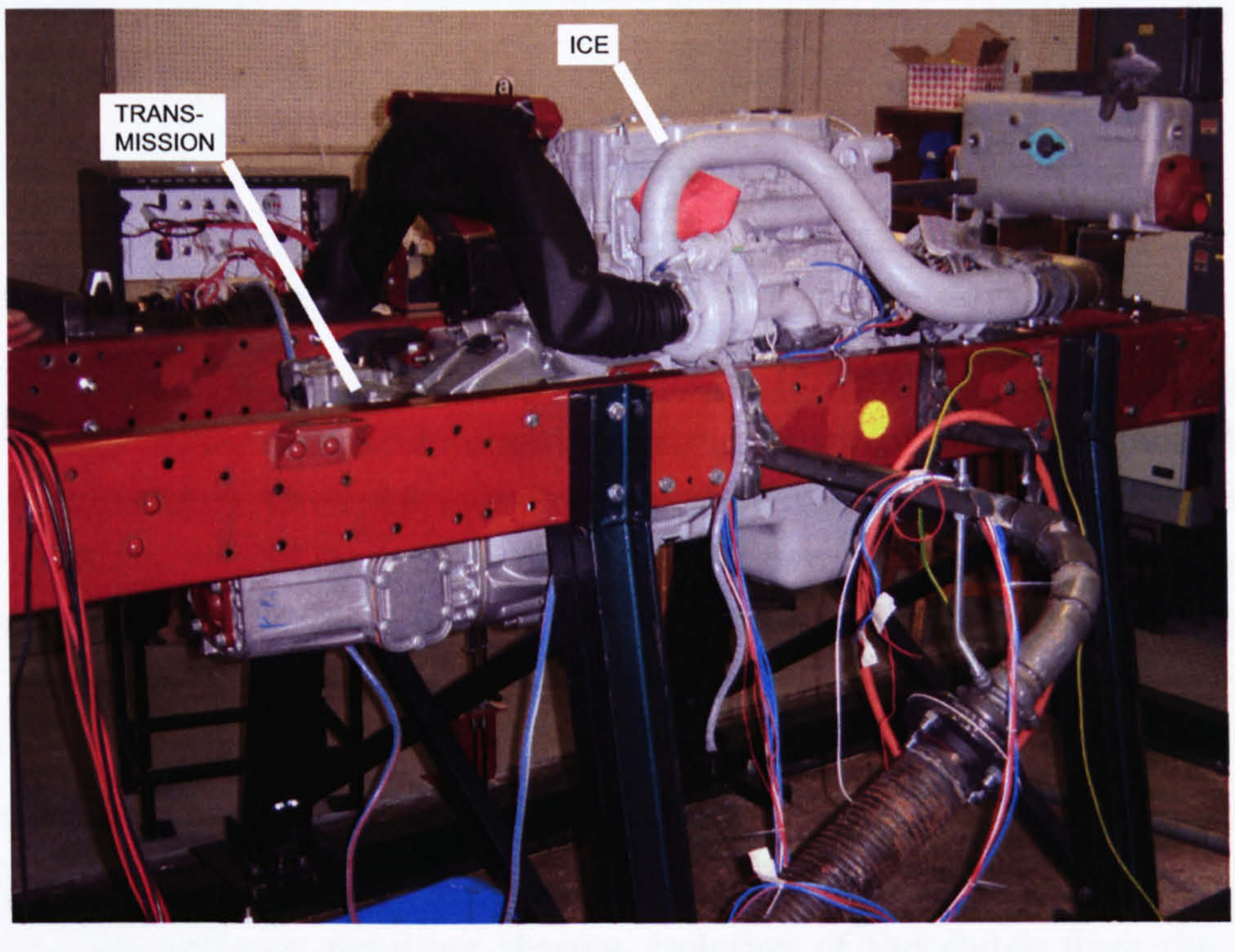


Figure 2.8: Powertrain assembly in lab.

2.3.6.1 Shaft Design

The machine shaft supports the friction plate of the second clutch and the flywheel–clutch assembly of the existing clutch. The shaft also takes the combined ICE and IMG peak torques.

Figure 2.6 illustrates the power curve for the *Iveco* 4-cylinder Tector ICE with maximum power of 125 kW at 2700 rpm ($T = 450$ Nm).

2.3.6.2 ICE Flywheel Housing

The available envelope is constrained by the mechanical interface between the machine housing and the ICE flywheel housing. The flywheel housing sizes include the flywheel and clutch sized for the maximum torque of the ICE [Eaton Corporation, 2004]. SAE standard J617C, summarised in Table 2.2, defines the flywheel housing dimensions.

Table 2.2: SAE J617C engine flywheel housings.

	Bore Diam. (A) [mm]	PCD (C) [mm]	No. Tapped holes	Size Tapped holes thread ["] x depth [mm]
00	787.40 +.25	850.90	16	1/2 x 13
0	647.70 +.25	679.45	16	1/2 x 13
1/2	584.20 +.20	619.12	12	1/2 x 13
1	511.18 +.13	530.22	12	7/16 x 14
2*	447.68 +.13	466.72	12	3/8 x 16
3	409.58 -.13	428.62	12	3/8 x 16
4	361.95 -.13	381.00	12	3/8 x 16
5	314.32 -.13	333.38	8	3/8 x 16
6	266.70 -.13	285.75	8	3/8 x 16

The ICE flywheel housing size is the limiting dimension on the IMG outside diameter. As these sizes are internationally recognised by engine manufacturers, they are repeated in Table 2.2 to indicate suitable machine sizes. The size for the engine used here was SAE2, indicated *, which is typical of most commercial vehicle and passenger transit engines up to a displacement size of 5litre.

2.3.6.3 Clutch

The IMG arrangement uses a push-pull clutch with a significant axial load in the released position of 14 kN. During slip, there is significant heat generated by the clutch friction surfaces, requiring thermal isolation of the clutch from the IMG, provided by a water jacket on either side of the IMG.

2.3.7 Electric Drive Operating Efficiency

This section describes the explicit efficiency analysis of the electrical powertrain. The figures have been calculated using the expressions provided in the previous Section. The material includes an analysis and operational control, which were presented in Walker [2003*d*] and Walker [2003*c*].

Attention has been paid to minimising the power losses during electric-only driving. The gear selection control assumes higher speed and lower torque provide lower battery and motor currents.

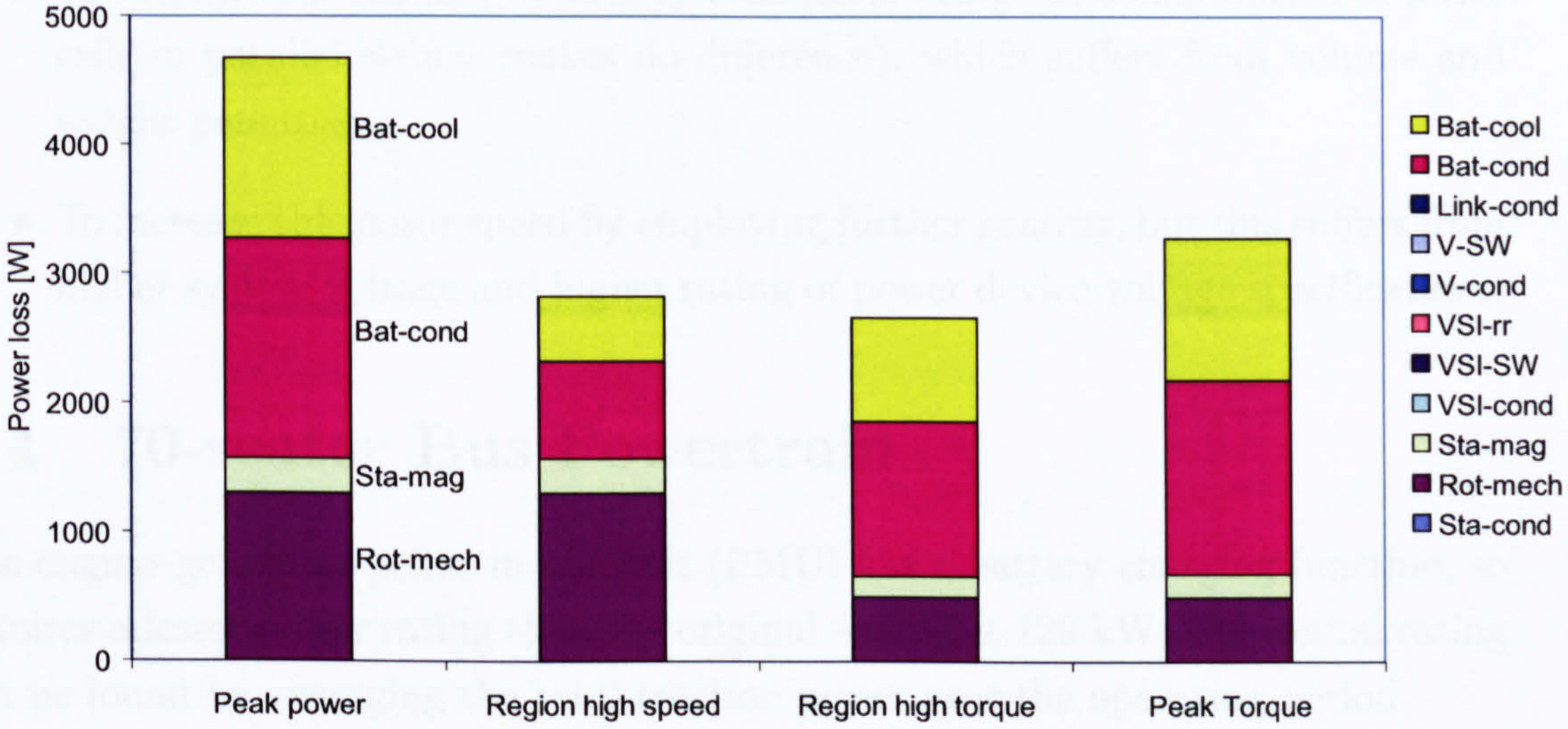


Figure 2.9: Power loss components for operating points of interest. (Data given in Table 2.3.)

Table 2.3: Power loss components and system efficiency calculated for important operating points (battery SOC = 0.7).

Loss	Peak power Mi=0.9 G=1.0	Region high speed Mi=0.9 G=1.0	Region high Torque Mi=0.6 G=0.7	Peak torque Mi=0.7 G=0.9
P_{cool}^{bat} [kW]	1.4	0.5	0.8	1.1
P_{cond}^{bat} [kW]	1.7	0.75	1.2	1.5
P_{cond}^{link} [mW]	10	2	10	10
P_{SW}^{V} [mW]	25	9	25	25
P_{cond}^{V} [mW]	35	10	35	35
P_{rr}^{VSI} [mW]	5	1	4	4
P_{SW}^{VSI} [mW]	25	9	25	25
P_{cond}^{VSI} [mW]	30	19	30	35
P_{mag}^{sta} [W]	270	270	160	180
P_{mech}^{rot} [kW]	1.3	1.3	0.5	0.5
P_{cond}^{sta} [mW]	24	2.5	22	24
η_{syst} [%]	87	79	87	89

The analysis provides reasonable approximations for the power losses, from which the system's efficiency has been found, given in Figure 2.9 and Table 2.3. The largest loss contributions come from the battery loss (both conduction and cooling pumping) and the traction machine's mechanical rotating loss, which is predominantly the fan pumping. A water or oil cooled machine would not be dominated by this loss.

With battery current and motor current being the principal power loss factors, the options for reducing current levels in both these components and improving efficiency are:

- To increase the number of battery cells (as altering the configuration of series cells in parallel strings makes no difference), which suffers from volume and weight penalties.
- To increase the motor speed by employing further gearing, but this suffers from higher system voltage and higher rating of power device voltage specifications.

2.4 70-seater Bus Powertrain

The engine–generator prime mover unit (PMU) has a battery charging function, so requires a lesser power rating than the original engine at 120 kW. The actual rating can be found by averaging the total traction power over the operating period.

Radial Flux generators previously used in this application are typified by the ELFA range of machines, manufactured by *Siemens* and integrated by *ISE Corp.* [ISE Corp., 2004]. The PM generators are rated at 85, 120 and 200 kW, as described in Table 2.4. All machines are water-glycol cooled, with ports shown in Figure 2.10 where the generator is mounted with a 2:1 gear and engine shaft spline, facilitating higher speed operation. It is apparent that the machine space envelope is not compatible with the engine envelope.

Table 2.4: *Siemens* ELFA PM generators and Induction motor [ISE Corp., 2004].

Characteristic	PM Generator		
Rated Power [kW @ rpm]	85 @ 2500	120 @ 4000	200 @ 7200
Rated Voltage [VDC]	650	650	650
Rated Torque [Nm]	320	320	600
Max. Torque [Nm]	450	450	1200
Rated Current[A]	170	170	265
Max. Speed [rpm]	4,000	4,000	8,000
Dimensions (w x h) [mm]	245 x 245	245 x 245	245 x 245
Length [mm]	560	560	NA
Weight [kg]	120	120	200

2.4.1 Duty Cycle

Several drive cycles exist for real world local public transport bus operation. Figure 2.11 illustrates Braunschweig, RATP Paris and TNO [*Braunschweig Bus Drive Cycle*, n.d.; *Orange County Bus Drive Cycle*, n.d.]. In addition, the FIGE cycle



Figure 2.10: Radial Flux PM generator and geardrive to ICE, manufactured by *Siemens*.

obtained from monitoring 20 goods vehicles and buses in Germany includes urban, suburban and motorway driving, with limited engine idling [*FIGE Drive Cycle*, n.d.]. Another cycle was compiled by Millbrook Proving Ground from data logged on the London omnibus route 159 [Millbrook Proving Ground Ltd., 1996].

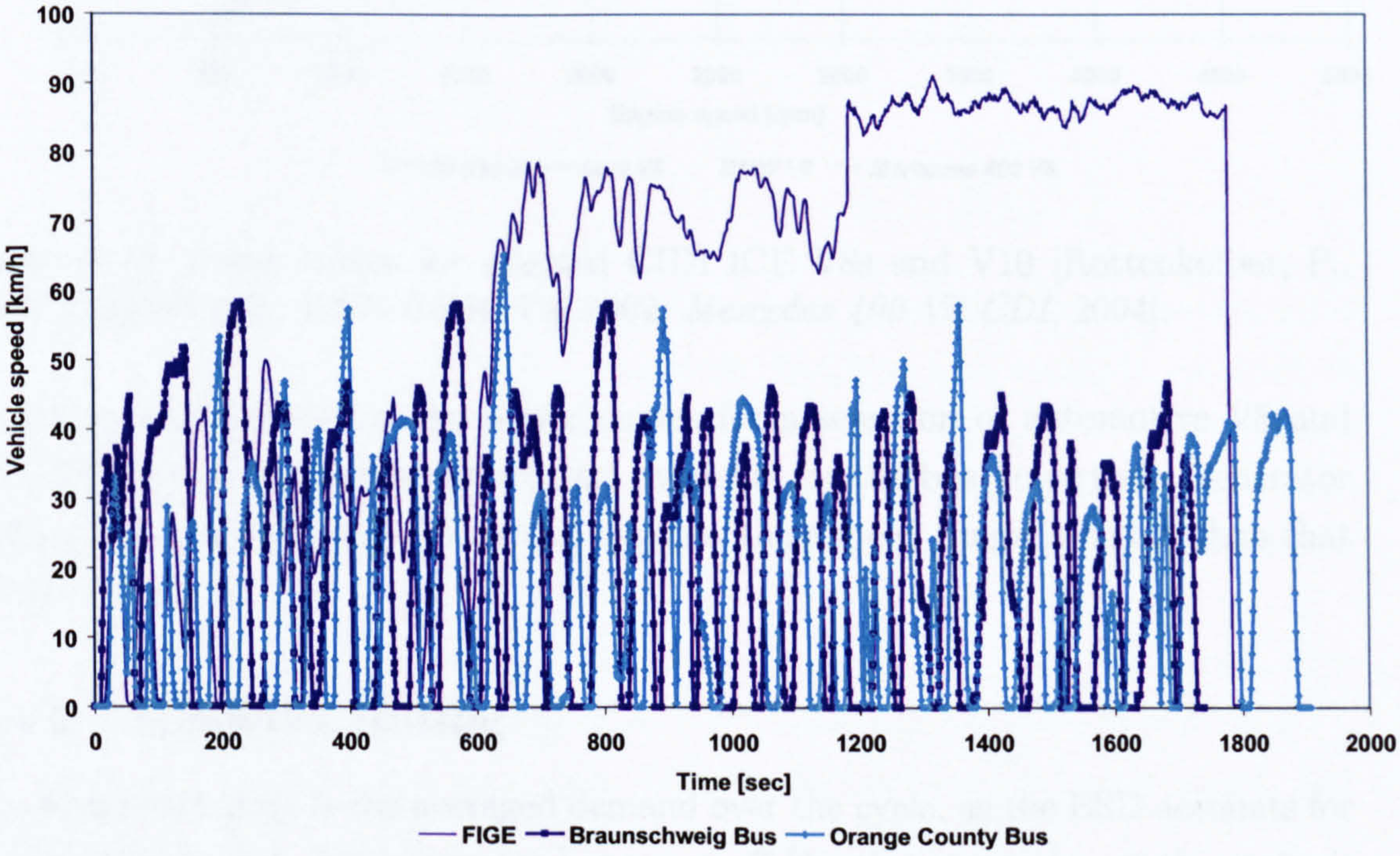


Figure 2.11: Real world bus drive cycles.

Figure 2.11 illustrates real world drive cycles obtained from the operation of buses and CVs. The FIGE cycle was logged from the operation of 17 goods vehicles and 3 local public transport buses in Germany. This cycle includes urban, extra-urban and motorway driving and omits idling, making it less representative of either

bus or CV operation. The Braunschweig and Orange County bus cycles were logged from extensive bus operation, making them more representative of bus operation alone. These cycles can be repeated to account for one complete day of vehicle operation.

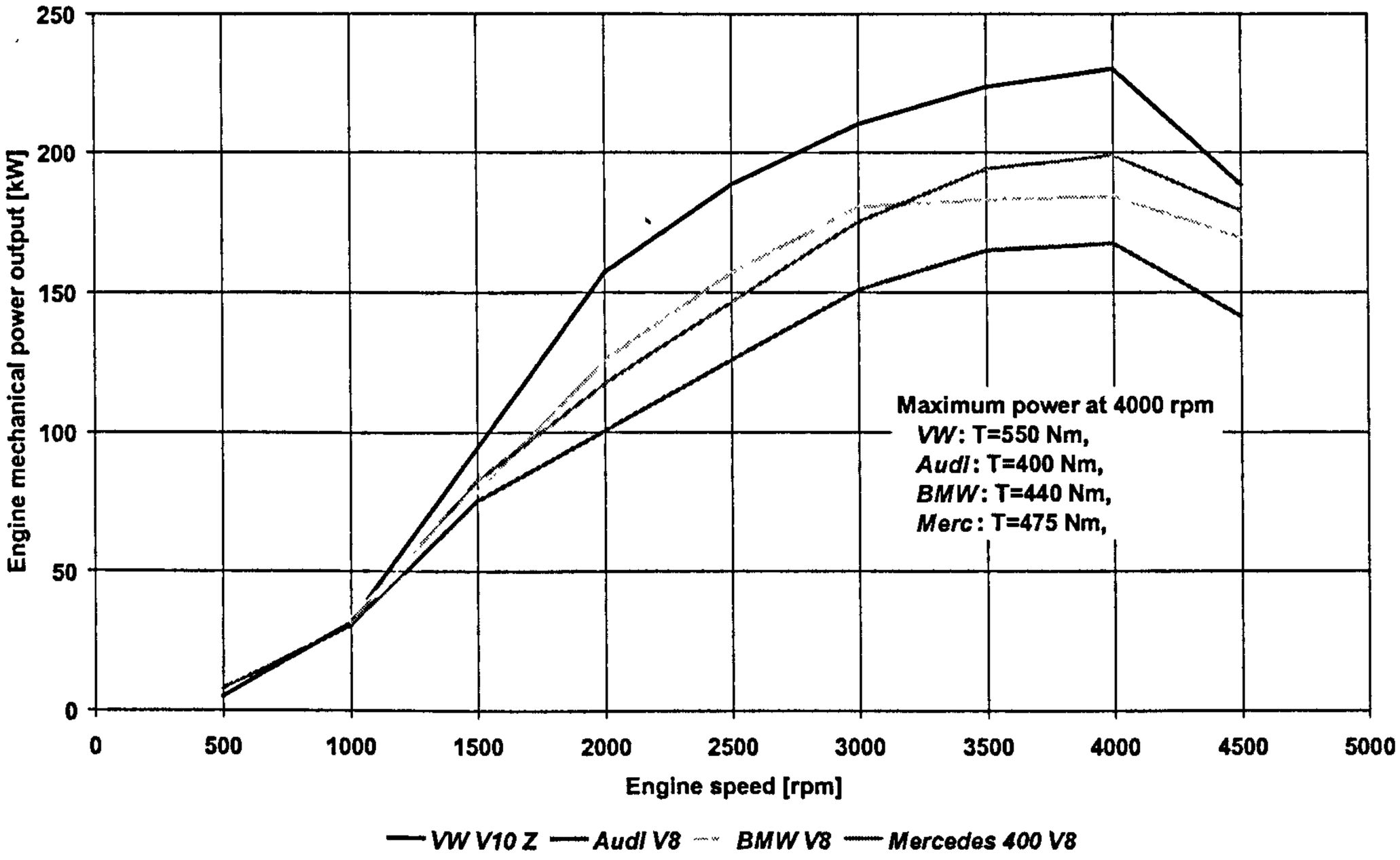


Figure 2.12: Power curves for selected CIDI ICE V8s and V10 [Rottenkolber, P., 2000; Ziegler et al., 1997; *BMW V8*, 2002; *Mercedes 400 V8 CDI*, 2004].

Figure 2.12 illustrates the power curves for a selection of automotive V8 and V10 ICEs from German manufacturers available for the bus powertrain Generator application. As these are automotive engines, their speed range is higher than that of the CV engine.

2.4.2 Specified Rating

The Generator duty is the averaged demand over the cycle, as the ESD accounts for transient operation. The generator has an on-off function, operating at the engine's specified best fuel economy according to the BSFC map, which is 65 kW, or on the Optimum Operating Line close to this point of best fuel economy, but not reaching maximum power of the engine.

2.4.3 ICE Integration

The *Audi* 3.0 litre V8 is selected, providing 400 Nm at 4000 rpm [Bauder et al., 1997]. However, the flywheel housing size is SAE6, which is rather small. This indicates a small machine, with lower torque, therefore higher speed including gearing is required.

2.5 Summary

The fuel economy figures from the powertrain modelling for both the conventional and hybrid powertrains are compared. For both applications, these are given in Table 2.5.

Table 2.5: Fuel economy figures from modelling both case study powertrains.

Vehicle	Fuel consumption [l/100km]	Improvement [%]
7.5 tonne delivery CV (Figure 2.4 cycle)		
conventional	92	-
hybrid	70	24
70-seat bus (Figure 2.11 cycles)		
conventional	168	-
hybrid	102	39

The envelope size, power and torque performance specifications, and aspect ratio have been established for the HEV powertrain machine case studies. Analysis of the electric traction system using simple expressions for the power losses of each component provides approximations for system efficiency at important steady-state operating points. For the 7.5t CV electric drive, the battery and motor currents are found to dominate.

However, the overall system efficiency is high, even at high power operation. One possibility for improving this is use of an automated manual transmission (AMT), the control of which allows lower gear selection to increase the motor speed, but design of an optimised gear set would be preferred.

The design constraints for the 70-seat bus HEV powertrain machine have been achieved. The machine design employs the analytical equivalent magnetic circuit model, which is described in Chapter 5.

Chapter 3

Review of Axial Flux Machines and Analytical Electromagnetic Models

This chapter provides a review of the previous published work on Axial Flux PM machines and the use of selected machines in HEV powertrain applications.

The Axial Flux machine topology is far less common than the Radial Flux topology, and as such there are only a few publications addressing issues related specifically to the Axial Flux topology.

Several analysis methods exist for evaluating machine performance. Of particular interest is appropriate methods for Axial Flux machines in HEV powertrain models, which match the level of detail employed to model other components.

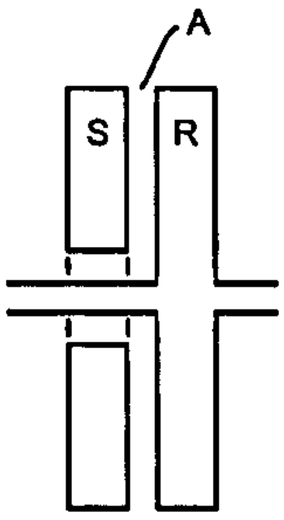
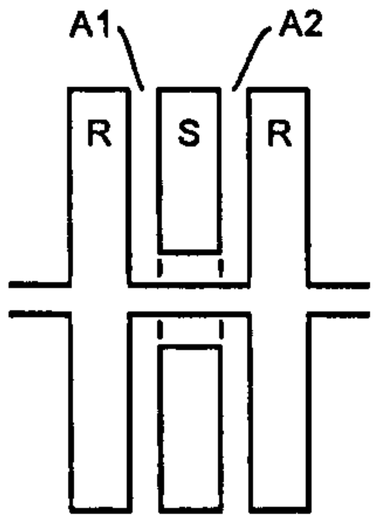
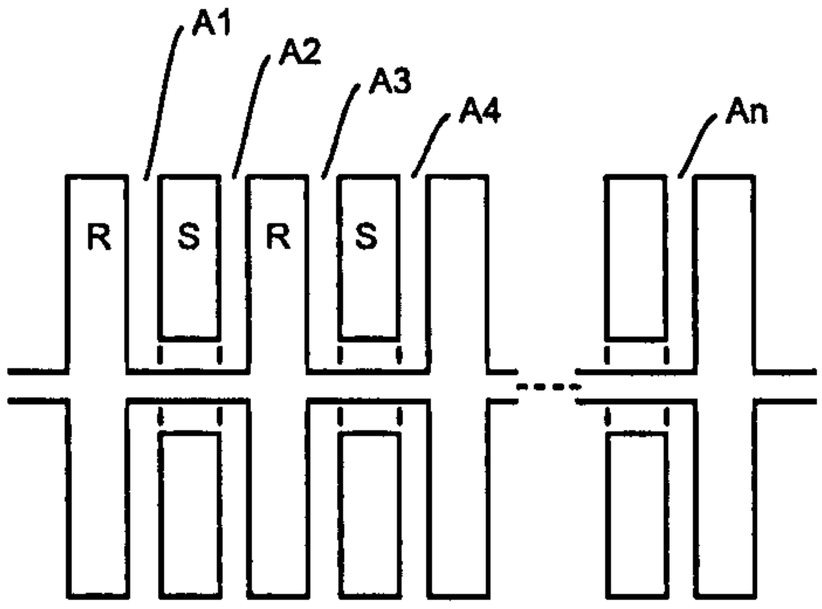
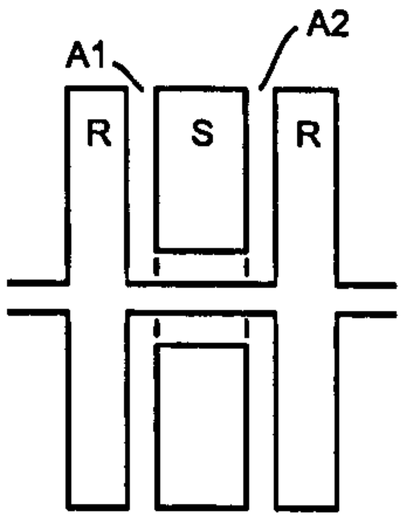
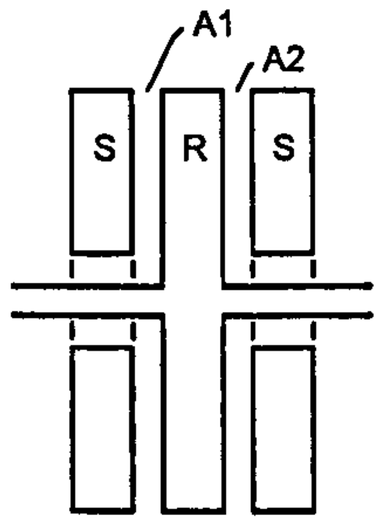
3.1 Categories of Axial Flux Machine

The mechanical arrangement of Axial Flux topology machines can be evaluated by magnetic path structure and can therefore be categorised in relation to their airgap(s), as shown in Table 3.1. Single, double and multiple-airgap machine designs are now considered in detail, using public domain research data.

3.2 Single Airgap Machines

The stator has an iron core, which is typically tape-wound laminated electrical steel, and normally slotted on one-side to accommodate the winding. With the single airgap Axial Flux machine, a significant magnetic attraction force develops between

Table 3.1: Axial Flux machine configurations. (A: airgap, R: rotor, S: stator)

Single Airgap	Double Airgap	Multiple Airgaps
	Internal Stator	
		
Torus Machine	Internal Rotor	
		

the stator and rotor, and this thrust load must be supported by the shaft bearings, which can affect longer term durability.

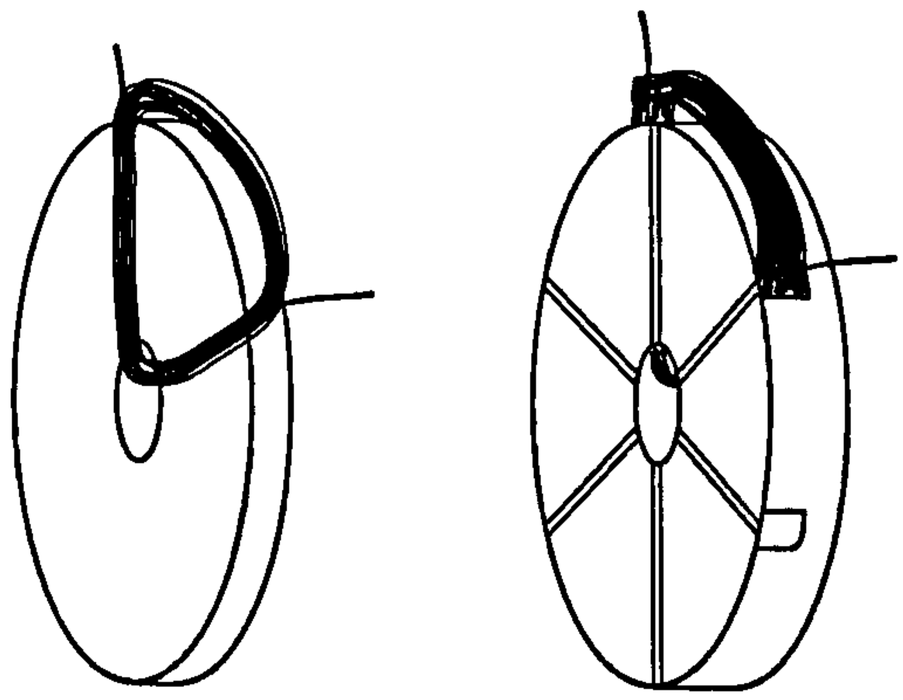


Figure 3.1: A single coil mounted on a slotless and a slotted stator.

The Torus machine is categorised in Table 3.1 along with the single airgap machine, despite having two airgaps. This is due to the main magnetic flux path, which is equivalent to that of the single airgap machine.

3.2.1 Slotted Stator Machines

A machine design by Patterson [1996] for a direct drive, hub-mounted wheel motor application in a solar-powered car was based on low rotor inertia and total mass.

Van Tichelen and Peeters [2003] demonstrated a single airgap machine in a small series hybrid commercial vehicle, with a stator comprising U-cores and concentrated windings. Zhang et al. [1997] reported a similar, yet smaller, motor with stator and rotor cores made from powdered iron, for a servomotor application. The performance advantage for selecting powdered iron was lower cogging torque when compared against a laminated steel version. Shurflo Co. [2000] use powdered iron cores, which require no manufacturing operations after compaction, other than minor deburring of the tooth tips. Jang et al. [1997] compared the cogging torque for different skew factors of poles in a 9–12 machine by 3D FEM. The effect of the axial variation of the pole and yoke at different radial positions was further investigated by Fourier analysis [Jang and Yoon, 1999].

Eastham and Evans [1978] proposed a single airgap Induction machine with an alternative manufacturing process to machining a wound lamination core. The design consisted of teeth of stacked laminations in the $r-z$ plane, and a core of stacked round lams in $r-\theta$ plane. The laminations can be grain-oriented, aligned with the flux in different parts of the main flux path.

3.2.2 Slotless Stator Machines

Takano et al. [1992] proposed an airgap winding machine. For a given machine length, 2:1 is the ratio of PM height to airgap winding thickness proposed for minimum winding eddy current losses. The empirical method involves PM height and armature thickness measurements on an existing motor. This proposed 2:1 ratio is less than for the typical permeance coefficient for maximum specific torque, which is 4 or 5:1 for slotted machines.

3.2.3 Torus Machines

The main flux path of the Torus machine is equivalent to two single airgap machines with back-to-back stators. However, conductor coils are wound around both sides of the stator, resulting in a current direction that is equivalent to the single airgap machine during the active part, but in the $z-$direction rather than the $\theta-$direction in the endwindings, as in Figure 3.2.

A slotless stator generator was introduced by Spooner and Chalmers [1990],

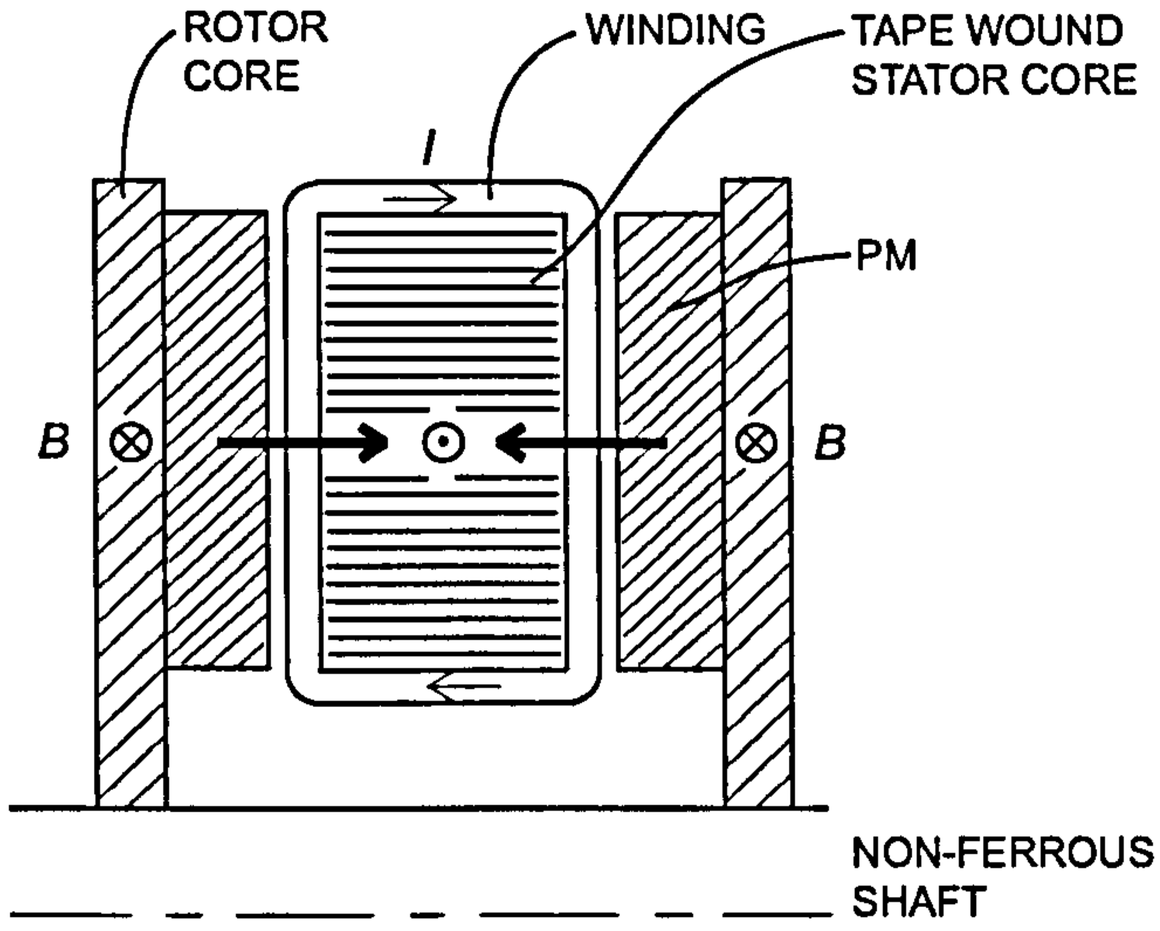


Figure 3.2: Torus electromagnetic operation [Huang et al., 1999, orig.].

[1992*a*] and [1992*b*]. Further such machines have been reported by Elmissiry and Chari [1992], Huang et al. [1999] and Zhang et al. [1997].

Slotted stator machines are reported by Cirani [1999], Şimşir and Ertan [1999], Dubois et al. [2001], Aydin et al. [2001*a*], Caricchi et al. [2001*a*] and [2001*b*], and Qu et al. [2003]. These publications report a higher aspect ratio than the Through Flux machine due to a longer $z-$direction stator core and smaller housing radius. The longer stator provides a higher total machine mass, and correspondingly the iron losses are higher due to more alternating flux in iron.

3.3 Through Flux Double Airgap Machines

The Through Flux machine has a main flux path stretching the length of the machine. In double airgap machines this crosses both magnetic airgaps twice to complete the main flux circuit.

As shown in Table 3.1, the internal rotor machine has a rotor mounted between two stators and the internal stator version has a stator mounted between two rotors.

3.3.1 Internal Rotor

The stators at either end are symmetrical so the rotor does not provide any flux return path, resulting in a very low rotor inertia [Platt, 1989]. The stators may be slotted or slotless. Offset slotted stators give a balanced reluctance of the main flux path. Geetha and Platt [1992] proposed a 16-pole servomotor with identical concentrated winding single phase stators, which were offset by a half pole pitch to

achieve two phases.

Eastham et al. [1995] and [1996*b*] presented an 8-pole machine for an EV wheel motor application with a rotor that can rotate eccentrically, as the poles are longer in the radial direction than the stator core active length. Madlena et al. [1996] reports an equivalent magnetic circuit model for use in calculating the control of this machine. The first configuration was with open slots, and the second was semi-open slots, where the tooth tips were powdered iron.

Cho et al. [1993] investigated the axial attractive force, which arises from an offset rotor position with respect to both stators. Yang et al. [2002] presented a wheel-mounted motor with the wheel installed on the outside of the rotor. The fractional coil pitch design gave constant attractive force with the rotor position, which also neutralises most of the reluctance torque to minimise cogging torque. The lower permeability of powdered iron material offers lower torque pulsations and is relatively easily shaped for the Axial Flux machine [Hredzak et al., 1996*a*].

Sahin et al. [2001] reported the mechanical considerations of a high speed (16000 rpm) flywheel application. Thermal and rotor stress analyses are the main considerations, along with windage losses. Thermal management is easier with the internal rotor structure, as cooling can be passed around the back of the stators [Jensen et al., 1992].

Aydin et al. [2001*b*] compared slotted and slotless (airgap winding) stators. The constant reluctance of the main flux path of the slotless stator ensures low cogging torque, but requires more magnetic material so the overall axial length is longer.

Further papers by Amaratunga et al. [1985], Gair and Yang [1990], Shurflo Co. [2000], U. of Eindhoven [2001], Parviainen et al. [2001] and Perm Motor GmbH [2003] report similar issues with internal rotor machines.

3.3.2 Interior Magnet Internal Rotor

The Interior Magnet (IPM), or Buried Magnet, machine is attractive for operation in a flux weakening regime. Because less $d-$axis current demagnetization flux passes through the PMs, the structure protects the PMs against irreversible demagnetization.

Profumo et al. [1998] and [2000], and Cavagnino et al. [1999] and [2000], reported a machine with rotor magnets covered by pole caps and powdered iron "leakage" poles, incorporating flux barriers. The PMs are well protected against demagnetisation from the reactive field under large current, while the pole caps provide a near-sinusoidal airgap field waveform under open circuit.

Further IPM Axial Flux machines have also been reported by Dubois et al. [2001], Hanitsch et al. [1994] and Huang et al. [1999], with a significant aspect being a higher volume of stationary iron resulting in higher iron losses.

3.3.3 Internal Stator

3.3.3.1 Coreless Winding

A coreless stator (airgap winding) machine is light-weight, but the longer magnetic airgap requires a larger PM volume to maintain airgap flux density. For the flux path return at both ends, a coreless winding machine has an internal stator structure and there are no magnetic attraction forces on the stator. As this makes thermal management more difficult, Caricchi, Crescimbini, Mezzetti and Santini [1996] presented an interesting coreless, direct-drive wheel motor with a cooling water duct, where the core would otherwise be located, removing heat from within the winding.

The winding inductance is extremely low, but eddy current and copper losses are significant. Sullivan [2001] investigated the conductor geometry and related eddy current losses considering both the number of coil turns and conductor twisting introduced during winding of Litz wire coils. However, copper has a very high heat transfer coefficient, which gives a good thermal performance. Assuming the convective heat transfer coefficient of the winding to air to be 20 $Wm^{-2}K^{-1}$, Lovat et al. [1998] selected an airgap winding on the grounds of higher efficiency as, leaving aside the iron losses, there is more space for the winding allowing more copper, reducing the current density and lowering the copper losses. Litz wire was employed to limit eddy current losses, also by Wang and Kamper [2002].

3.3.3.2 Iron Cored Winding

The magnetic airgap of a slotted core machine is smaller than for a coreless winding, so less PM material is required. The core material is an important consideration, with both laminated steel and powdered iron having been used in prototype machines reported by Weh and Boules [1980], Wallace et al. [1997], Profumo et al. [1997] and Di Napoli et al. [2000]. The slotted machine has redundant core material at the bottom of the slots, which may be removed, if suitable mechanical integrity can be achieved.

As the internal stator double airgap and Torus machines are similar, the dimensions are compared in Table 3.2, and the grounds for selection identified.

Table 3.2: Torus and Internal stator double airgap machine comparison

Machine dimension	Torus	Internal Stator Double Airgap (Int. Stat. $2g$)	Priority for selection
Length	$h_{Fes} + 2h_{Fer}$ $[h_{Fes} = 2h_{Fer}]$	$2h_{Fer}$	short length $\rightarrow$ Int. Stat. $2g$
Radial ext. dim's (2 coils per slot)	$r_o + h_c$ $r_i - h_c$	$r_o + \tau_s/2[r = r_o]$ $r_i - \tau_s/2[r = r_i]$	small diameter if $h_c < \tau_s/2 \rightarrow$ Torus (depends on pole no.)

3.3.4 Comparison of Internal Rotor or Internal Stator Machines

The double airgap Axial Flux machine configurations with either internal stator or internal rotor, as shown in Figure 3.3, have near equivalent parametric performance indicators, such as Motor and emf Constants. The electromagnetic consideration relates to the portion of the flux path in static ferrous material, which sustains classic iron losses.

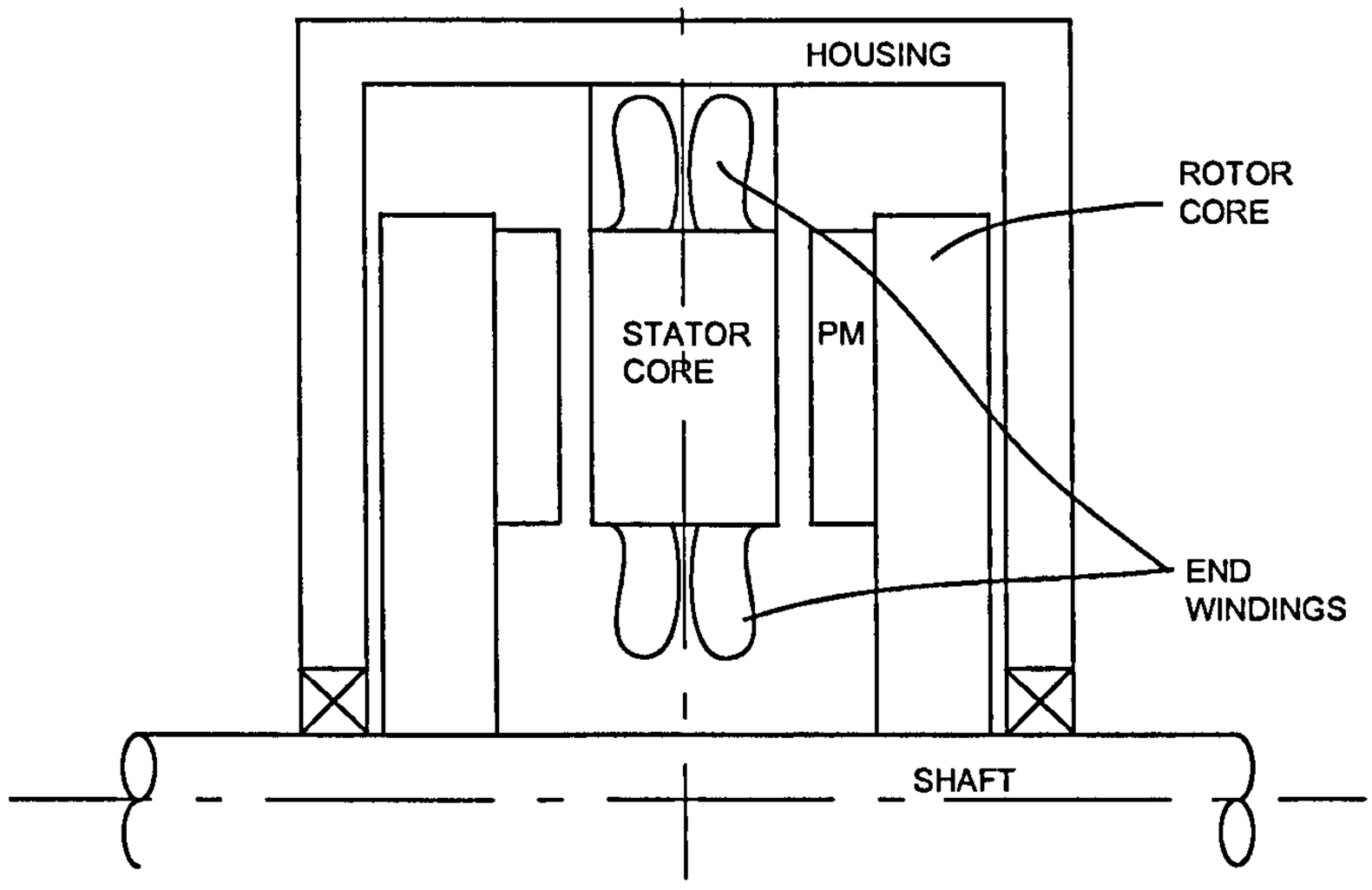
3.3.4.1 Rotor Surface Losses

A slotted stator with large flux variation has equivalent variation in both configurations. However, the iron rotor yokes of the internal stator design experience this variation along with the magnet poles, and both sustain eddy current losses. The PM poles of the internal rotor design also experience this variation, but the rotor has no iron.

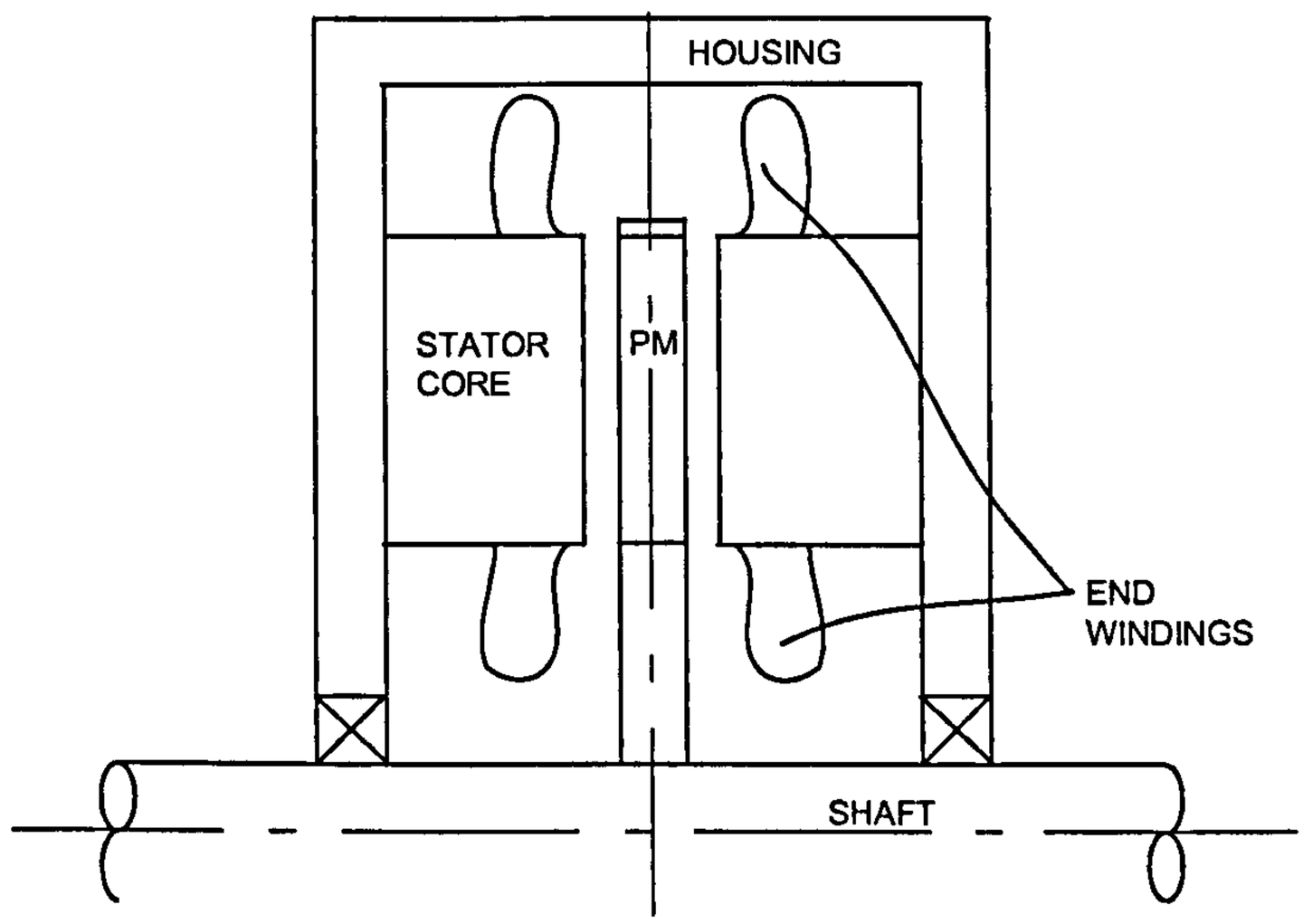
The internal rotor design, however, has a longer portion of the flux path in the stator, which is an alternating flux in static iron and incurs classic iron losses that increase with the volume of material. Further features of the internal rotor design are given in Table 3.3.

3.3.5 Comparison of Single and Double Airgap Machines

Sitapati and Krishnan [2001] compared Axial Flux BLDC machine configurations with single and double airgap internal rotor machines with slotted and slotless stator cores. These had equivalent wire size r_c, slot fill factor K_{sf}, phase resistance R_ϕ, airgap flux density B_g and temperature rise. The 100 Nm (10 kW) machines are interpreted in Table 3.4. Slotless machines require a larger diameter for the additional coil turns (to sustain emf with a weaker excitation field in a longer airgap). This leads to more copper, due to more turns, and more PM material so there is a poorer T/I ratio for this constant torque. The internal rotor in double airgap machines has



(a) Rotor–Stator–Rotor



(b) Stator–Rotor–Stator

Figure 3.3: Double airgap rotor–stator configurations.

no iron so rotor mass is less, while single airgap machines do have rotor iron.

The torque density and specific torque of some Axial Flux machines reported are collated in Table 3.5, which illustrates the variation in machines according to designs.

Table 3.3: Internal rotor and internal stator features.

	Internal rotor	Internal stator
stator return yoke thickness h_{Fe}	avoid saturation, occurs if $h_{Fe} < \tau_m$	n.a.
hysteresis iron losses	with AC flux in stator core (not only teeth)	shorter AC flux stator path
eddy currents in mounting plate	induced by AC flux in the iron	in housing wall if significant leakage from rotor back iron
cooling circuit position	far from conductors and airgap, iron core conducts heat from active area	close to coil outer endwinding
rotor stiffness	reduced without rotor core, structural rigidity requires $h_{Fer} > h_m$	maintained by rotor back iron
stator core mounting	fasteners interrupt flux paths in core – minimised by centre tooth position	same fasteners problem

Table 3.4: Normalised characteristics of Axial Flux BLDC machines [Sitapati and Krishnan, 2001, orig.]

Machine Airgap and Core	T/I [Nm/kgm^2], normal.	T/M_{active} [Nm/kg], normal.	T/Vol_{active} [kNm/m^3], normal.
Single, Slotted	460, 1.0	4.8, 1.0	48, 1.00
Single, Slotless	320, 0.7	4.8, 1.0	80, 1.70
Double, Slotted	560, 1.2	4.8, 1.0	42, 0.90
Double, Slotless	420, 0.9	4.8, 1.0	45, 0.95

Table 3.5: Comparison of selected reported Axial Flux machines.

Axial Flux Machine	Torque Density [kNm/m^3]	Specific Torque [Nm/kg]
Torus Motor [Cirani, 1999; Caricchi, 1996]	16.7 - 24.0	3.1 - 4.5
Kaman Motor [Millner, 1994]	15	4.8 - 7.2
Motor, low p - high p [Şimşir and Ertan, 1999]	-	1.5 - 7
Slotless motor, double airgap [Sitapati and Krishnan, 2001]	45	4.8

3.4 Multiple Airgap Machines

The reported machines with multiple airgaps are repeated versions of the through flux machine with an internal stator structure. Only the end rotors have keeper plates allowing the main flux path circuit to cross all airgaps twice. All these ma-

chines have coreless windings. Many have been designed for high speed applications.

3.4.1 Conventional Speed

At conventional speed, the concentration of copper and PM material achieves a very low weight machine.

Mbidi et al. [2000] investigated a four-airgap machine, but did not remove the iron from the middle rotor, in order to maintain structural stiffness during assembly when the attractive axial forces are unbalanced, and strengthened the end rotors. However, coreless stators were employed so these attractive forces on the middle rotor should have been managed during assembly, allowing a mechanical design primarily for operation.

Hill-Cottingham et al. [2001] and [2002] presented a coreless multi-stage motor for an aircraft propeller drive application, focusing on the conductor eddy current losses due to axial and tangential airgap field components. Multiple smaller conductors wound in hand were employed.

3.4.2 High Speed

The multi airgap configuration was employed at high speed by Turbo Genset Co. [2002]. The rotor discs aid the rotor dynamics in controlling vibration modes as the centrifugal forces keep the shaft aligned. El-Hasan et al. [2000] presented a modular design for 50000 rpm operation, manipulating number of turns according to conductor forces, machine efficiency, Litz wire strand and bundle size.

Pullen [1991] reported an etched disc making concentrated coils of required conductor size, and filled the etched space with powdered iron. Hanitsch et al. [1994] also presented a multi-layered stator with coils etched from copper disc, noting a thinner package when repeated in the $z-$direction. Although the high speed machines were originally designed to be directly driven by a micro gas turbine, and employed for Series HEV generator application, the poor efficiency of this engine has prevented their widespread use in HEVs.

3.5 An Introduction to Analytical Electromagnetic Modelling Methods

The rest of this chapter deals with the background to analytical models, which facilitate computer-based analysis of electric machines. Expert use of the Finite Element

Method (FEM) is generally accepted as the most accurate method for computing the electromagnetics of complex geometries, and properties such as inductance. Such expertise lies in sectioning the geometry, applying boundary conditions and meshing. However, as a design tool, FEM is expensive in terms of computer time to construct the model in a pre-processor before solving and analysing. Subsequent changes to the geometry require reconstruction before recalculation, making parametric investigation the most expensive. An analytical model of a simplified geometry, which can be solved quickly to give engineering results, is interesting for such parametric studies.

Accurate calculation of the peak airgap flux density and waveform are of particular interest to evaluate performance and when considering electrical efficiency. Some of the analytical modelling methods that are available for Axial Flux machine analysis are "lumped parameter", "surface point charge", "equivalent magnetic circuit", and "field solution".

Assumptions in simple analytical models, which calculate performance based on flux densities, are:

- The machine has no magnetic saturation, i.e. is operated within a linear $B-H$ curve for the magnetic materials,
- The airgap reluctances, including leakage and fringing, can be approximated with the Overlapping Area Method,
- In the simplest form, the flux passes straight across the airgaps, where leakage may be estimated by inclusion of a leakage factor, and in the more advanced form, leakage paths are individually modelled.

The equivalent magnetic circuit model has been selected for the present work, but a brief background of each modelling method and the appropriateness to Axial Flux machines is given first. The characteristics of each are summarised in Table 3.6.

3.6 Lumped Parameter Model

The lumped parameter model is a circuit with general values for machine inductance and phase resistance. The LRC values are derived separately by analytical relations or more commonly by FEM.

The non-salient pole SM PMSM machine circuit is given in Figure 3.4, while the general form for the salient-pole machine, with non-equivalent $d-$ and $q-$axes inductances, is given in Figure 3.5. The flux linkage provides the induced emf and

Modelling Method	Provides ϕ_g (B_g) waveform	Models iron saturation	Models leakage	Complexity (time to build)	Solution time comparison
Lumped Parameter				low	fast
Surface Point Charge Representation		✓	✓	low	fast
Regional Field	✓	✓	✓	high	slow
Airgap Field Co-energy				low	fast
Equivalent Magnetic Circuit 2D		✓	✓	low	fast
3D	avail.	✓	✓	high	fast

Table 3.6: Comparison of analytical modelling method characteristics.

the model renders terminal voltage and current values according to the operating conditions.

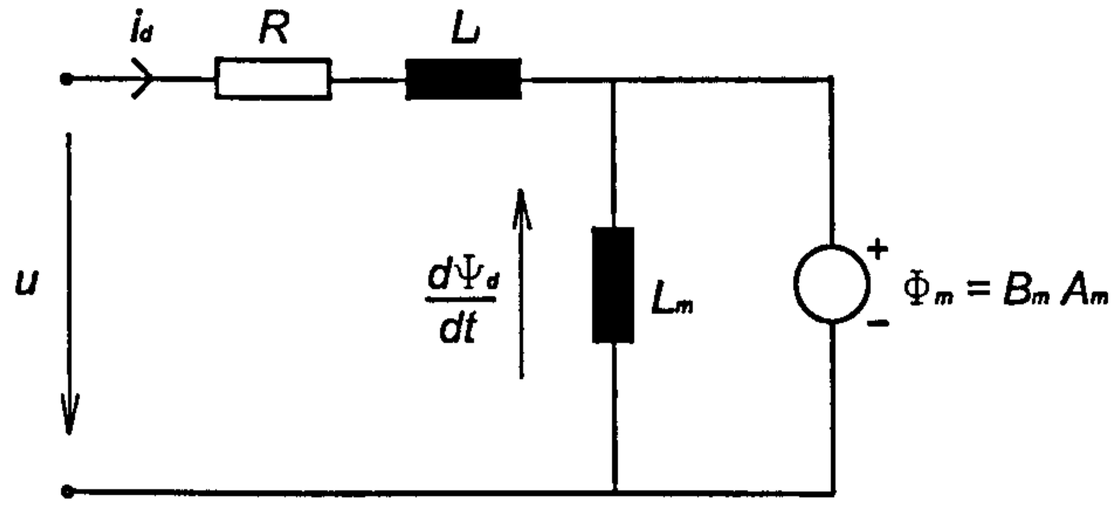
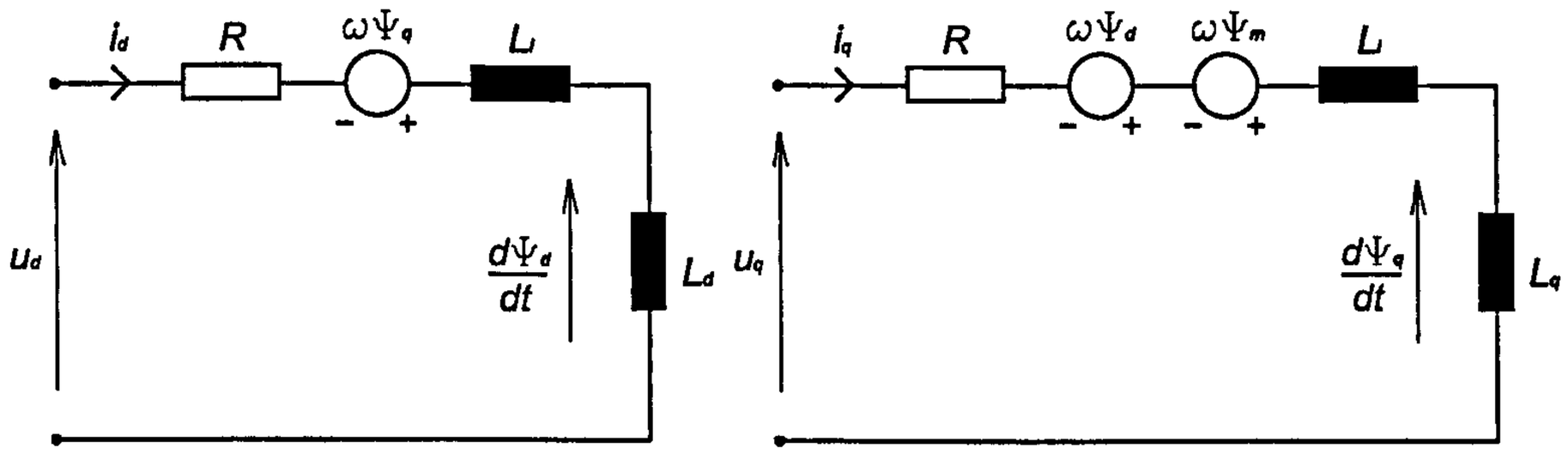


Figure 3.4: Lumped parameter circuit for non-salient pole (SM PMSM) machine.



(a) $d-$axis circuit

(b) $q-$axis circuit

Figure 3.5: Lumped parameter circuits for salient pole machine.

This is a useful tool when a specified machine is part of an electric powertrain, but of limited usefulness for evaluating the electromagnetic operation. Yang et al.

[2002], for example, performed a lumped parameter model analysis of an Axial Flux machine for an EV Traction motor application. The LRC values may be initially accurate but vary with operation and conditions.

Parametric studies of the machine design within the powertrain may not be achieved as the LRC values are not computed. The further methods model the machine electromagnetics and airgap magnetic field, allowing parametric studies of the machine design.

3.7 Surface Point Charge Representation

A method for representing Permanent Magnets is the "surface point charge" method, also known as the "method of images", which is solved by the Boundary Element Method (BEM), to give the distribution of the airgap field [Furlani and Knewtson, 1997]. The accuracy of this method is poor close to the boundary, where the space between points has an influence, or with excessive pole-to-pole leakage, such as with an airgap winding. For the Axial Flux topology, this method has acceptable accuracy in the central region of the airgap only [Walker, 1999]. It should be noted that this method is different to modelling PMs in FEM by current loops in infinitesimal areas at the pole edges. The magnitude of the charges is determined by the magnet remnant flux density, size and number of charges. The "image charges" are located in the rotor core to a depth equivalent to the magnet height, as in Figure 3.6.

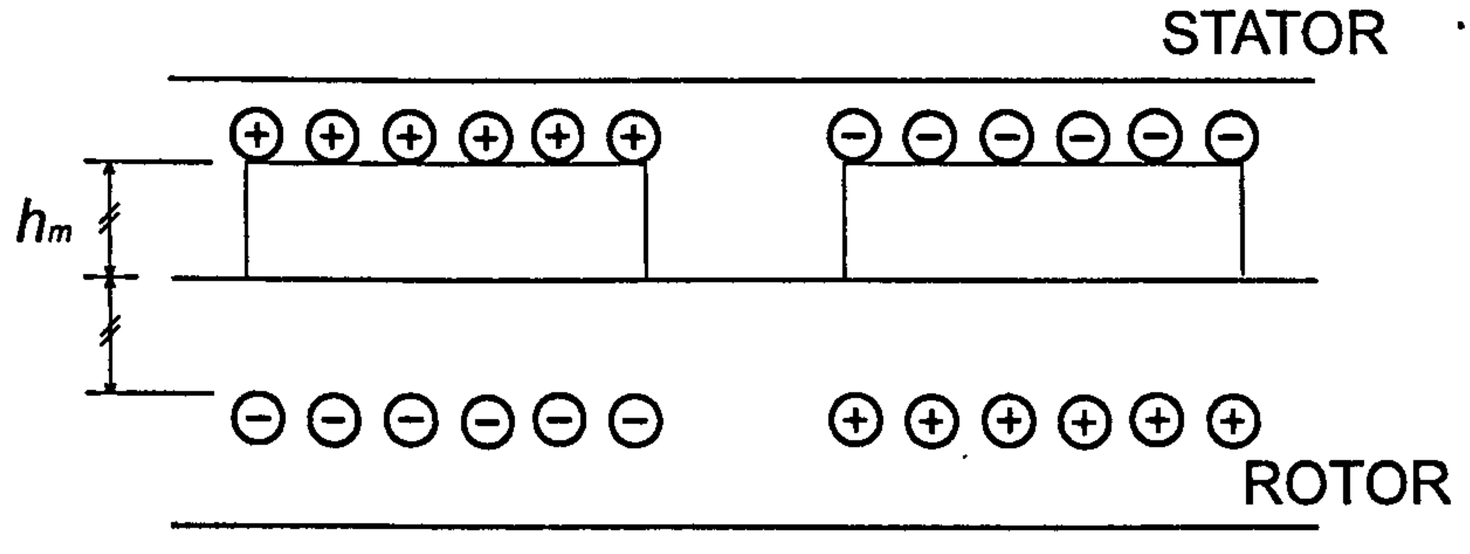


Figure 3.6: Permanent Magnet representation by surface point charges.

3.8 Regional Field Solution Model

Zhu and Howe [1992] used Maxwell equations in separate regions and the product of an airgap permeance function and the mmf to give the airgap field for Radial Flux machines. Zhilichev [1998] employed this technique on a slotless Torus machine by dividing the geometry into regions. The 3D problem complexity required expensive

computation, in particular for iteratively solving the continuity over boundary conditions. The 3D Torus machine model provided a correction factor for flux fringing at the ends of the airgap for a 2D version, which is computed more cheaply. This is a suitable method for a parametric study of multiple designs, where simple region boundaries can be defined, such as for a slotless machine with constant airgap permeance function.

Although the accuracy decreases with a varying permeance function, Barakat et al. [2002] overcame this with separate expressions for the cogging torque for a parametric study.

3.9 Airgap Field Co-energy

The field co-energy within the airgap is comprised of the individual components for allignment, cogging and reluctance torques [Yang et al., 2002]. The torque is obtained from the rate of change of the field stored energy, which for a linear magnetic system, is equivalent to the co-energy, where the change is given by $L_\phi I_\phi^2 = R_{mg}\Psi_{c\phi}^2$ [Hanselman, 2003]. However, the linear magnetic system only describes the machine at low current as no saturation is present.

Inductance can be evaluated using the co-energy stored by the inductance and the co-energy stored in the field from the coil for volume. Another method must be employed to provide the reluctances and fluxes, but, by evaluating each torque term separately, the change in performance due to design alterations can be appreciated.

3.10 Equivalent Magnetic Circuit Model

The "equivalent magnetic circuit" describes the main flux circuit and leakage circuits, which can be solved by a Kirchoff network [Brown et al., 2000]. Flux is equivalent to current in an electric circuit, reluctances are equivalent to electrical resistances and PMs and coil $mmfs$ are equivalent to current and voltage sources. For an Axial Flux machine, the machine geometry may be modelled in 2D, quasi-3D or 3D.

3.10.1 2-Dimensional Model

A simple analysis of Radial Flux machines is often achieved by considering a 2D slice, with variables multiplied by the machine length. The Axial Flux machine offers no similar 2D slice for simple analysis, so a pseudo-2D slice is achieved by selecting a

$\theta - z$ plane through the machine at constant radius r to form a rectilinear model [Campbell, 1975], which includes rotor, airgap and stator as shown in Figure 3.7. The common radial position for this slice is the mid-position of the active area at $r = (r_o + r_i)/2$.

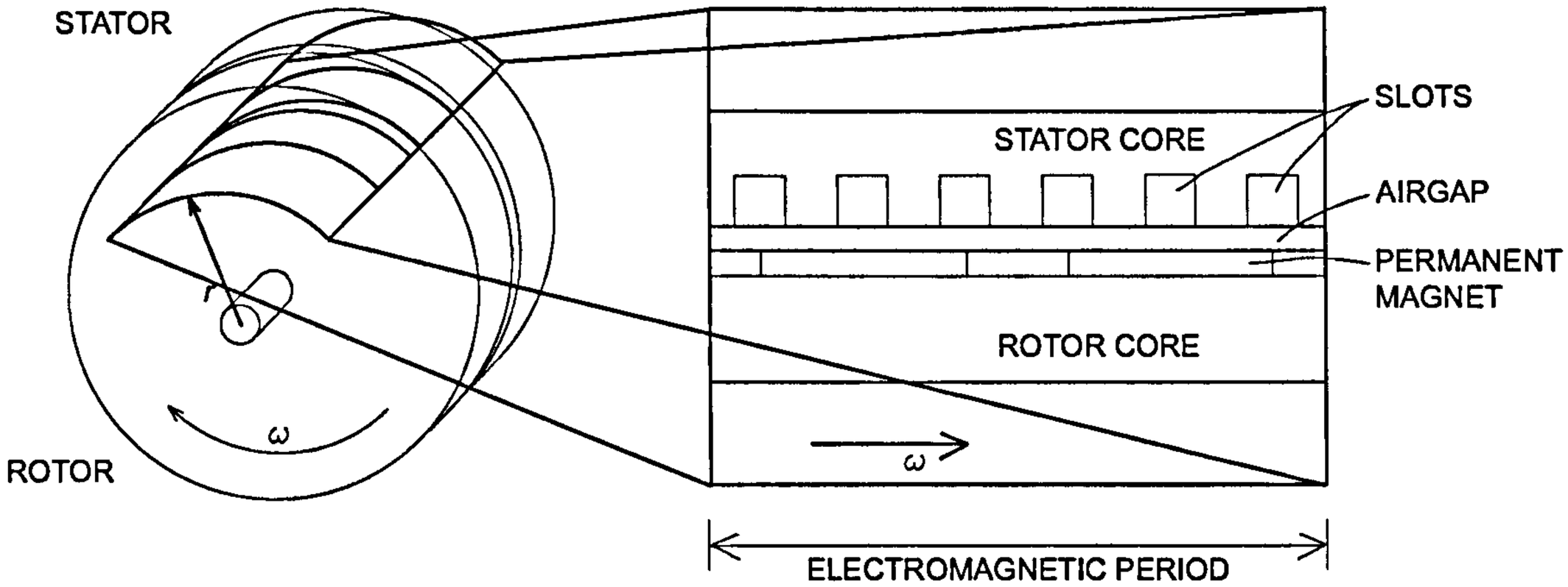


Figure 3.7: Rectilinear slice at a constant radial position.

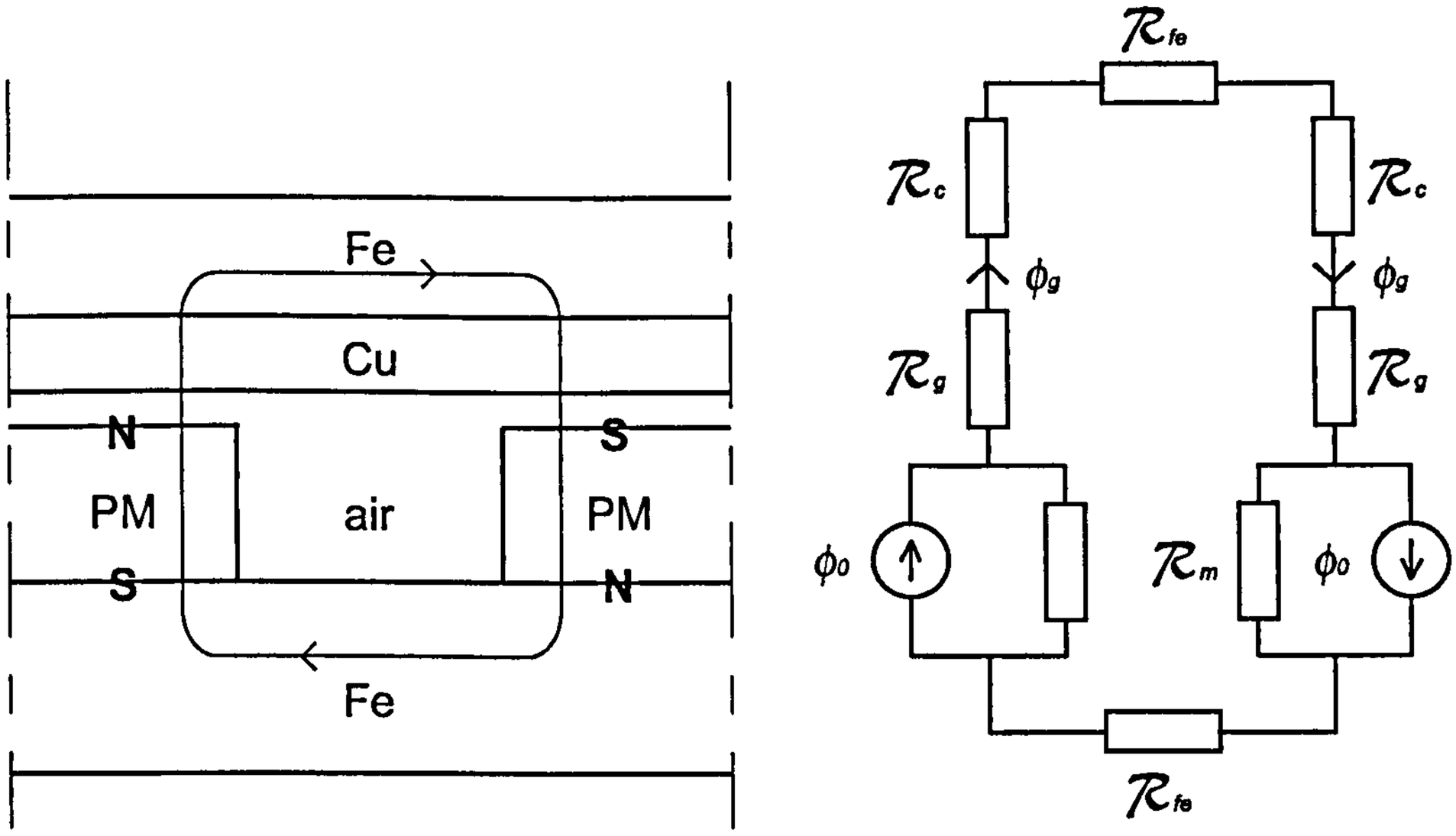


Figure 3.8: 2D equivalent magnetic circuit of main flux path of airgap winding.

The 2D equivalent magnetic circuit for the main flux path of an airgap winding is shown in Figure 3.8, depicting the reluctances and flux sources without any leakage paths. The reluctances $\mathcal{R}_{g,m,fe,c}$ are of the airgap, magnet, iron core and winding. The flux sources ϕ_0 are the magnet poles. ϕ_g is the airgap flux and is the useful flux with leakage neglected. In order to define the reluctances and flux sources, the cross-sectional area is required, which uses the length in the 3rd dimension (into the

page). This 2D model of an Axial Flux machine assumes it to be the active length $r_o - r_i$. With a 2D rectilinear model, where ϕ_0 denotes the flux source of a magnet with reluctance $\mathcal{R}_m$ and the variation in the magnet and airgap path $\mathcal{R}_{mg}$ is defined against rotor position, the flux linkage can be evaluated, which may be used to solve the airgap field co-energy model [Furlani, 1992][1994].

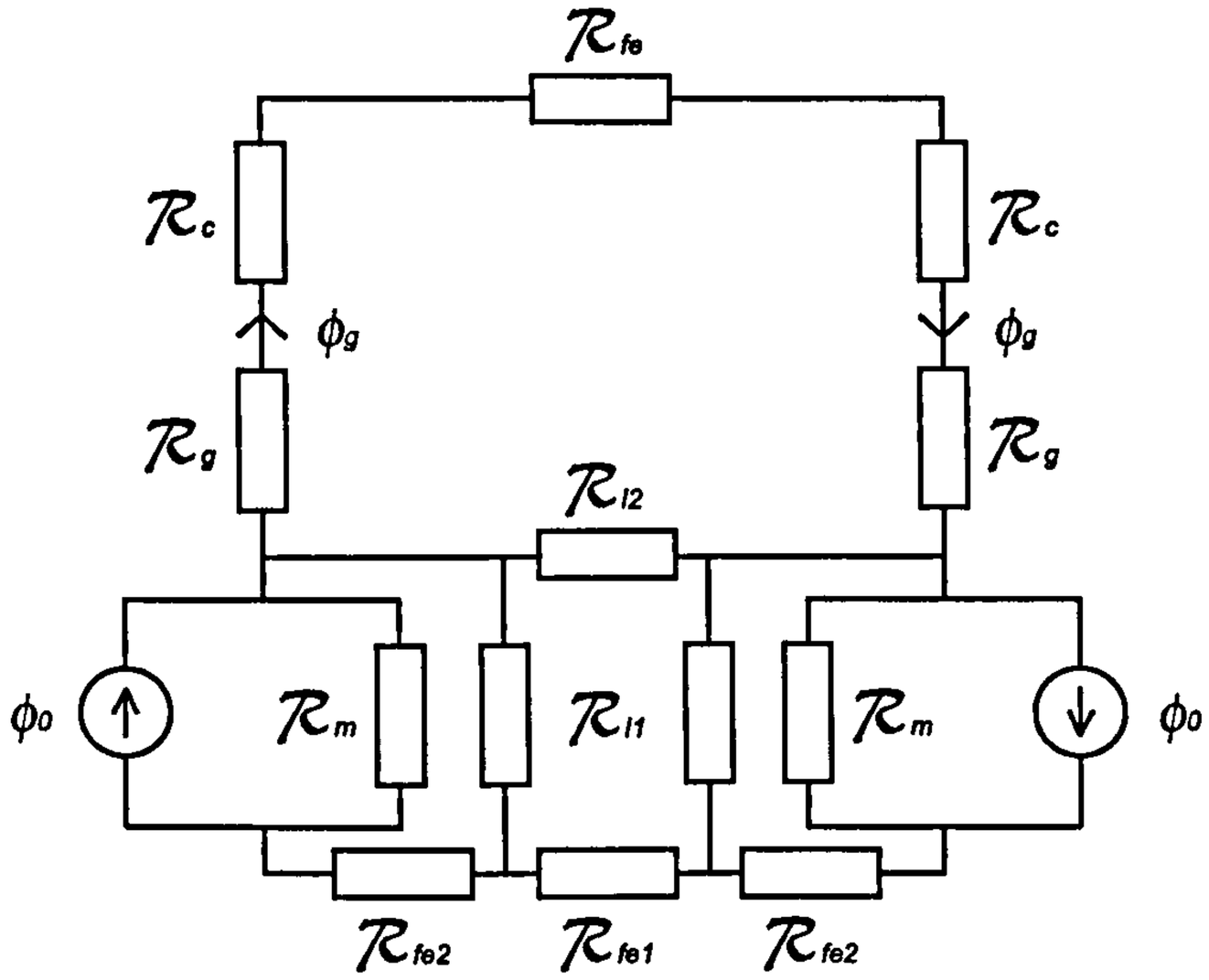


Figure 3.9: 2D equivalent magnetic circuit for main flux path and leakage paths of airgap winding.

The circuit in Figure 3.8 is improved by including the leakage flux paths, shown in Figure 3.9. The leakage path for short circuited flux from a pole to the keeper has reluctance $\mathcal{R}_{l1}$. The core has two reluctances $\mathcal{R}_{fe1}$ and $\mathcal{R}_{fe2}$ to allow for different lengths of the useful and leakage paths. The leakage path for short circuited flux from pole to pole has reluctance $\mathcal{R}_{l2}$.

The airgap flux resulting from *mmf* of the coils is found in the same way with the magnets "switched off". Ni is the *mmf* source of the coil, with RH rule polarity. Figure 3.10 illustrates c parallel flux paths between the stator and rotor for c coils. The net flux for the *mmf* $\mathcal{F}_r$ is zero as this is rotor core which returns all flux to the airgap or rear leakage paths, and Kirchhoff's voltage law gives a value for the flux of Ni divided by the sum of series reluctances. As the total flux linked by all coil turns is the product of flux and the number of turns, this gives an airgap inductance of the number of turns squared divided by the sum of series reluctances, which, according to the description of inductance in Section 4.2 for all coils connected in series with

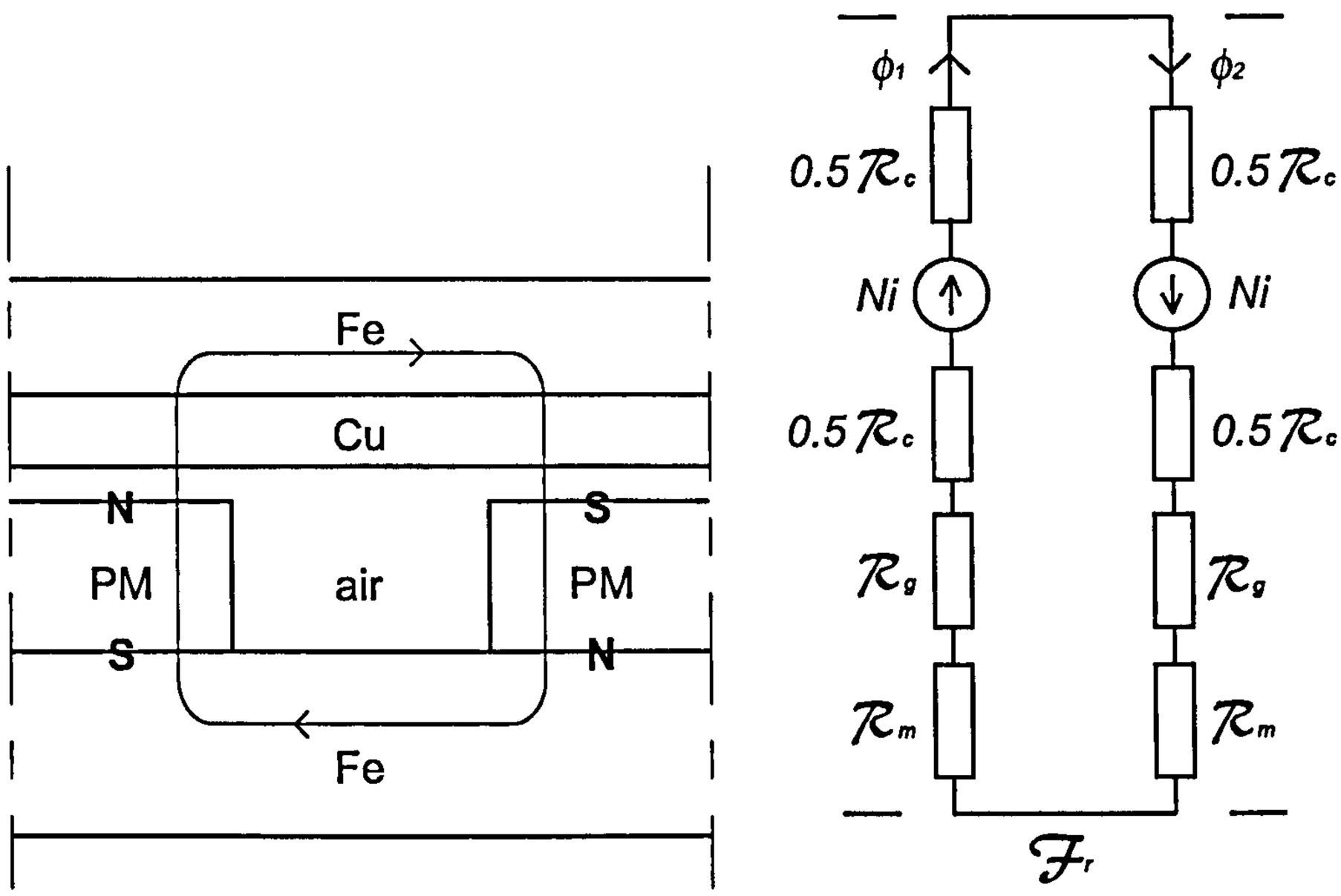


Figure 3.10: Equivalent magnetic circuit for inductance calculation.

no leakage, resolves as:

$$L_g = \frac{\pi \mu_0 (r_o^2 - r_i^2)}{g + \dfrac{h_m}{\mu_{r_PM} k_{ppitch}} + \dfrac{h_c}{\mu_{r_Cu} k_{cpitch}}} N^2 \tag{3.1}$$

where the "pole pitch factor" is $k_{ppitch} = \tau_m / \tau_p$ using the pole pitch τ_p.

3.10.2 Stacked 2-Dimensional and 3D Models

The 2D simplification of the Axial Flux geometry has inaccuracy arising from the simplified length in the 3rd dimension, which defines the cross-sectional area of reluctances and flux sources.

In order to improve the accuracy, the geometry may be sectioned in the radial direction, and repeated with a new smaller length in the 3rd dimension. This is a technique also employed in FEM [Cho et al., 1993].

The sections of the stacked 2D model are accurate nearer the mean radius, but not at the inner and outer radii due to leakage and fringing. Unlike at the ends of the Radial Flux machine, the leakage and fringing on the inner and outer radii of the Axial Flux machine are not equivalent.

Compared to FEM, there are still relatively few unknowns and computation time is short for even the most complex models. Therefore, constructing a 3D model for

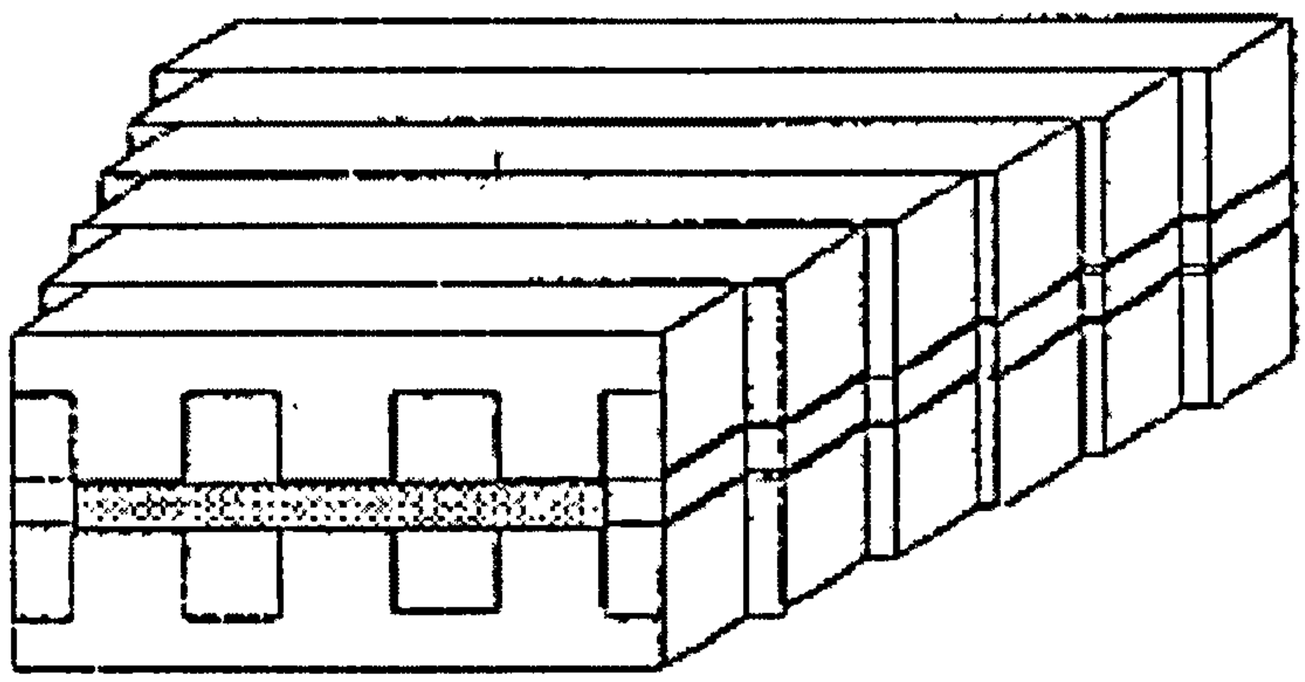


Figure 3.11: Stacked 2D model of double airgap, internal rotor machine [Cho et al., 1993, orig.].

a parametric investigation is worthwhile [Furlani and Knewtson, 1997].

3.11 Summary

This review of the published knowledge about Axial Flux machines indicates that although there are several design types, the understanding is incomplete regarding the association between design and application. In particular, the application of such machines in HEV powertrains, to which they are well suited due to the envelope aspect ratio, has not been suitably addressed.

For the purposes of modelling Axial Flux machines within HEV powertrain models, the comparison of analytical modelling techniques, which have previously been used for Radial Flux machines, indicates the advantage of using equivalent magnetic circuit modelling.

Chapter 4

Cored Axial Flux Permanent Magnet Synchronous Machine Theory

The electromagnetic relations describing Radial Flux machines are well established, but not for Axial Flux machines. Similarly, the published literature on Axial Flux machine research is much less than that published on Radial Flux machines. Having reviewed the key publications, the relations that are required to describe the Axial Flux Permanent Magnet synchronous machine (PMSM) performance are now derived and outlined in this chapter.

Axial Flux machine analysis is complicated by the radial-dependence of torque, whereas a single radius can be used for the Radial Flux machine. The airgap flux density and stator current loading change over a continuous range of radii. Furthermore, multiple airgaps are often present.

The theory of Radial Flux PM machine design can be found in modern electric machine textbooks, such as Hanselman [2003], Sadarangani [2000] and Nasar and Unnewehr [1984]. Some of the equivalent theory for Axial Flux PM machines is given by Hanselman [1998] and included here. Additional derivation of the design equations is provided in Appendix A. Figure 4.1 illustrates the geometrical directions for current, flux and force, which differ for the machine topologies.

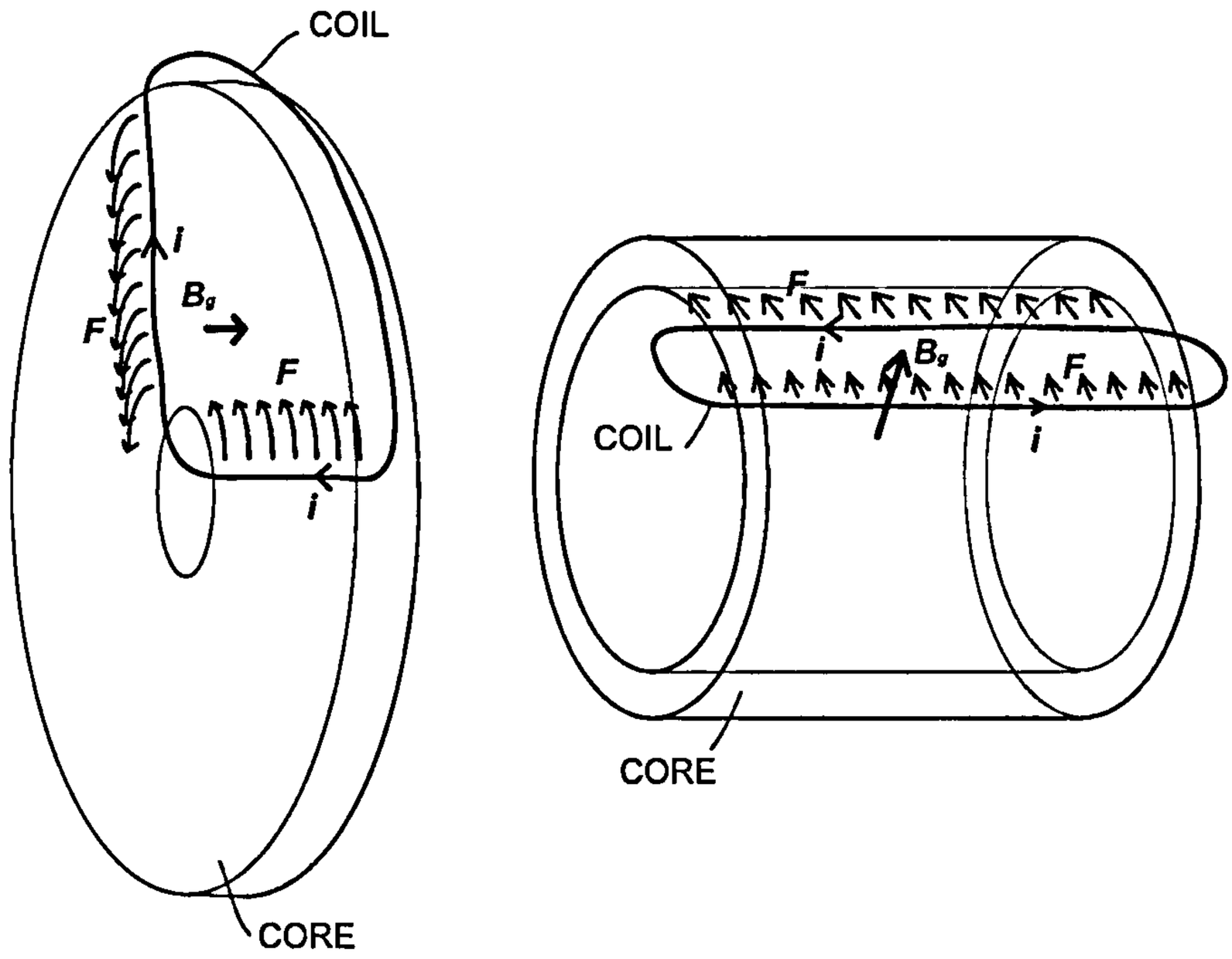


Figure 4.1: Flux, current and force vectors (B, i, F) for Axial Flux machine compared with Radial Flux [Chan, 1987, orig.]

4.1 Electromagnetic Operation of the Permanent Magnet Synchronous Machine

A machine's torque rating is derived from the product of the magnetic shear stress σ_g (which describes the electromagnetic shear force per unit area) and the active area at the moment arm radius. Therefore, the machine size scales with torque and has negligible dependence on speed up to the mechanical stress limit of the rotor materials.

4.1.1 Alignment, Reluctance and Cogging Torque

The Permanent Magnet (PM) excitation field is always present. The torque arising from interaction of this field with the field from current in the stator winding is the "alignment torque" T_{align} (or mutual torque). If, with change in the rotor position, there is variation in the reluctance of (i) the main magnet flux path, there is a "cogging" torque T_{cog}, without current to the coils, or (ii) the main flux path from the excited coil, there is a "reluctance" torque T_{rel} irrespective of the PMs [Yang et al., 2002]. The torque may be divided into these components, an example of

which is shown in Figure 4.2:

$$T = T_{align} + T_{cog} + T_{rel}$$

The Surface Mounted machine with non-salient poles only renders reluctance torque if the PM material has a relative permeability different to air. Cogging torque is present with a slotted stator core, but does not contribute useful torque. Therefore, the alignment torque, rather than reluctance and cogging torques, is considered here.

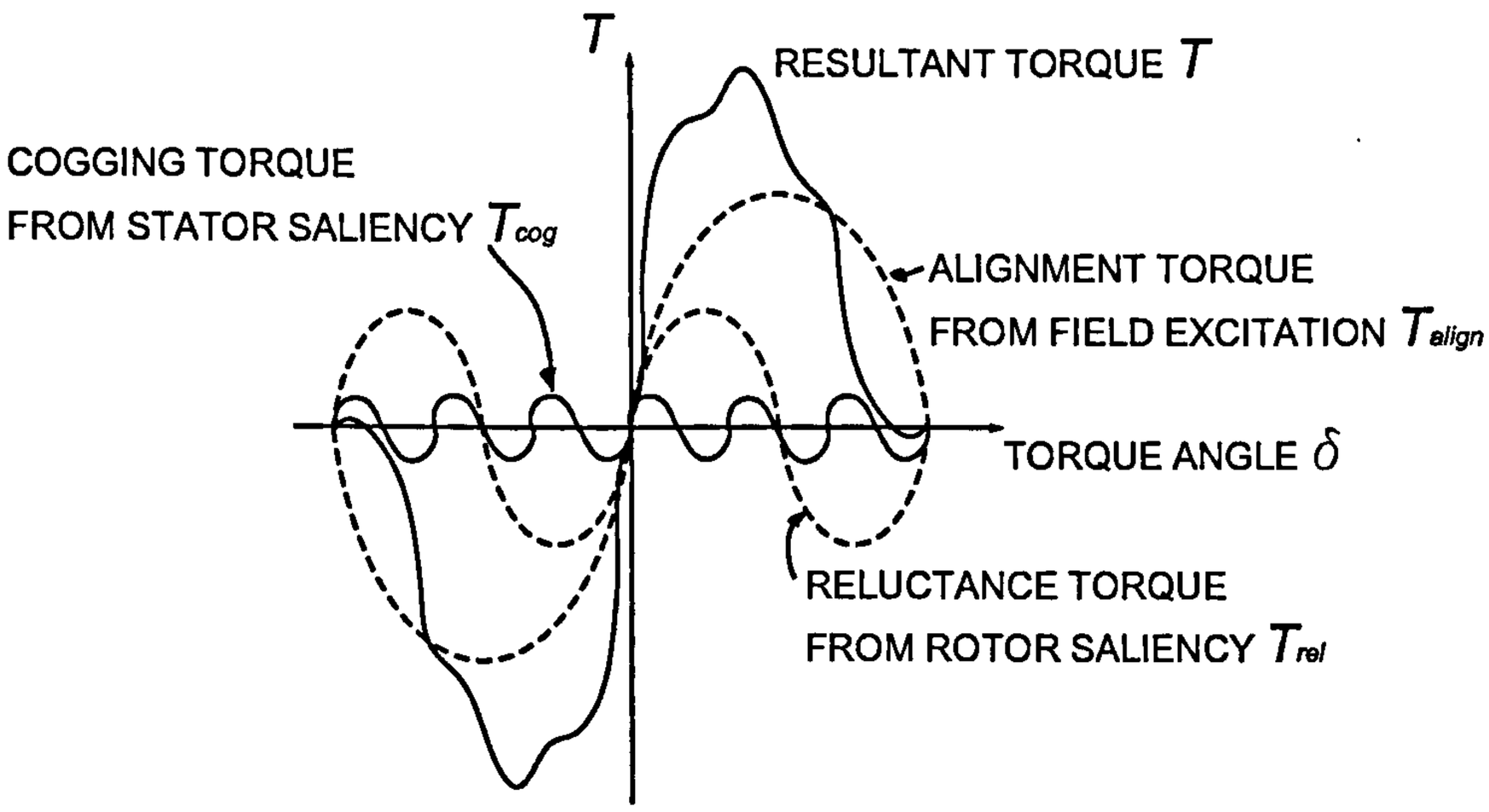


Figure 4.2: Torque according to torque angle for salient pole PM machine.

4.1.2 Airgap Flux Density

The description of alignment torque begins with evaluation of the airgap flux density B_g due to the Permanent Magnets' flux. In the first instance, spatial harmonics in the airgap flux density distribution are not considered, only the fundamental. The analysis can be repeated for harmonic components. From Figure 4.3, the highest peak value for B_g with a sinusoidal waveform from an ideal square wave for the magnet flux density of parallel magnetised PMs is:

$$\hat{B}_g = \frac{4}{\pi} B_m \sin \frac{\tau_m}{2} \tag{4.1}$$

where B_m is the magnet flux density and τ_m is the magnet pitch in electrical degrees. This highest value assumes no flux leakage.

Airgap length g is an important parameter, typically $1 - 3$ mm, or longer for machines with an airgap winding. Large airgaps require a high magnet coercivity

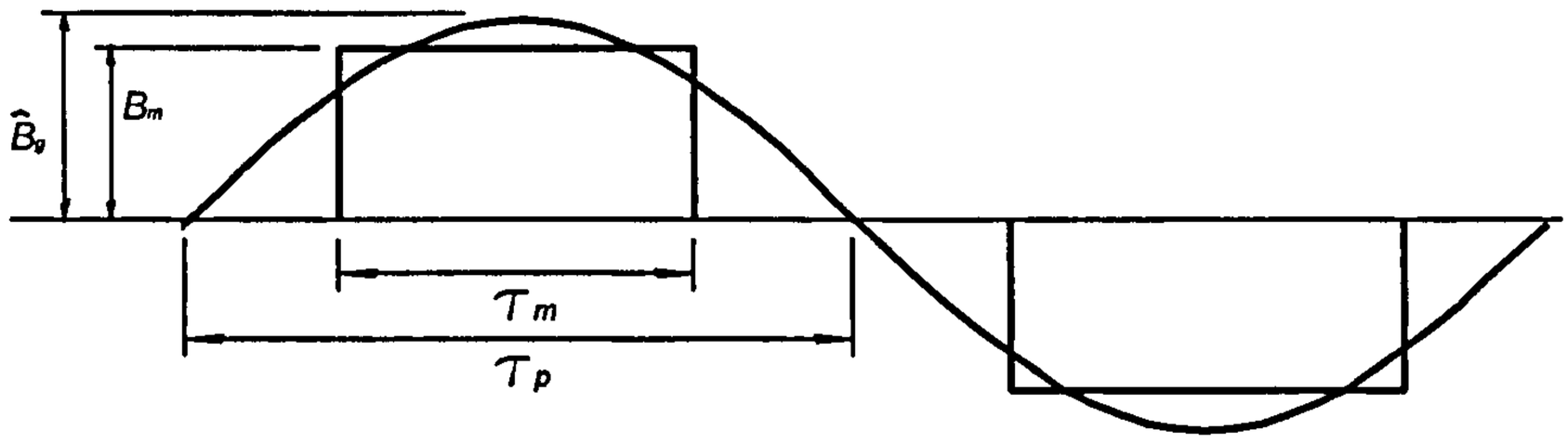


Figure 4.3: Square wave of magnet flux density and ideal sinusoidal wave of airgap flux density, $B_g = \hat{B}_g \sin\theta$.

H_c to maintain sufficient airgap flux density.

By ignoring leakage, and using the reluctance of the airgap alone, the simplest expression for flux density in the magnets is:

$$B_m = B_r \frac{1}{1 + \mu_{r(PM)} \frac{g}{h_m}} \tag{4.2}$$

where B_r is the magnet remnant flux density for the operating temperature and g is the airgap length. A modified airgap length g' is more representative, using the Carter Coefficient K_{c1} to take into account flux fringing for the pole type, $g' = K_{c1} g$ [Carter, 1926].

In order to account for the non-ideal case where rotor flux leakage occurs, an empirical constant k_l can be used, where $0 < k_l < 1$. Puting Equation (4.1) into (4.2), the magnet height required to provide the desired airgap flux density becomes:

$$h_m = \frac{\mu_r g'}{\frac{B_r 2\sqrt{2} k_l \sin\frac{\tau_m}{2}}{\hat{B}_g \pi} - 1} \tag{4.3}$$

which illustrates the relationship between magnet height and airgap length. Hanselman [2003] describes this relationship with the "Permeance Coefficient" P_c.

4.1.3 Pole Pitch Factor

In order to evaluate the airgap flux, the airgap area is required $\phi_g = B_g A_g$. The magnet area is described by the inner and outer radii r_i and r_o and the magnet pitch τ_m. Fractional pitched poles, as shown in Figure 4.4 are defined by the "pole pitch

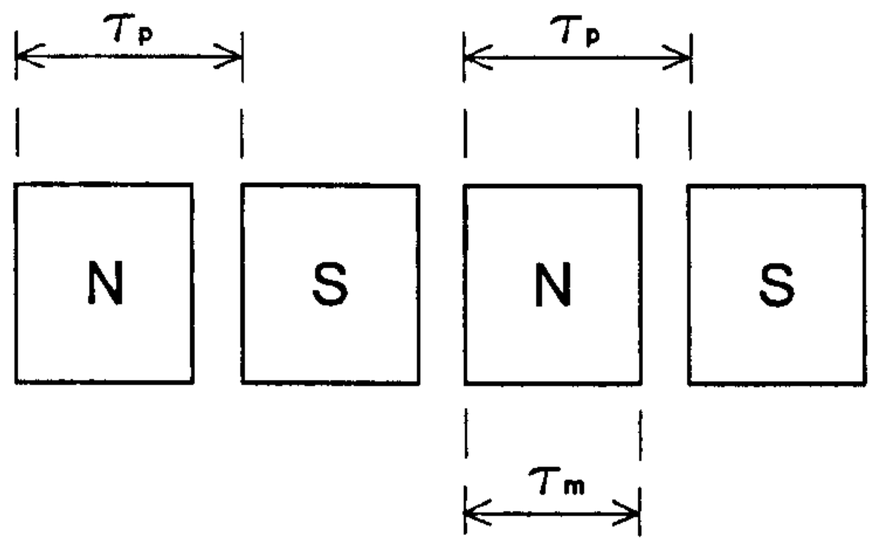


Figure 4.4: Fractional pitch poles with the pole pitch angle marked.

factor" $k_{ppitch} = \tau_m/\tau_p$, where τ_p is the pole pitch. The area for a sector pole in an array of p pole pairs becomes $k_{ppitch}\pi(r_o^2 - r_i^2)/2p$. For a PMSM, k_{ppitch} is typically 2/3. An increased magnet pitch τ_m, up to 180 electrical degrees (°E), increases the peak airgap flux density for machines with a standard airgap, but airgap flux leakage between neighbouring poles does not contribute to flux linkage. To avoid wasting PM material, the gap between poles is much larger than the magnetic airgap. In long airgap machines, where the difference between pole width and magnet width is equivalent to the airgap length, $(w_p - w_m) = g$, a further increase in the magnet width w_m increases the leakage rather than the airgap flux density. Here, the pole and magnet widths are lengths, rather than mechanical or electrical angles, meaning a radial position must be selected for the evaluation (usually the inside radius $r = r_i$).

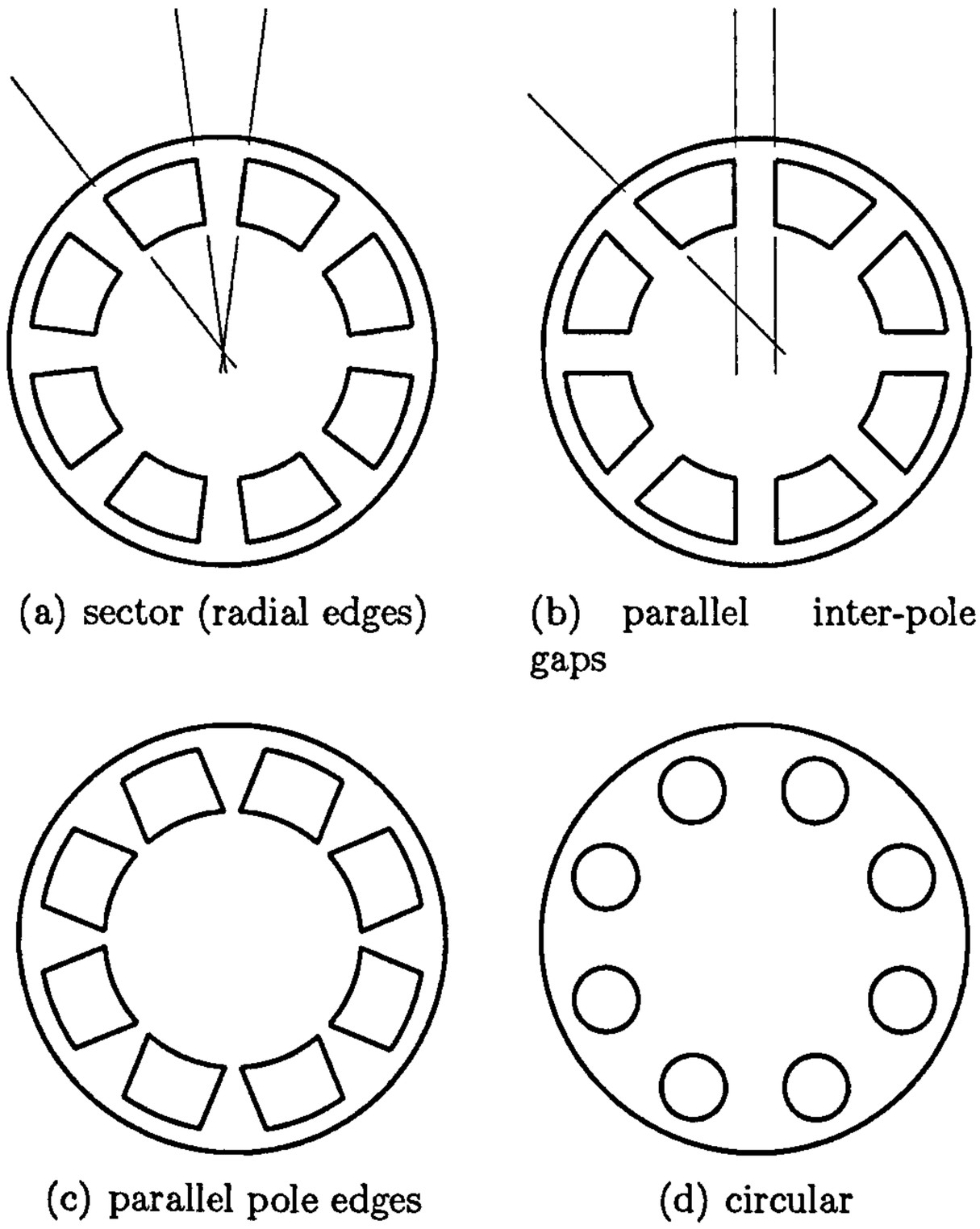
The peak airgap flux density definition becomes:

$$\hat{B}_g = \frac{\frac{4}{\pi} k_l \sin\frac{\tau_m}{2} k_{ppitch}}{1 + \frac{\mu_{r(PM)} g' k_{ppitch}}{h_m}} B_r \tag{4.4}$$

Figure 4.5 illustrates the common pole shapes previously reported, ignoring skew. Type (b) is employed by Hanselman [1998] with a pole area $A_m = \alpha_m \frac{\pi}{2p}(r_o^2 - r_i^2)$; $\alpha_m = 1 - \frac{2pw_f}{\pi(r_o - r_i)}$; w_f is the gap between magnets. Because the gap between magnets is constant in Type (b), the reluctance of the pole-pole airgap leakage path becomes $\mathcal{R}_l = [\frac{\mu_0(r_o - r_i)}{\pi} \ln(1 + \pi\frac{g}{w_f})]$. The Carter coefficient employed must be an average to account for the constant slot openings with increasing slot pitch with radius.

4.1.4 Geometric Variations

The design equations presented by Hanselman [1998] hold for the machine with a magnet shape with parallel inter-pole spaces. With this array design, it is relatively simple to define the leakage factor k_l using straight line–arc permeances. In this



(a) sector (radial edges)

(b) parallel inter-pole gaps

(c) parallel pole edges

(d) circular

Figure 4.5: Axial Flux multi-pole array shapes.

case:

$$k_l = 1 + \frac{4h_m p}{\pi^2 \mu_r \alpha_m (r_i + r_o)} \ln(1 + \pi \frac{g}{w_f}) \tag{4.5}$$

4.1.5 Induced *emf*

The induced *emf* is the derivative with respect to time of the flux linkage waveform. Assuming a sinusoidal excitation flux waveform, and the phase winding links with all useful flux:

$$E = \frac{4\sqrt{2}}{\pi} N B_m k_l \sin\frac{\tau_m}{2} \underbrace{\pi(r_o^2 - r_i^2) k_{ppitch}}_{2pA_m} \omega_{mech} = K_e \omega_{mech} \tag{4.6}$$

where N is the number of turns per coil and ω_{mech} is the mechanical speed, which agrees with Lorentz law for $\hat{e} = Blv$. K_e is the "Back *emf* Constant", which has units V/radM/s.

Where the phase winding does not link with all the flux, the winding factor k_w

is introduced, which accounts for pitch and distribution of the winding with respect to the excitation.

4.1.6 Fractional Pitch Coils

Machines with a sinusoidal waveform do not typically have full pitch windings.

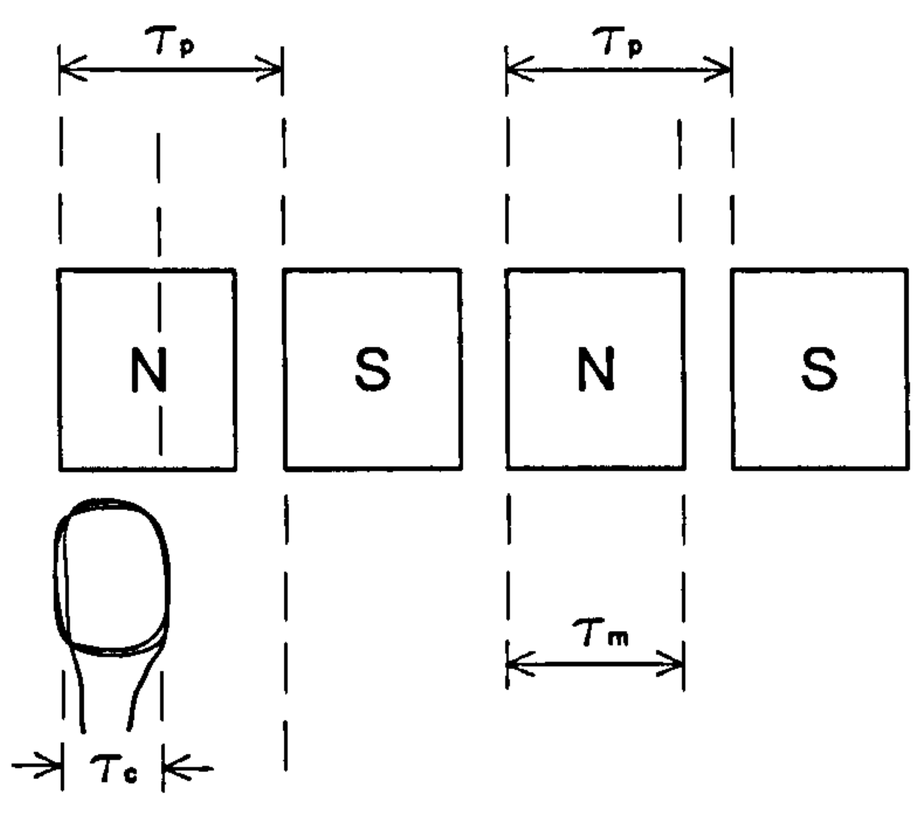


Figure 4.6: Fractional pitch coils with the coil pitch and pole pitch angles marked.

The ratio of coil pitch to pole pitch, $k_{cpitch} = \tau_c/\tau_p$, or the "coil pitch factor", shown in Figure 4.6 describes the coil span when less than 180°E. The flux linkage is reduced by the coil pitch factor and its waveform with respect to rotor position has a flat peak. The induced emf is zero during the flat peak of the flux linkage waveform, and the torque waveform also has the same shape.

4.1.7 Torque

Various relations for Axial Flux machine torque have been given, such as by Aydin et al. [2001*b*] for a double airgap machine with assumed efficiency. Using an assumed efficiency makes the relation essentially empirical. The relation discussed here applies to the active area alone so may be multiplied for multiple airgaps. However, efficiency is not included so any value obtained is an ideal estimate.

Assuming ideal machine efficiency, applying $EI = T\omega_{mech}$ to Equation (4.6) determines the torque produced by an ideal rms conductor current I, with an equivalent sinusoidal waveform:

$$|T| = \frac{EI}{\omega_{mech}} = \frac{4\sqrt{2}}{\pi} N B_m k_l \sin\frac{\tau_m}{2} \underbrace{\pi(r_o^2 - r_i^2) k_{ppitch}}_{2pA_m} I = K_T I \tag{4.7}$$

By using irregular line current waveforms, but regular voltage waveforms, the machine torque is not constant over the electromagnetic cycle (i.e. ripple torque is present), despite the use of balanced three phases. However, by assuming constant torque, a "Torque Constant" K_T with units Nm/A can be used, which is equivalent to the "Back emf Constant", $K_T \equiv K_e = \frac{4\sqrt{2}}{\pi} N B_m k_l \sin\frac{\tau_m}{2}\pi(r_o^2 - r_i^2)k_{ppitch}$. So these airgap flux, flux linkage, induced emf and torque expressions for an ideal PMSM machine use the square B_m waveform to determine the rms value of an ideal sinusoidal B_g waveform. For a non-sinusoidal $B_g(\theta)$ waveform, manipulating Equation (4.1) with the actual waveform allows derivation of the descriptions above.

4.1.8 Radial Dimensions

Leaving aside rotor inertia, Lovat et al. [1998] described how it is desirable to position the active area at the maximum radial position possible, giving the maximum torque to volume of active area. Caricchi, Crescimbini, Honorati, Di Napoli and Santini [1996] illustrated curves for torque and specific torque according to the ratio of radial dimensions of the active area r_o and r_i, given in Figure 4.7. This gives peak torque at $r_i/r_o = 1/\sqrt{3}$.

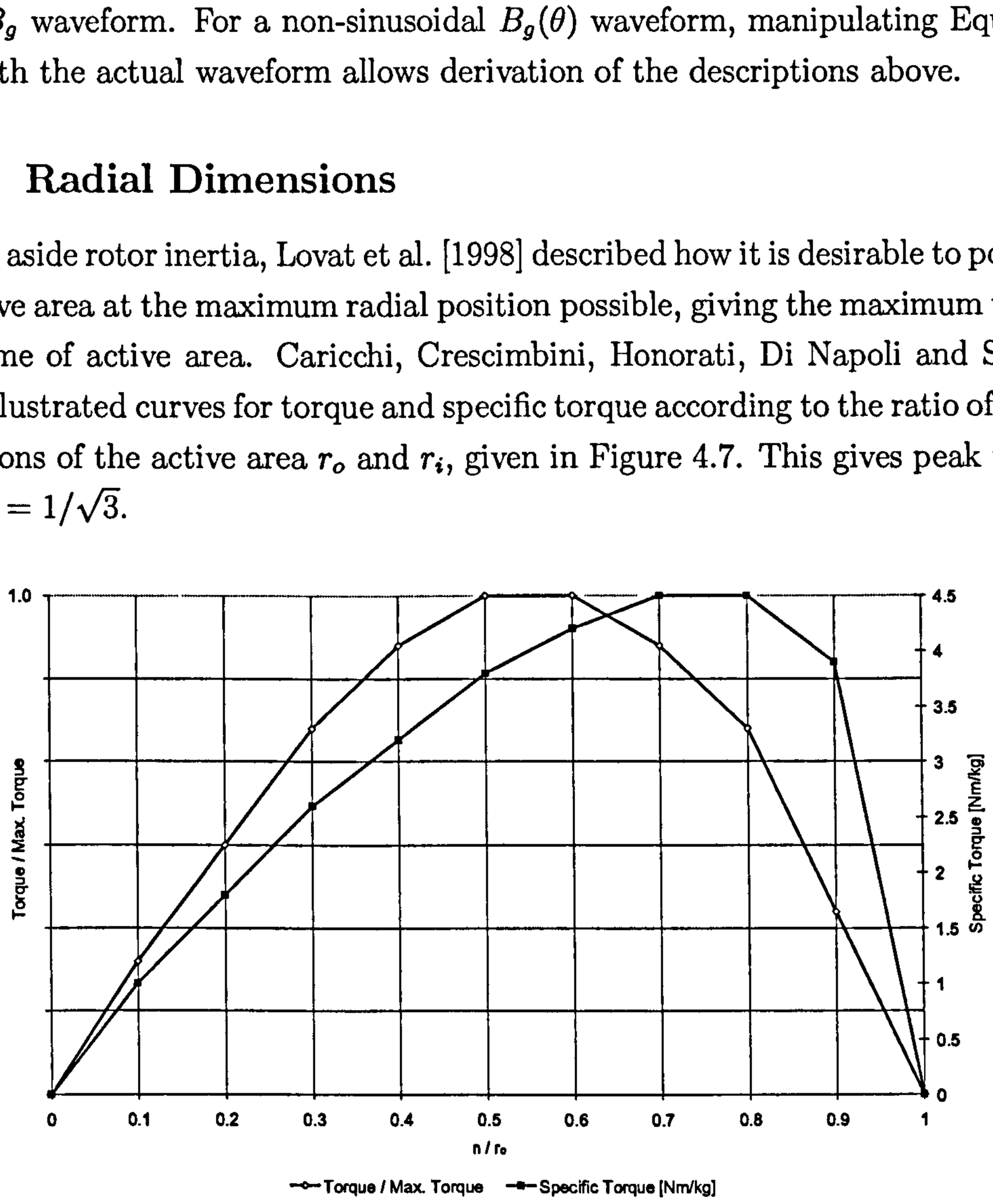


Figure 4.7: Torque and specific torque for ratio of active area radial dimensions for an 8 pole Axial Flux machine [Caricchi, Crescimbini, Honorati, Di Napoli and Santini, 1996, orig.].

4.1.9 Airgap Magnetic Shear Stress

The expression for torque given in Equation (4.7) uses current and magnet flux density, for which the machine designer has experience of realistic values based on physical constraints. However, in evaluating electromagnetic performance, the airgap magnetic shear stress is useful as a single measure. This describes the specific tangential force (per unit rotor surface area), with the units $\mathrm{Nm/m^2}$:

$$\sigma_g = \frac{2}{\pi} N B_g k_{ppitch} I \ln(r_0 - r_i) \tag{4.8}$$

The stator current loading is thermally constrained, defining a constant Ni product. This emphasises the dependence σ_g has on B_g. So for the airgap magnetic shear stress ratings given by Hanselman [2003] of typical airgap magnetic shear stress values for standard BLDC and PMSM machines of $1 < \sigma_g < 3$ $\mathrm{kN/m^2}$, with values for higher performance machines of $\sigma_g \leqslant 10$ $\mathrm{kN/m^2}$, and large liquid cooled machines reaching $\sigma_g \leqslant 20$ $\mathrm{kN/m^2}$, the parameters of airgap flux density and coil ampere-turns are balanced for performance.

4.1.10 Stator Current Loading

The distribution of the stator current loading S_1 depends on the distribution of conductors. An ideal sinusoidal distribution can be assumed where the peak current loading $\hat{S}_1$ reduces linearly with increasing radial location. The exact current loading is found by discretising the active length $l = r_o - r_i$. Assuming an ideal sinusoidal loading, $\hat{S}_1$ is given by:

$$\hat{S}_1 = n_s \frac{\hat{I}_1}{\tau_s} \tag{4.9}$$

where $n_s \hat{I}_1$ is peak total current per slot and τ_s is the slot pitch, which gives:

$$S_1 = \hat{S}_1 \sin\left(\frac{\pi}{2} - \vartheta + \theta\right) = \hat{S}_1 \cos\left(\theta - \vartheta\right) \tag{4.10}$$

where θ is rotor electrical angle position and ϑ is the angle between peak $\hat{S}_1$ and zero B_g, $(\vartheta = \theta_{S_1 = \hat{S}_1} - \theta_{B_g = 0})$, shown in Figure 4.8, which for Surface Mounted PM machines is usually zero. In the Axial Flux structure the radial location affects τ_s and, as the current at the inner radius must be the current at all radial locations

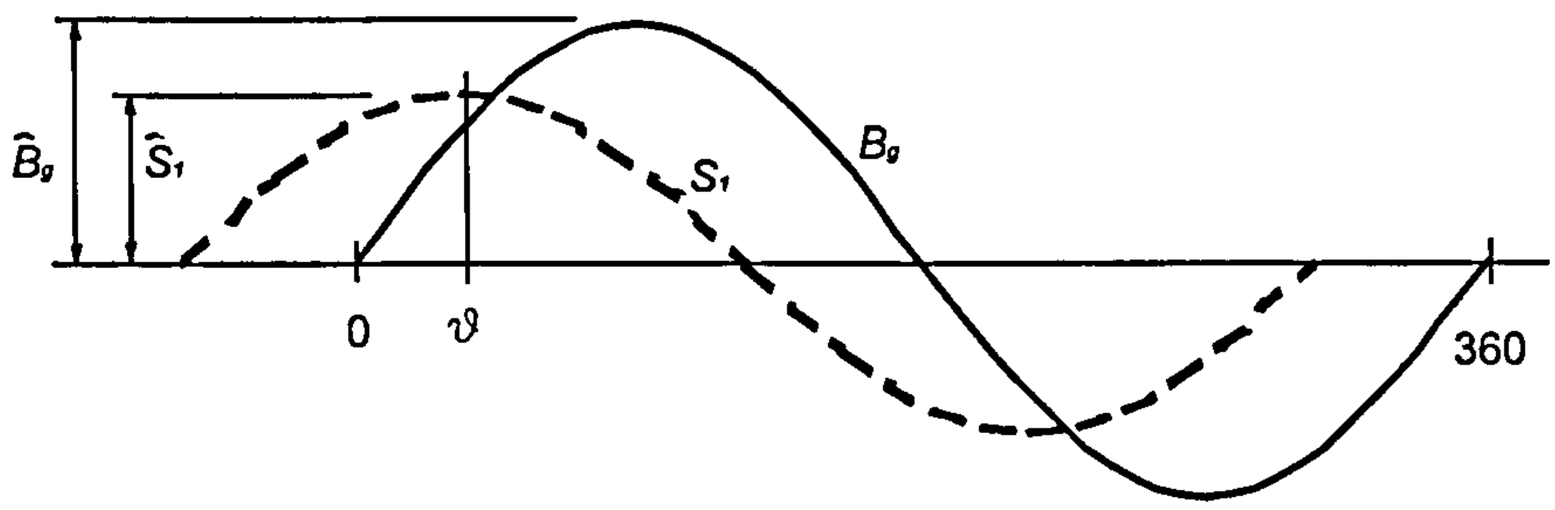


Figure 4.8: Current loading S_1 and airgap flux density B_g out of phase by $(90° - \vartheta)$.

along the active length $I(r) \equiv I(r_i)$, the total current over one pole pair is:

$$I_p = 2mk_w qn_s I_1 \tag{4.11}$$

where m is number of phases and q is the number of slots per pole per phase, which gives the current loading over the pole pair at the inner radius of:

$$S_p = \frac{I_p p}{2\pi r_i} \tag{4.12}$$

4.1.11 Force on Conductors

The calculation of force on the conductors by Lorentz law is:

$$dF = Bdri \tag{4.13}$$

which gives an incremental torque of:

$$dT = rdF = B(\theta)J_c(r,\theta)r^2 d\theta \frac{1}{p} dr = \frac{1}{p} B(\theta) r_i S_1(\theta) r d\theta dr \tag{4.14}$$

where the elemental current is for conductor current density J_c is $di = J_c(\theta) r d\theta \frac{1}{p}$. Caricchi et al. [1997] describe the radial variation in $B(\theta)$ and the effect on $dF(r)$, arising from k_{ppitch} variation with respect to r, and flux fringing and leakage at the inner and outer radii, and propose a weight function $w(B_{zk}, r_j)$ employed at discrete radial positions, or active area slices, which must be defined according to pole shape.

4.1.12 Torque from Conductor Forces

By integrating over the active length, with $B_g(\theta) = \hat{B}_g \sin\theta$ and $S(\theta) = \hat{S}_1 \cos\theta$:

$$T_p = \int_0^{2\pi} \frac{1}{2p} \hat{B}_g \hat{S}_1 \sin\theta \cos\theta r_i (r_o^2 - r_i^2) \tag{4.15}$$

The torque per side is given by:

$$T_{side} = \frac{\pi}{2} B_g S_1 r_{mean} \left(r_o^2 - \frac{r_o^2}{\sqrt{3}^2} \right) = \frac{\pi}{2} B_g S_1 \frac{r_o^3}{3} \left(1 - \frac{1}{\sqrt{3}} \right) \tag{4.16}$$

According to position of a conductor with respect to the radial axis, it may effectively be skewed. In this case, the F vector is not in a tangential direction, so the "skew factor" k_{sk} is included.

The theoretical torque is:

$$T = p \int_{\theta=0}^{2\pi} dT d\theta = p \hat{B}_g k_{sk} \int_0^{2\pi} \sin\theta \cos\theta d\theta \int_{r_i}^{r_o} r dr \hat{S}_1(r) \tag{4.17}$$

The more common form of the torque expression gives:

$$T = \pi \frac{(r_o^3 - r_i^3)}{6} S_1 B_g \sin\beta \tag{4.18}$$

where the rms values of S_1 and B_g are used, and β is the electrical angle between the current vector (90°E in advance of the current loading) and the flux vector. At $\beta = 90°$, S_1 and B_g are in phase so produce maximum torque in the Surface Mounted PM machine.

The output power is:

$$P_{output} = \omega_{mech} T = \frac{\omega_{elec}}{p} S_1 \frac{(r_o^3 - r_i^3)}{6} B_g \pi \sin\beta \tag{4.19}$$

4.2 Inductance

The stator winding inductance is necessary to evaluate the machine performance, particularly if the line current is used to determine torque control. Due to complexities in the geometry and winding arrangement, inductance is often calculated by Finite Element Methods (FEM) software, as shown by Madlena et al. [1996] and Profumo et al. [1998].

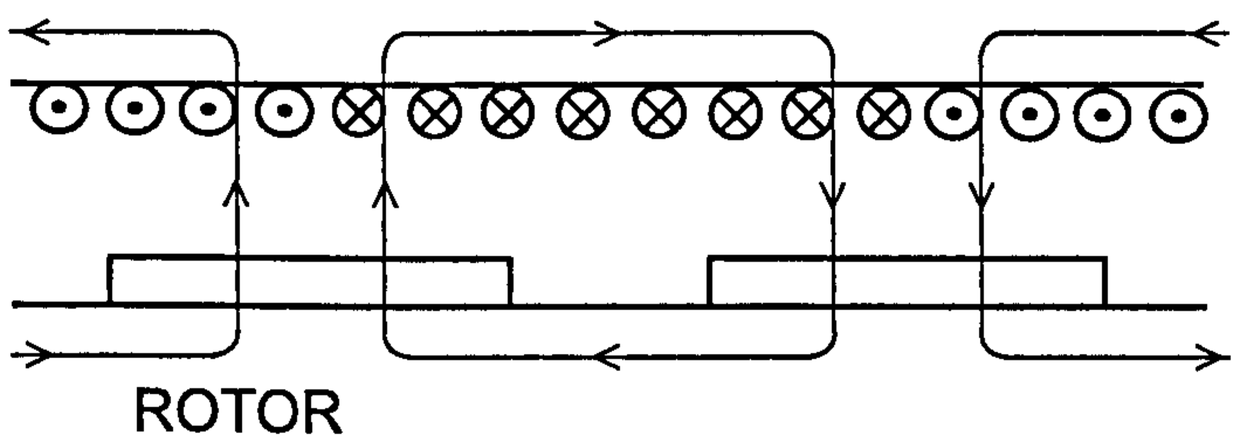
Cavagnino, Cristino, Lazzari, Profumo and Tenconi [2000] noted that estimating the magnetising inductance is possible with the ratio of the fundamental component of the phase flux linkage $\psi_{\phi 1}$ and the amplitude of the stator current, but leakage inductances are difficult to estimate.

4.2.1 Coil Inductance

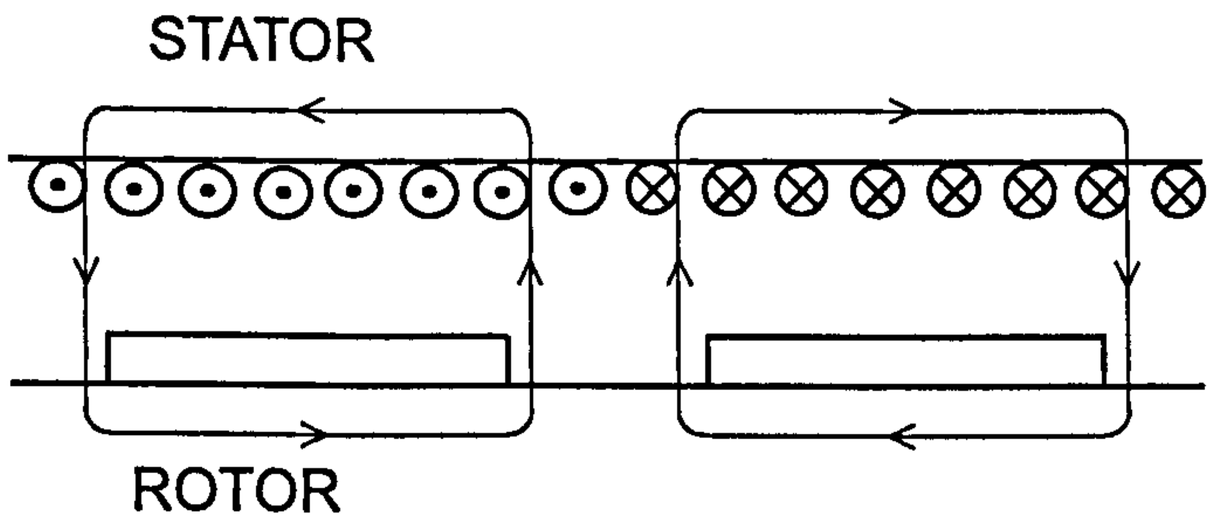
With a current control drive, an analytical estimate of the inductance without the exact time constant of the windings may be sufficient.

The phase winding inductance is given by a sum of the individual inductances for parts of the winding with related flux, the airgap and the slot and endwinding leakages:

$$L_\phi = L_g + L_s + L_{end} \tag{4.20}$$



(a) $d-$axis



(b) $q-$axis

Figure 4.9: The flux from current in the $d-$ and $q-$axes.

The flux arising due to current in the $d-$ and $q-$axes is illustrated in Figure 4.9. The inductance is taken from the ratio noted by Cavagnino, Cristino, Lazzari, Profumo and Tenconi [2000], and using the relations $\mathcal{F} = \Phi\mathcal{R}$ and $\mathcal{F} = Ni$, can be

found in terms of the flux path reluctance:

$$L_{d,q} = \frac{\hat{\psi}_{d,q_stat}}{\hat{I}_{d,q}} = \frac{N\hat{\phi}_{d,q_stat}}{\hat{I}_{d,q_stat}} = \frac{N\hat{\mathcal{F}}}{\hat{I}_{d,q_stat}\mathcal{R}_{d,q}} = \frac{N^2\hat{I}_{d,q_stat}}{\hat{I}_{d,q_stat}\mathcal{R}_{d,q}} = \frac{N^2}{\mathcal{R}_{d,q}} \tag{4.21}$$

which negates the need to know the stator flux. Combined with the airgap permeability, the stator mmf gives the airgap flux density. A near unity recoil permeability of the magnet material, and the magnet height compared to mechanical airgap, means the armature reaction flux density in the airgap is small – typically 10 % of the excitation airgap flux density.

Axial flux machines with an airgap winding are common. With larger g, the inductance reduces. The time-harmonic currents (with the associated losses) are not suppressed. This is often the case in high speed machines where iron is omitted due to high frequency [El-Hasan et al., 2000].

The unsaturated $d-$axis inductance, using the stator flux, is:

$$L_d = \frac{\hat{\psi}_{d,stator}}{\hat{I}_d} = \frac{N\hat{\phi}}{\hat{I}_d} = \frac{qn_s k_{w1}\hat{B}_{d_stator}\left(r_o^2 - r_i^2\right)}{\hat{I}_d} \tag{4.22}$$

The salient rotor structure has a difference between the inductances for the $d-$ and $q-$axes given by:

$$L_{d,q} = \frac{6}{\pi}(qn_s k_{w1})^2 \frac{\mu_0}{g' + \dfrac{h_m}{\mu_{r(PM,air)}}}(r_o - r_i)^2 \tag{4.23}$$

where the $d-$axis is the rotor pole axis so includes μ_r for PM material, but the $q-$axis uses only μ_r for air. This is proportional to the active area and inversely proportional to the magnetic airgap. The similar values for $\mu_{r(\mathrm{PM})}$ and $\mu_{r(\mathrm{air})}$ allow the equivalence of both inductances ($L_d = L_q$).

With $\hat{\psi} = L\hat{i}$ and $\mathcal{F} = Ni$, the airgap flux density arising from a winding current I is given by:

$$\hat{B}_s = \frac{3\sqrt{2}\mu_0}{\pi p g'} k_{w1} N I_s \tag{4.24}$$

where k_{w1} is the winding factor 1st harmonic and $\hat{B}_s$ is the peak airgap flux density from the winding alone. Further harmonics may be included for the winding factor, which alternatively add to or subtract from $\hat{B}_s$.

4.2.2 Mutual Inductance

The mutual inductance, especially between coils in different phases, is complex yet is smaller than the self inductance (typically about 10 %) [Hanselman, 2003]. The mutual inductance between coils of the same phase is greater. Mutual inductance is considered along with the number of coils per slot.

4.2.3 End Winding Inductance

Endturn inductance accounts for the leakage field around endturns. As endturns are usually located in air outside the stator core, the field distribution is not constrained, making this inductance difficult to define. By assuming a cylindrical field with circumferential field intensity $H_\theta = i/2\pi r$ for radius $r > r_c$, the inductance becomes:

$$L_{end} = \frac{\mu_0 l_{end}}{2\pi} \ln\left(\frac{r}{r_c}\right) N^2 \tag{4.25}$$

For Axial Flux machines, there are no published relations describing End Winding inductance. In order to derive such expressions, endturns are assumed to be semi-circular, as described in Appendix A.5, with a turn radius of half the coil pitch $\tau_c/2$. A concentrated winding Axial Flux topology with two coils per slot, has an end turn radius of $\tau_c/2 - w_s/4$. The endturn cross-sectional area is half the slot area A_s, so N turns gives:

$$L_{end1} = \frac{\mu_0 \left(\tau_c - w_s/2\right)}{4} \ln\left(\frac{\left(\tau_{cp} - w_s/2\right)\sqrt{\pi}}{\sqrt{2\left(A_s/2\right)}}\right) N^2 \tag{4.26}$$

With 2 coils per slot, there are $2Q/m$ endturn bundles per phase. As there is no mutual coupling of coil endturns in the same phase, the per phase endturn inductance becomes:

$$L_{end_\phi} = p\mu_0 \left(\tau_c - w_s/2\right) \ln\left(\frac{\left(\tau_{cp} - w_s/2\right)\sqrt{\pi}}{\sqrt{2\left(A_s/2\right)}}\right) N^2 \tag{4.27}$$

4.2.4 Coil Connections in Phase

The DC bus voltage in many HEV applications may limit the achievable performance of motor designs with a low number of turns per coil. This prevents the series-connection of coils in the same phase. Parallel-connection of the coils results in a lower phase resistance, but if the induced emfs of the individual coils are not exactly

in phase, circulating currents occur, which do not contribute useful flux to torque production but do contribute to losses.

The phase inductance for parallel-connection is modified in a similar way to the resistance, if the coils do not share common flux [Nasar and Unnewehr, 1984].

4.3 Supply Waveform

Of particular importance to machines in motoring applications, such as the IMG, is the inverter topology. For bi-directional power flow enabling motoring and generating (such as regenerative braking) operation, two- or four-quadrant operation must be possible.

4.3.1 Inverter Types

The standard drive types are Voltage-source (V-source) inverter

Pulse Width Modulation (PWM). For HEV application of PMSMs, the step switching V-source inverter is not used due to poor control of the supply waveform. The I-source and PWM V-source inverters have different advantages. The I-source has less high frequency switching, which is attractive for efficiency. It also has bi-directional capability facilitating regenerative braking. However, the supply waveform cannot be manipulated, so extended constant power operation is not available. The PWM V-source inverter offers full control over the supply waveform. However, two back-to-back inverters are required to provide regenerative braking. The PWM V-source inverter with a good digital signal processor (DSP) supplies a sinusoidal current, which contains only high frequency harmonics at the switching frequencies. The I-source inverter supplies a sinusoidal current according to the back-emf along with some high frequency harmonics from switching, but less than the PWM V-soource.

4.3.2 Inverter Control

The commutation of multiphase Brushless DC (BLDC) and Permanent Magnet Synchronous (PMSM) machines are square driving voltage (although trapezoidal back-emf) and sinusoidal functions respectively. There are some differences in design as a result.

4.3.3 Three-phase BLDC Machines

Three-phase BLDC machines are either star- ("Y") connected or delta- ("Δ") connected.

4.3.3.1 Star- and Delta-connection

The magnet width for Y−connection is 180°E [Şimşir and Ertan, 1999]. For a full pitched winding, two active phases always see a rotor pole, while one phase always has zero current, maintaining a constant torque.

To achieve constant torque during switching current phases, the non-salient rotor construction is preferred. Advancing the commutation points in relation to the rotor position facilitates higher speed operation, but field weakening to control the voltage is difficult.

The difference in $\Delta-$connection relates to the magnet width w_m, or τ_m shown in Figure 4.3, which in turn affects iron return thickness h_{Fe}. The magnet width for $\Delta-$connection is less than maximum, typically similar to the PMSM. $\tau_m/\tau_p = 2/3$ eliminates triplean harmonics, minimising circulating currents in the Δ-connection.

There is current flow in each phase, with $0.667i$ in the "activated" phase and $0.333i$ in the other two. With the smaller pole pitch, and same current loading, there is approximately 13 % less torque for the same peak airgap flux density, than from the Y−connection design. However, with less total flux, a thinner iron return path is possible, giving $h_{Fe}(\Delta) = \frac{w_m(\Delta)}{w_m(\mathrm{Y})}\, h_{Fe}(\mathrm{Y})$. Thus, the torque density of $\Delta-$connection is similar to that of Y−connection [Hanselman, 2003].

Control sensors to feedback position are only required to indicate 60°E intervals for coil switching a BLDC machine, so Hall sensors or simple encoders suffice. The torque ripple, which arises from coil switching and the resulting square wave commutation, can only be eliminated by increasing the number of phases m.

4.3.4 Multi-phase PMSM Machines

The PMSM characteristics resemble those of traditional synchronous machines. The same multi-phase stator is used, but there is no direct control of the rotor field so reactive power is typically regulated by field weakening with "vector control".

As in the Δ-connected BLDC, a magnet width of 120°E minimises triplean harmonics in the airgap flux density waveform [Şimşir and Ertan, 1999]. Thus, the back emf waveform closely matches sinusoidal supply currents, with all phases constantly active.

The torque is 1.5 times that for the Y−connected BLDC machine. However, the sinusoidal current may be affected by drive harmonics, and the stator mmf is affected by the distribution of conductors. Furthermore, a sinusoidal induced emf is not possible from standard magnets and a slotted stator core.

The PMSM requires a signal of the exact rotor position, as current is fed to all phases, so a precise encoder is required.

4.4 Motor Constant

Hanselman [2003] considered the Torque and Back emf Constants of limited usefulness for design because they do not account for both components of the Ni product, which remains constant with variation of most design parameters. The Back emf Constant scales linearly with N, but does not account for the inverse relationship with i.

A useful measure is the "Motor Constant". This expresses efficiency according to the torque and Ohmic resistance losses, which is the desired output against energy cost, although a square root is required as torque is linearly proportional to current:

$$K_M = \frac{T}{\sqrt{I^2 R}} \tag{4.28}$$

K_M remains unchanged for many interdependent parameters. Assuming endturn lengths are approximately 50 % of the total conductor length, the Axial Flux motor constant is:

$$K_M = \frac{B_g(r_o + r_i)}{\sqrt{\rho}} \frac{\sqrt{V_{Cu}}}{Q} k_{ppitch} \tag{4.29}$$

where A_{Cu} and V_{Cu} are the cross-sectional area of the copper wire and the total volume of copper, given by $2NQ(r_o - r_i)A_{Cu}$. This assumes $V_{Cu}(\text{slot}) = V_{Cu}(\text{endwind})$. K_M is therefore independent of current and relates to N through the slot fill factor, affecting V_{Cu}. Increasing the airgap flux density or increasing the overall size, which is unattractive in an HEV powertrain application, become the tools to manipulate K_M. The Ohmic losses per slot become:

$$P_{Cu_s}^{loss} = \frac{\rho_{Cu}(r_o - r_i)k_{sk}}{A_{Cu}}(n_s I_1)^2 \tag{4.30}$$

where $\rho_{Cu} = \rho_{Cu_0}(1+0.00433(T_s - T_0))$, T_s is stator winding temperature, $n_s I_1$ is the rms total current per slot and ρ_{Cu,Cu_0} are winding resistivities at the operating and

ambient temperatures. The total winding loss, according to k_2 for approximating endturn length by $k_2\pi(r_o + r_i)/2p(r_o - r_i)$, is:

$$P_{Cu_m\phi}^{loss} = P_{Cu_s}^{loss} Q \frac{1 + k_2\pi(r_o + r_i)}{2p(r_o - r_i)} \tag{4.31}$$

It should be noted that the motor constant only reflects the actual Ohmic losses when all the harmonics of the true current waveform are included.

4.5 Design Optimisation

The knowledge of previous designs and parametric studies can be applied to the design process, rendering closer-to-optimum design parameter values.

4.5.1 Objective: Torque Density

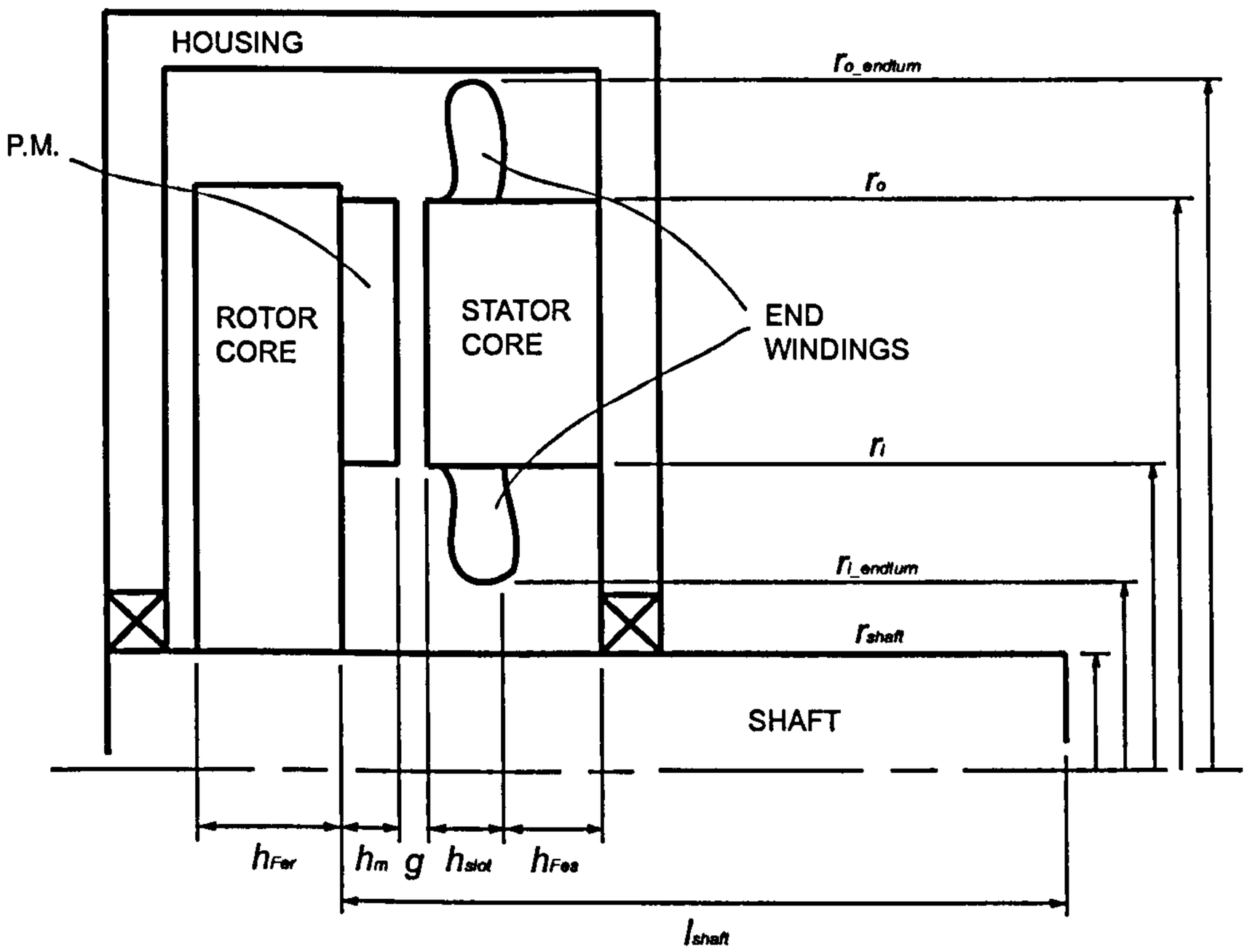


Figure 4.10: Shaft and active volume dimensions.

There are two aspects of the machine axial length: the magnet, airgap and conductor regions, and the flux return cores. The axial length of the cores is determined by the flux density and the pole number. For constant electric and magnetic loadings, the inner and outer radii for maximum torque are related by the ratio

$r_i/r_o = 1/\sqrt{3}$. In practice, the ratio may be in the range $0.6 - 0.7$ due to manufacturing constraints [Caricchi, Crescimbini, Mezzetti and Santini, 1996]. However, the torque density depends on maximising torque and minimising the redundant volume within the inner radius r_i. With a shaft of sufficient diameter for the required torque output, the arrangement for maximum torque density shown in Figure 4.10 becomes:

$$l_{shaft} = h_m + g + h_s + h_{Fes} + h_{bear} + h_{ext} \tag{4.32}$$

with h_{ext} variable.

Lovat et al. [1998] outlined how the pole pair number p is inversely proportional to the flux return path widths h_{Fer} and h_{Fes}, so p determines the machine length. A high pole number reduces the length and space of the end windings. To determine with optimum radial dimension $r_i/r_o = 1/\sqrt{3}$ gives $(1 - \sqrt{3})r_o \geqslant l_{end_o} + l_{end_i}$.

The fundamental and harmonic frequencies determine (i) the iron losses in stationary components, (ii) the eddy current losses in an airgap winding, and (iii) the efficiency of the power electronics according to the switching frequency of the power devices in the inverter, which depends on the maximum rotational speed and pole number.

The pole-to-pole leakage in relation to the airgap length varies with pole number, as the interpole space must change. The advantage of a high pole number is the short length of end windings and smaller outside radius. Cavagnino et al. [2002] note that Axial Flux motors are attractive for high pole numbers ($\geqslant 8$).

The simplest selection method is to equate the active length with the pole pitch at the mean radius:

$$p = \frac{2\pi r_{mean}}{(r_o - r_i)} = \pi \left(1 + \frac{\sqrt{3}}{2}\right) \tag{4.33}$$

giving $p \simeq 6$.

The T-r_{shaft} relationship is based on the elastic torsion formula:

$$\tau_{shear_max} = \frac{T r_{shaft_min}}{J_{rot}} = G\gamma_{max} \tag{4.34}$$

$$r^3_{shaft_min} = \frac{2T}{\pi \tau_{shear_max}} \tag{4.35}$$

where τ_{shear_max} is the maximum elastic shear stress, J_{rot} is the polar moment of inertia $J_{rot} = \pi r_o^4/2$, and γ_{max} is the maximum shear strain for elastic behaviour.

G is the shear modulus of rigidity, which is used in Hooke's Law. Typical standard values for steel are $G = 80$ GPa and $\gamma_{max} = 0.001625$.

J_{rot} is also used to calculate dynamic operation, where the acceleration is given by $\dot{\omega}_{mech} = T/J_{rot}$.

The torque density using rotor volume is useful to compare machines:

$$\frac{T}{V_{rot}} = \frac{T}{\pi r_o^2 l_{\text{rot}}} = \frac{2NB_g i}{\pi z_{\text{rot}}} k_{ppitch} \left(1 - \left(\frac{r_i}{r_o}\right)^2\right) \tag{4.36}$$

where l_{rot} is the rotor axial length, h_{Fer} plus h_m. However, torque per unit rotor volume does not consider optimisation of the redundant hollow volume inside the active area ($0 < r < r_i$). The required torque determines the shaft diameter for mechanical strength. Between the shaft and inside of the active area are the stator end turns, so the complete volume can be optimised for torque density.

The Figure 4.10 dimensions of the active volume and shaft diameter may be optimised for torque while optimising the remaining volume in the radial direction minimises the envelope dimensions. The end winding geometry is reduced according to the pole number and the winding pattern.

4.5.2 Objective: Alternative Measures

Sadarangani [2000] outlines important design optimisation objectives for PM machines, other than torque density, repeated in Table 4.1 with related outcomes.

Table 4.1: Alternative design optimisation objectives.

OBJECTIVE	OUTCOME
Minimise amount and cost of magnets	Reduced cost
Maximise rated and peak thermal and overload capabilities	High temperature operation
Minimise risk of magnet demagnetisation	Operate with a strong stator field (high inductance)
Maximise speed and constant power speed range with minimum electrical frequency	High speed operation without high frequency losses
Minimise rotor saliency	Reduced reluctace torque
Minimise cogging torque	Reduced cogging torque
Maximise efficiency	Reduced losses/cooling requirement

4.6 Axial Flux Machine Parameter Calculation Program

The relations provided in published texts, and improved with those described here, have been employed by the author in the Axial Flux Machine Parameter Calculation (AFMPC) programs. These are useful tools for the machine designer.

AFMPC program: Type (b) parallel interpole spaces, constant w_s(r)

USER-DEFINED VALUES		CALCULATED VALUES	
RATINGS			
Power, P_kW [kW]	40	Efficiency, eta [%]	98.08
at Rated speed, S_r [rpm]	3000		
ELECTRICAL VALUES			
Maximum back emf, E_max [V]	500		
Maximum slot current density, J_max [A/m^2]	5000000		
Number of phases, N_ph	3		
RADIAL DIMENSIONS			
Outside radius, r_o [m]	0.2	Stator heat density, q_st [W/m^2]	2080
Inside radius, r_i [m]	0.1		
Lamination stacking factor, k_st	1		
AXIAL DIMENSIONS			
Airgap length, g [m]	0.001	Stator axial length, L [m]	0.058
Magnet length, l_m [m]	0.005	Back iron width, w_bi [m]	0.018
		Total slot depth, d_s [m]	0.039
MAGNET PROPERTIES			
Number of magnet poles, N_m	12		
Magnet spacer width, tau_f [m]	0.02		
Magnet remnance, B_r [T]	1.3		
Magnet recoil permeability, mu_r	1.1		
FLUX DENSITY			
Maximum steel flux density, B_max [T]	1.30	Airgap flux density, B_g [T]	0.46
SLOTS			
Number of slots per phase, N_sp (N_sp>=N_m)	18	Number of turns per slot, n_s	11
Conductor packing factor, k_cp	0.6	Slot bottom width, w_sb [m]	0.008
		Tooth width at inner radius, w_tbi [m]	0.004
		Slot heat density, q_s [W/m^2]	1722
SHOES			
Slot opening, w_s [m]	0.005		
Shoe depth fraction (d_1 + d_2)/w_tb, alpha_sd	0.2	Total shoe depth, split between d_1 and d_2, d_1+d_2 [m]	0.001

Figure 4.11: AFMPC program user interface for initial machine design.

The AFMPC program whose interface is shown in Figure 4.11, uses required ratings and fixed parameters as input to design calculations for the full design. User-defined values are input on the left half of the screen, producing the calculated values on the right half, with example values shown in this instance. Figure 4.12 illustrates the calculation process for this AFMPC program. The application determines the required ratings and desired space envelope. While magnet selection determines the magnet properties, the user should have an appreciation for the acceptable flux density, along with both slot number and shoe dimensions. However, these final user-defined values are quite often standard, so may remain unchanged between designs.

The design optimisation objectives of torque density etc., given in Section 4.5, are employed. Versions of the program are suitable for airgap winding machines and multi airgap machines. A performance prediction version of the program shown in Figure 4.11 uses the full machine design and operating conditions as input to the

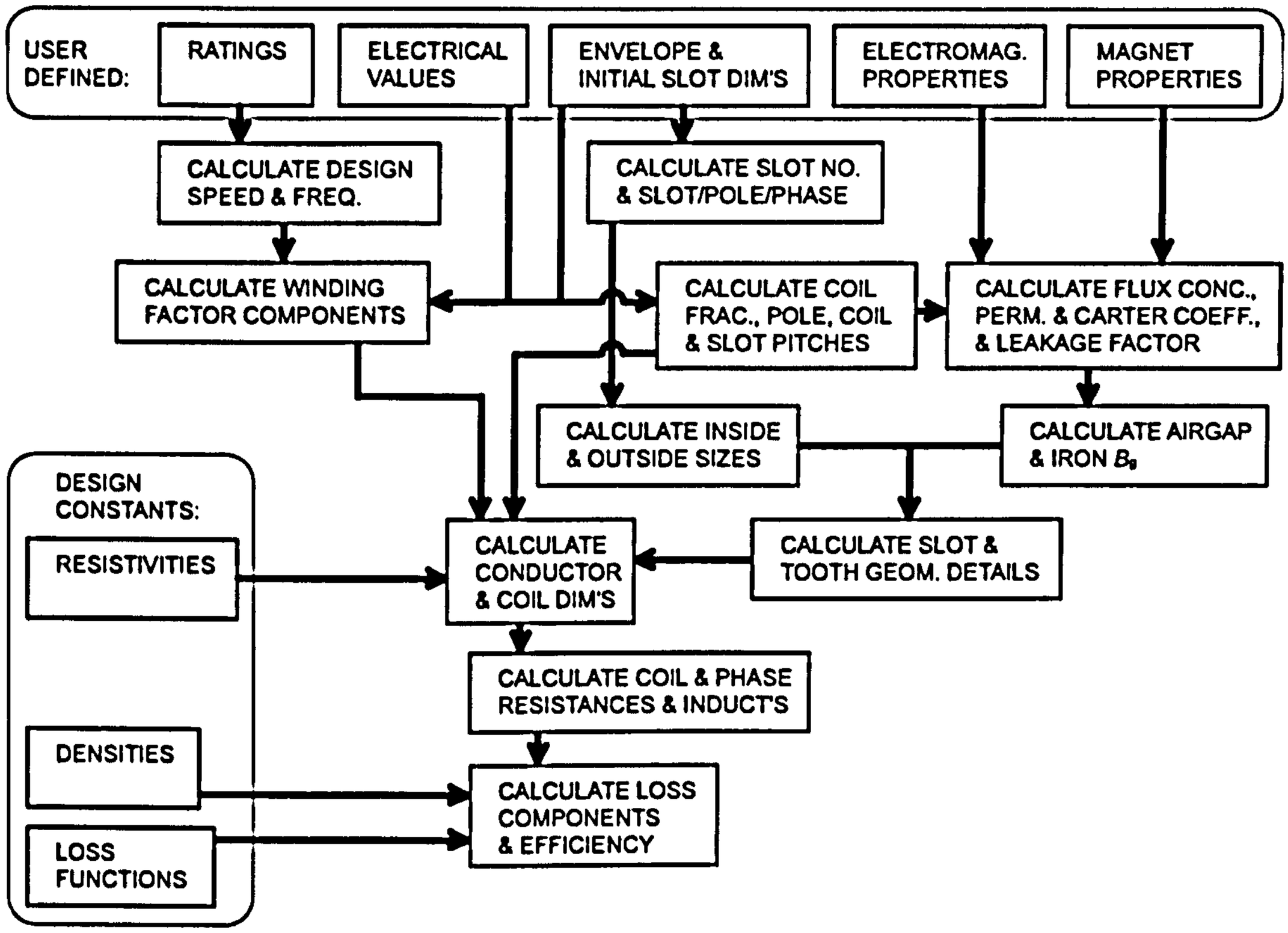


Figure 4.12: Calculation process for AFMPC program shown in Figure 4.11.

performance calculations. This is suitable for the machine in both motoring and generating operation.

Programs for estimating machine design or performance are often employed by companies. In most cases these include libraries of material characteristics, wire sizes, motor drive characteristics and steady-state thermal characterisation, which have been collated over many years [Hanselman, 1998].

4.7 Parametric Analyses

The process to find the optimum machine design involves manipulation of many geometric and electromagnetic parameters. Figure 4.13 illustrates the use of the AFMPC program to find approximate values for these parameters, which are then further refined with Finite Element Method modelling.

In order to verify the accuracy of AFMPC program calculations, and to gain insight into selected design trade-offs, some comparisons can be made with the results of the parametric analyses reported in literature on double airgap, slotted

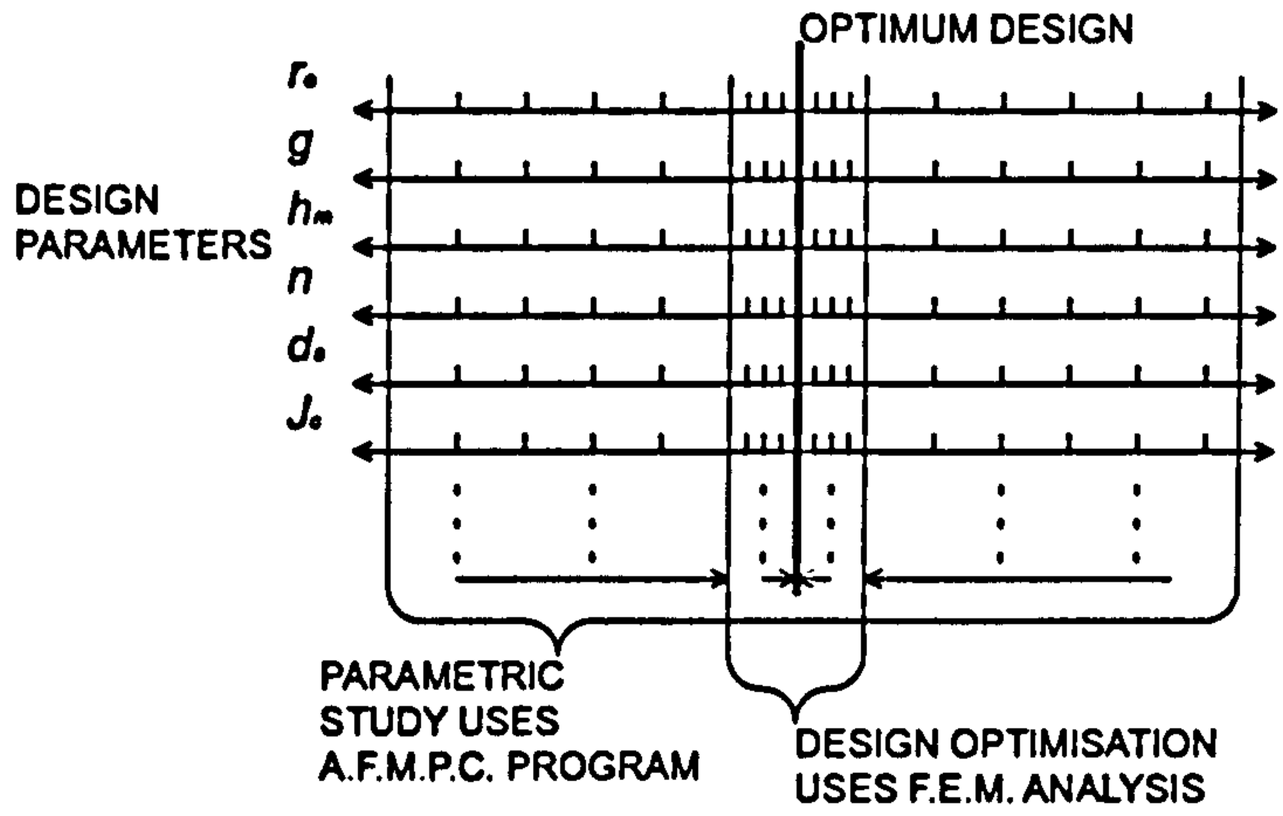


Figure 4.13: Optimised design process with parametric and FEM calculations.

machines, by Yang and Chuang [2005], Sitapati and Krishnan [2001], and Huang et al. [1999]. The machine designs generated using the AFMPC program have 12 poles, with rated torques of 10, 50, 100, 150 and 200 Nm.

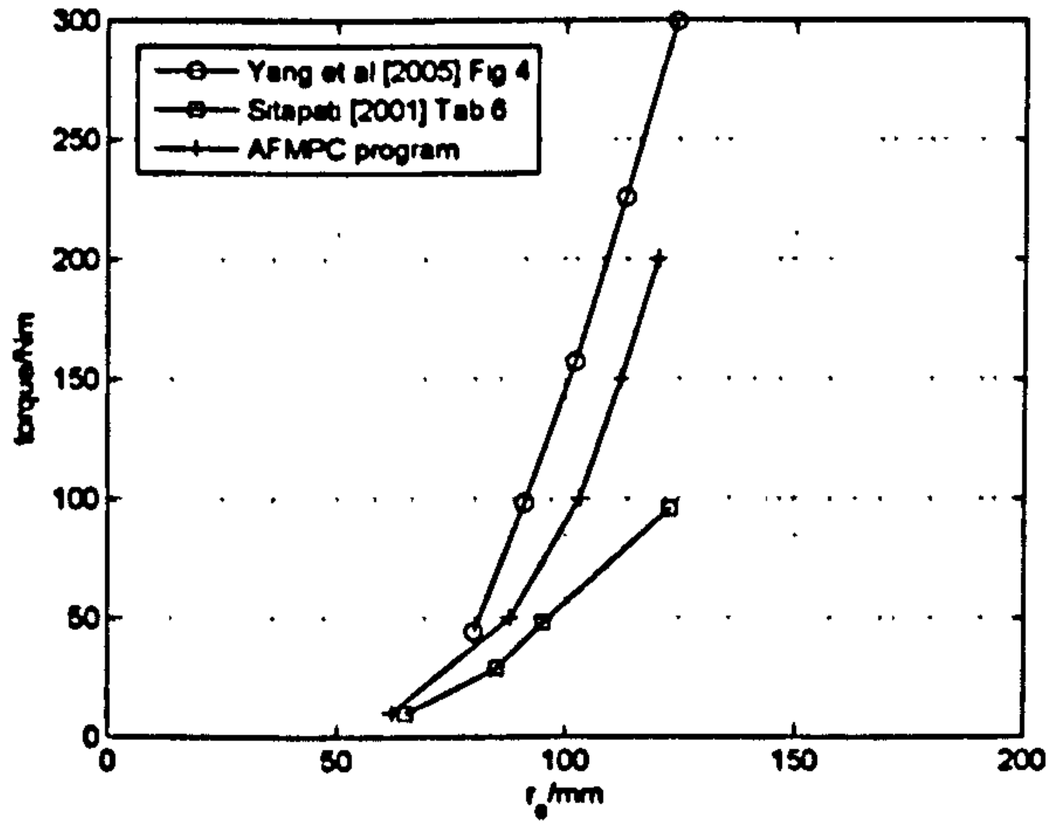


Figure 4.14: Torque from optimum designs with defined outside radius r_o.

The rated torque of the optimum designs with defined outside radii, are shown in Figure 4.14. Yang and Chuang's [2005] rated torque is greater than Sitapati and Krishnan's [2001], yet the AFMPC program provides torque values between both.

The specific torque and torque density of the optimum designs with defined torque, are shown in Figures 4.15 and 4.16. The torque density depends on the pole number only when other geometric parameters are fixed, as the optimum pole number and geometry are closely related. This can be seen in the similarity between curves in Figure 4.16.

The specific torque values of Sitapati and Krishnan [2001], Huang et al. [1999]

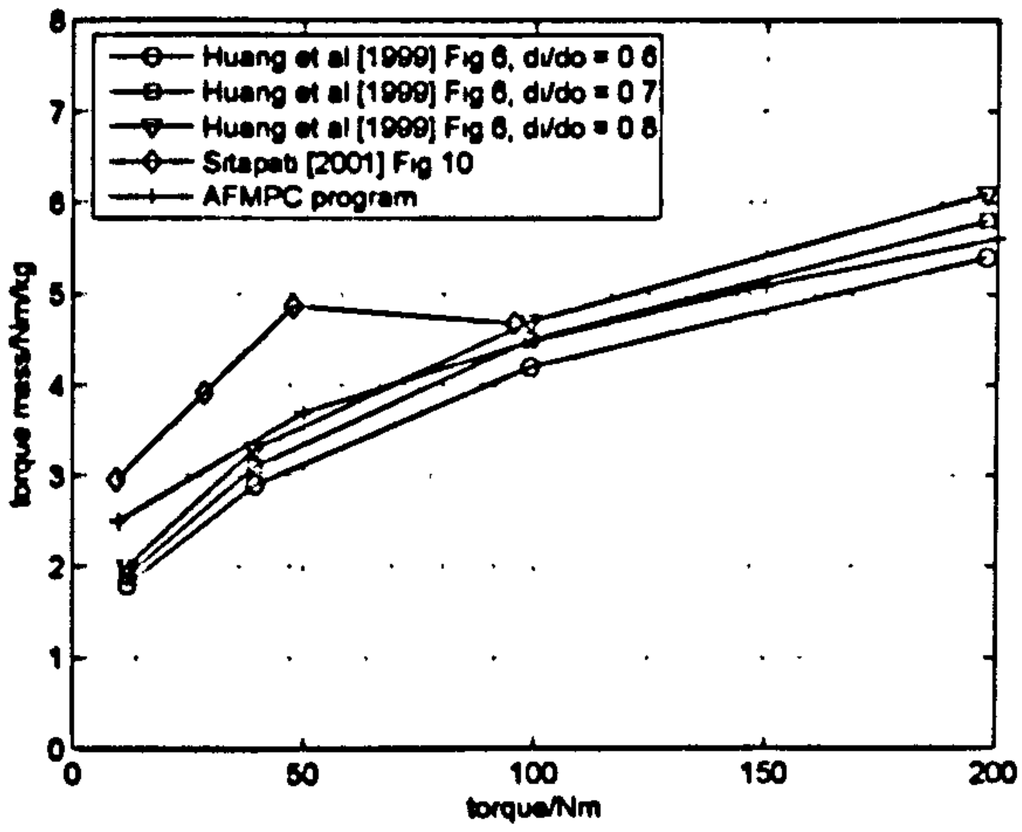


Figure 4.15: Specific torque for optimum designs with required torque.

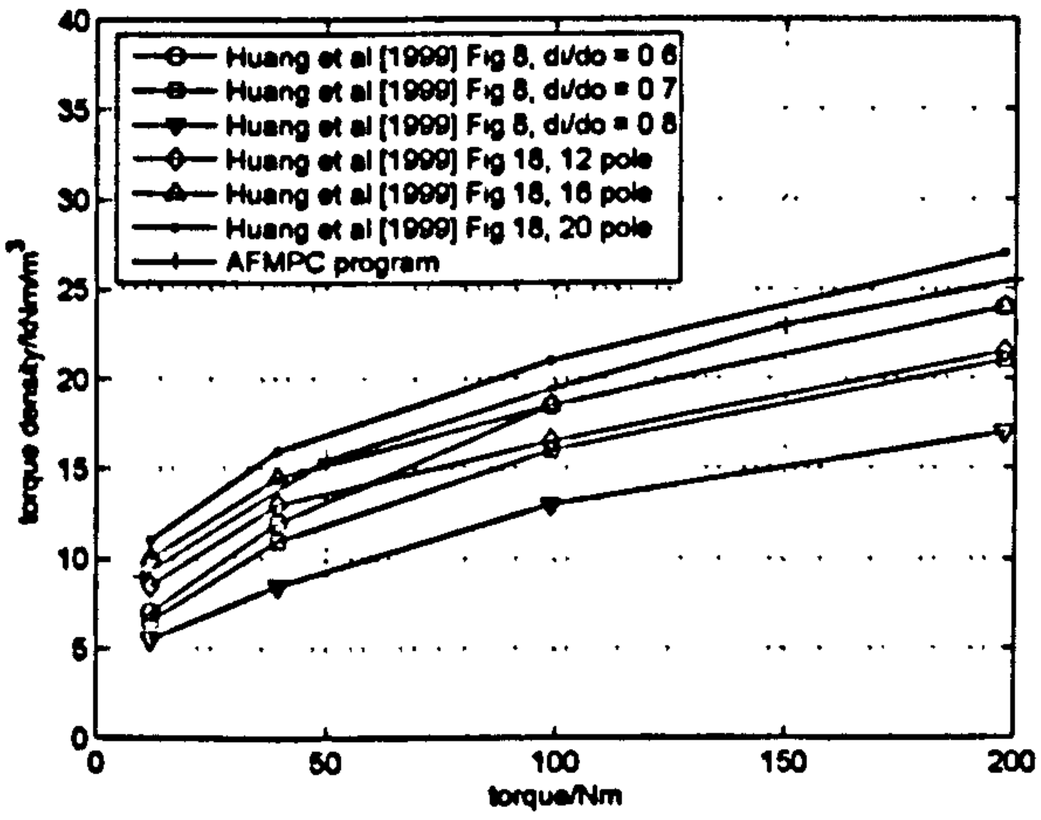


Figure 4.16: Torque density for optimum designs with required torque.

and the AFMPC program agree closely above 100 Nm, and the torque density values of the AFMPC program match Huang et al.'s [1999] 16-pole designs above 100 Nm.

Huang et al.'s [1999] and Sitapati and Krishnan's [2001] optimum designs for specified torque have similar copper losses to those of the AFMPC program, shown in Figure 4.17 as the conductor current density and resistance are approximately equivalent. The iron losses shown in Figure 4.18 illustrate Huang et al.'s [1999] are greater, but by only a small margin when normalised against the machine speed, yet the AFMPC program provide values between both.

Huang et al.'s [1999] and the AFMPC program's values for efficiency of the optimum designs for specified torque, shown in Figure 4.19, converge above 100 Nm although the difference is minimal below 100 Nm.

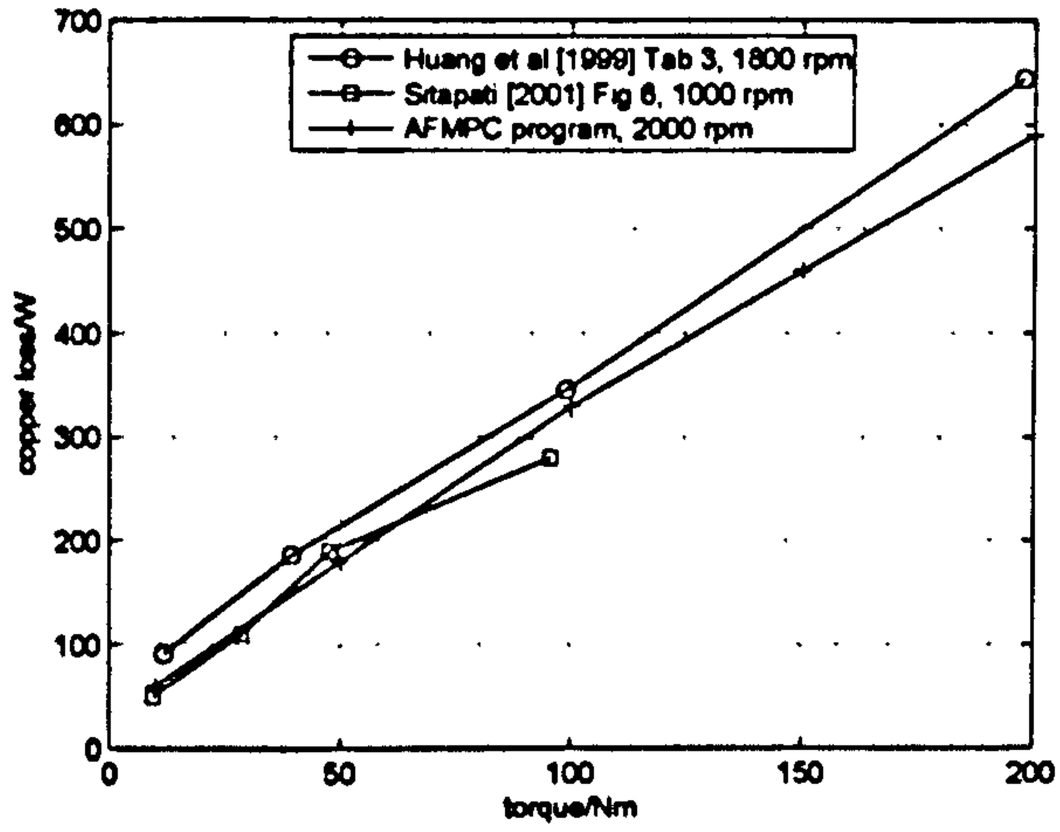


Figure 4.17: Copper losses for optimum designs with required torque.

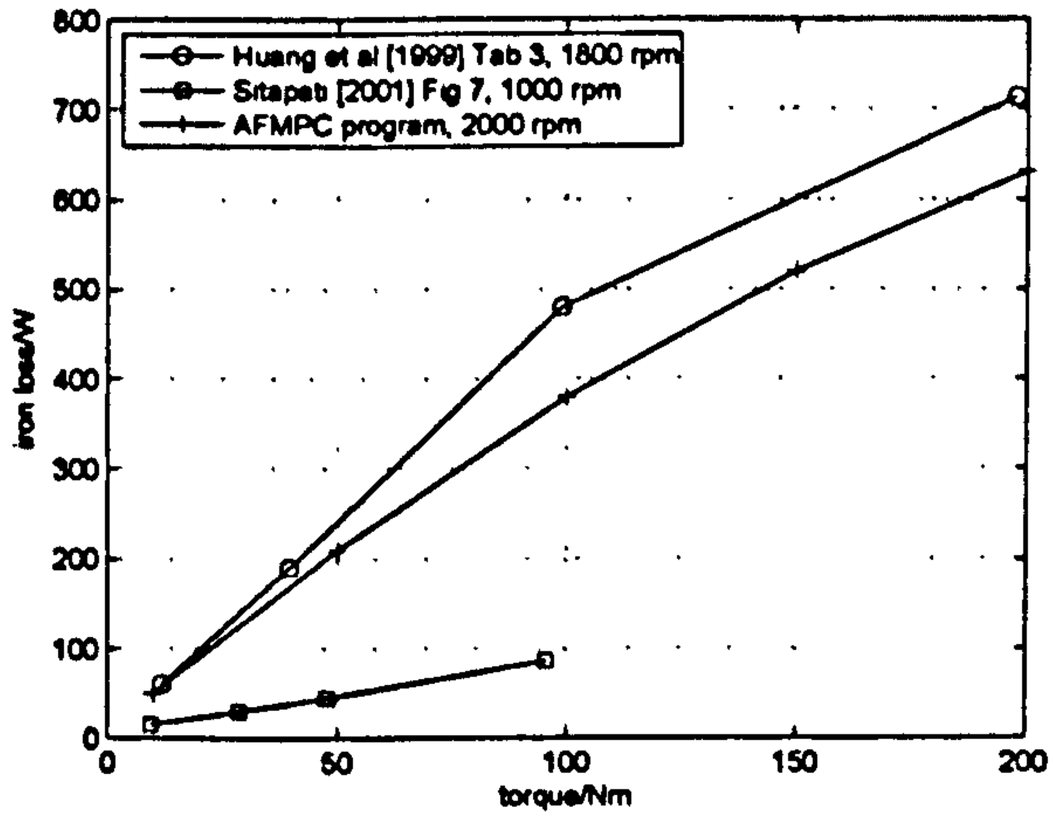


Figure 4.18: Iron losses for optimum designs with required torque.

4.8 AFMPC Program Use in Initial Machine Design

4.8.1 IMG Initial Design

The AFMPC program allows estimation of the current loading, airgap flux density and active area for the Axial Flux PM IMG. The bore diameter for the SAE2 flywheel housing is 447.68 +0.13 mm, defining r_h. Between r_h and the outside radius of the active area r_o is the space for endwindings. According to the endwindings space dimensions given in Appendix A.5, this favours active area dimensions of $r_i = 165$ and $r_o = 95$ mm. These dimensions render an airgap active area which gives a

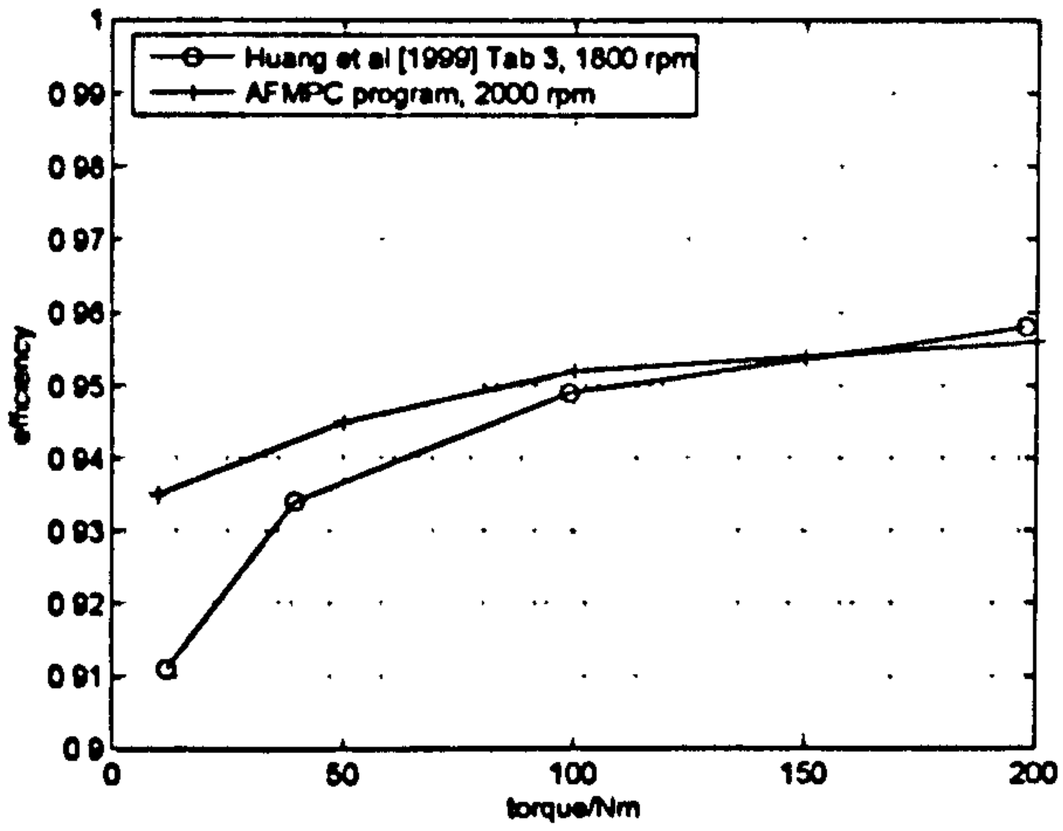


Figure 4.19: Efficiency for optimum designs with required torque.

torque of approximately 90 Nm at 12 kN/m^2 per single airgap. Therefore, a double airgap machine is required for the SAE2 size of flywheel housing. Using the active area dimensions, the pole number providing maximum torque is 12. The maximum speed is 2700 rpm to match the diesel engine maximum speed. Due to potentially lower iron losses and the single cooling circuit, the internal stator is preferred, made using a compressed powder iron core and round wire concentrated coils, and cooled by force-ventilated air. Although this requires a separately mounted fan, cooling can be independently controlled according to the torque demand (current loading).

While the specified torque and speed duty cycle defines the electric machine shaft power, there are also specified electrical parameters such as the drive and ESD voltages, which define the electric machine electrical input. In the case of generating operation, the inputs are mechanical and outputs electrical. A DC voltage supply of 288 V, selected for appropriate battery pack sizing, provides the desired open circuit voltage at maximum speed (2700 rpm). Note, no field weakening is employed so the maximum speed is effectively the base speed. This desired open circuit voltage and excitation frequency are achieved with approximately 50 turns per coil, the exact number depending on the exact excitation flux density.

These were the parameters derived by the author to outline the initial design, and which were subsequently used by Coles, P. [2003-4] to propose stator slot numbers (Q = 9 and 18) and coil conductor sizes (N_{tot} = 50 x Ø1.50 mm, 200 x Ø1.00 mm and 350 x Ø0.75 mm) for investigation.

4.8.2 Generator Initial Design

The limited diameter according to the flywheel housing size provides a limited torque. Without gearing between ICE and Generator, the torque for the fixed diameter requires the multiple airgap topology, increasing overall length.

Using a selected airgap magnetic shear stress of 8 kN/m^2, the AFMPC program described in Section 4.6 offers the torque from the active area radial dimensions. For a single airgap, this is $T_g \simeq 60$ Nm. With the ICE providing 100 kW at 2600 rpm, resulting in a mechanical torque of $T_{mech} \simeq 240$ Nm, a four airgap design is employed.

The generator voltage for 2600 rpm operation must provide a peak of 600 V as a rectified DC voltage.

The pole number employed is 12 ($p = 6$). This provides the machine aspect ratio including the length of each slice, plus the flux circuit return at each end. The pole width, from circumference and pole number, determines the radius of the flux circuit return ($= h_{Fe}$). As the pole number selection is a trade-off between flux return paths and electrical frequency, the pole size and flux return size are used for pole number determination with optimum r_i/r_o of $1/\sqrt{3}$ (for maximum torque).

4.9 Summary

By using the general relations covered here for the overall machine operation, the machine designer can quickly arrive at a good overall design for an Axial Flux PM machine. A new contribution is that these relations have been compiled in the AFMPC programs to facilitate machine sizing and early design for HEV powertrain applications.

The AFMPC programs produced for both design and performance analysis do not require the designer to have significant prior experience of the design trade-offs in Axial Flux machine design. Further optimisation depends on detailed investigation of electromagnetic parts of the machine, which does depend on the designer's experience or use of more accurate yet computationally more complex and expensive Finite Element Method (FEM) modelling.

The AFMPC programs could be extended using established optimisation techniques. This would involve replacing the design knowledge, or relations interpreted from experience of previous machine designs, with parameter search algorithms meeting the desired constraints.

Chapter 5

3D Equivalent Magnetic Circuit Model for a Double Airgap, Airgap Winding Machine

This 3D equivalent magnetic circuit model, used together with models for drive and electrical ESD components, is also described by Walker and Anpalahan [2005].

A 3D equivalent magnetic circuit model of a double airgap machine with airgap winding, shown in Figure 5.1 has been created. This is employed in the generator analysis reported in Chapter 2, to develop the initial generator design given in Chapter 4, and as part of the winding analysis reported in Chapter 7.

5.1 Leakage and Fringing

The fringing and leakage reluctances denoted by $\mathcal{R}_{fxx}$ and $\mathcal{R}_{lxx}$ are included in the model as illustrated in Figure 5.2. These are defined by the overlapping area method.

5.2 Solution

The mathematical terms for the flux sources and reluctances are explicitly given in Appendix B.3. The model is solved for useful airgap flux linkage by $[\Phi] = [\mathcal{R}]^{-1}[\mathcal{F}]$, where $[\mathcal{R}]$ is a 10x10 matrix and $[\Phi]$ and $[\mathcal{F}]$ are 10x1 arrays. The useful airgap flux ϕ_g is found from two terms; $\Phi_{(3)} - \Phi_{(4)}$, which gives the flux linkage using the number of turns per coil.

The model was encoded within the Mathcad environment. The instantaneous

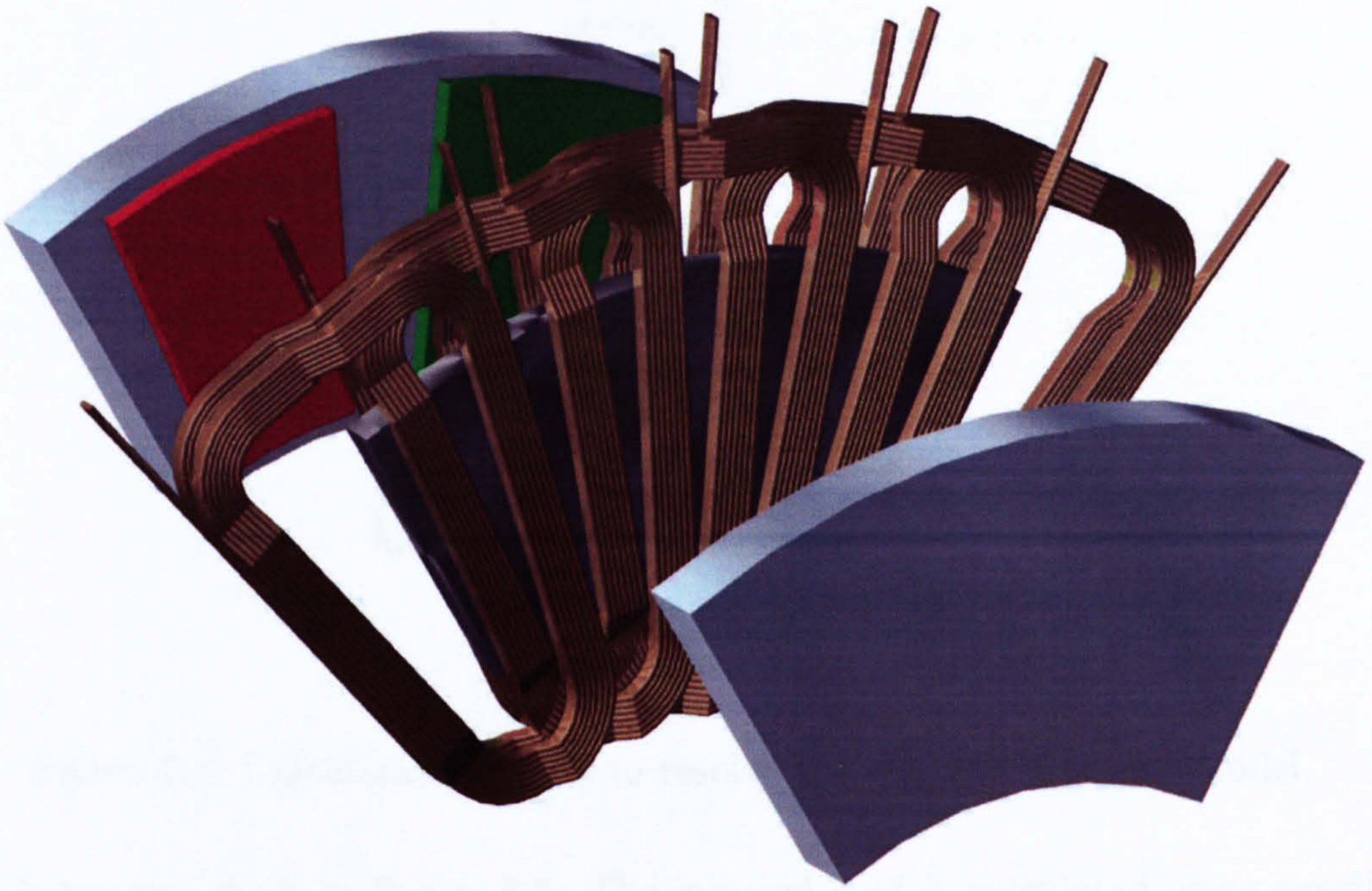


Figure 5.1: Double airgap, airgap winding for 3D equivalent circuit model.

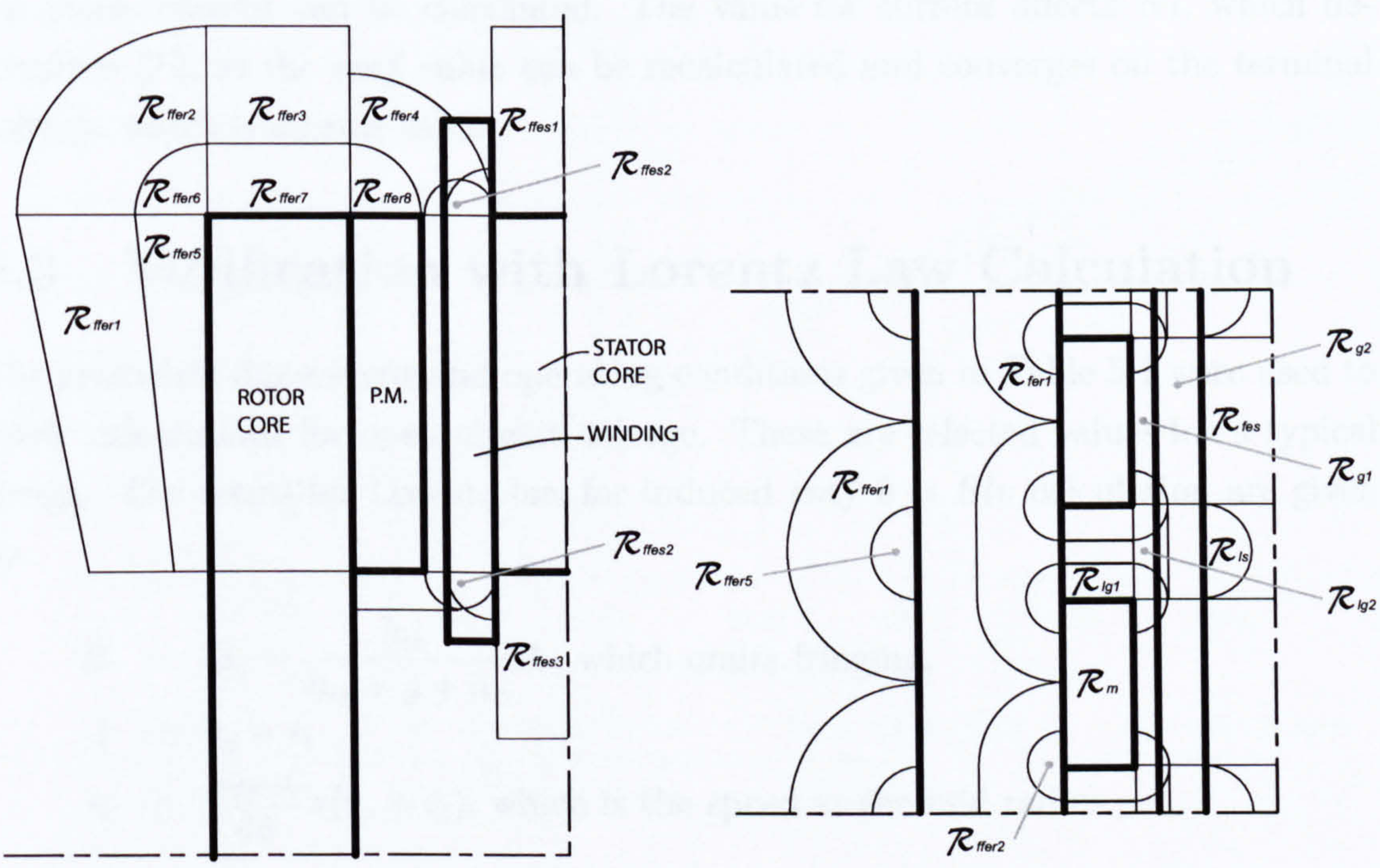


Figure 5.2: Elevation and plan of double airgap, airgap winding model fringing and leakage reluctances.

operation is calculated by including the coil mmf and PM flux sources, but the phase current creating coil mmf must be derived.

The machine operating condition is calculated with the required output, follow-

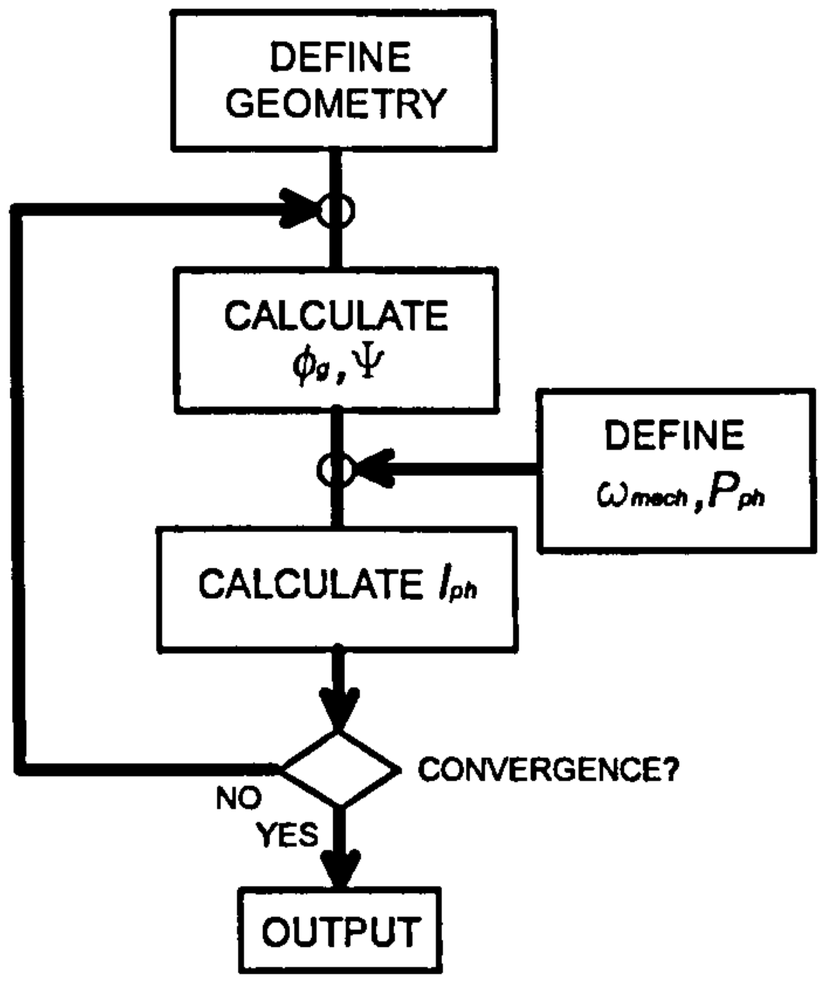


Figure 5.3: Calculation process to resolve the equivalent circuit model.

ing the process given in Figure 5.3. The induced emf is calculated using specified mechanical speed. By specifying the mechanical power and efficiency at this speed, the phase current can be calculated. The value for current affects Ni, which determines $[\mathcal{F}]$, so the emf value can be recalculated and converges on the terminal voltage, which is an rms value.

5.3 Verification with Lorentz Law Calculation

The geometric dimensions and operating conditions given in Table 5.1 were used to verify calculations for open circuit voltage. These are selected values for a typical design. The terms for Lorentz law for induced emf $\hat{e} = Blv$ calculation are given by:

$$\begin{aligned} B &= B_g = \frac{h_m}{h_m + g + h_c} B_r, \text{ which omits fringing,} \\ l &= r_o - r_i \\ u &= \frac{\omega_{mech}}{60} \pi (r_o + r_i), \text{ which is the speed at the mid radius.} \end{aligned}$$

The operating speed of 4000 rpm renders a peak induced emf of 389 V, compared with the equivalent magnetic circuit model value of 320 V. This approximate 20 % difference may arise from the approximation for airgap flux density in Blv without flux leakage. However, it indicates the equivalent magnetic circuit model result is reasonable. The rms terminal voltage with respect to speed is given in Figure 5.4 for an electrical output between 0 and 20 kW.

Table 5.1: Typical geometric dimensions and operating conditions selected for model verification.

airgap length	g [m]	0.001
magnet height	h_m [m]	0.005
rotor iron thickness	h_{Fer} [m]	0.015
inner radius	r_i [m]	0.095
outer radius	r_o [m]	0.165
pole pairs	p	6
stator iron thickness	h_{Fes} [m]	0.008
coil height	h_c [m]	0.004
pole pitch factor	k_{ppitch}	2/3
number turns per coil (per side)	N	7
number coils per phase	N_{c_ph}	8
relative permeability iron	μ_{r_Fe}	1000
relative permeability PM	μ_{r_PM}	1
relative permeability air	μ_{r_air}	1
relative permeability Cu	μ_{r_Cu}	1
remnant flux density PM	B_r [T]	1.29
operating speed	ω_{mech} [rpm]	4000
power per phase	P_ϕ [W]	0 (i.e. open circuit)

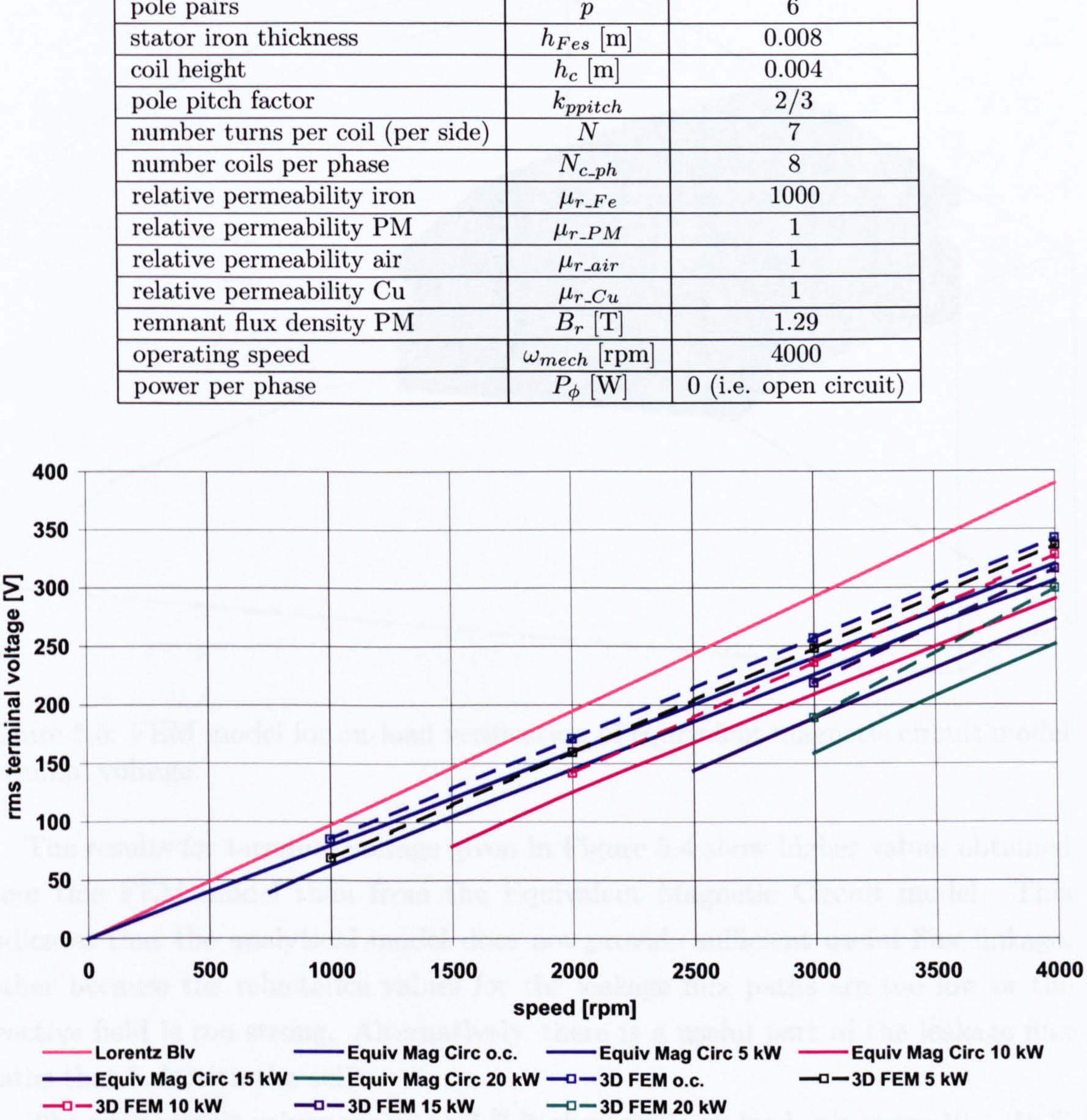


Figure 5.4: Rms terminal voltage values from equivalent magnetic circuit model, Lorentz *Blu* and FEM calculations, for the geometry given in Table 5.1.

5.4 Verification with FEM

Calculations for on-load voltage of the same geometry were verified using the FEM software MagNet 3D [Infolytica Corporation, 2002]. The model shown in Figure 5.5

was evaluated using the time-harmonic solver, as there is a time-varying magnetic field in and around coils, which were modelled as stranded. The values for terminal voltage against speed, with selected phase output power of 5, 10, 15, and 20 kW are given in Figure 5.4.

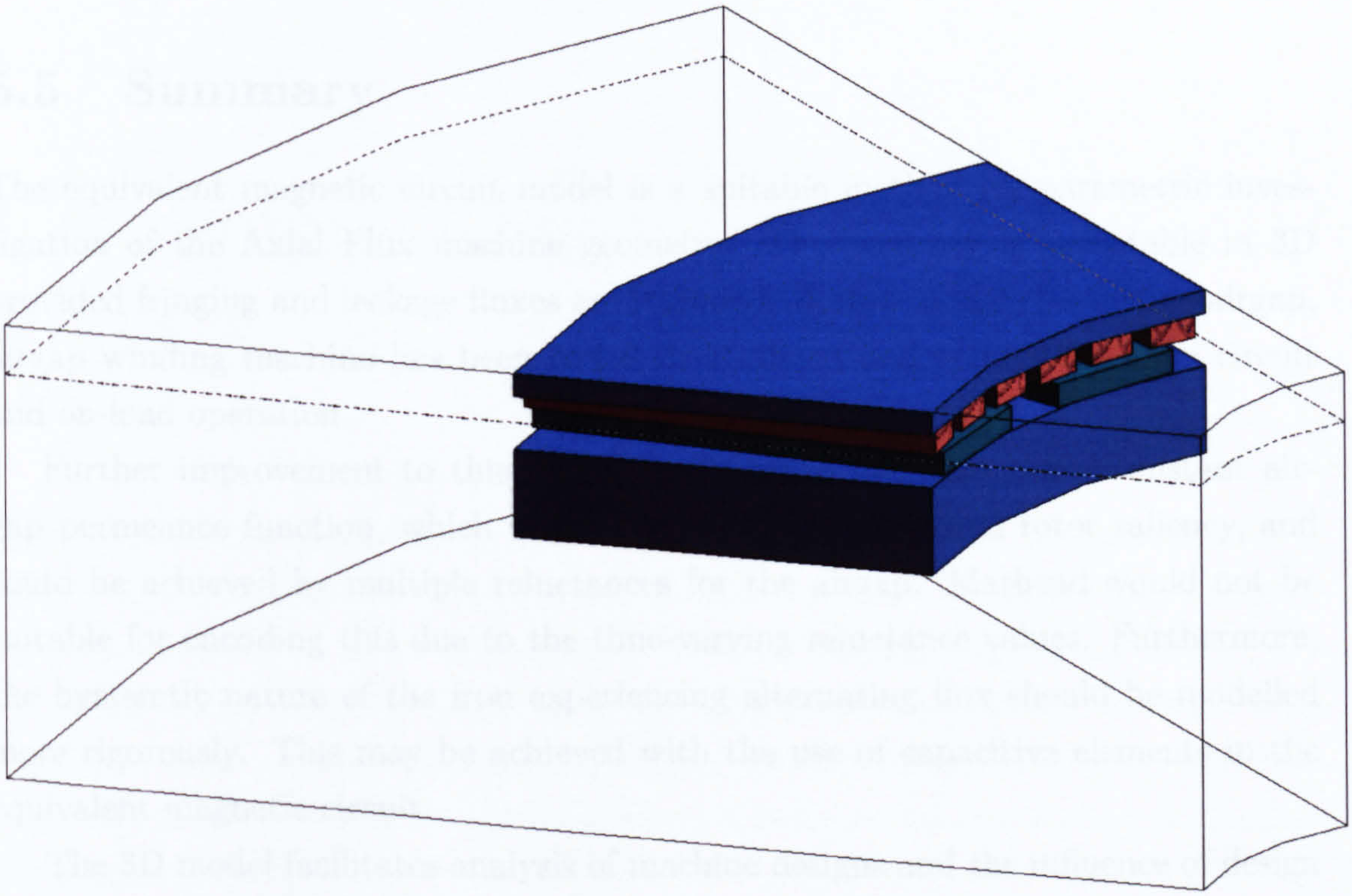


Figure 5.5: FEM model for on-load verification of equivalent magnetic circuit model terminal voltage.

The results for terminal voltage given in Figure 5.4 show higher values obtained from this FEM model than from the Equivalent Magnetic Circuit model. This indicates that the analytical model does not provide sufficient useful flux linkage, either because the reluctance values for the leakage flux paths are too low or the reactive field is too strong. Alternatively, there is a useful part of the leakage flux paths that link with the coils.

The open circuit values are up to 7 % higher, while on load values are $10 - 18$ % higher for 5 to 20 kW output. Although it is acceptable for generator operation as the electrical power output will be underestimated, the modelling of the reactive field and coil-core and coil-coil leakage require more detailed consideration to improve overall accuracy.

The FEM computations were made using bundled conductors. Although the strand number was specified, the conductors were not individually modelled. Therefore, the coil-core leakage, which links with some conductors, could not be considered

explicitly. However, the accuracy of results from this Equivalent Magnetic Circuit model are equivalent at all power levels so are acceptable for comparative analyses, making the model useful for further design work, which then can employ FEM for design refinement.

5.5 Summary

The equivalent magnetic circuit model is a suitable method for parametric investigation of the Axial Flux machine geometry. The accuracy is acceptable in 3D provided fringing and leakage fluxes are included. Such a model of a double airgap, airgap winding machine has been coded in Mathcad and verified for open circuit and on-load operation.

Further improvement to this model would be to facilitate a non-constant airgap permeance function, which would account for slotting and rotor saliency, and could be achieved by multiple reluctances for the airgap. Mathcad would not be suitable for encoding this due to the time-varying reluctance values. Furthermore, the hysteretic nature of the iron experiencing alternating flux should be modelled more rigorously. This may be achieved with the use of capacitive elements in the equivalent magnetic circuit.

The 3D model facilitates analysis of machine designs and the influence of design parameters on the harmonic losses, which is addressed in following chapters.

Chapter 6

Permanent Magnet Excitation Field Study

This chapter investigates the excitation field created by an array of Surface Mounted Permanent Magnet pieces. The material includes numerical evaluation and experimental measurement that was presented in Walker [2003*a*] and Walker [2003*e*].

The excitation field is described by the airgap flux density B_g waveform with respect to rotor position θ at time t, thus determining induced emf with respect to t. As described in Section 1.8, field waveform harmonics are detrimental to machine efficiency.

The analysis is undertaken by means of FEM and flux density measurements with a Hall probe in the $r-$, $\theta-$ and $z-$ directions.

6.1 Field Waveforms

6.1.1 Waveforms

The field spatial harmonics relate to the lower order harmonics. The ideal BLDC and ideal PMSM waveforms are rectangular and sinusoidal, yet actual waveforms are usually trapezoidal.

Flux leakage between neighbouring poles prevents poles sharing the same edge. To avoid wasting Permanent Magnet material, gaps are left between poles. However, pole-to-pole fringing still exists and the selection of the pole pitch factor k_{ppitch} is important.

6.1.2 Spatial Harmonics

To differentiate between rotating space and time harmonics, the spacial harmonics are distributed with respect to θ around the airgap, defined by $B = \hat{B}_g \cos(k\theta - \omega_{elec}t)$, and pulsate at frequency ω and rotate at angular speed ω/k, while time harmonics have the same spatial distribution, defined by $\mathcal{F} = \hat{\mathcal{F}}_g \cos(k\omega_{elec}t - \theta)$, but pulsate at frequency $k\omega$. The time harmonics in the airgap mmf are produced by current harmonics in the phase windings, while space harmonics are produced by harmonics in the winding distribution.

The origin of space harmonics requires looking at airgap flux density, being the product of airgap permeance per unit area and airgap mmf.

$$B(\theta,t) = \frac{\mu_0}{g(\theta,t)} \cdot \mathcal{F}(\theta,t) = \Lambda(\theta,t) \cdot \mathcal{F}(\theta,t) \tag{6.1}$$

where $\Lambda(\theta,t)$ is permeance per unit length and $g(\theta,t)$ and $\mathcal{F}(\theta,t)$ are airgap and mmf. The Surface Mounted PM machine with an airgap winding has non-salient rotor and stator giving a constant permeance function $\Lambda(\theta,t)$. The airgap mmf therefore contains spatial harmonics, which contribute.

To resolve into a Fourier series, as given in math theory textbooks such as Swarowski [1995], the induced emf is:

$$e = \sum_{n=0,1,2,3,\ldots} E_n \sin(n\omega_{elec}t) \tag{6.2}$$

where the second term in the series $n = 1$ is the fundamental harmonic. In this case, the waveforms under consideration are symmetric about the $d-$axis (the PM centreline) so harmonic terms $n = 0, 2, 4, 6, \ldots$ tend to zero and the harmonics are in phase. The remaining terms define a general excitation waveform, such as a rectangular waveform described by:

$$e = \frac{4}{\pi}\left(E\sin\omega_{elec}t + \frac{E}{3}\sin 3\omega_{elec}t + \frac{E}{5}\sin 5\omega_{elec}t + \ldots\right) \tag{6.3}$$

6.2 Peak Airgap Flux Density

6.2.1 Maximum Airgap Flux Density

The maximum peak value for airgap flux density can be determined by summation of the individual spatial harmonics:

$$\max\left(\hat{B}\right) = \sum \hat{B}_n \sin\left(\frac{n\pi}{2}\frac{\tau_m}{\tau_p}\right) \qquad n = 1,5,9,13,17,21,\ldots \tag{6.4}$$

where B_n is given in Equation (6.5).

This can be verified with 2D FEM analysis. The program employed for this was FEMM V3.3 [Meeker, 2002], using a parameterised script. Figure 6.1 illustrates the peak axial ($z-$) direction flux density $\hat{B}_z$ in relation to the pole pitch ratio, and the pole aspect ratio, and Figure 6.2 illustrates the amplitude of individual harmonic components. The common PMSM pole pitch ratio is $k_{ppitch} = 2/3$, which ensures no triplean harmonics. This is the pole pitch ratio value for maximum $\hat{B}$ as the 3rd harmonic is left out of the expression (Equation (6.4)).

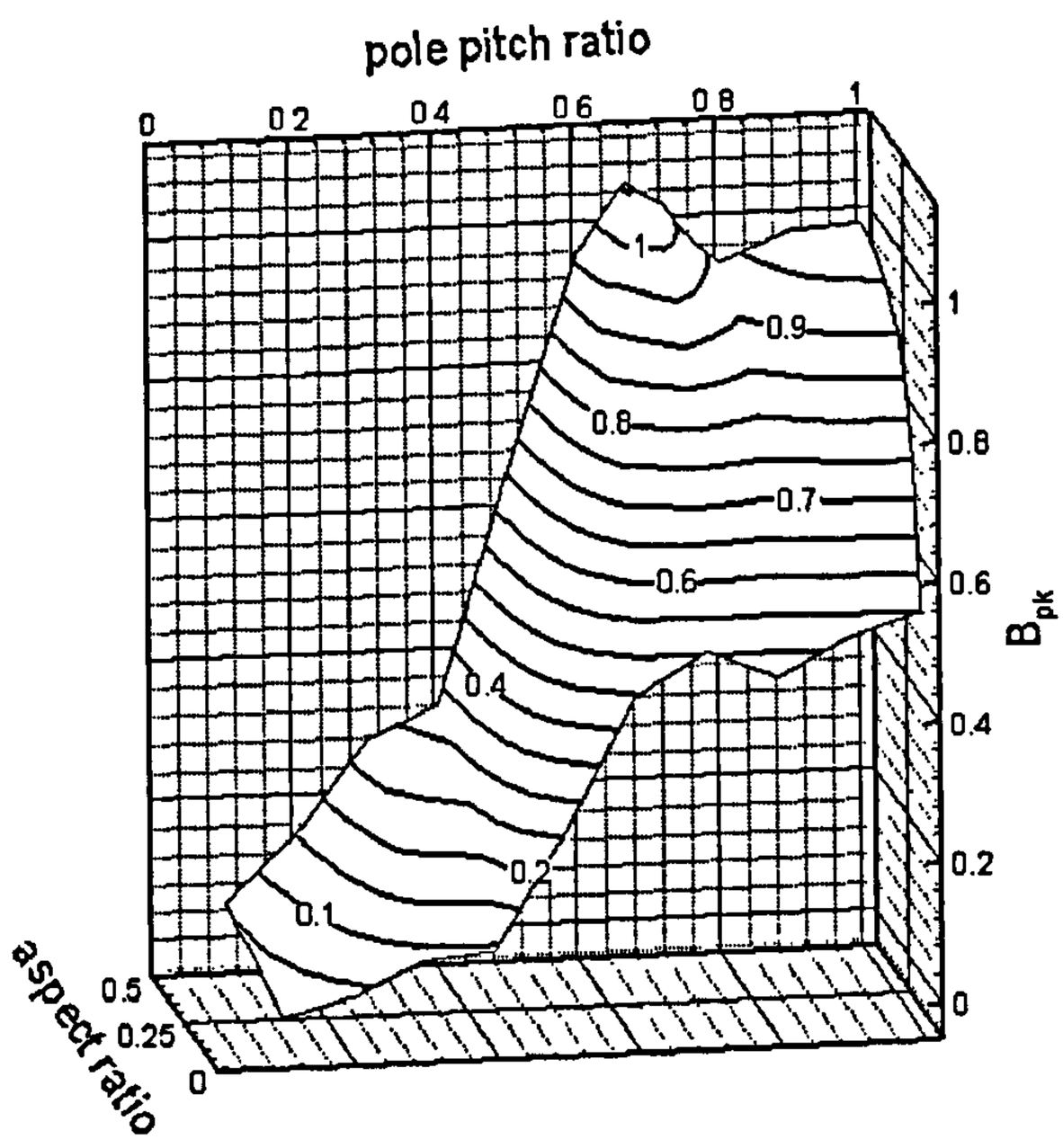


Figure 6.1: Peak flux density for pole aspect ratio (h_m/τ_m) and pole pitch ratio k_{ppitch}.

The Fourier analysis, which derives Figure 6.2, facilitates the harmonic magni-

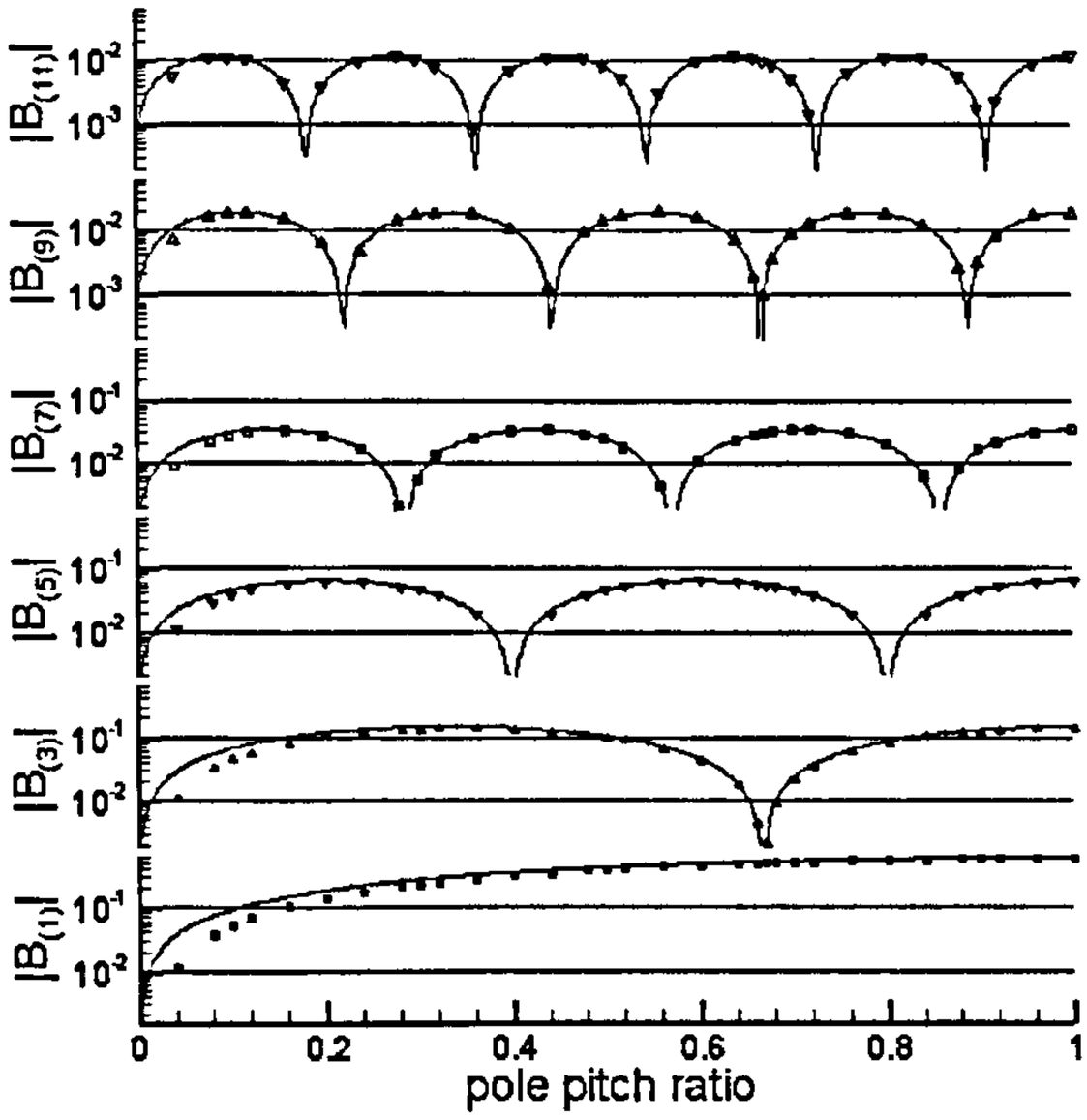


Figure 6.2: Harmonic components according to k_{ppitch}. Points are individual FEM models and lines are analytical relations.

tude using the magnet remnant flux density B_m:

$$B_n = \frac{4B_m}{n\pi} \sin\left(\frac{n\pi}{2}\frac{\tau_m}{\tau_p}\right) \tag{6.5}$$

6.2.2 PM Height to Airgap

The relationship between PM height and airgap length relates to the peak airgap flux density. Previous studies indicate the required PM height is 0.8 times the magnetic airgap, i.e. the high reluctance path through magnet and mechanical airgap [Hanselman, 2003]. Figure 6.1 shows the pole aspect ratio h_m/w_m up to 0.5, which, considering the pole pitch ratio, provides a constant height ratio h_m/g rather than constant pole height, giving $\max(\hat{B}/Vol_{PM})$ at $h_m/g \simeq 4/5$.

The PM height also relates to the interpole space $(w_p - w_m)$ and leakage flux between PM poles and keeper iron. Figure 6.3 illustrates these pole-to-pole and pole-to-keeper iron leakage paths. Pole-to-keeper leakage is reduced with increasing h_m, so $w_p - w_m$ can be increased. Reducing g reduces the pole-to-pole leakage, so $w_p - w_m$ can be reduced, giving the machine designer further options. Provided g is less than r_{leak_m-m} or r_{leak_m-rot}, the airgap length determines the total leakage and k_{ppitch} determines the proportion of each.

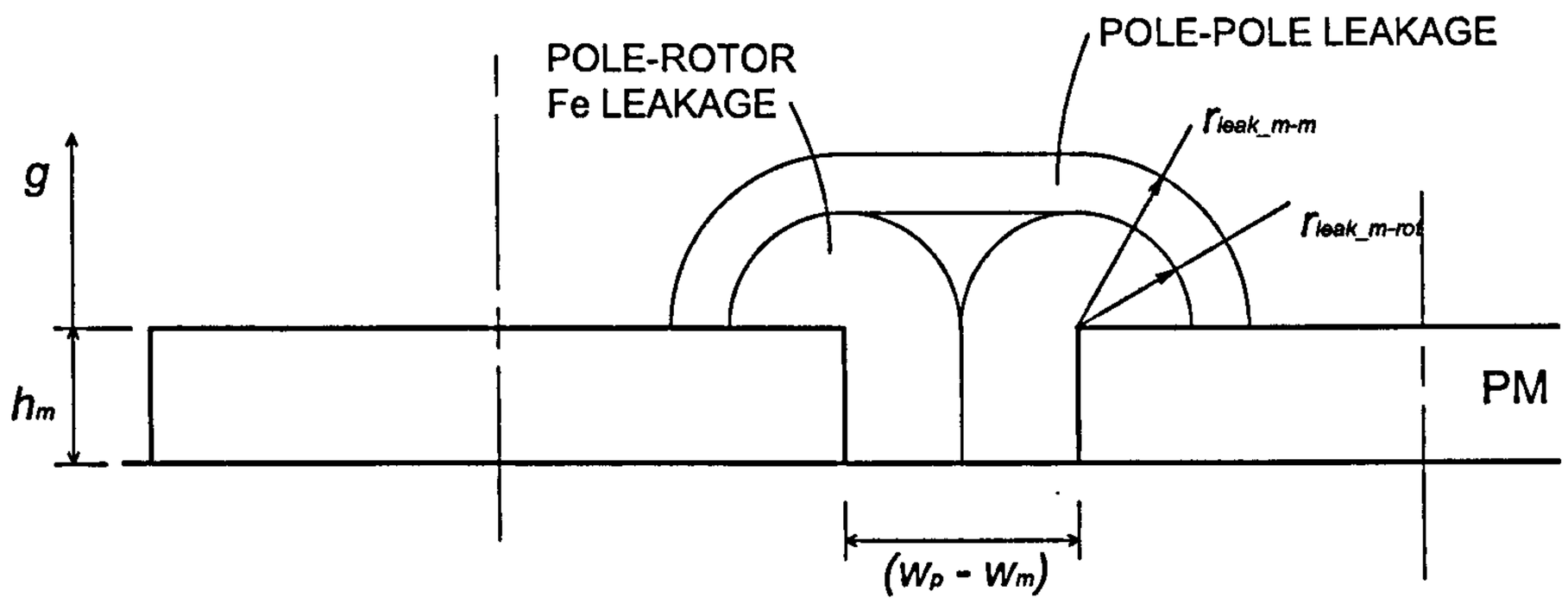


Figure 6.3: Neighbouring poles without stator showing pole separation, height and leak paths.

6.2.3 Discussion of $\hat{B}_g$

Pole height ratio is an established machine design parameter and applies equally to Axial Flux as to Radial Flux. However, the pole pitch and pole aspect ratios are considered for the Axial Flux machines because pole size can vary with r according to the pole shapes given in Figure 4.5, an example of which is shown in Figure 6.4.

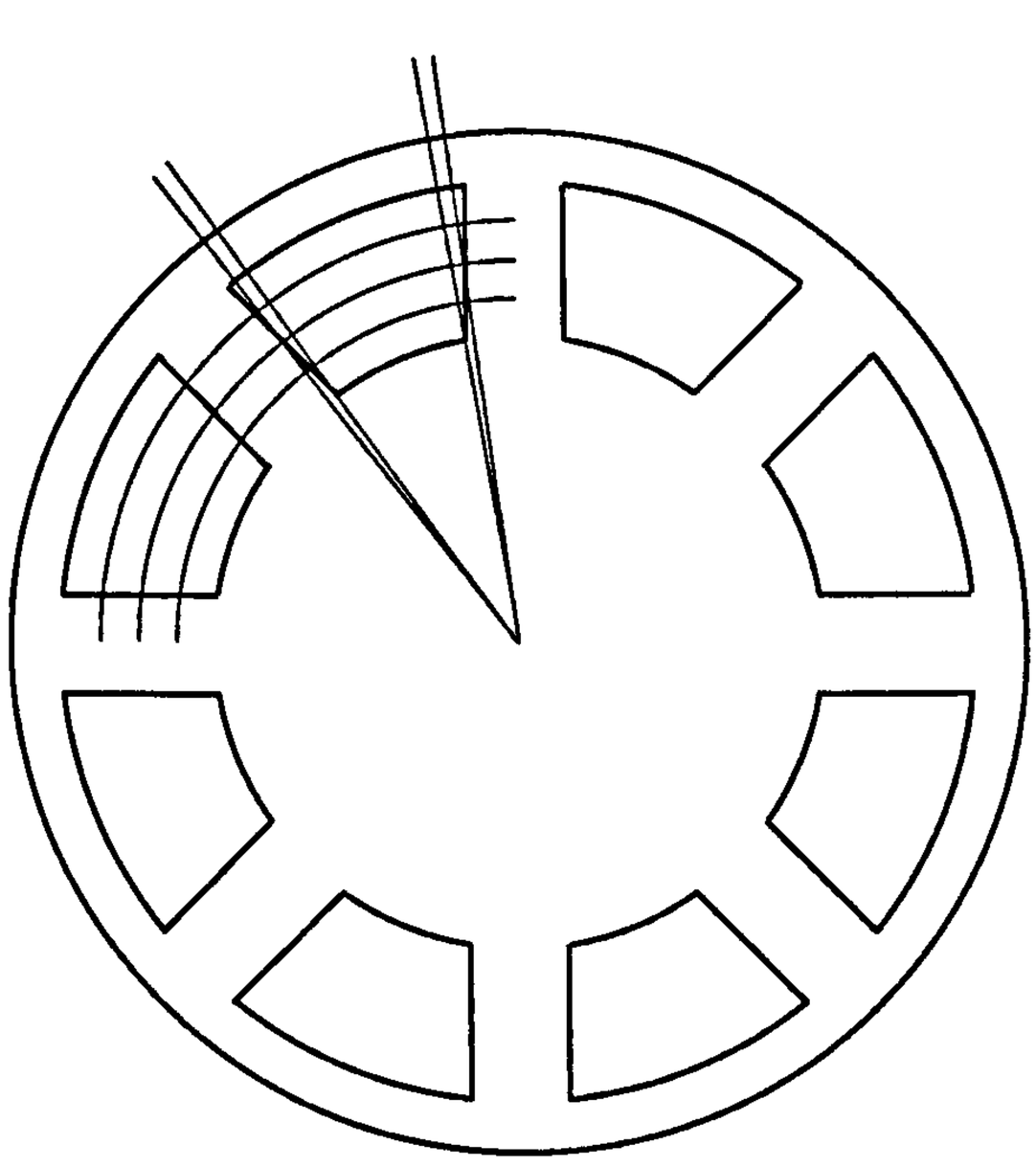


Figure 6.4: Variation in k_{ppitch} with radial position.

6.3 Single-piece Poles

Arrays of single-piece poles are employed in the machines reported in Chapter 3. These are selected for the IMG and Generator applications selected for case studies. However, the rest of this chapter reports efforts to reduce the harmonic contents.

6.3.1 Field Measurements

Scaled rotors with sector poles and new pole shapes were manufactured and measurements made using a testrig described in Appendix C. Figure 6.5 shows one rotor with an 8-pole PM array.

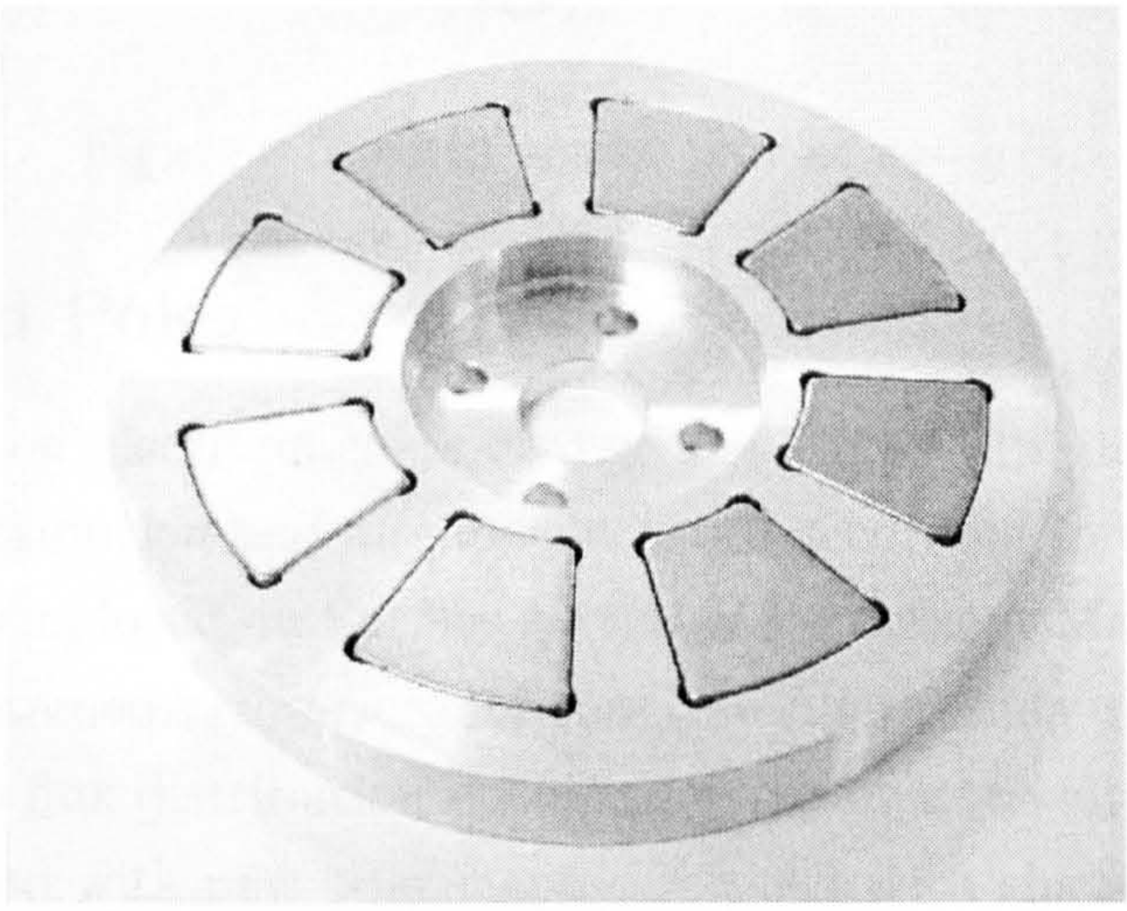


Figure 6.5: 1 rotor with 8 pole array.

Figure 6.6 shows the vector plot of the excitation field at the mid-airgap position ($z = g/2$), and Figure 6.7 shows the plots of $z-$direction flux density at airgap positions $z = g/2, g/10$ and $g/20$. The probe dimensions were 1 mm x 4 mm, allowing the nearest measurement to the rotor surface at $g/20$ for $z-$direction measurements and $z = g/5$ for lateral ($\theta-$ and $r-$direction) measurements.

Figure 6.8 shows similar plots in the $\theta-$ and $r-$directions at $z = g/5$, indicating fringing. Flux density in the $\theta-$direction peaks at the pole edges rather than midway between poles, indicating substantial pole-to-keeper leakage. Flux density in the $r-$direction extends to the sides of the measured region outside the pole areas, which means end turns require a larger radius. Comparing airgap positions illustrates the difference a large airgap winding conductor experiences. The most interesting part of the airgap is that occupied by an airgap winding. B_z should remain constant in the $z-$direction where the conductors sit and avoid eddy currents.

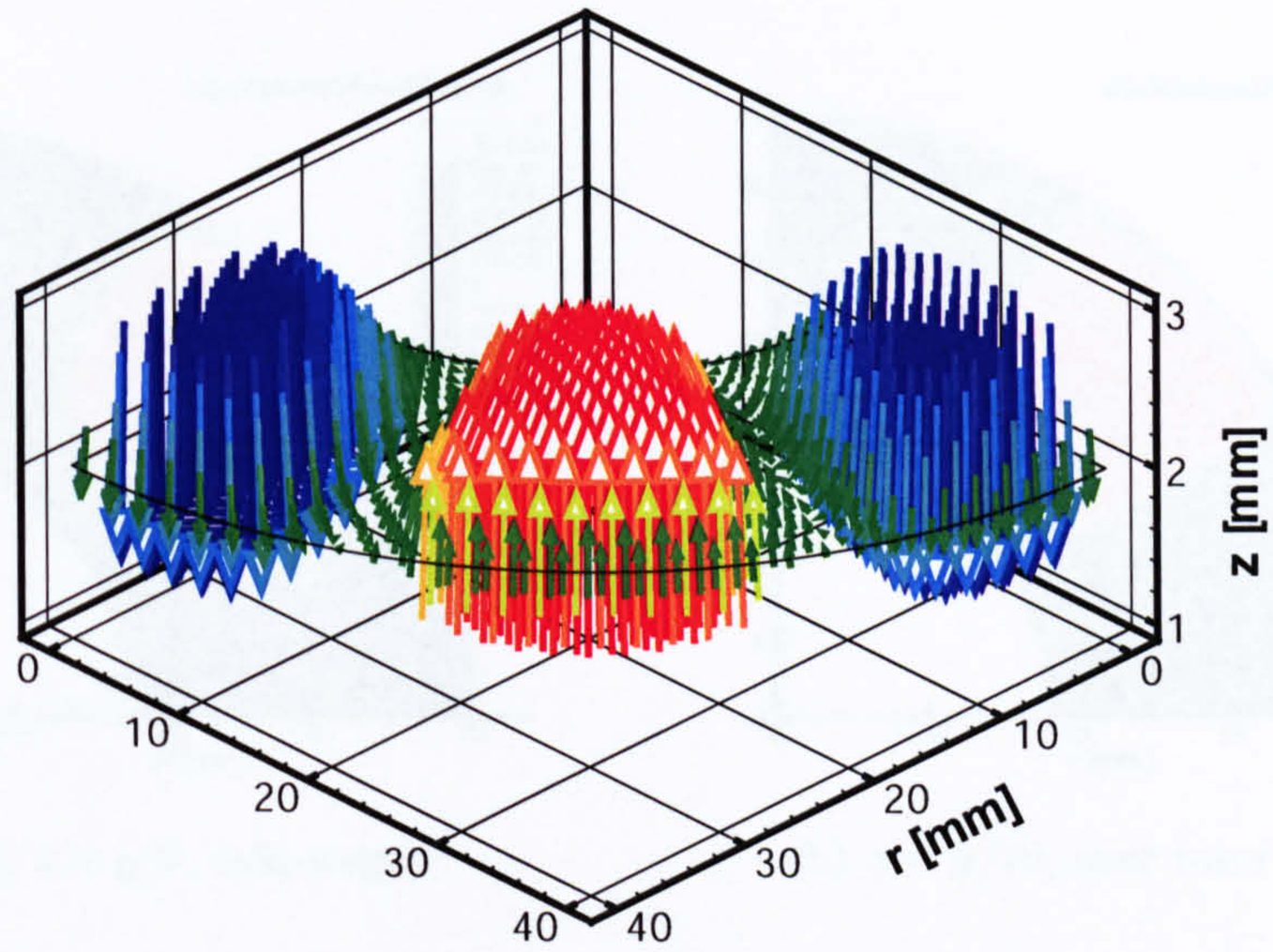


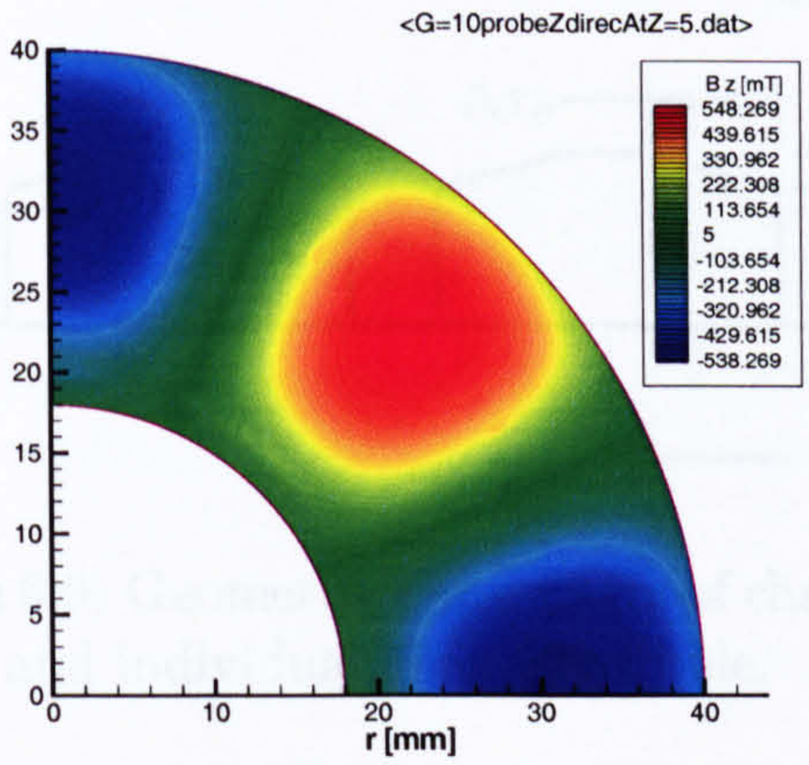
Figure 6.6: Field vector plot at $z = g/5$.

6.3.2 Shaped Poles

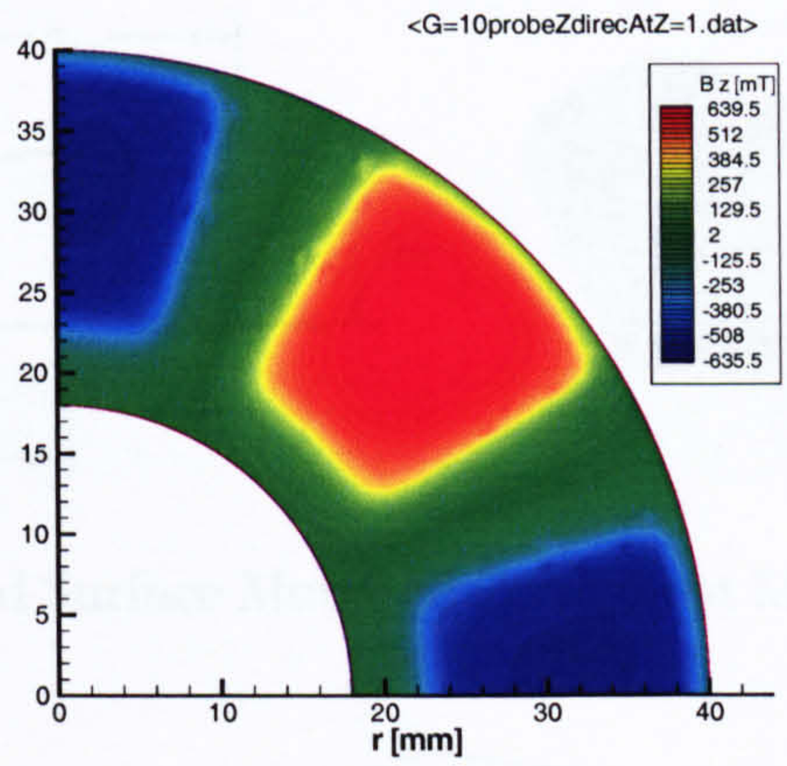
Shaped pole caps on electromagnets change the airgap flux density waveform, altering the flux distribution and airgap reluctance according to the rotor position θ. Pole caps are not employed on Surface Mounted Permanent Magnets, as the airgap reluctance is maintained. However, shaping poles with unity relative permeability changes the airgap flux distribution but does not change the airgap reluctance. The rotors manufactured with new pole shapes are poles with chamfered edges.

The analytical expression for the harmonic components given in Equation (6.5) no longer holds. The magnitude of harmonic components in the airgap flux density waveform with respect to chamfered edge dimensions for an 8-pole array with pole pitch and aspect ratios of 0.667 and 0.270 respectively, were obtained from eighty 2D FEM models. The chamfered edge dimensions ranged from 0 to 1 for $2\Delta\tau_m/\tau_p$ and $\Delta h/h_m$. It was found that the fundamental harmonic B_{z1} increased in magnitude by around 4% due to reduced fringing. The harmonics 3–9 were found to remain the same or reduce, although the 5th increased slightly. However, the harmonic magnitudes depend on the pole pitch ratio, so variation in this requires recalculation of the harmonics.

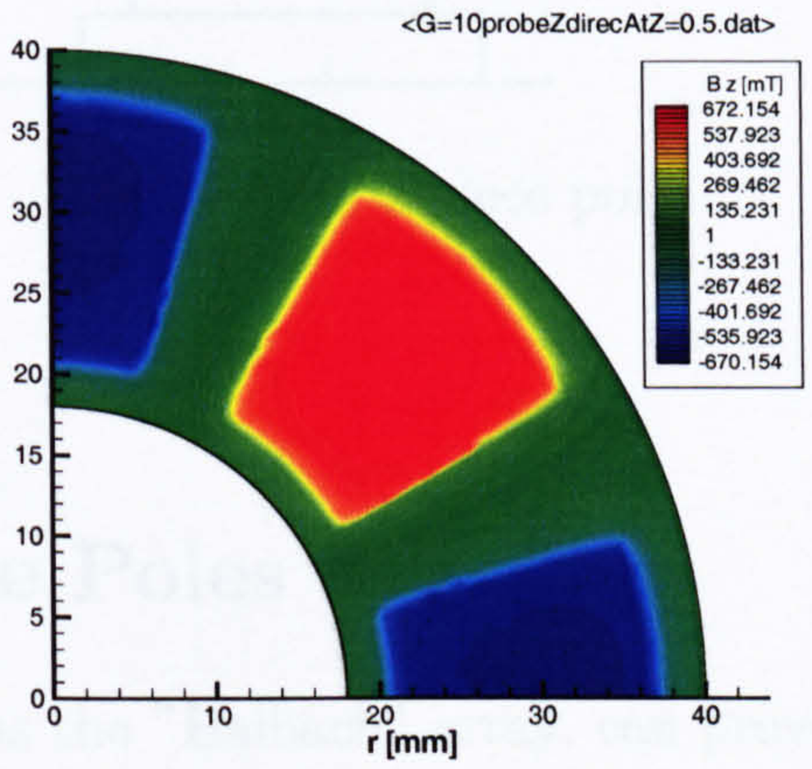
The chamfered pole is a reduction in the PM material towards the pole edges. Figure 6.10 illustrates the use of two PM pieces per pole with similar material reduction to the chamfer. This facilitates a constant "chamfer ratio" with varying radius, illustrated in the 3D view. The manufacture of this pole shape in small quantities is easier than the chamfer, but the rotor assembly with multiple layers



(a) $z = g/2$, mid-airgap

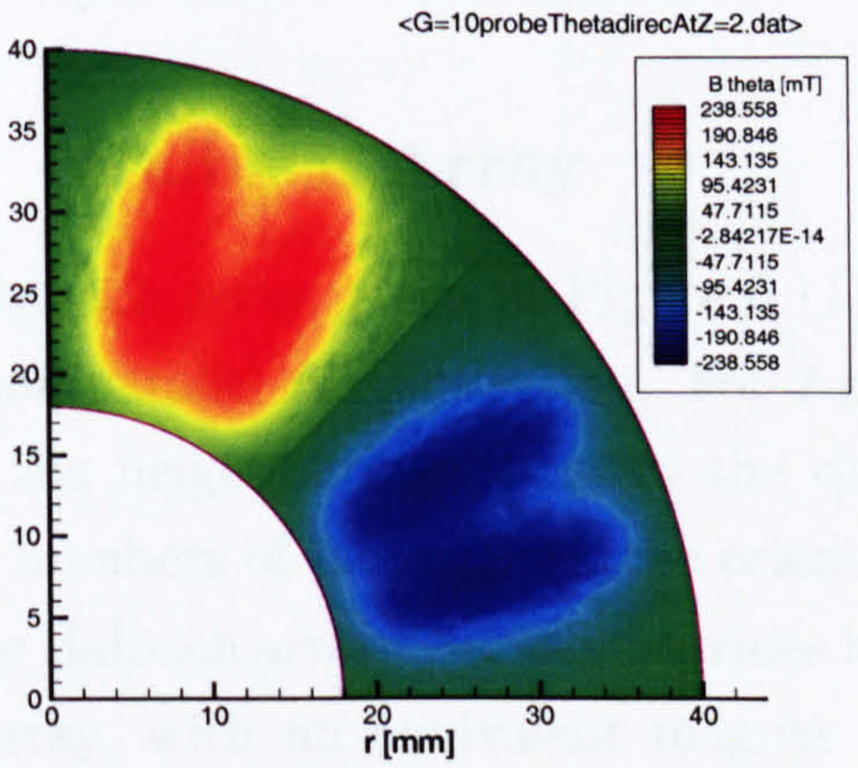


(b) $z = g/10$, near rotor surface

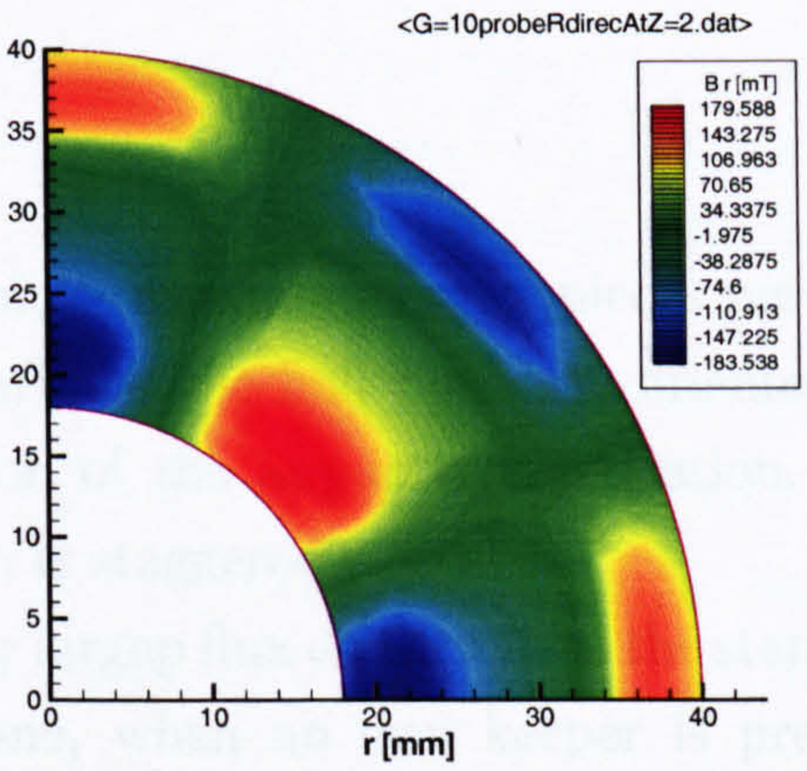


(c) $z = g/20$, nearest rotor surface

Figure 6.7: Measurement of airgap field B_z.



(a) B_θ



(b) B_r

Figure 6.8: Measurement of airgap field at $z = g/5$.

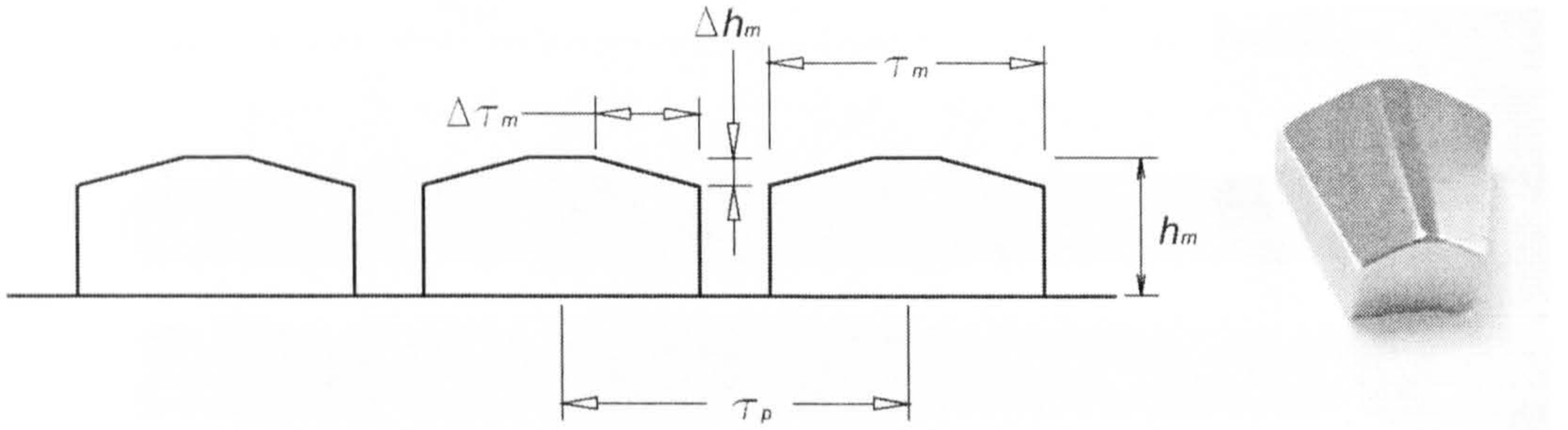


Figure 6.9: Geometric parameters of chamfered Surface Mounted Permanent Magnet poles, and individual chamfered pole.

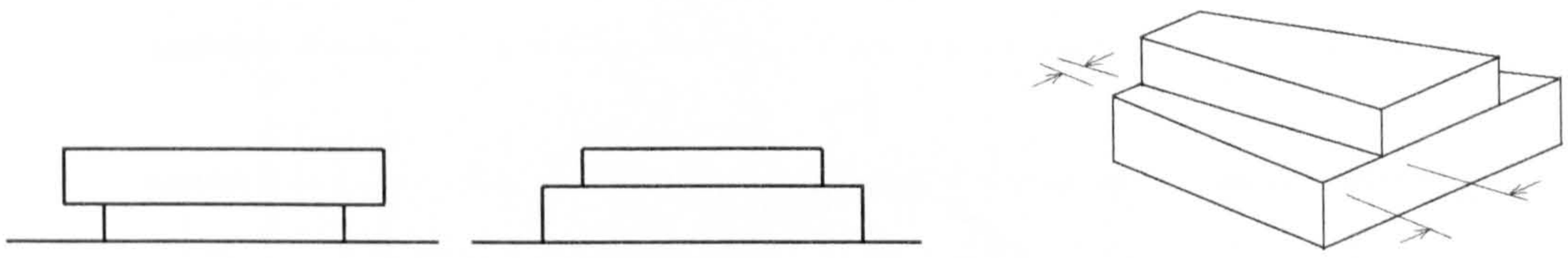


Figure 6.10: 2-piece poles.

can be difficult.

6.4 Multi-piece Poles

Multi-piece arrays, such as the "Halbach" array, can provide a higher peak airgap field density or reduce the amount of active magnetic material used [Atallah and Howe, 1998]. A sinusoidal waveform for flux density variation can also be achieved [Ofori-Tenkorrang and Lang, 1995]. These advantages must be balanced with the complexity and cost of manufacture.

6.4.1 Halbach Array

The Halbach array, given in Figure 6.11, employs multiple magnet pieces per pole with non-parallel magnetisation. For 2-pieces/pole, the half poles are oriented towards the neighbouring poles, in the direction of the airgap magnetisation. For higher numbers of pieces/pole, the orientation is staggered.

The Halbach array typically provides higher airgap flux density than the standard pole array, with an equivalent magnet volume, when no iron keeper is present. However, in the norm, an iron keeper is present, and the standard array provides higher flux density for a low magnet volume while the Halbach is again superior at a high magnet volume, say $\tau_{Vol} > 0.8$ [Ofori-Tenkorrang and Lang, 1995].

For maximum airgap flux density with minimum rotor mass, Lovat et al. [1998]

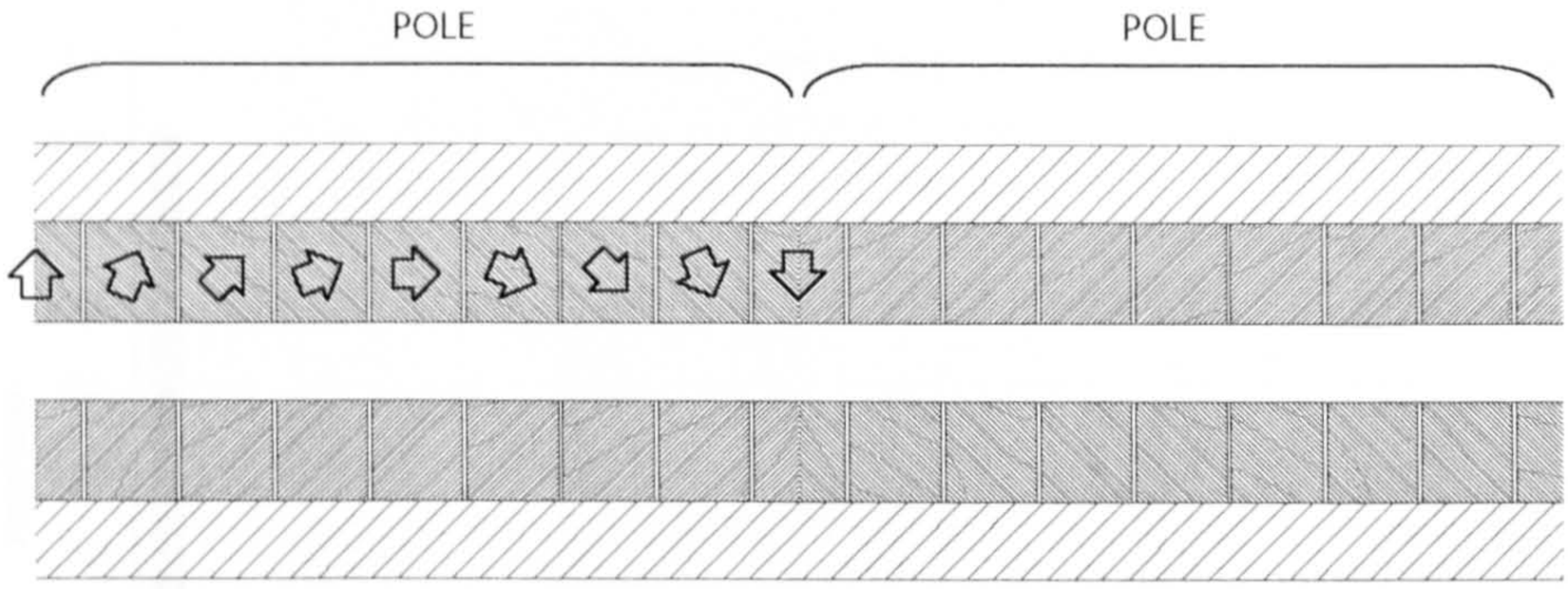


Figure 6.11: A Halbach array with 8 pieces/pole.

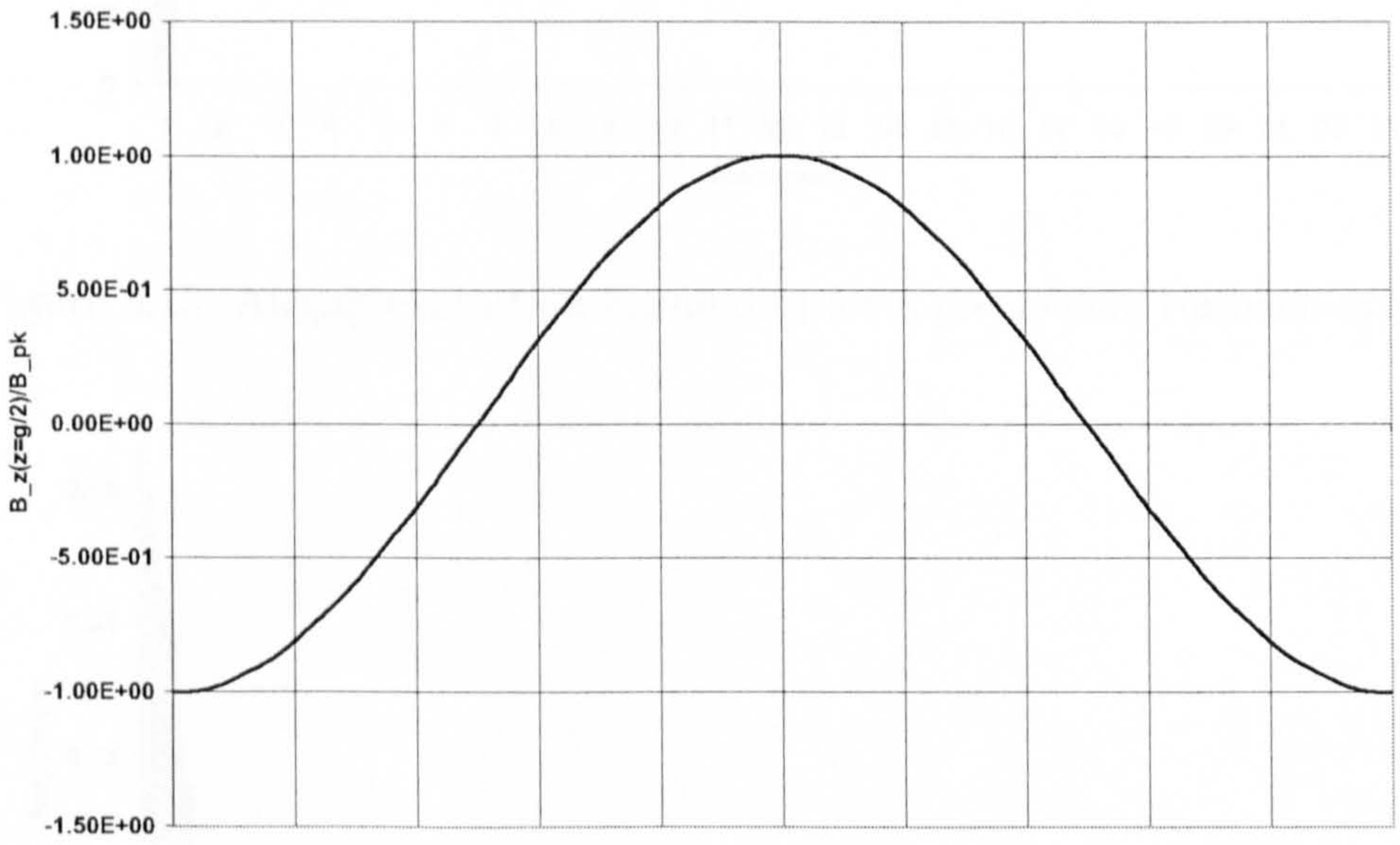


Figure 6.12: Airgap excitation waveform for 8 piece/pole Halbach array.

employed a Halbach array. The optimisation of maximum B_g increase for minimum number of magnet pieces was 4 pieces/pole. Although $Vol(PM)$ was not given, it was most likely unity, as there was no iron keeper used. The staggered magnetisation angles were 30° and 60° to the $z-$direction.

The harmonic components in the Halbach array excitation waveform are less with increasing pieces/pole. The harmonics present are $n = i * 2\text{piece/pole} \pm 1$. The magnitude of all others is less than 0.01 pu. This is shown in the example 8 piece/pole array given in Figure 6.11, where the waveform components given in Figure 6.13 are present at $n = 15$ and 17. These components grow in magnitude with larger gaps between the pole pieces.

As Lovat et al.'s [1998] optimised selection was 4 pieces/pole, this was selected to examine $Vol(PM)$. Figure 6.14 illustrates the magnitude of the harmonic components for arrays with different gaps between the individual pieces/pole, but defined

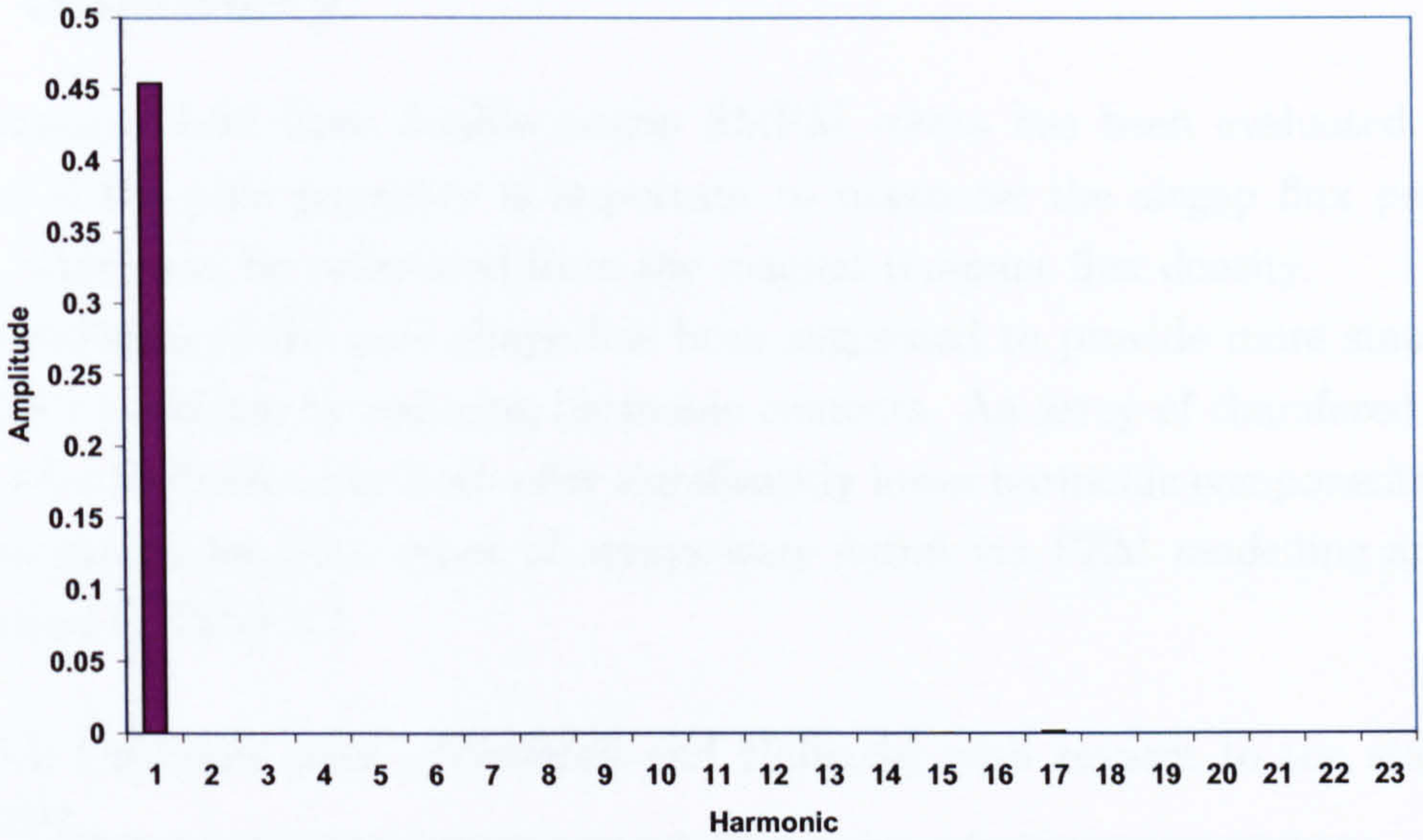


Figure 6.13: Airgap excitation harmonics for 8 piece/pole Halbach array.

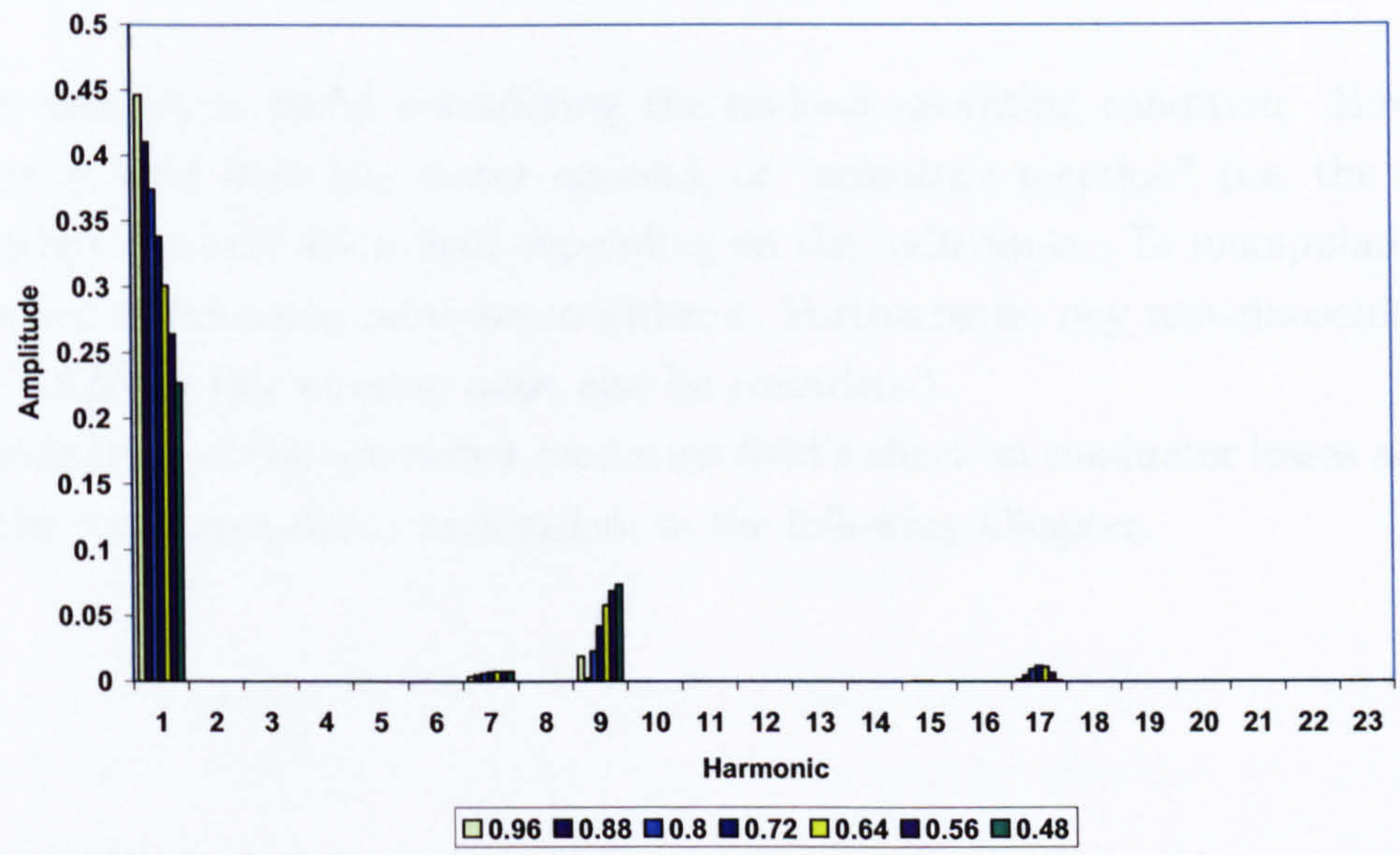


Figure 6.14: Harmonics in airgap excitation waveform for 4 piece/pole Halbach array with respect to volume of PM material.

by the proportional volume of PM material. 1.0 has no inter-pole gaps.

Figures 6.13 and 6.14 indicate no inter-pole gaps are desirable for minimum harmonic components. This contrasts with the single piece poles, where k_{ppitch} determines $Vol(PM)$ and $k_{ppitch} = 2/3$ is preferred.

6.5 Summary

The excitation field from double airgap SMPM rotors has been evaluated. The selection of the pole geometry is important to maximise the airgap flux per unit volume, which can be calculated from the magnet remnant flux density.

Manipulation of the pole shape has been suggested to provide more sinusoidal airgap field waveform by reducing harmonic contents. An array of chamfered single pieces and a Halbach array both offer significantly lower harmonic components. The optimum shapes for both types of arrays were found via FEM modelling and are summarised in Table 6.1.

Table 6.1: Optimum pole (chamfered and Halbach) with respect to the standard sector pole

Pole	$2\Delta\tau_m/\tau_p$	$\Delta h/h_m$	τ_{Vol}	$Ave(\phi_{tot})$	$\lvert\hat{B}_z\rvert$ [p.u.]
Plain	0.0	0.0	1.0	1.0	1.0
Optimum Chamfer 1	0.6	0.2	0.94	0.99	1.04
8-piece/pole Halbach	-	-	1.0	1.1	1.0

This analysis is useful considering the no-load operating condition. However, the reactive field from the stator on-load, or "armature reaction" (i.e. the stator mmf), alters the excitation field depending on the inductance. To manipulate this, the winding distribution must be considered. Furthermore, any non-sinusoidal line current profile in the winding must also be considered.

Examination of the controlled excitation field's effect on conductor losses according to the conductor size is undertaken in the following Chapter.

Chapter 7

Conductor and Coil Geometry for Airgap Winding Study

This chapter considers conductor sizes and shapes, and coil geometries for the Axial Flux machine with a slotless core airgap winding. Following the last chapter's description of minimising excitation field harmonics with the distribution of magnet material, the slotless core offers minimum harmonics as the airgap permeance is constant. Winding distribution harmonics can initially be ignored, until the coil design is determined. However, the conductors are exposed to the full varying excitation flux so it is important to select the correct conductor size and shape to minimise eddy current losses.

7.1 Current and Copper Losses

The electrical losses relate to the excitation waveforms considered in Chapter 6. Copper is the standard wire material for electric machine windings, due to a high electrical conductivity at standard operating temperatures. Other wire materials such as high temperature superconductors, which require large cooling systems, or ceramic conductors, which operate at an elevated temperature, are growing in interest, but copper continues to be the standard conductor material and is employed here.

Text books, such as Sen [1997] and Sadarangani [2000], provide fuller explanations of conductor theory than included here, while those such as Hammond [1997] and Lammeraner and Stafl [1966] provide complete derivations of skin effect and ac resistance.

7.1.1 Conductor Current Density

A conductor with cross sectional area A has a potential difference ΔV across its length l_c (resulting from the electric field E), which causes current I.

While electric conductivity σ_{elec} remains constant, the conductor current density J_c varies proportionally with the electric field $J_c = \sigma_{elec}E$. The cross sectional area is related by:

$$J_c = \sigma_{elec}E = \sigma_{elec}\frac{\Delta V}{l_c} = \frac{I}{A} \tag{7.1}$$

From Equation (7.1), harmonic components in ΔV result in harmonic components in the current.

7.1.2 Stator Current Loading

The current loading S is the product of conductor current and number of conductors per unit length around the stator (N_{tot}/l_s), as given in Equation (7.2). The current loading is limited by temperature and the thermal resistance of the insulation material. For small motors, S is typically in the range $15 - 50$ kA/m [Hanselman, 2003].

$$S = \frac{QN}{l_s}I \tag{7.2}$$

As illustrated in Figure 7.1, there is no single value for current loading of the Axial Flux machine. S is maximum at the inner radial position $r = r_i$, but, as S is required to evaluate machine performance and cooling requirements to remain within operating temperature limits, the inner radial position is too close to end windings to be used. A more representative single value for S is found at either the mid-radius or the mid area; $r = (r_o + r_i)/2$ or $(r_o^2 + r_i^2)/2(r_o - r_i)$ respectively, while S reduces linearly from r_o to r_i.

7.1.3 Conduction Loss

The inverse of the electrical conductivity of the wire material, which determines the conductor current, is electrical resistivity ρ_{elec}. Joule-effect heating is a power loss for dc current in the conductor, which is proportional to the conductor resistance R_c. Conductor resistance, according to the material electrical resistivity, is temperature dependent:

$$R_c = \frac{\rho_{elec_ref}l_c}{A}\left(1 + \alpha_{\rho_{elec}(T)}(T - T_{ref})\right) \tag{7.3}$$

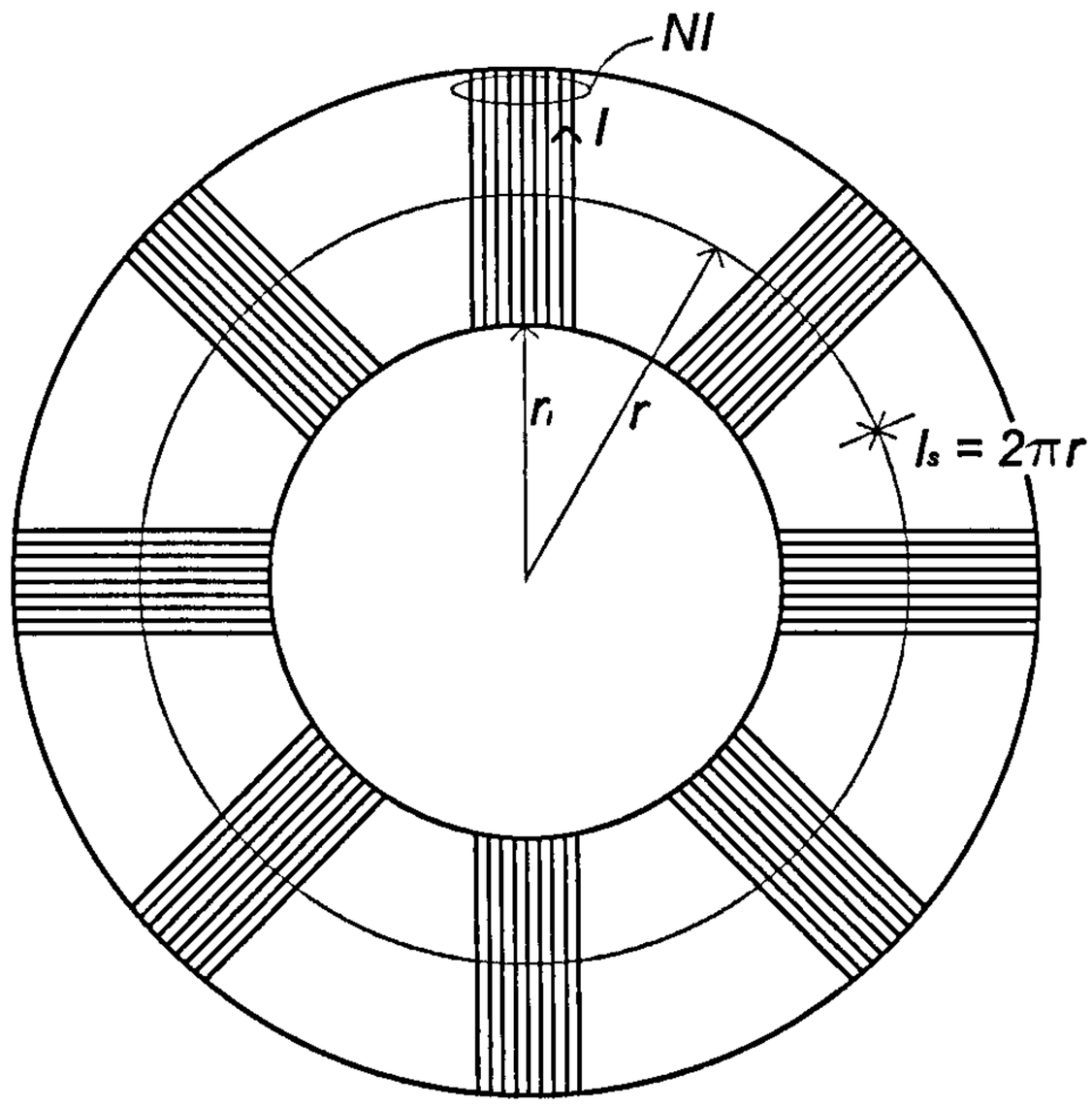


Figure 7.1: Current loading for an Axial Flux stator.

where $\alpha_{\rho_{elec}(T)}$ is the temperature coefficient of electrical resistivity for the conductor material at temperature T.

Equations (7.1) and (7.3) give the familiar version of Ohm's Law: $\Delta V = IR$. The conduction power loss is therefore given by:

$$P_{cond}^{loss} = VI = I^2 R_c \tag{7.4}$$

7.1.4 Skin Effect and AC Resistance

The moving current in the conductor effectively gives the magnetic field energy inertia, leaving a hysteretic current distribution track, which depends on material resistivity [Stoll, 1974; Krawczyk and Tegopoulos, 1993]. The skin effect is the tendency for alternating current to flow near the surface of the conductor, rather than evenly across the full cross sectional area of the conductor. This causes the effective resistance of the conductor to increase, as the current experiences a smaller cross sectional area. This is important in large conductors or operation at high electrical frequency.

The "skin depth" or "penetration depth" δ_p is useful to describe the distance from the conductor surface, where the field experiences a defined level of attenuation and current is concentrated:

$$\delta_p = \frac{1}{\sqrt{\pi \mu_0 \mu_r f \sigma_{elec}}} \tag{7.5}$$

where f is the electrical frequency in Hz. With harmonics in the current with respect to time, δ_p can be calculated for multiples of f.

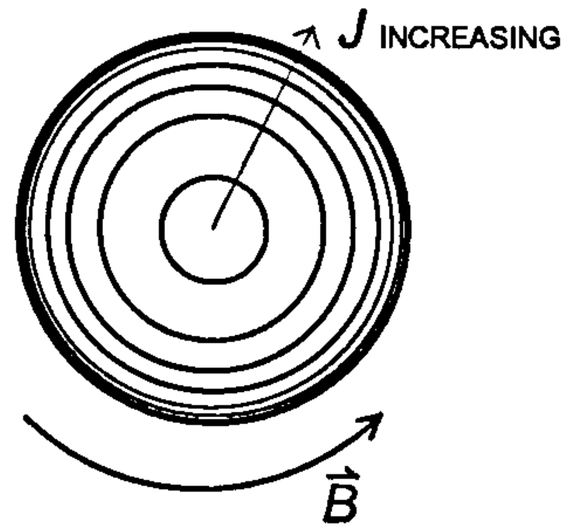


Figure 7.2: Skin effect due to alternating current.

Figure 7.2 illustrates the skin effect, which concentrates current nearer the conductor surface, reducing the effective cross sectional area and increasing the current density J_c. This results in higher conduction loss through Equation (7.4).

Conductors in close proximity also affect the conduction loss, , due to internal proximity effects. Equation (7.4) may be modified to $P_{cond}^{loss} = k_{T_air} I^2 R_c$ where, for m_c layers of conductors in air:

$$k_{T_{air}} = 1 + (m_c^2 - 0.8)h'^4/36 \qquad 0 \leqslant h' \leqslant 1 \tag{7.6}$$

The actual conductor resistance is no longer the dc resistance. $R_n = \kappa_n R$ employs the "skin effect correction factor":

$$\kappa_n = \frac{\xi_n}{2}\left[\frac{\sinh \xi_n + \sin \xi_n}{\cosh \xi_n - \cos \xi_n}\right] \tag{7.7}$$

where $\xi_n = \sqrt{2b_c^2 f_{elec_n} \mu_{Cu} f_{Cu}}$.

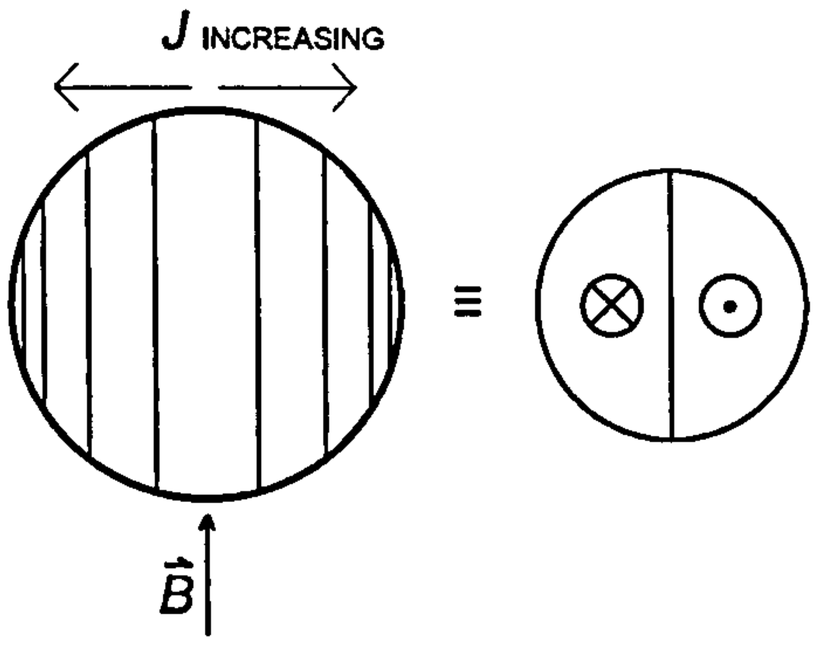
7.2 No-load Losses

7.2.1 Eddy Current Losses

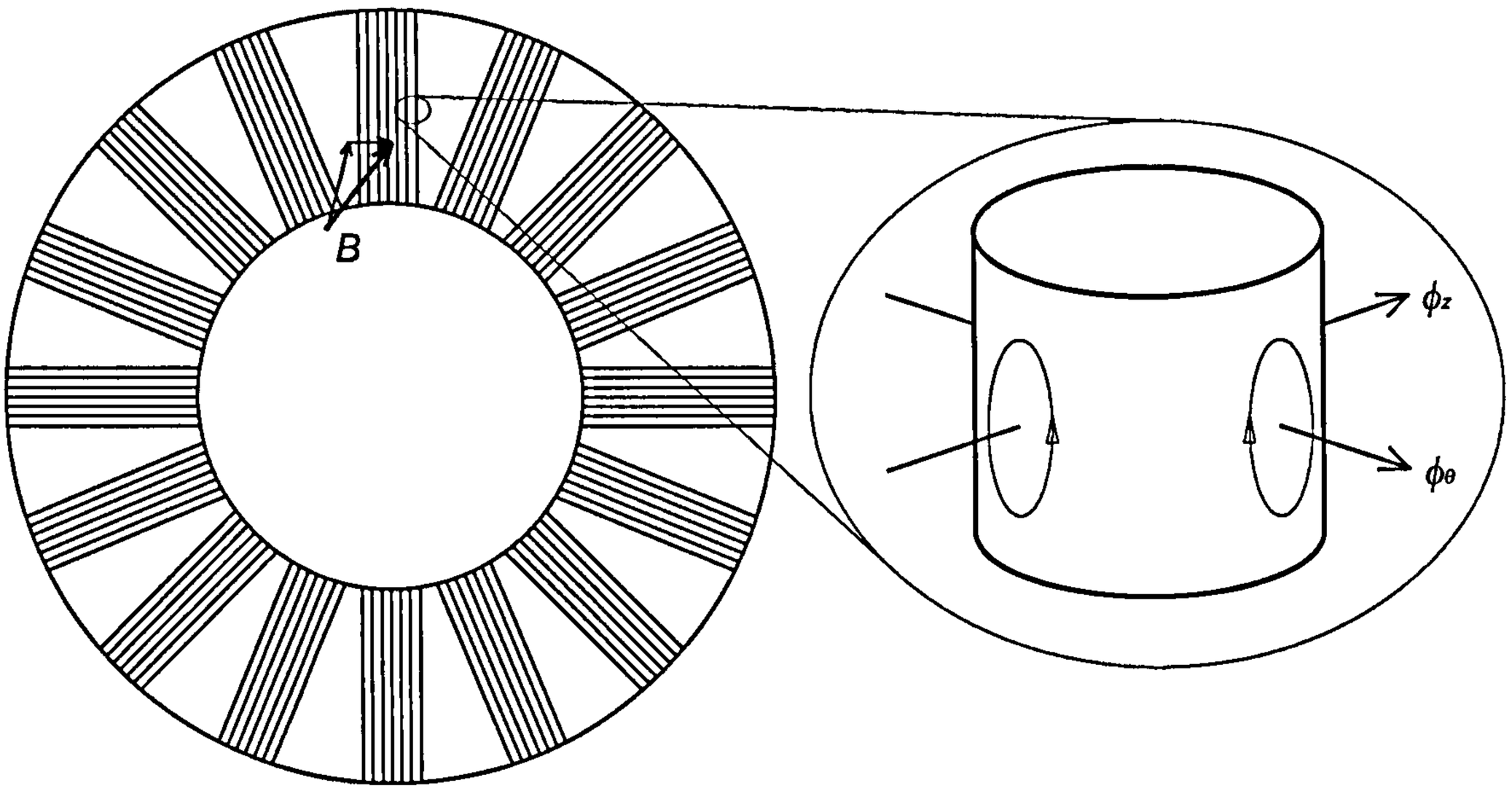
The alternating external field creates eddy currents, which flow to oppose the external field, as seen in Figure 7.3(a).

There is no change in net conductor current as these eddy currents have equivalent contribution. However, they do produce a power loss P_{EC}^{loss}.

Without skin effects, the distribution of eddy currents is equivalent in all conductor layers. With skin effects eddy currents reduce, if the penetration depth is less



(a) Eddy currents arising due to an alternating external field.



(b) The eddy currents produce a field to oppose the excitation field.

Figure 7.3: Eddy currents in airgap winding conductors.

than the conductor size. Assuming the conductor size is less than the penetration depth, the time-averaged power dissipation of the winding with round conductor radius r_c is:

$$P_{EC}^{loss}(\text{round}) = \frac{\pi}{4}\sigma_{elec} l_c \omega_{elec}^2 B^2 r_c^4 \tag{7.8}$$

Lovat et al. [1998] quote half this expression as the eddy current power loss from the conductor active length. For rectangular conductors, Lammeraner and Stafl [1966] and others give the eddy current power loss based on the conductor width b_c (the side exposed to the excitation field) and conductor depth d_c:

$$P_{EC}^{loss}(\text{rect.}) = \frac{1}{6}\sigma_{elec} l_c \omega_{elec}^2 B_{pk}^2 b_c^3 d_c c \tag{7.9}$$

where c is an empirical coefficient related to the conductor aspect ratio (b_c/d_c).

The excitation field varies across the airgap and conductors at different axial positions experience different axial and tangential flux components, as shown in Figure 7.3(b). For airgap windings, Wang and Kamper [2002] established that P_{loss}^{EC} must be evaluated for each conductor individually.

7.2.2 Open Circuit Operation

The eddy currents resulting from the higher spatial harmonic components in the alternating external field exist, while the machine operates in the open circuit condition.

These are the no load electrical losses. The no-load losses are particularly relevant to PM machines in HEV powertrains, as the excitation field is always present and the duty cycle of an HEV application often requires that the machine rotates with open circuit or low load operation. The Figures of duty cycles in Chapter 2 illustrate such periods where the vehicle is stationary $(u = 0)$.

7.3 Optimal Conductor Geometry

The waveforms of both the axial and tangential components of the excitation field dictate the conductor eddy current power loss. To evaluate this loss on conductors with various geometries, selected measurements have been performed. These measurements were reported in Walker [2003*a*].

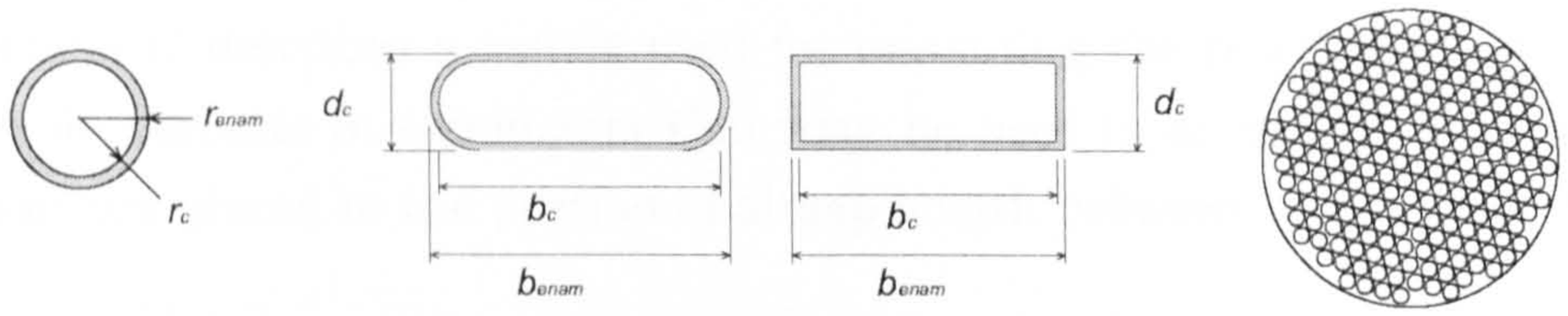
Equations (7.8) and (7.9) were based on a sinusoidal excitation field at the electrical frequency ω_{elec}. To assess the effect of all excitation field harmonic components, these expressions are repeated using the magnitude and frequency and summed for the total eddy current power loss.

7.3.1 Conductor Shape

The common conductor shape in low voltage machines is round wire. Other shapes are shown in Figures 7.4(b), (c) and (d).

The bare wire radius r_c is used to size round wire and the enamel radius r_{enam} is used for the conductor packing factor.

Flat wire is produced by flattening round wire. For example, standard sizes are 5x1.5 mm and 4x1.25 mm, flattened from round wire with $r_c = 1.5$ and 1.25 mm respectively. For both flat and rectangular wire, the dimensions b_c and d_c are used



(a) Round conductor (b) Flat conductor (c) Rectangular conductor (d) Litz wire

Figure 7.4: Conductor geometries, showing copper and enamel

together with the axial and tangential flux density components for sizing according to the conductor orientation. These conductors are considered in this study.

Litz wire consists of many individually insulated strands (typically > 100). The current is equal between strands, provided the combination of twists and end turns ensures all strands are of equal length [Lampérth, 2000]. Litz wire with the same total copper has lower AC losses than the round, which is important at higher operating frequencies, but more enamel is present so the space occupied by the conductor volume is greater, reducing the fill factor.

Etched conductors have also been examined for Axial Flux machines. Hanitsch et al. [1994] presented a 4-layer etched stator and conductors with dimensions 0.4x0.1 mm (active length 70 mm).

7.3.2 Conductor Eddy Current Measurements

The measurement on the arrays of conductors, such as shown in Figure 7.5, were reaction torque measurements, as illustrated in Figure 7.6(a). The mechanical speed of the excitation field was used to calculate the eddy current power, illustrated in Figure 7.6(b).

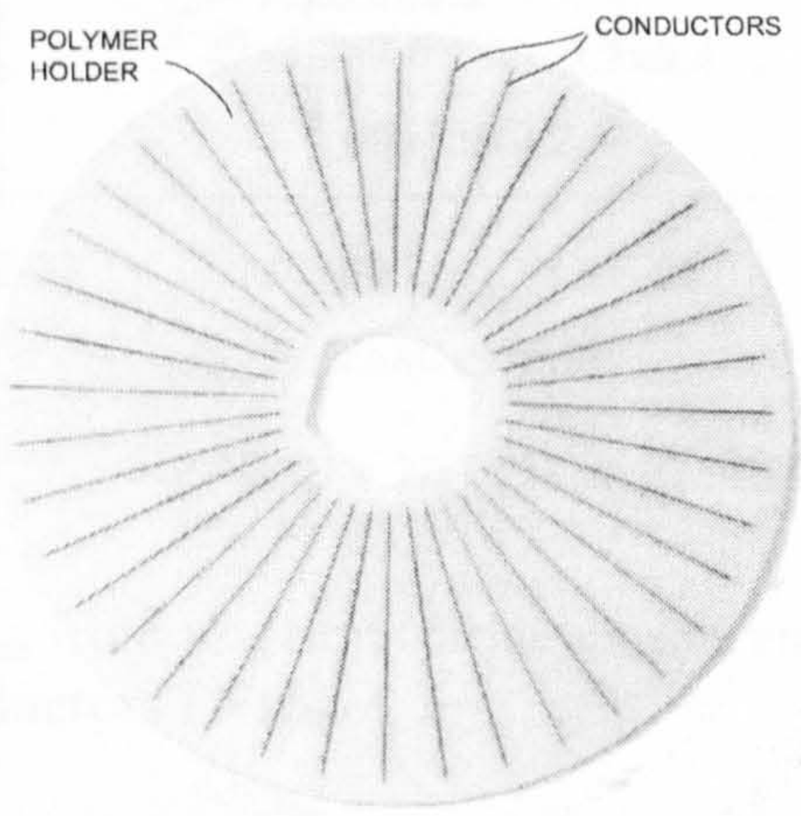
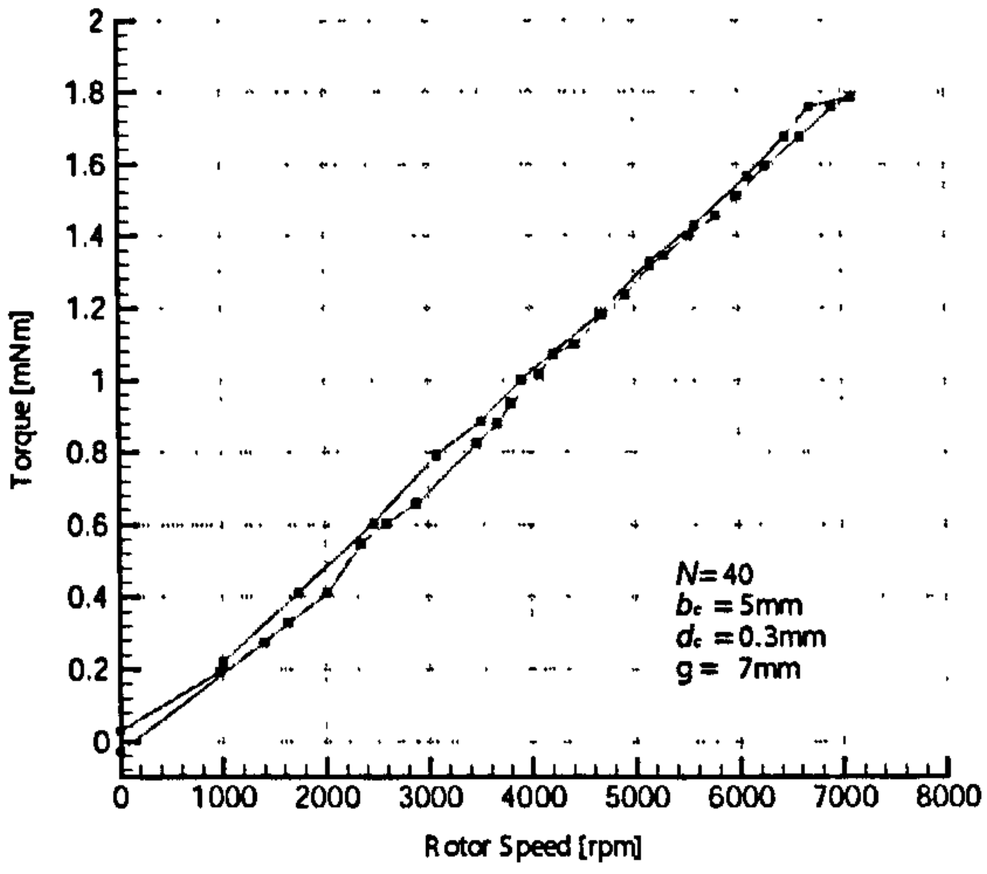
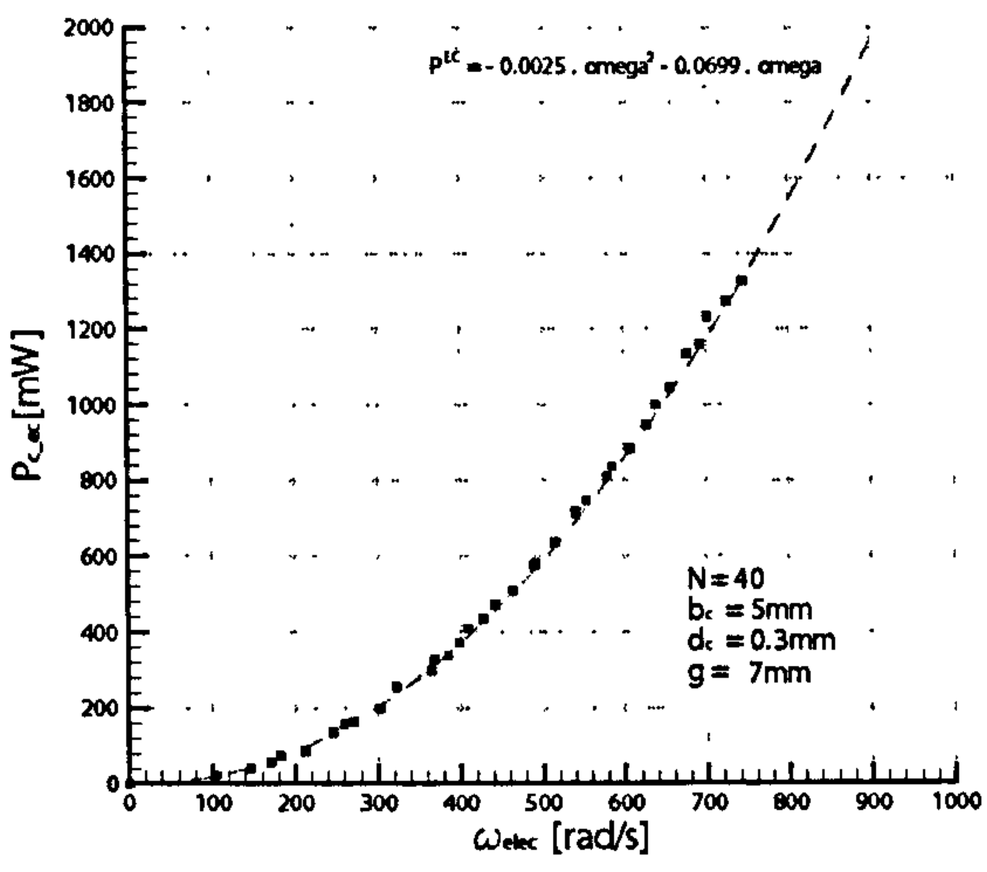


Figure 7.5: Array of selected conductors in a polymer holder.

Appendix C describes a testrig used for measuring the reaction torque caused by the eddy currents in conductors that may be used in an airgap winding. The conductors are placed in the portion of airgap length between $z = g/5$ and $4g/5$.



(a) measured T



(b) calculated P_{EC}^{loss} from T measurements

Figure 7.6: Testrig torque measurements and calculated P_{EC}^{loss}

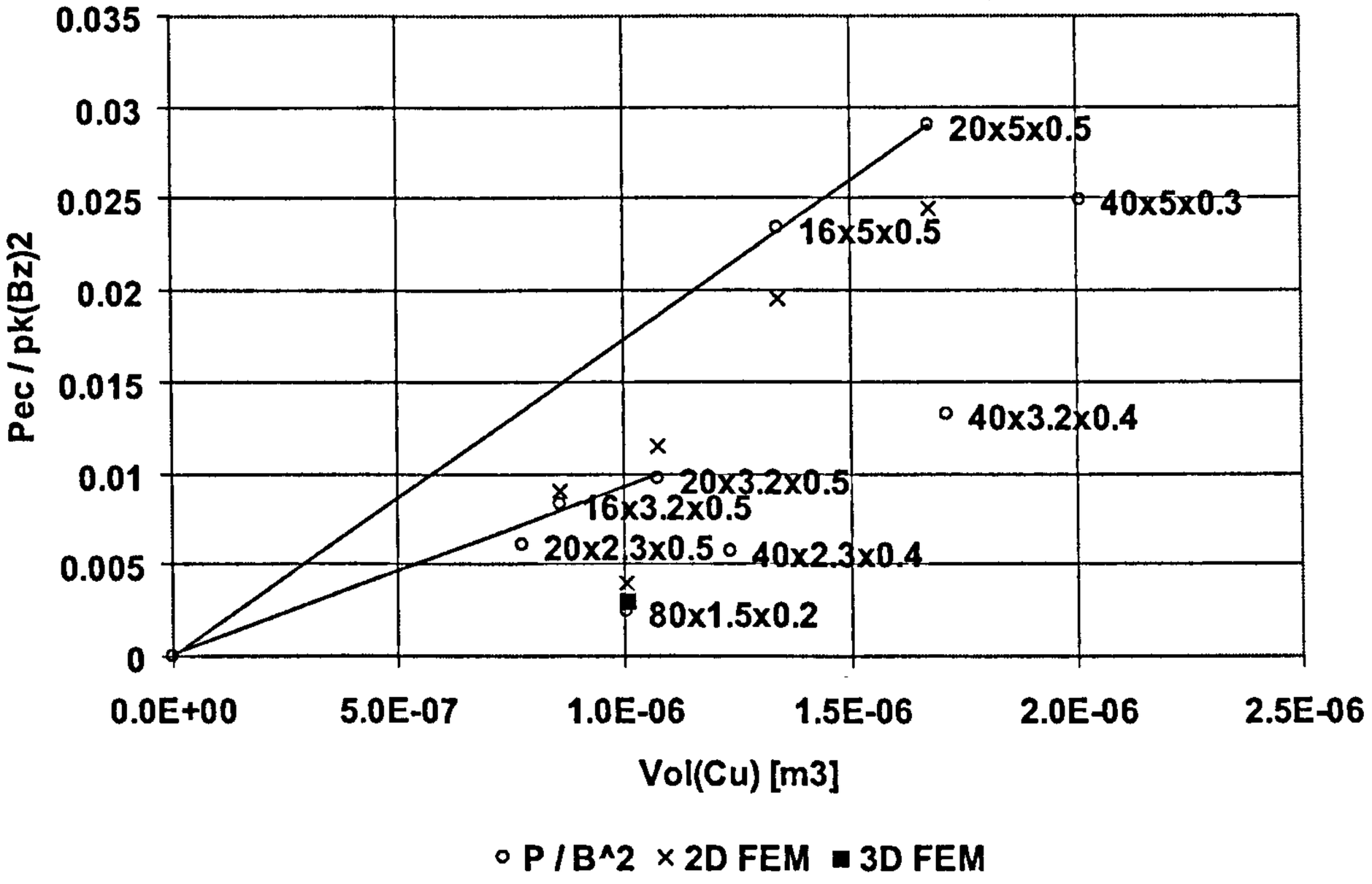


Figure 7.7: Calculated P_{c_ec} from reaction torque measurements and FEM at 200 Hz for selected arrays of conductors (Nxb_cxd_c).

The interaction between the field arising from eddy currents caused by the alternating external field and the field itself induces the torque. The conductors are

suspended on a torsion spring, which allows an angular deflection proportional to the applied torque. The angular deflection is measured, and the torque and mechanical speed used to calculate the eddy current power loss.

Figure 7.7 provides the results for selected arrays of N conductors of size b_cxd_c with equivalent l_c throughout. These are presented with eddy current power normalised against the square of peak axial flux density $\hat{B}_z^2$. The electrical frequency is the same for each. The lower right-hand region of the plot indicates low eddy current power loss for a larger volume of copper, which is desirable. Conductors were oriented such that the excitation field $z-$component encountered the smaller conductor dimension d_c. However, the results indicate that the larger conductor dimension b_c has a significant impact on eddy currents.

7.3.3 FEM Computation of Eddy Currents

The calculation of eddy current losses is complex, but may be achieved numerically using 3D FEM. A model constructed with the software MEGA [U. of Bath, 1996] is shown in Figure 7.8. This was used to control the measurement result for the 80x1.5x0.2 conductor array shown in Figure 7.7, with $< 10\%$ deviation.

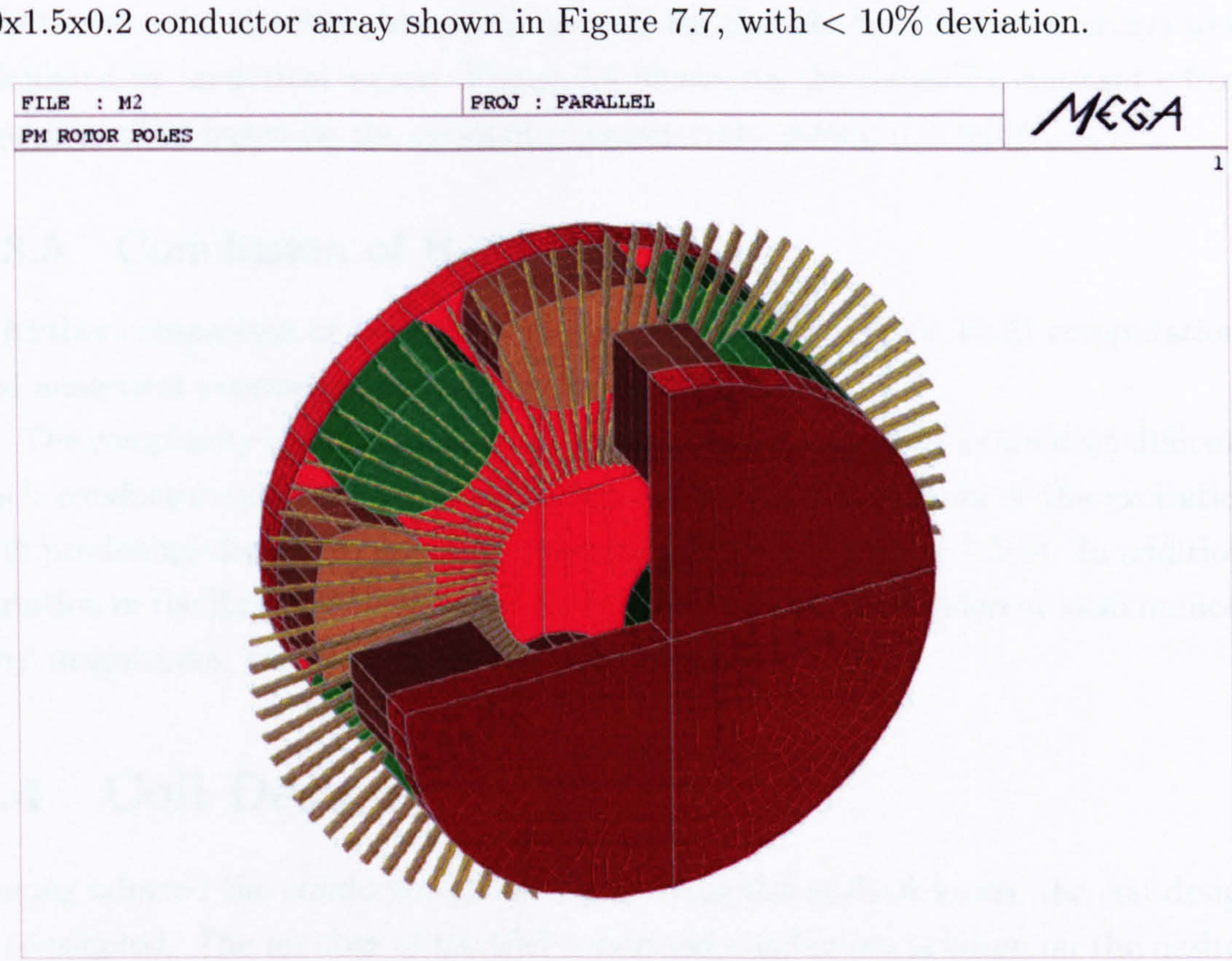


Figure 7.8: MEGA model of the 80x1.5x0.2 conductor array and rotors.

7.3.4 Eddy Current Calculations

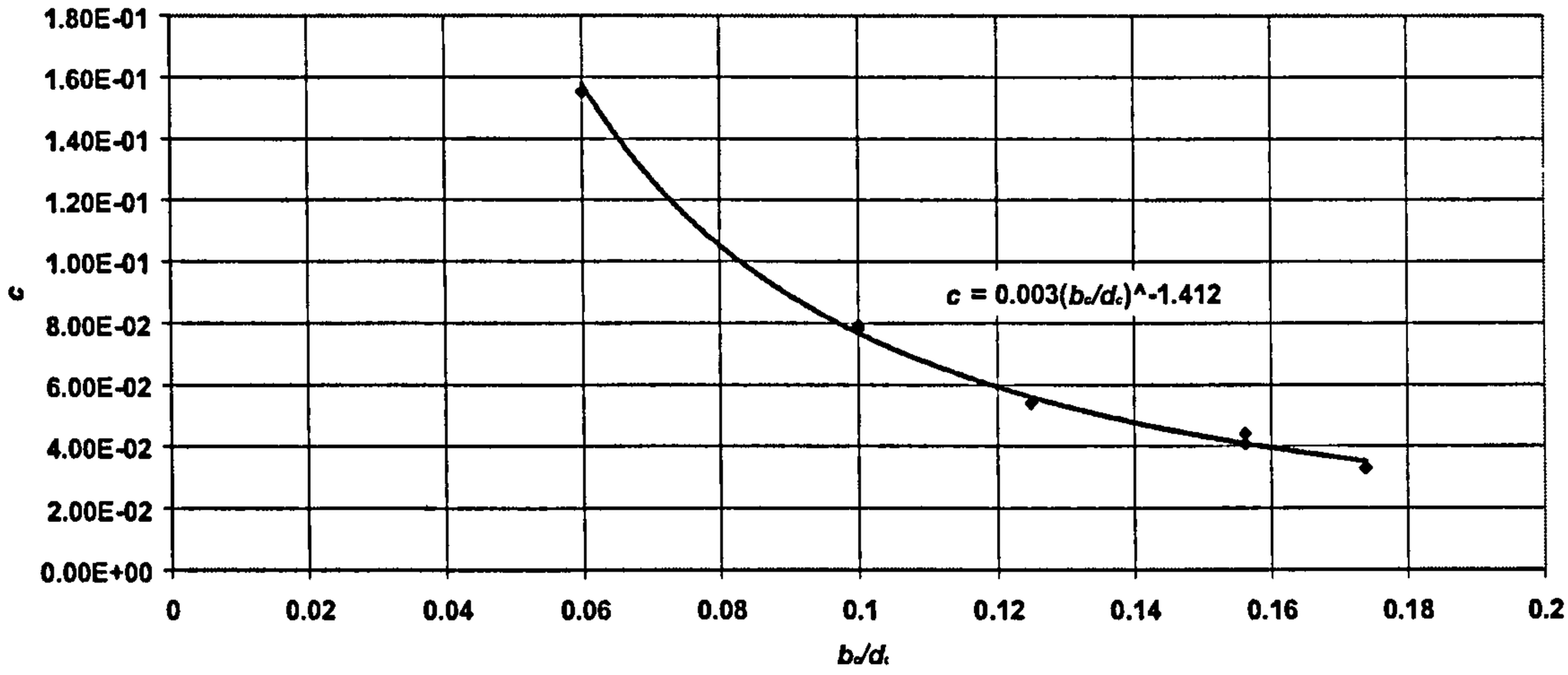


Figure 7.9: Constant c for Equation (7.9) from measurements.

Using the amplitude and frequency of the harmonic components of the excitation field in the axial direction, the eddy currents for the selected conductor arrays were calculated by analytical means. Figure 7.9 illustrates the values for constant c from Equation (7.9) based on the conductor aspect ratio, giving $c = 3\text{e-}3(d_c/b_c)^{\sqrt{2}}$.

7.3.5 Conclusion of Results

A further comparison of the results obtained by measurements, FEM computations and analytical expressions is given in Figure 7.10.

The complexity of the eddy current problem makes analytical evaluation difficult. Each conductor experiences the axial and tangential components of the excitation field producing the conductor eddy currents as shown in Figure 7.3(b). In addition, variation in the flux density between $z = g/5$ and $g/2$ produce different local induced emf magnitudes, resulting in further eddy currents.

7.4 Coil Design

Having selected the conductor geometry, limiting the no-load losses, the coil design is considered. The number of parallel connected conductors is based on the desired phase current and conductor current density limit.

The single airgap "air cored" winding machine topology requires a slotless core to return the main flux circuit, shown in Figure 7.11(a). The double airgap, internal

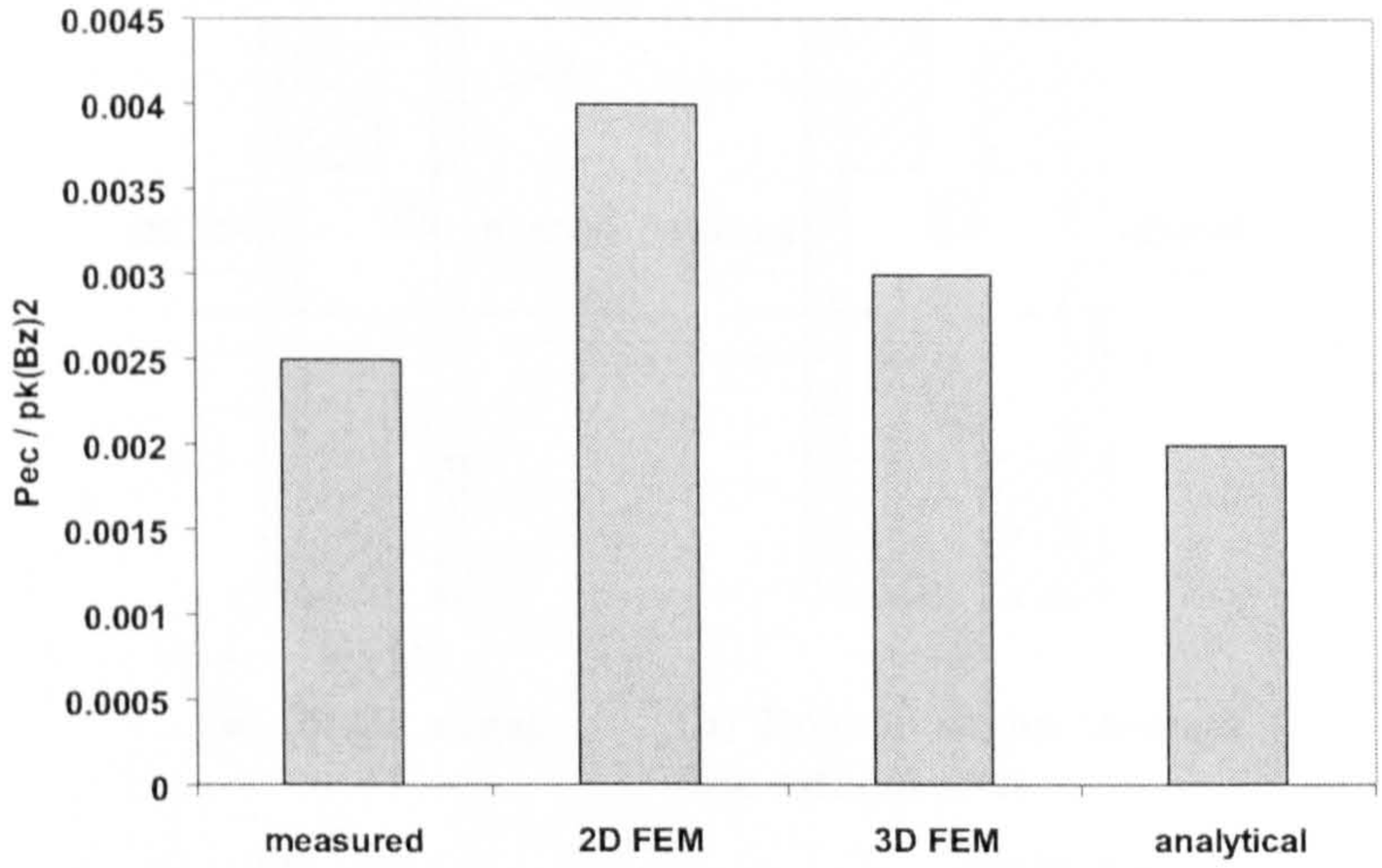


Figure 7.10: Comparison of eddy current calculations with measurements for the 80x1.5x0.2 conductor array, shown in Figure 7.7.

stator through flux topology has a winding mounted between rotors without or with a slotless core, shown in Figures 7.11(b) and (c), and the slotless Torus machine includes an iron core, shown in Figure 7.11(d). The Radial Flux version of the through flux airgap winding, shown in Figure 7.11(b), is the "basket motor" [Unique Mobility, 2002]. Similar coils may be used in all but the Torus machine.

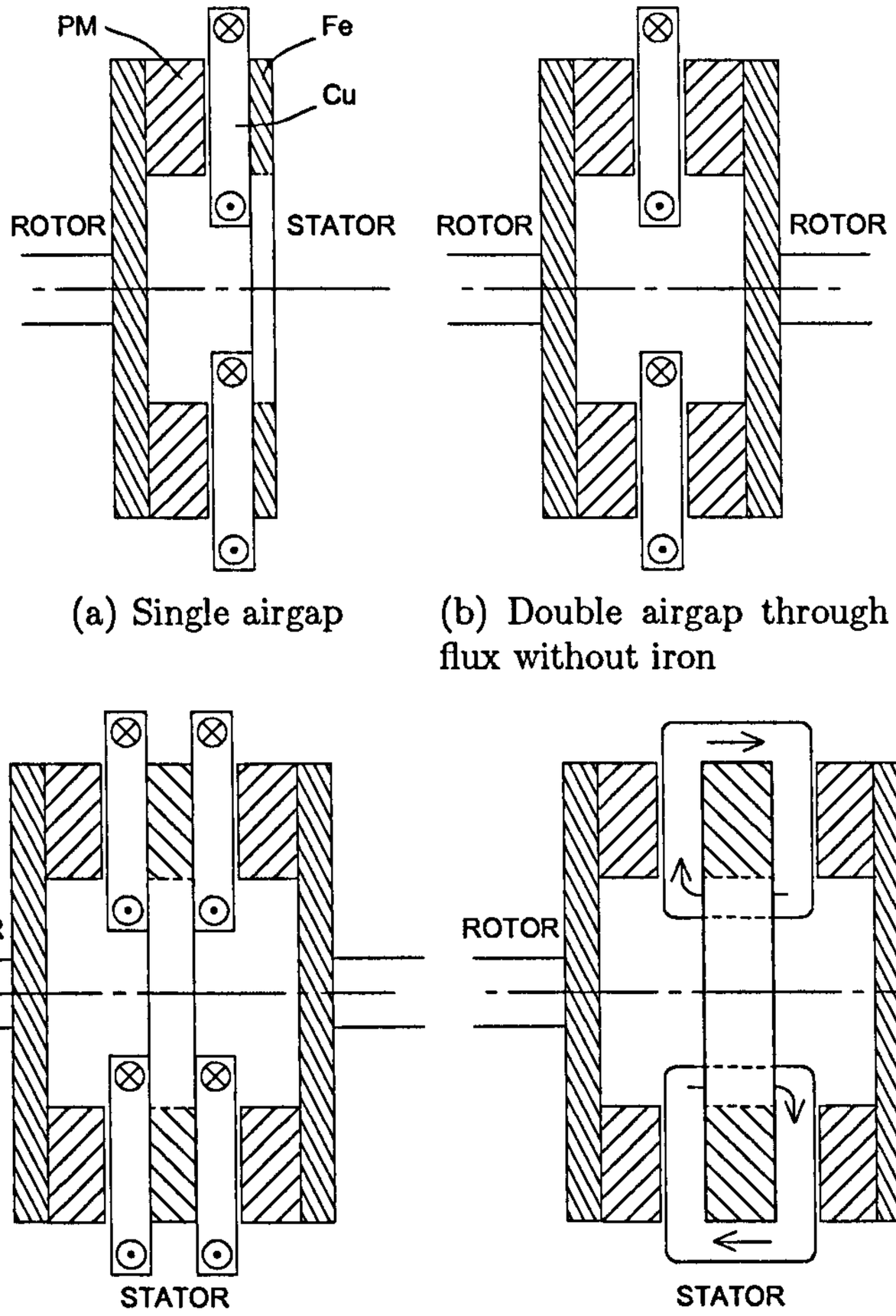
Due to shorter end windings, and the ease of manufacture, concentrated winding coils were selected for this study.

7.4.1 Concentrated Coil Geometries

The published multi-airgap Axial Flux machines with coreless airgap windings all have concentrated coil windings [El-Hasan et al., 2000; Hill-Cottingham et al., 2001; Turbo Genset Co., 2002]. Those using round wire make endturns and coil connections in the same $z-$position plane as the conductor active length, which overlaps and squashes the conductors. Those using flat wire interleave the coils by making endturns and coil connections in a different plane.

A patented concentrated coil geometry for the airgap winding shown in Figure 7.11(b), is the *Segmented Array* [Visual Computing Systems Corp., 1997], illustrated in Figure 7.12. The winding consists of nested (or "interleaved") coils with the active sides of each coil in the same $z-$position plane and endturns overlapping in a different plane.

Due to the compact nature of the overlapping endturns, the *Segmented Array* requires a further $r-\theta$ plane to make the coil connection from inside the coil.



(a) Single airgap

(b) Double airgap through flux without iron

(c) Double airgap through flux with slotless iron

(d) Slotless Torus

Figure 7.11: Axial Flux machines with airgap windings.

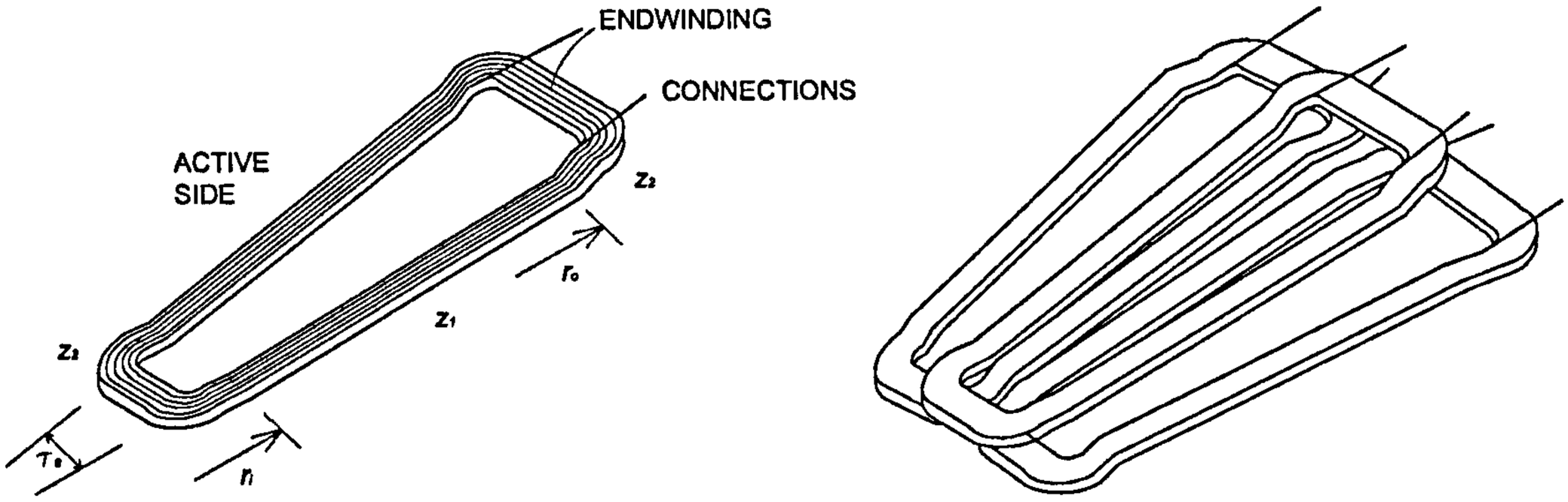


Figure 7.12: Patented *Segmented Array* concentrated coils [Visual Computing Systems Corp., 1997, orig.].

Figure 7.13 illustrates a concentrated coil proposed by Caricchi et al. [1998] for a nested winding with active sides in different planes. This Rhomboidal coil has shorter endturns, increasing the proportion of the coil length which is active length.

Between planes there is space for a cooling circuit, so angle α_{rh} was optimised according to r_o, r_i and τ_c to achieve this space yet maintain sufficient current.

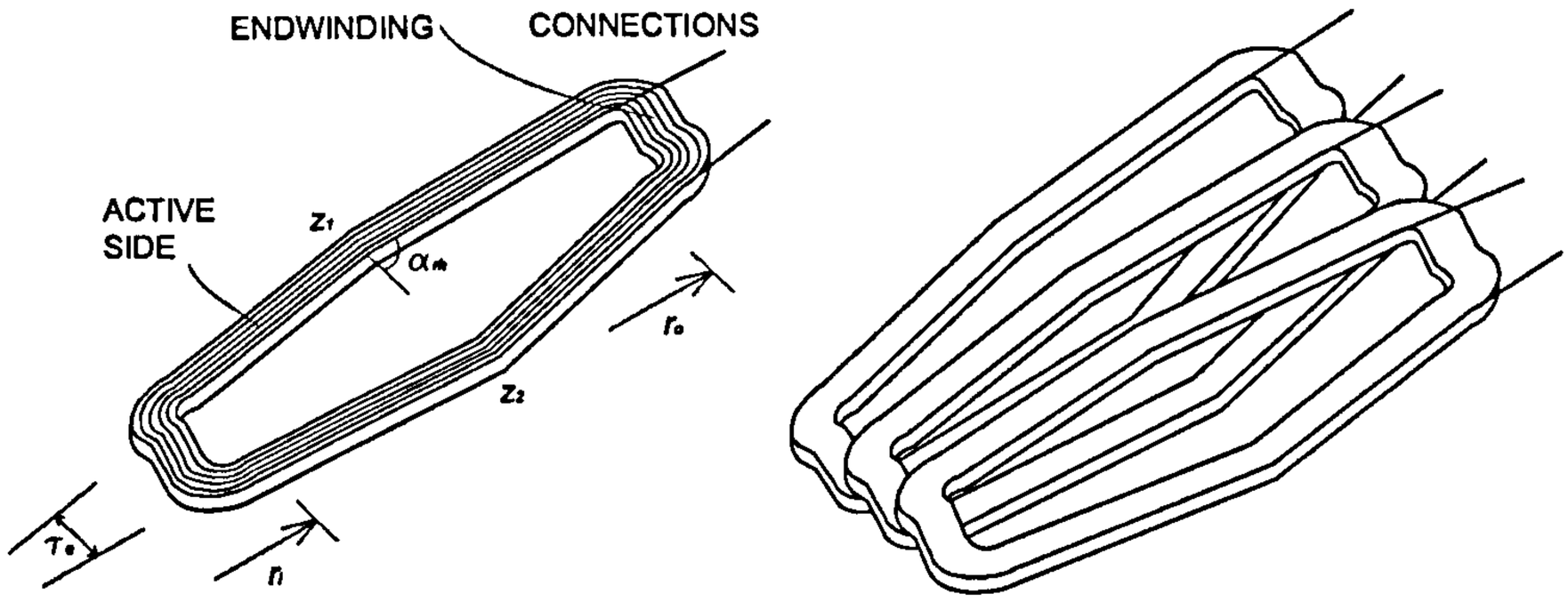


Figure 7.13: Rhomboidal concentrated coils.

The Rhomboidal coil has two planes for the overlapping endturns, providing space for the coil connections.

7.4.2 Proposed Coil

The coil illustrated in Figure 7.14 is an improved coil for such a winding, which avoids problems with coil connections.

The manufacturing of these proposed coils is documented in Appendix 8. Therefore, a coil is proposed for a coreless winding such as shown in Figure 7.11(b), which meets the nested characteristic of the *Segmented Array* winding and incorporates the easy connections of the 2-plane rhomboidal winding.

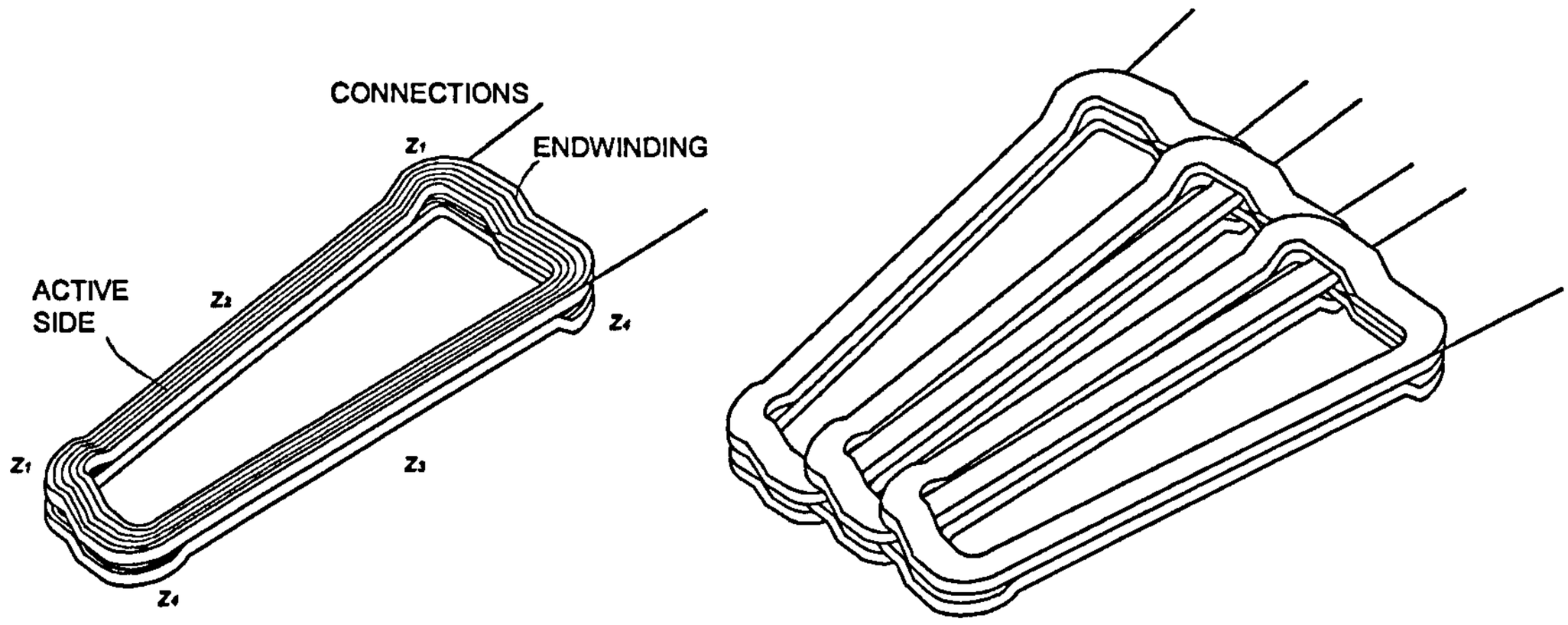


Figure 7.14: 14-turn concentrated coil of flat wire conductor for coreless airgap winding and coils nested.

The proposed coil for a coreless winding is shown in Figure 7.14. Although the endwindings are out of plane, a longer airgap than the *Segmented Array* coil is used

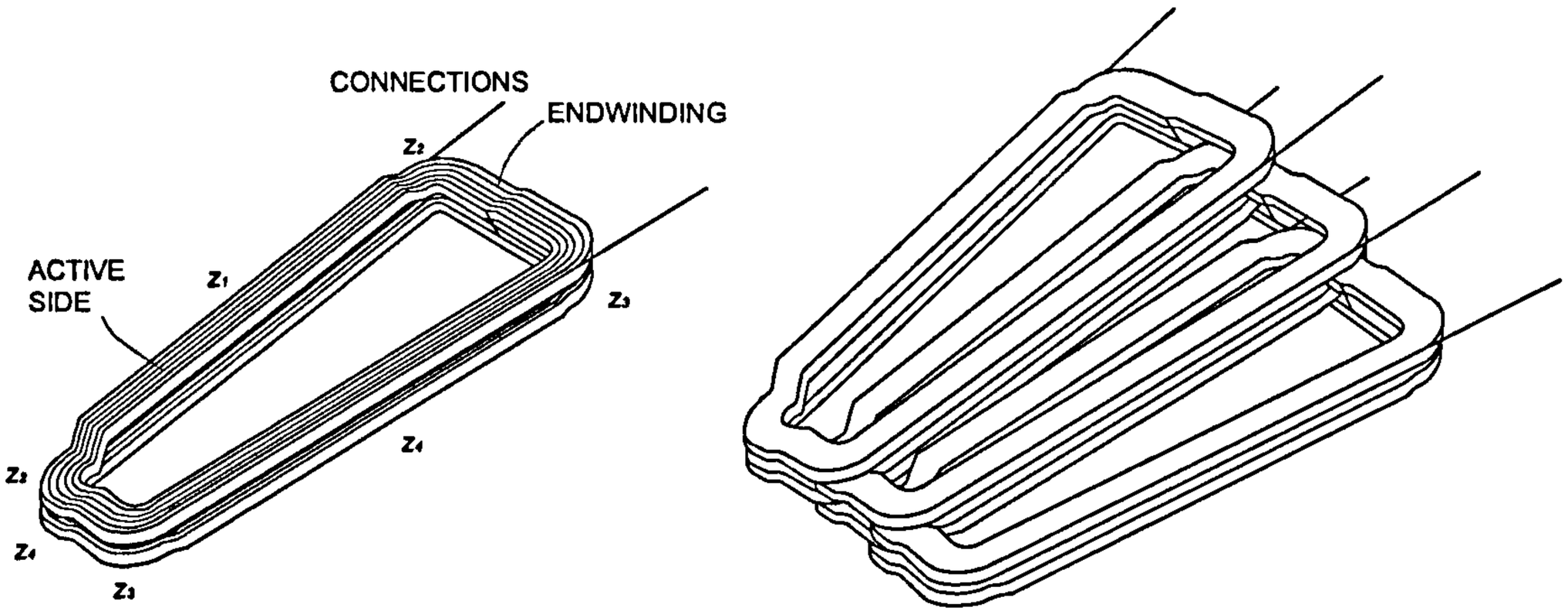


Figure 7.15: 14-turn concentrated coil of flat wire conductor for cored airgap winding and coils nested.

for the same conductor size, but the end connections are simple to make. The active part occupies $z = 2, 3$ while the shaped endwindings for the nested coil overlaps occupy $z = 1, 4$.

Figure 7.15 illustrates a similar version proposed for an iron cored winding, such as shown in Figure 7.11(c). This coil was used for verification of the 3D analytical models, shown in Figure 5.1. It occupies the same four $r - \theta$ planes, but the active part occupies planes $z = 1, 4$ and the shaped end turns occupy planes $z = 2, 3$. With the iron core occupying planes $z = 2, 3$, a package with uniform stator thickness is achieved from the inner radius end turns to outside, which can offer beneficial thermal performance. Table 7.1 summarises the properties of all the concentrated coils described.

Table 7.1: Properties of concentrated coil airgap windings.

Type	Airgap length	Conductor planes	Endwindings	Connection planes
SEMA	minimum (1x b_c)	1	not in plane	2
Rhomboidal	longer (2x b_c)	2	in plane	2
improved SEMA	as SEMA (1x b_c) and connections out	2	simple	4
overlapping		1	in plane	

7.4.3 Copper Fill Factor

The proposed coils use flat wire, thereby occupying more available space with copper than if round wire were used. By comparison, Table 7.2 illustrates a fill factor of 82.28 % for flat wire and 58.37 % for round wire using 3 conductors in hand to achieve the same number of turns. This translates into approximately 25 % more

Table 7.2: Copper fill factor for flat wire for proposed coil and equivalent round wire.

Flat wire

conductor copper height	d_c [m]	0.00400
conductor copper width	b_c [m]	0.00125
conductor copper area	A_c [m^2]	4.6647 x 10^{-6}
insulated conductor height	d_{enam} [m]	0.00420
insulated conductor width	b_{enam} [m]	0.00135
insulated conductor area	A_{enam} [m^2]	5.2789 x 10^{-6}
number conductors	N	7
total copper area	A_{c_tot} [m^2]	32.6529 x 10^{-6}
total area	A_{enam} [m^2]	39.6900 x 10^{-6}
Copper fill factor	f_{Cu} [%]	82.25

Round wire

conductor copper radius	r_c [m]	0.000625
conductor copper area	A_c [m^2]	1.2272 x 10^{-6}
insulated conductor radius	r_{enam} [m]	0.000725
insulated conductor area	A_{enam} [m^2]	1.6513 x 10^{-6}
number conductors	N	21
total copper area	A_{c_tot} [m^2]	25.7712 x 10^{-6}
total area	A_{enam} [m^2]	44.1525 x 10^{-6}
Copper fill factor	f_{Cu} [%]	58.37

copper using the flat wire, and therefore 25 % lower conductor current density.

7.4.4 Winding Factor for Proposed Coils

With the winding factor describing the reduced flux linkage, due to short pitched coils or phase belt, compared to the maximum flux linkage, the pitch and breadth factors are employed. The pitch factor is given by:

$$k_p = \sin \frac{n\tau_c}{2} \tag{7.10}$$

where τ_c is the coil pitch. The breadth factor is given by:

$$k_b = \frac{\sin(nm\gamma/2)}{m \sin(\gamma/2)} \tag{7.11}$$

where γ is the breadth of coil turns.

Hill-Cottingham et al. [2001] presented winding factors for Axial Flux airgap concentrated coil windings with a short-pitched $2\pi/3$ pitch (giving 0.866), a full-pitched π pitch (giving 1.0), and a long-pitched $4\pi/3$ pitch (also giving 0.866). The $4\pi/3$ pitch was selected as the result gave low cogging torque, without employing skew, and lowest Joule losses.

The concentrated coils have mmfs for each turn in phase, which negates the

breadth factor ($k_b = 1.0$). The pitch factor for each turn is different, with a smaller factor for inner turns. With a large number of turns, the mean could be selected, but the proposed coils have fewer turns. Magnussen and Sadarangani [2003] summarised the winding factors for single layer windings, which identifies a short-pitched $2\pi/3$ pitch with the highest winding factor for a 12-pole machine. However, the interleaved coils proposed have a coil throw of 3 coils (slots if the core were slotted), which attains the same winding factor as a double layer winding. The winding factor can be improved from 0.866, for a $2\pi/3$ pitch, to 0.906, for a $4\pi/5$ pitch. Higher winding factors of 0.951 can be achieved with higher pole numbers, bringing τ_c/τ_p closer to 1.0.

7.4.5 On-Load Armature Reaction and Resultant Airgap Field

As part of calculating the airgap inductance in Section 4.2, the airgap flux from coils was computed, which gives the airgap flux density considering the pole area.

Using an analytical calculation of the coil inductance an analytical description of the airgap flux due to current in the winding B_s may be approximated. The armature reaction field combines with the excitation field to produce an airgap field. The superposition of these fields is possible, taking into account the torque angle δ.

The stator mmf $\mathcal{F}(\theta, t)$ describes the airgap reaction flux waveform. The combination of sinusoidal rotor and stator-induced airgap mmf fields, B_m and B_s respectively, gives a B_g waveform where, in the case of no saturation, $\hat{B}_g = \hat{B}_s \sin(\alpha + \beta - 90°) + B_m$. For the non-salient pole surface mounted PM machine, the torque angle β is 90°E.

Therefore, with an ideal sinusoidal excitation field, the stator mmf should be sinusoidal to exclude spatial harmonics from the resultant airgap field waveform [Arkadan et al., 1992]. Figure 7.16 illustrates the ideal stator mmf with sinusoidal phase currents. Figure 7.17 presents the harmonic components of the B_s waveform at airgap positions 1 mm and 3.5 mm from the stator surface. These positions are the rotor PM surface and midpoint with $h_m = 5$ mm. The 3rd harmonic is minimal, but the magnitude of higher components is large. At $z = 3.5$ mm, further fringing reduces the harmonic magnitudes.

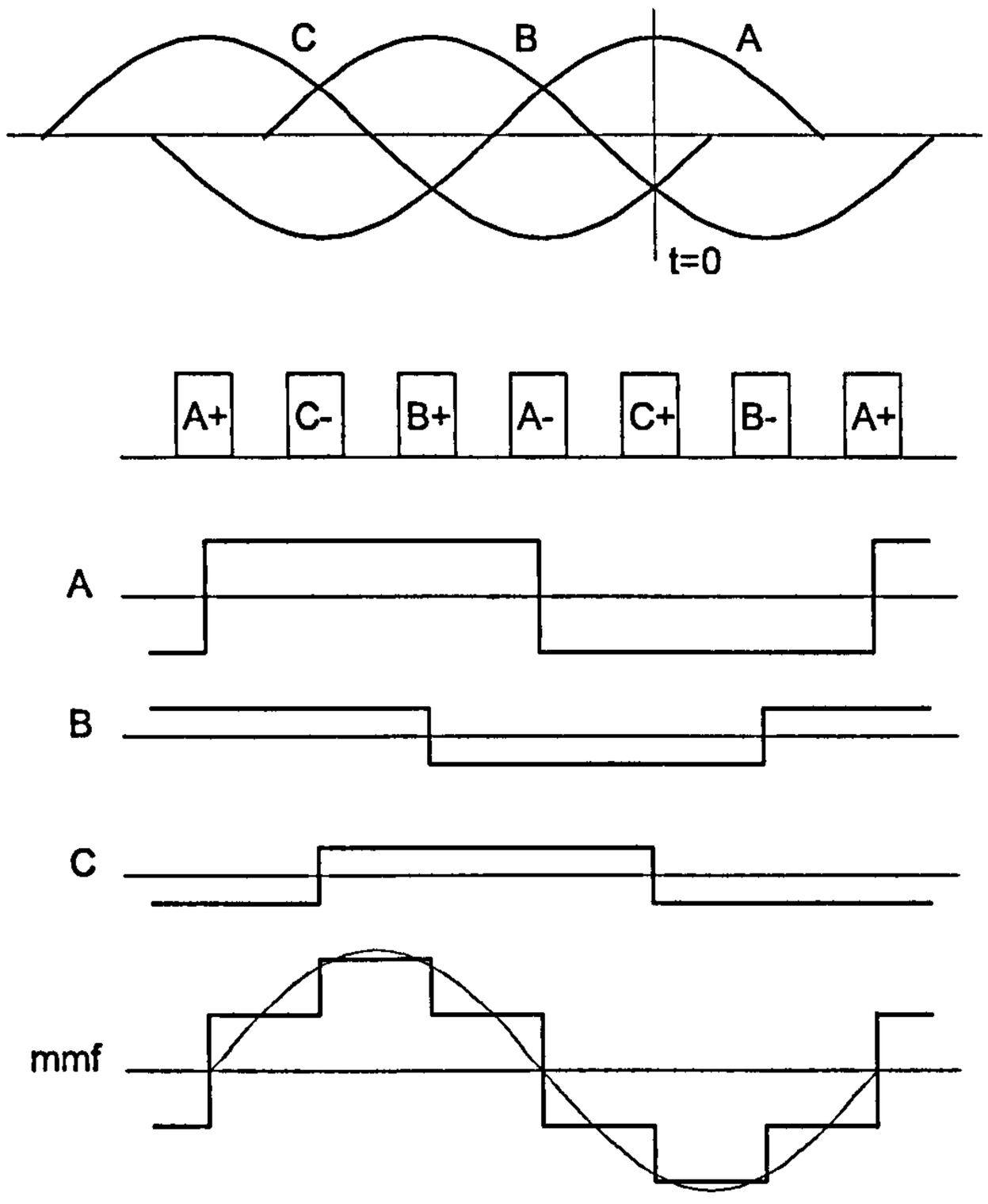


Figure 7.16: Ideal stator mmf for proposed nested concentrated coil.

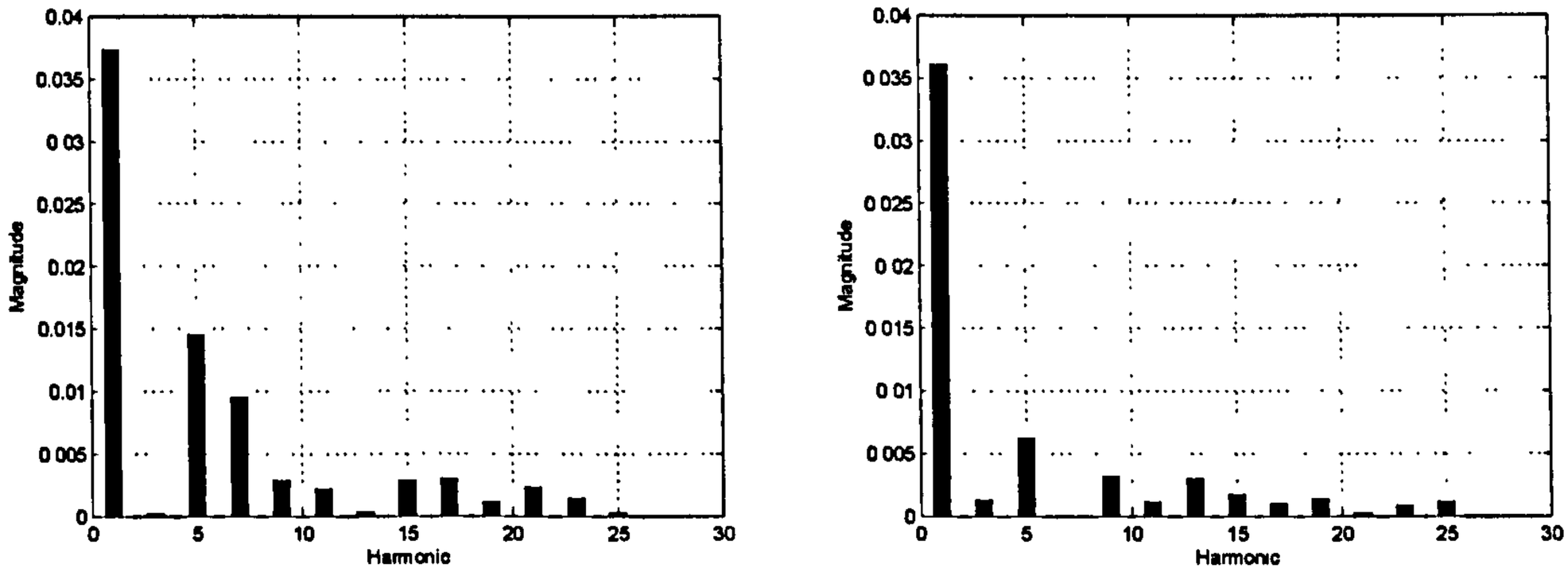


Figure 7.17: B_s waveform for proposed nested concentrated coil at $z = 1$ mm and $z = 3.5$ mm airgap positions.

7.4.6 Calculated No-load Coil Losses

The conductor losses for no-load operation are the excitation field-induced eddy currents alone. Using Equation (7.9) and the values for c according to conductor aspect ratio obtained from measurements, the no-load conductor loss P_{EC}^{loss} of the

Table 7.3: Geometric dimensions and operating conditions for evaluating eddy currents in proposed coil.

conductor height	d_c [m]	0.00400
conductor width	b_c [m]	0.00125
conductor x-sec area	A_c [m^2]	5 x 10^{-6}
conductor aspect ratio constant	$c(b_c/d_c)$	0.0155
inner radius	r_i [m]	0.095
outer radius	r_o [m]	0.165
conductor active length (per coil)	$l_{c_act}(coil)$ [m]	1.96
conductor total length (per coil)	$l_{c_tot}(coil)$ [m]	3.00
number turns per coil (per side)	N	7
number coils per phase	N_{c_ph}	8
conductor length (per phase)	$l_c(phase)$ [m]	24.00
pole pairs	p	6
operating speed	ω_{mech} [rpm]	4000
electrical frequency	f_{elec} [Hz]	400
electrical resistivity	$\rho_{elec}(Cu)$ [Ωm]	1.68 x 10^{-8}

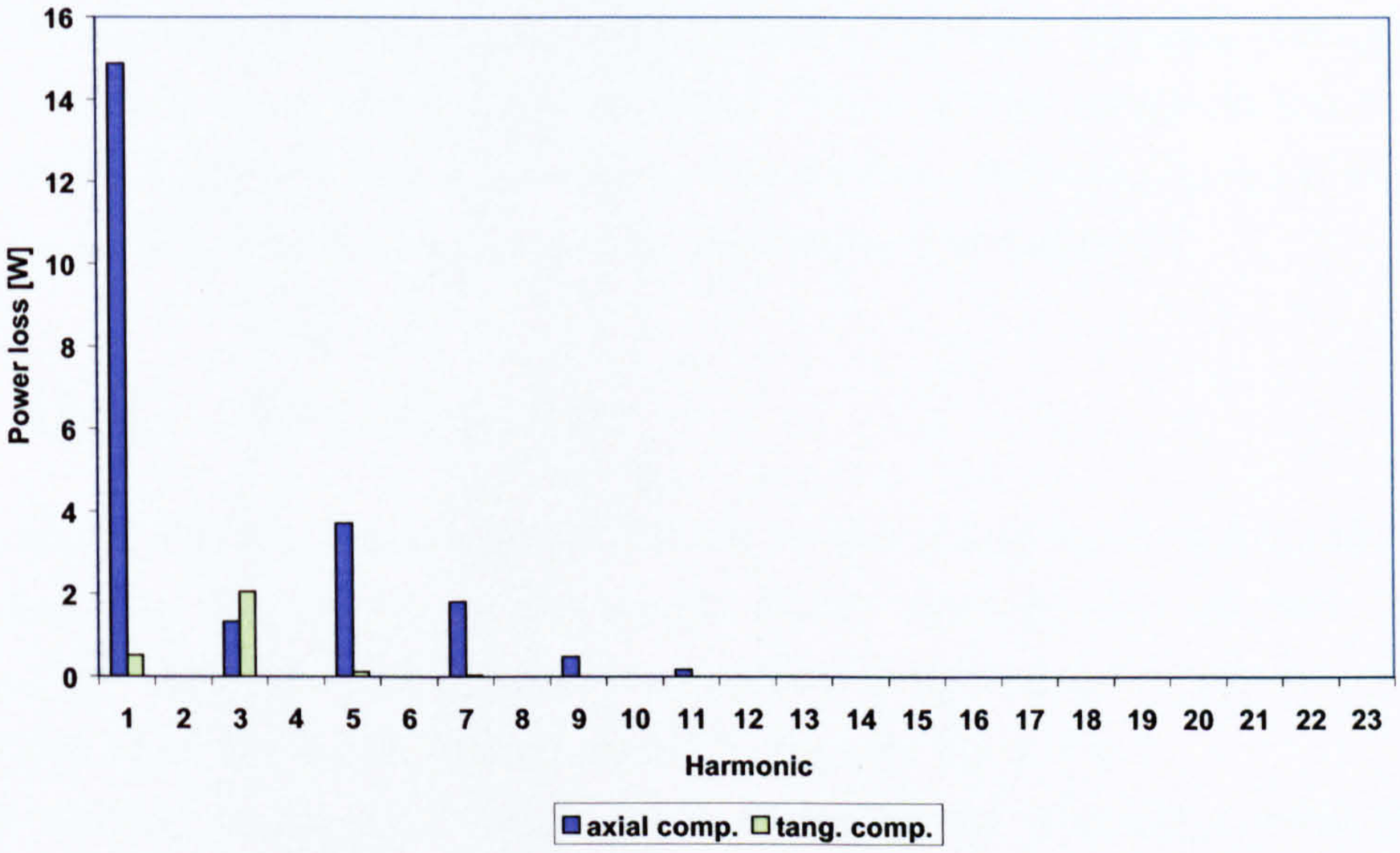


Figure 7.18: Individual coil eddy current power loss calculated for each harmonic, with fundamental electrical frequency 400 Hz.

proposed interleaved coil with design detailed in Table 7.3 were calculated.

The no-load losses for the proposed interleaved coil with a 400 Hz excitation frequency, containing harmonic components as outlined in Chapter 6, were calculated for individual coils and are shown in Figure 7.18. The losses arising from both $z-$ and $\theta-$direction flux were calculated at each harmonic frequency. Proximity effects could be included if the eddy currents were sufficient, but were not in this case. As the depth of penetration for higher frequencies reduces to less than d_c, the effective cross-sectional area of conductors reduces and resistance increases.

7.5 Summary

A sensitive reaction torque measurement was employed for experimental evaluation of no-load losses within individual conductors. The flat wire conductors offer low losses, if the tangential component of the excitation field is low.

Various concentrated coils designs for airgap windings have been compared and nested coils proposed, which offer a high copper fill factor for the smallest airgap. The copper fill factor, winding factor and low no-load losses make the proposed coil attractive.

A further step would be to extend the equivalent magnetic circuit model described in Chapter 5 to include conductor geometry, rather than just a conductor region, and render eddy current power loss provided the excitation waveform is sufficiency detailed.

Chapter 8

Experimental Machines

Based on the description of HEV powertrain applications for the Axial Flux machine case studies, machine designs have been proposed for the IMG [Coles et al., 2004] and for the Generator [Walker, A., 2002], which have been analysed through this work. The manufacture of parts for the Axial Flux machine designs in the selected HEV powertrain applications is described, with the manufacturability being of prime interest, including details of e.g. winding, machining and assembly.

8.1 IMG Manufacture

A minimum of two airgaps is required for the torque rating required from the specified active area dimensions, so the double airgap topology was selected for this machine. The electromagnetic design was initially proposed and analysed by Coles et al. [2004], with the 9-slot version shown in Figures 8.1 and 8.2.

Both internal stator and internal rotor versions were considered, with further parameters on the rotor pole shape and slot and coil numbers. The low rotor inertia of the internal rotor was previously demonstrated as particularly suitable for this application and was ultimately selected, but manufacture of both configurations was undertaken.

8.1.1 Rotor Manufacture

The rotors for the internal stator design were manufactured with shaped sintered N42H magnet pieces, Ni coated and magnetised by the manufacturer. They were glued into an aluminium alloy holder, or spider, which was mounted on the iron return plate. A version with skewed poles is shown in Figure 8.3. This was considered for hoop stress with the magnets, operating up to 4000 rpm. The integral strength



Figure 8.1: 9-slot stator design.

was sufficient without additional bandaging and dynamic balancing was conducted. Bonded NdFeB poles were employed in the internal rotor design, as shown in Figure 8.4.

The internal rotor had no flux return keeper, resulting in lower dynamic stiffness, while the rotor flux return plate of the internal stator had a minimum thickness to avoid saturation, which also provided improved mechanical strength.

The internal rotor design avoids rotor iron so surface losses exist in the magnets alone. Bonded magnets were selected to minimise these losses, although the lower remnant flux density of these magnets reduces the airgap flux density (and torque capability) of the design. The bonded pole pieces were machined to shape and magnetised prior to locating within the non-magnetic, non-conducting spider.

8.1.2 Stator Coil Winding

Concentrated coil windings with round wire were prepared with end wire connections on the outer radius. Winding jigs for concentrated coils are illustrated in Figure C.2.

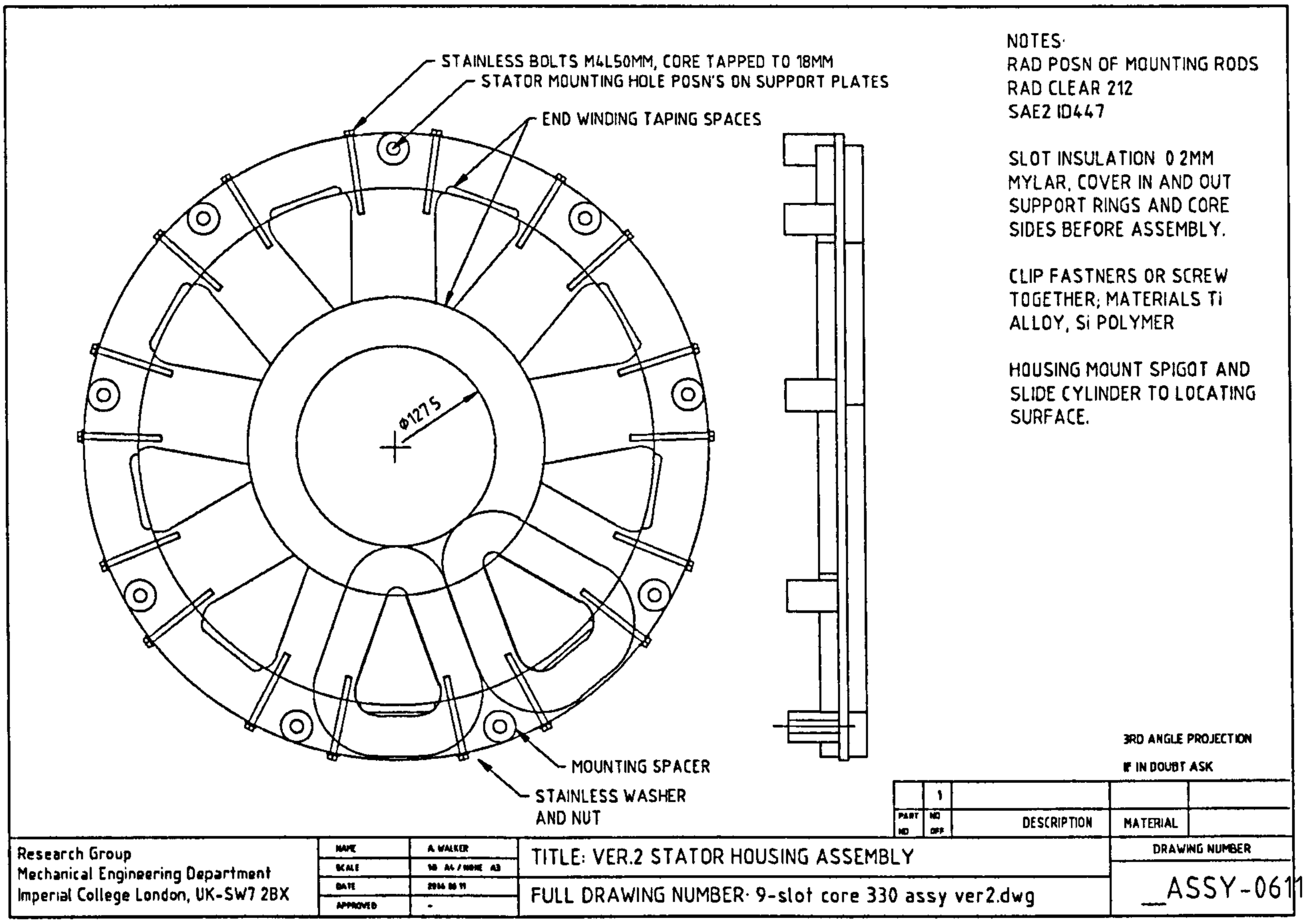


Figure 8.2: 9-slot stator design.

In the case of the 9-slot stator winding, seven conductors were wound in hand. This conformed with the 0.5 mm conductor diameter, providing minimum conductor eddy current losses and sufficient conductor cross sectional area to maintain the design current density. Rahman et al. [2004] proposed a suitable winding technique for concentrated coils with multiple conductors in hand. This involves winding single conductor layers and avoids multi strand cross overs when changing direction at top and bottom of the slot.

8.1.3 Stator Iron Core for 18-Slot Machine

The stator core(s) made from compacted insulated powder iron pieces were machined to shape, but in large scale manufacture, these can be compacted directly to the desired shape. The machining activity is complicated by the hardness and low mechanical strength of the compacted powder iron [Nafisi and Campbell, 1985].

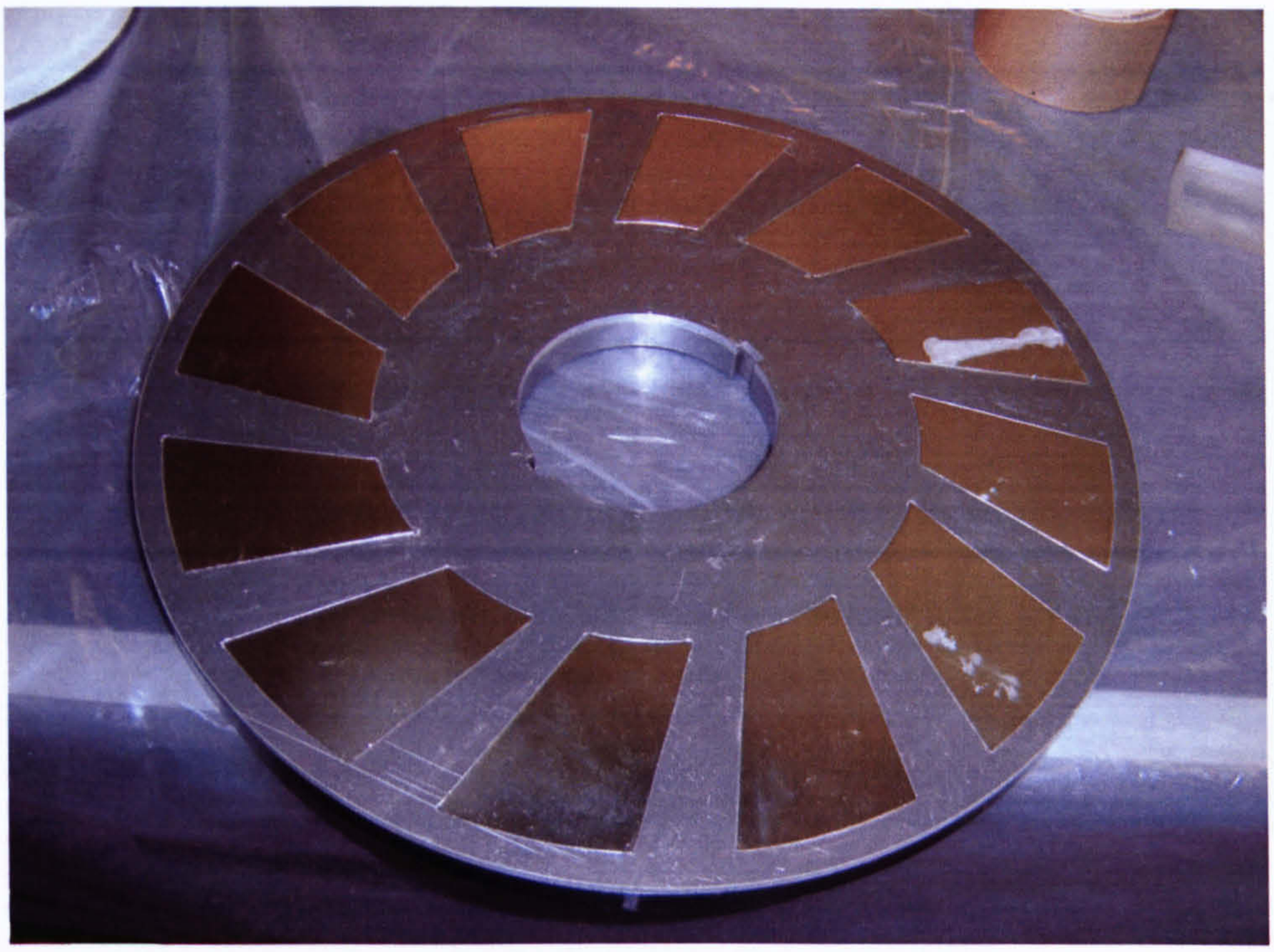


Figure 8.3: Internal stator rotor assembly with skewed poles.

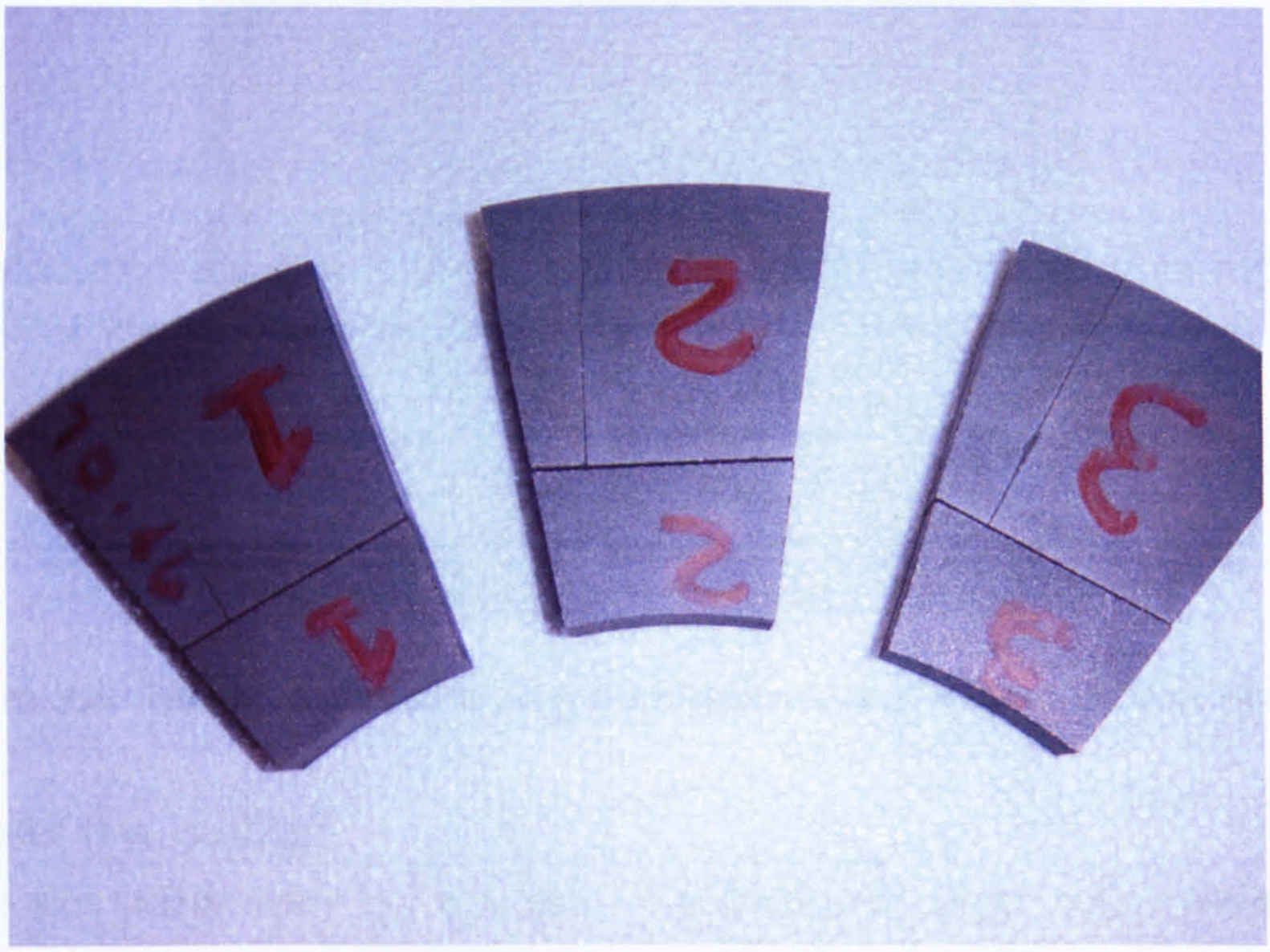
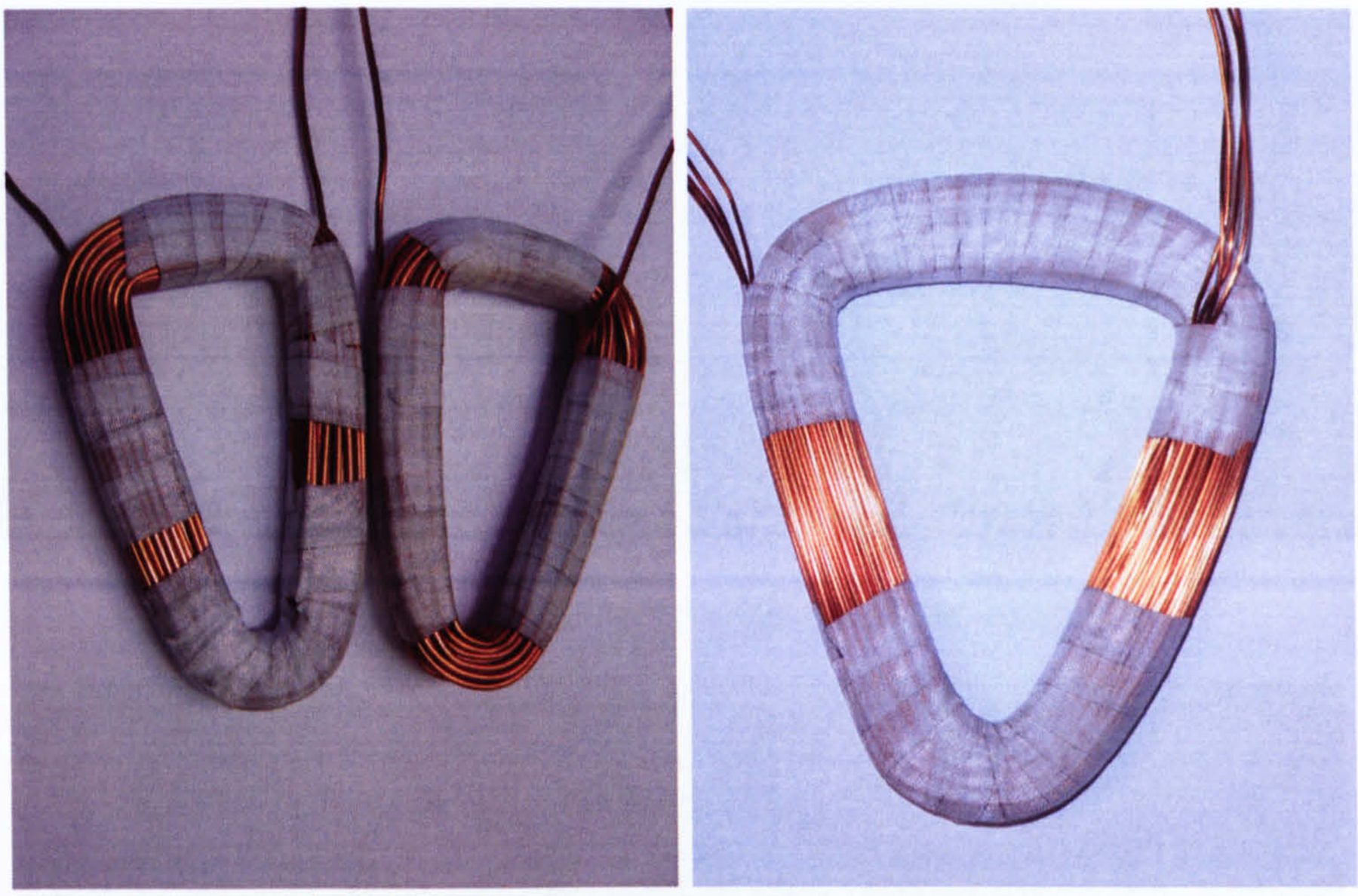


Figure 8.4: Sector bonded NdFeB poles.

8.1.4 Stator Assembly

Figure 8.7 illustrates the machined core for the 18-slot stator with coils mounted. Two coils are mounted, with space between facilitating additional surface area for



(a) 18-slot winding coil (b) 9-slot winding coil

Figure 8.5: Coils for concentrated windings.

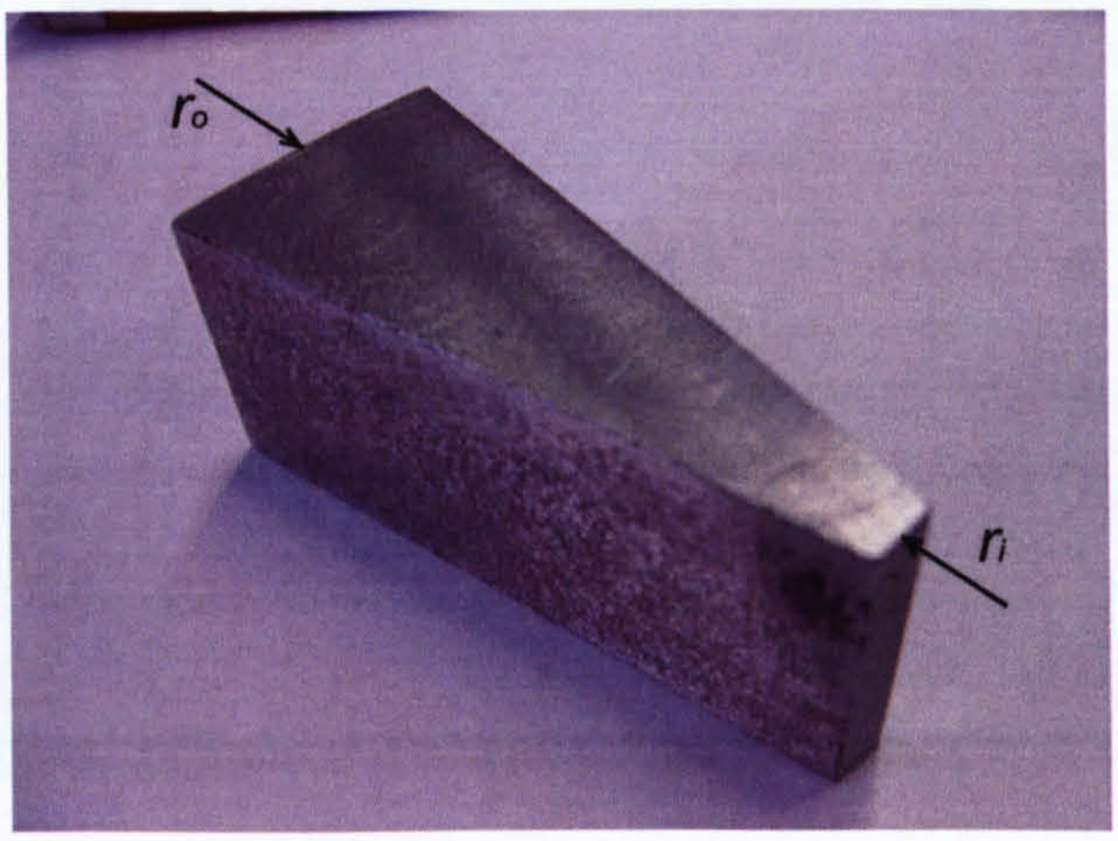


Figure 8.6: 18-slot internal stator core section of compacted iron powder.

heat transfer (i.e. cooling).

The 18 slot stator assembly was given mechanical strength without teeth bridges (or core back) using the impregnation, as reported in Anpalahan et al. [2004]. This is important for the axial attractive forces during assembly, shown in Figure 8.8.

8.1.5 Machine Assembly

The internal stator package is difficult to construct, as the second rotor can only be added to the shaft after the stator is mounted and the attraction forces must be

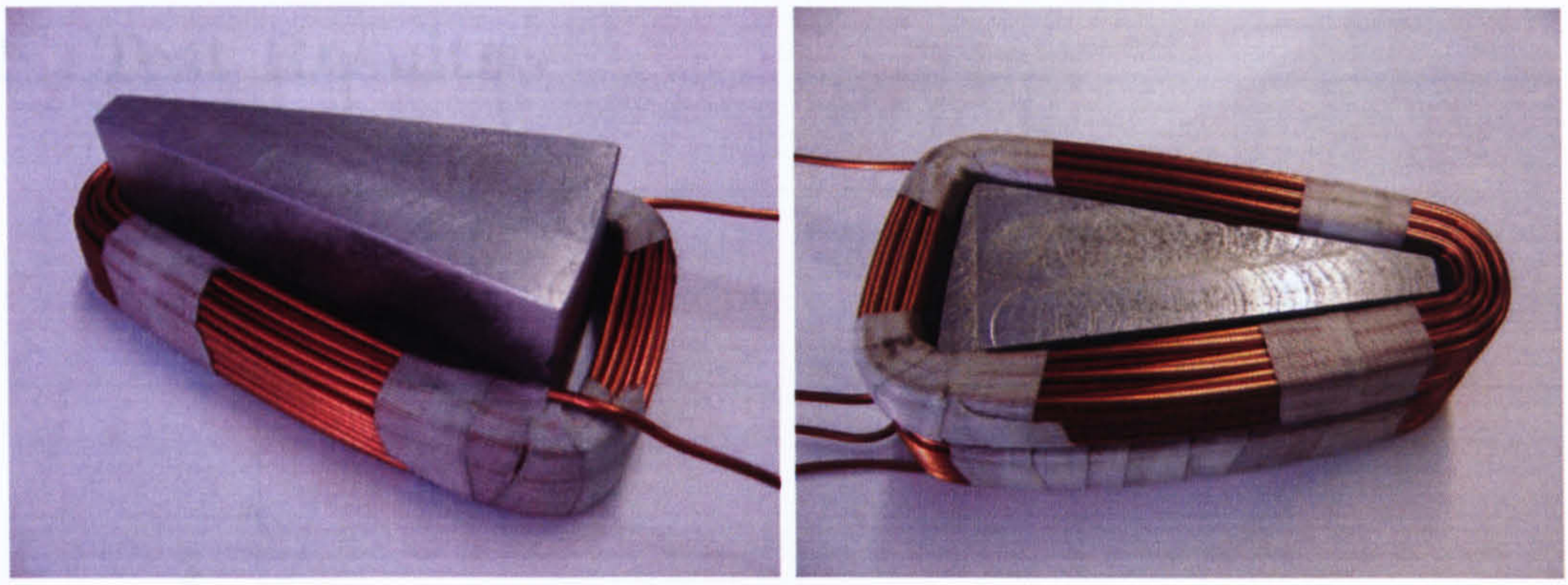


Figure 8.7: 18-slot core with mounted coil(s).

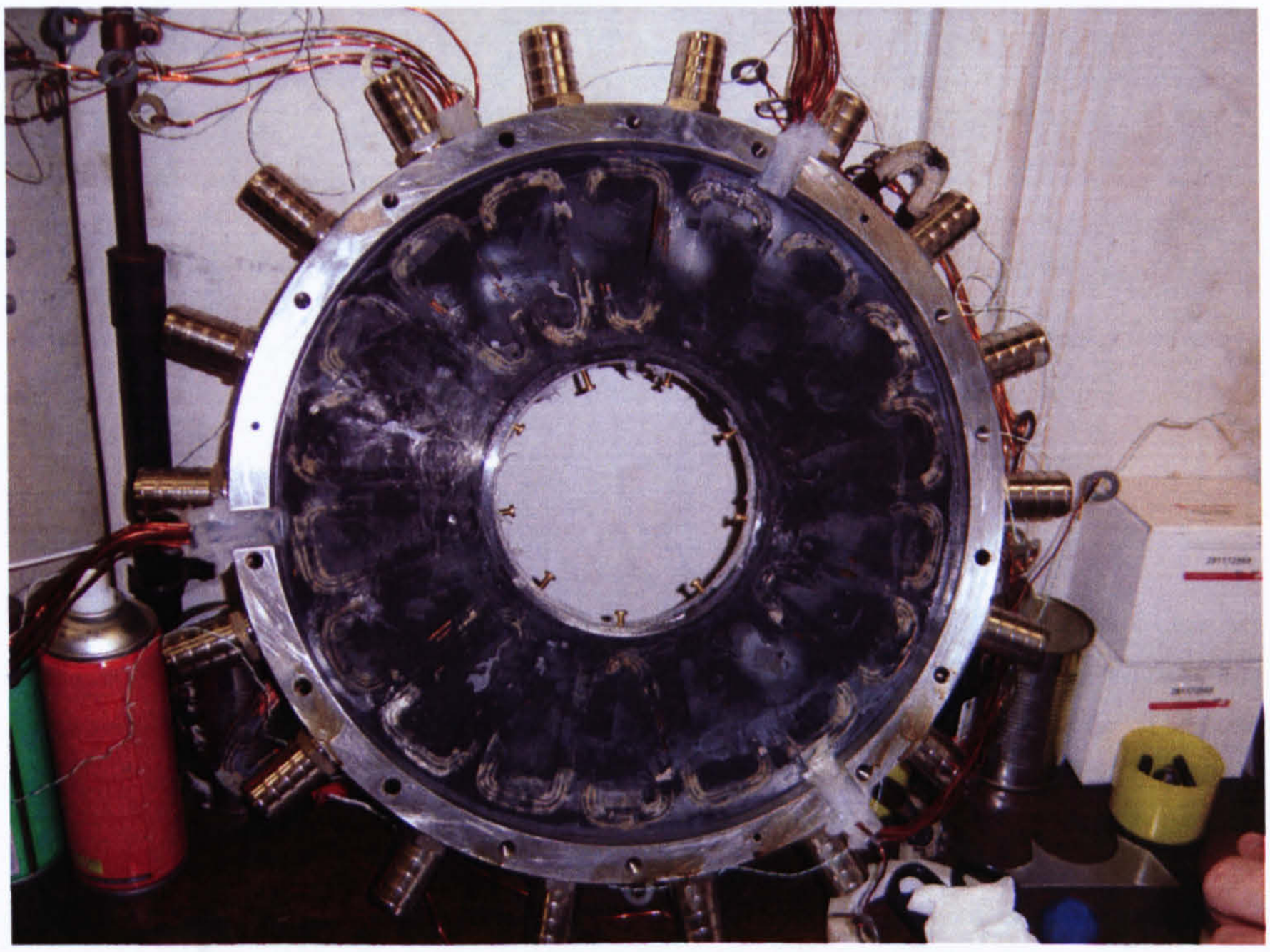


Figure 8.8: Assembled 18-slot internal stator.

managed. To overcome this difficulty, a series of assembly pulleys and tools were employed, but this method must be refined in automated production.

8.1.6 Mechanical Integration

The housing and shaft were designed to mate with the clutch and flywheel housing as previously described. The thermal analysis indicated that insulation was required from the clutch, which can reach 200° with frequent operation, and this was achieved by integrating cooling ducts with the mounting plates at the rear of the stator cores in the internal rotor design.

8.2 Test Results

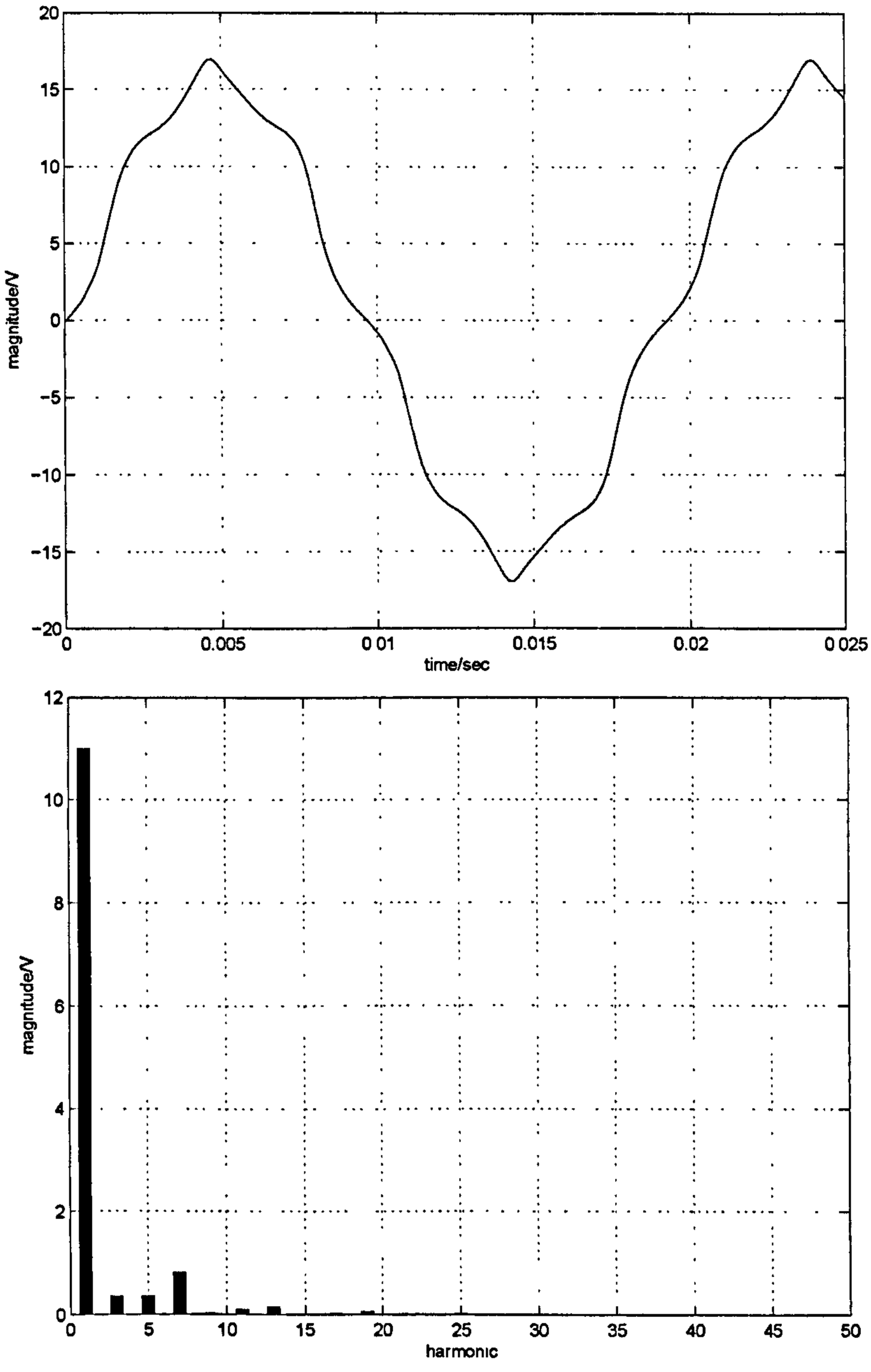


Figure 8.9: Open circuit voltage waveform and harmonics for one coil.

The open circuit induced *emf* for a single coil is shown in Figure 8.9, along with the harmonic components, for 500 rpm. The third and fifth harmonics are small, and the seventh is large, yet all are less than 0.1 p.u..

Figure 8.10 provides the open circuit induced *emf* waveforms for all coils in one phase. It can be seen that the waveforms are consistent, but that there is marginal difference in both phase and magnitude between coils. As the coils are connected in parallel, these differences drive recirculating currents, which do not contribute

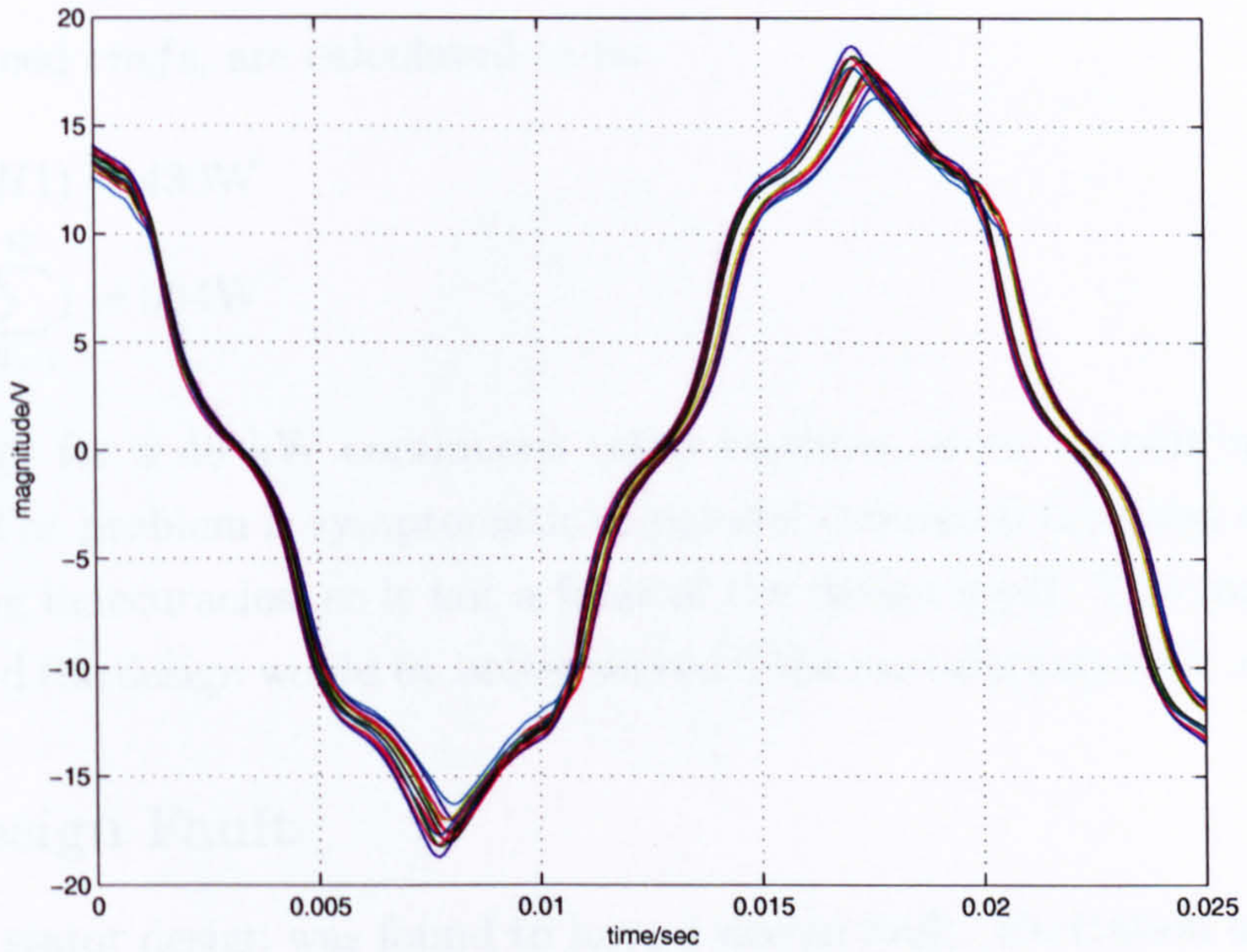


Figure 8.10: Open circuit voltage waveform for 12 parallel coils in phase.

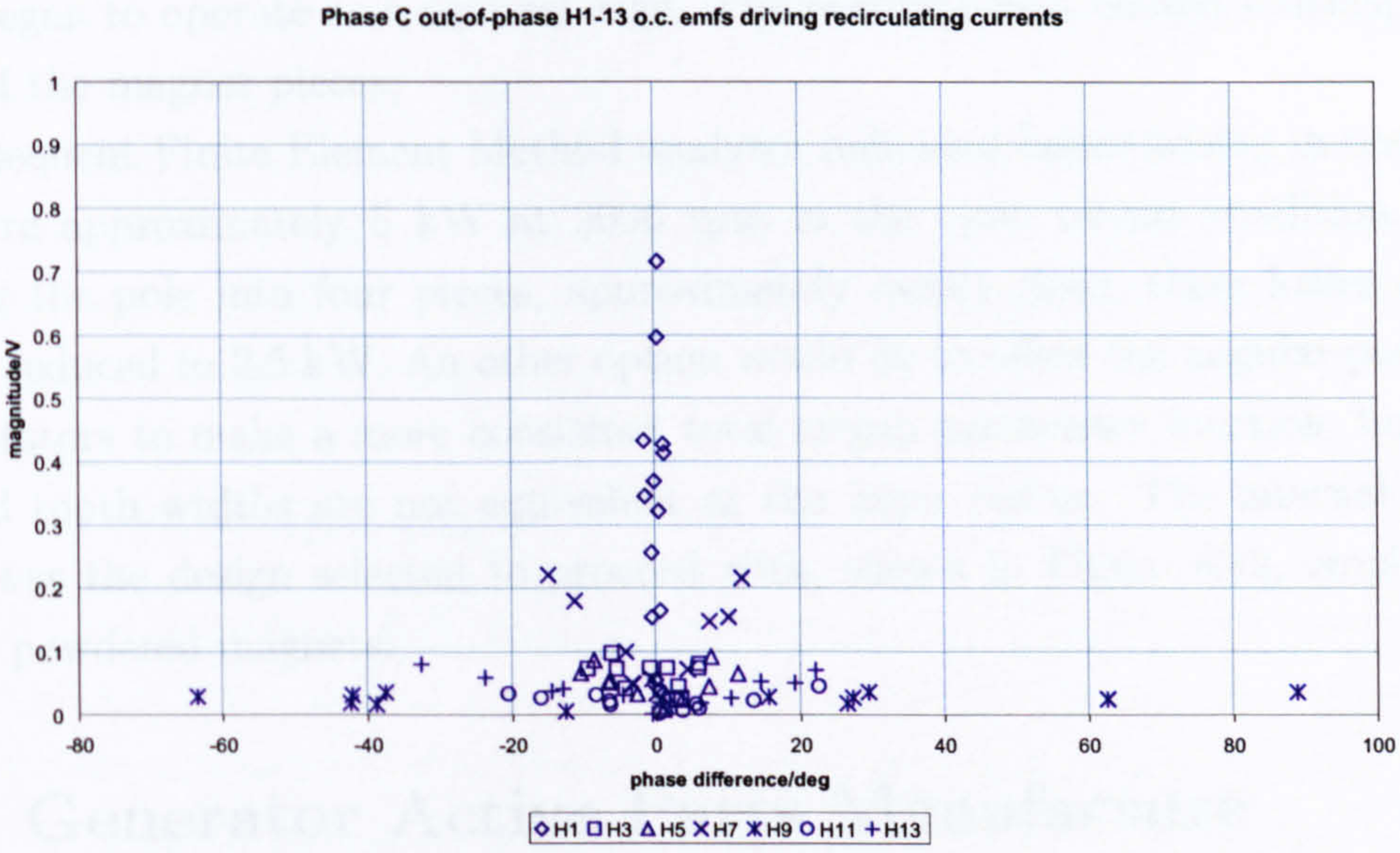


Figure 8.11: Difference between open circuit voltages of parallel coils in phase, driving recirculating currents.

to torque generation, but do cause Ohmic losses. The magnitude and phase of the difference between the induced emfs for each coil, and the mean emf for phase current, is given for harmonics 1 to 13 in Figure 8.11.

The Ohmic losses for the recirculating currents which arise due to these un-

matched induced emfs, are calculated to be:

$$P^{I^2R}_{\text{recirc.}}(H1) = 430\text{W}$$
$$P^{I^2R}_{\text{recirc.}}(\sum_{H=1}^{13}) = 504\text{W}$$

which are high for a 40 kW continuous rated machine, alone accounting for 1 % inefficiency. The problem is symptomatic of parallel connected coils and arises from manufacturing inaccuracies, so is not a fault of the design itself. This machine was hand built and the design would be better served if the manufacture were automated.

8.2.1 Design Fault

The internal stator design was found to have a design fault. Excitation array variation ΔB_m arose due to the airgap permeance function and caused significant pulsating flux with the magnets, also resulting in flux linkage with the aluminium spider which began to operate as a squirrel cage. The resulting heat caused a demagnetisation of the magnet pieces.

Subsequent Finite Element Method analyses indicated losses arising in one PM pole were approximately 5 kW at 2000 rpm in the open circuit condition. By splitting the pole into four pieces, approximately evenly sized, these losses could only be reduced to 2.5 kW. An other option would be to offset the angular position of the stators to make a more consistent total airgap permeance function, but the slot and tooth widths are not equivalent at the inner radius. The internal rotor design was the design selected to proceed with, shown in Figure 8.12, employing bonded powdered magnets.

8.3 Generator Active Parts Manufacture

A slotless core, airgap winding was employed in the internal stator machine, which is an attractive generator design due to the low inductance and therefore little variation in terminal voltage with change in current drawn [Atallah et al., 1998].

8.3.1 Stator Manufacture

Figure 8.13 illustrates the internal stator package, including 24 interleaved airgap winding coils.

Concentrated coils were wound independently and placed on the stator. Several

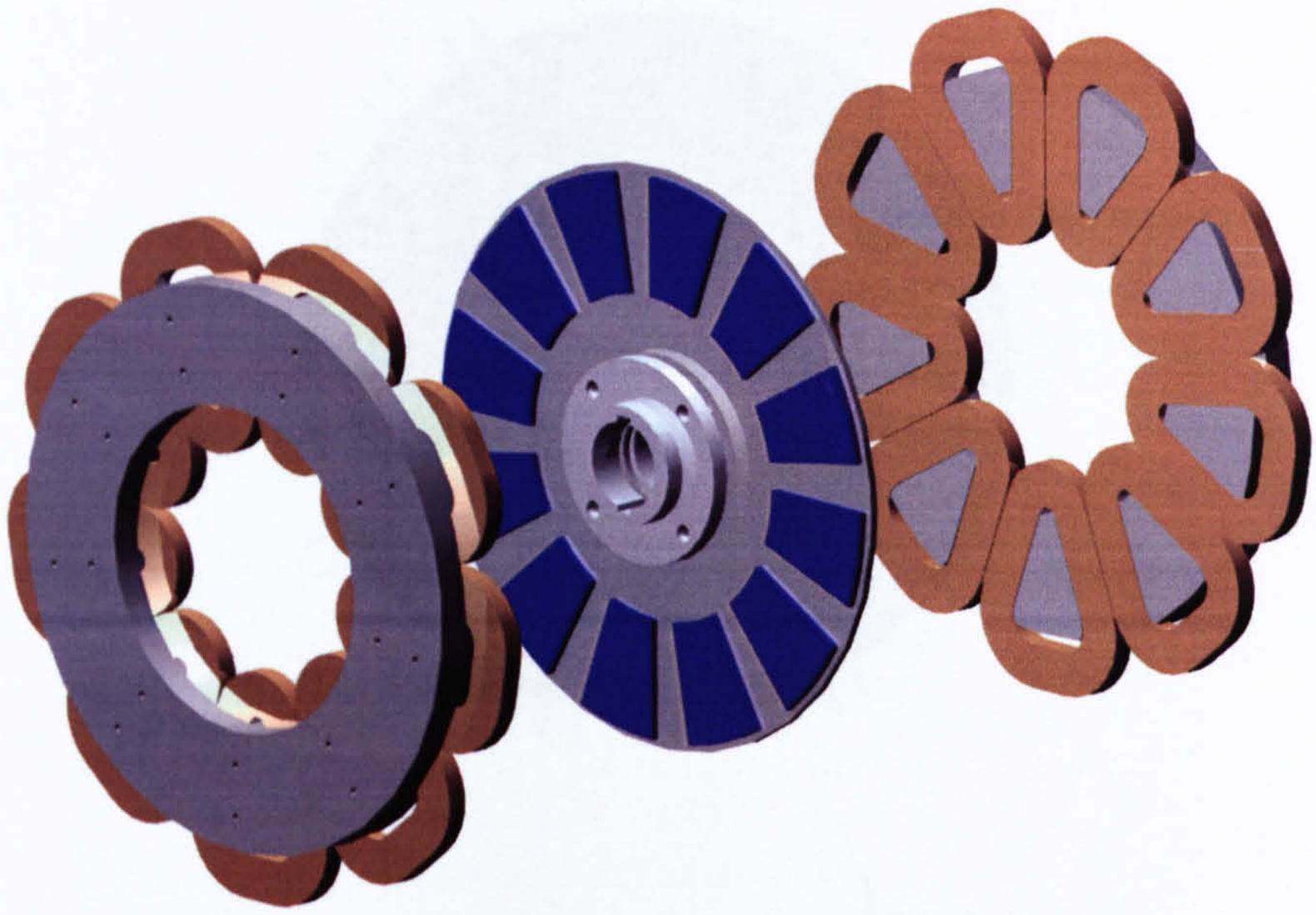


Figure 8.12: Internal rotor IMG design.

winding and forming jigs were employed in the manufacture of coils for the airgap winding, illustrated in Appendix C.3.

The design of concentrated coils using large flat conductors required consideration of the end connections. Achieving connections on the outside of concentrated coils requires a 2-plane coil with a cross over between planes on the inside, as the coil design proposed in Chapter 7.

8.3.2 Stator Assembly

The coils require mechanical support as they are not placed in slots. The coils occupy planes either side of the core, shown in Figure 8.15, and are interleaved, secured with standard coil ties used on the end windings. The coils shown in Figure 8.14 were mounted as search coils, with a version of the rotor shown in Figure 8.3 with sector (radial edges) poles.

8.4 Summary

The experimental machines described are the Axial Flux machines designed as case studies on HEV powertrain applications. The description highlights the new approaches to manufacturing problems required for aspects of these designs. The test results on the internal stator IMG machine highlighted a design fault, which led to proceeding the machine as an internal rotor design. It indicates that the airgap

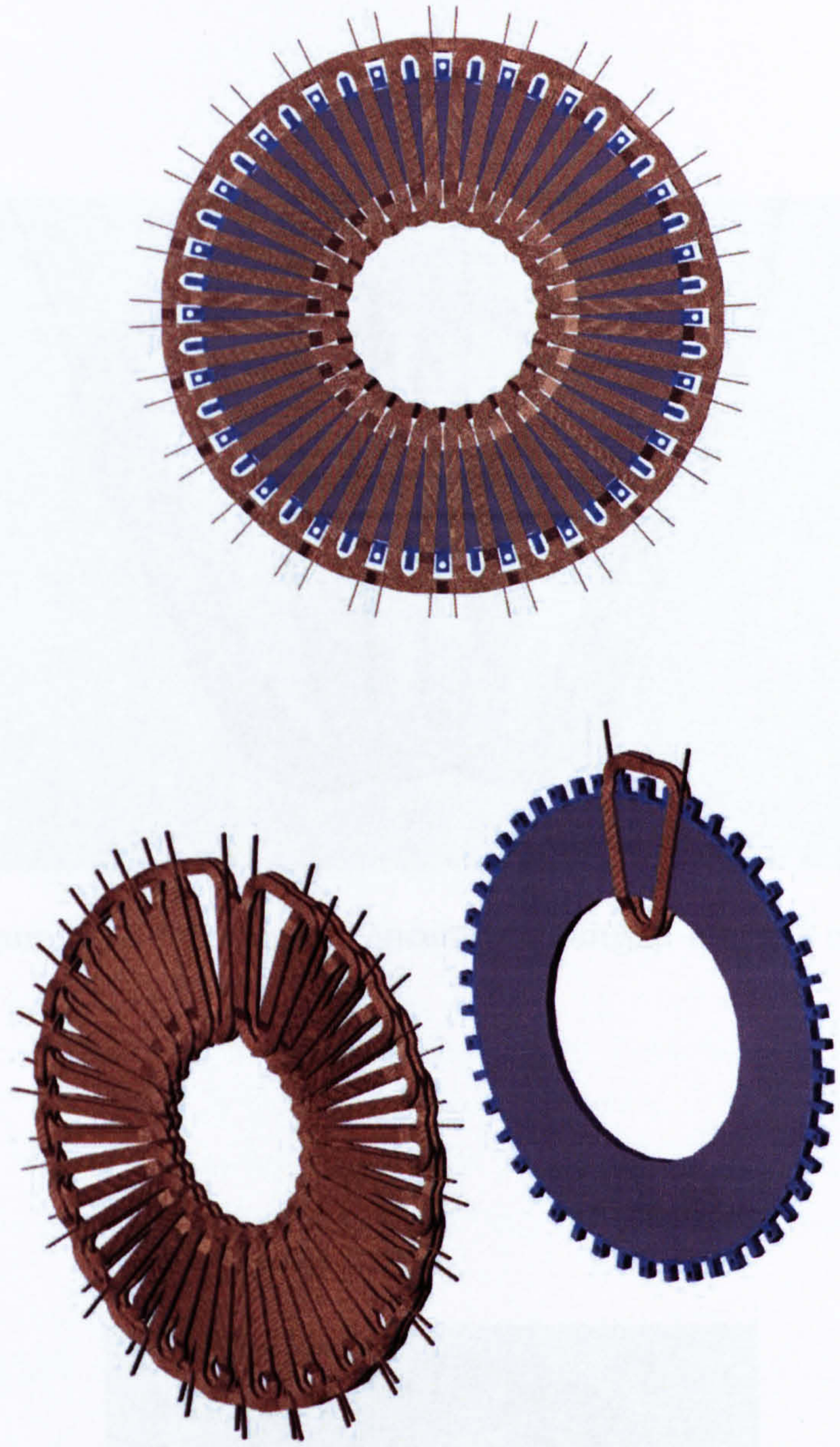


Figure 8.13: Interleaved concentrated airgap winding.

permeance function requires detailed analysis, which is taken up in the following chapter, and that the maximum fluctuation in the excitation flux at any rotor position should be limited due to the close relation to rotor losses.

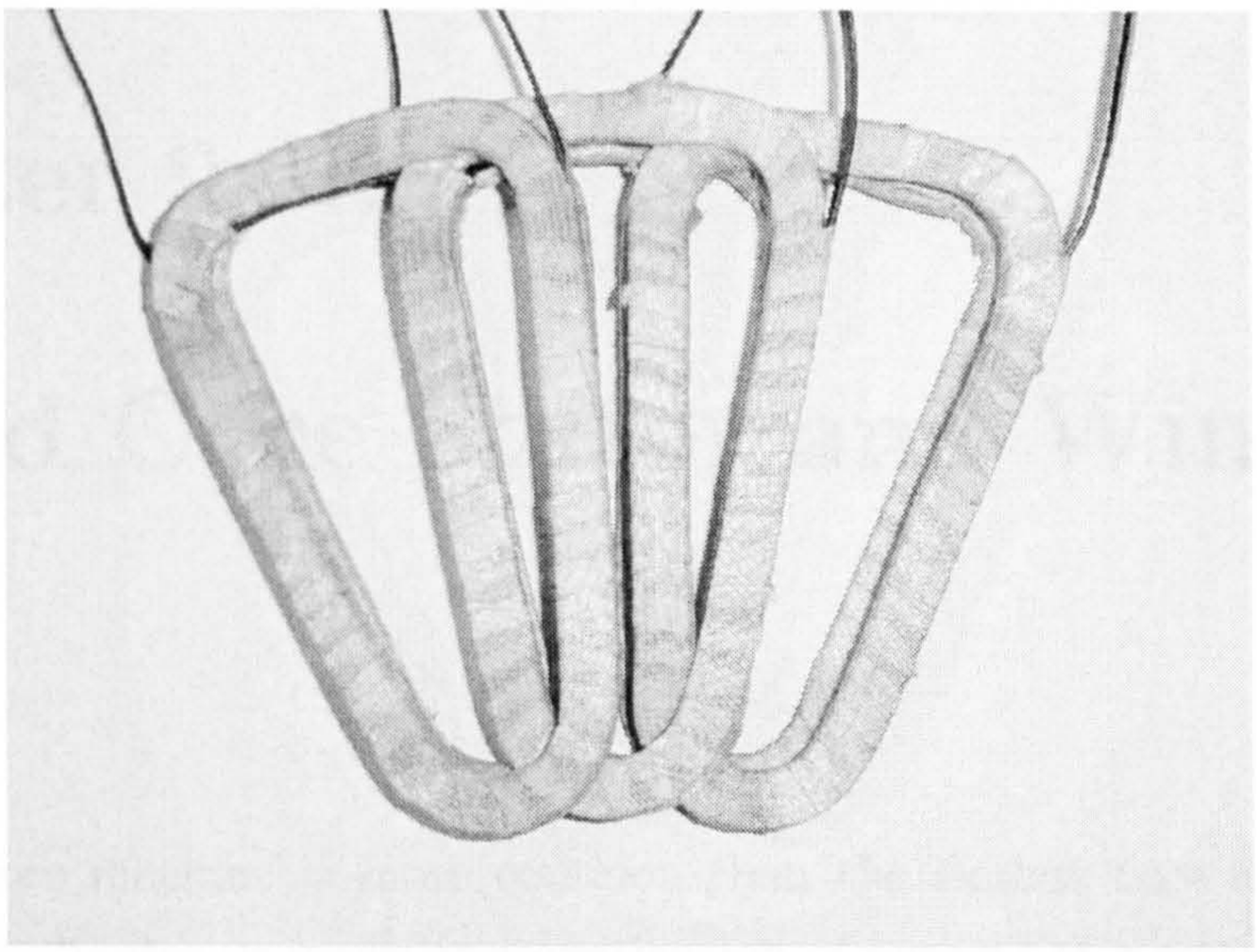


Figure 8.14: Interleaved concentrated airgap winding coils.

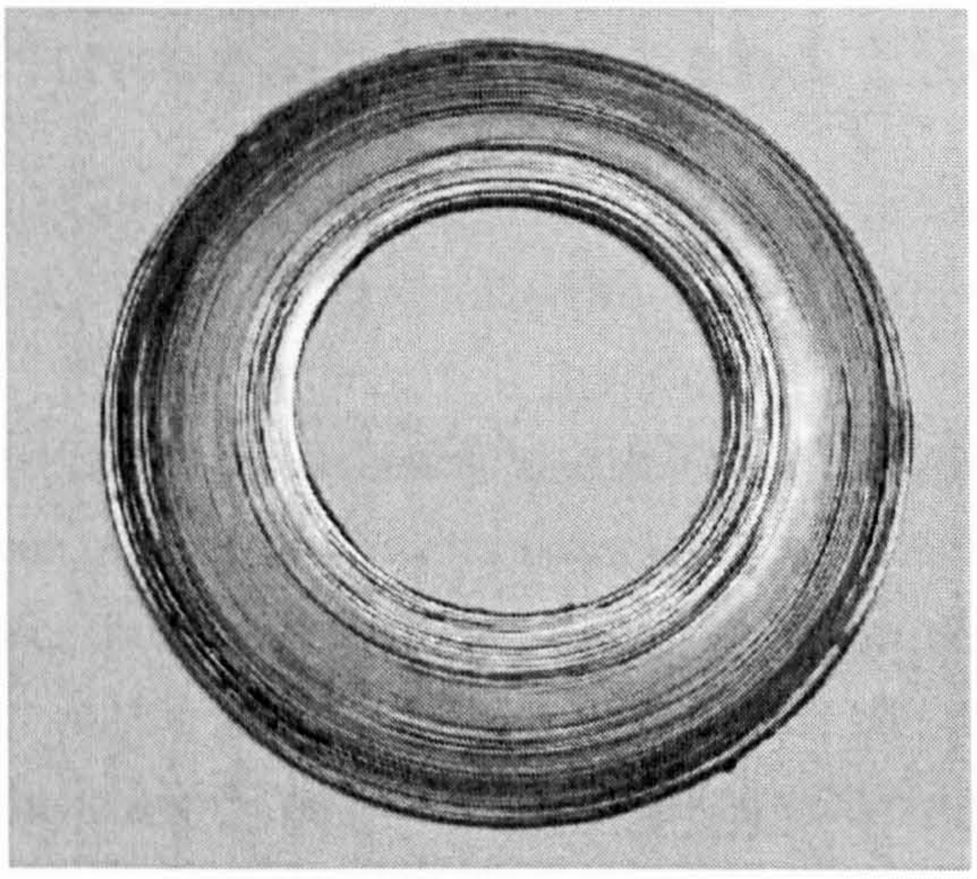


Figure 8.15: Wound core for airgap winding.

Chapter 9

Slotted Core Stator and Winding Study

The slotted core machine is more common than the slotless core airgap winding machine. This chapter presents an investigation of aspects of a slotted core stator and winding, with the conductor no-load losses considered along with stray losses. Iron losses are not investigated.

By introducing stator saliency, the airgap has a periodic varying permeance function Λ, and it is possible to evaluate the harmonics in the resulting excitation field waveform. Advanced machine design texts, such as Sadarangani [2000], provide background theory on stator slotting, which largely comes from induction machines.

9.1 Salient Stator Structure and Slot Leakage

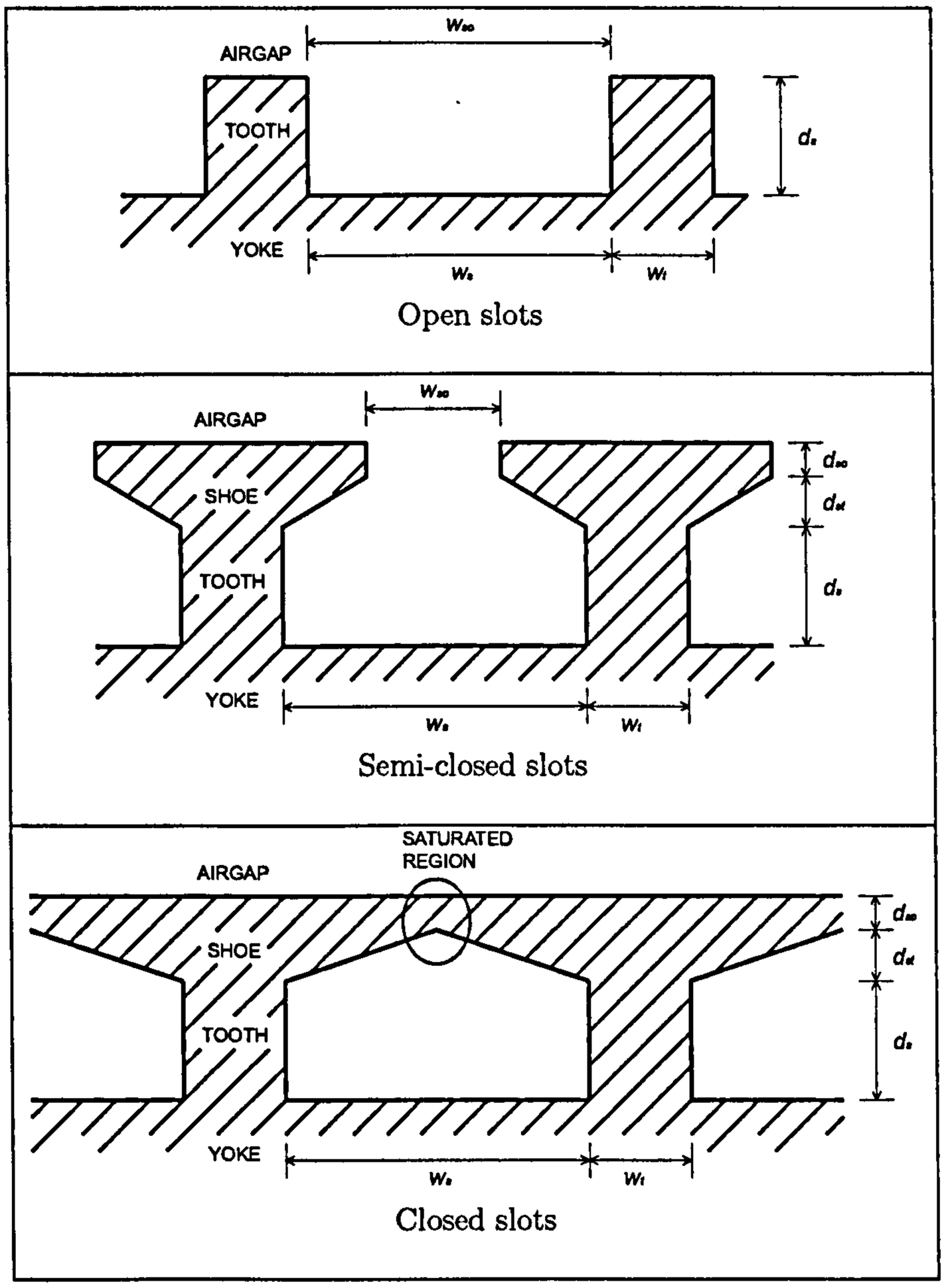
The response of flux linkage Ψ and inductance L to stator saliency can be investigated in the $dq-$system. Salient poles make the airgap permeance, and in turn the reluctance of the main flux path circuit, a function of the rotor position. Usually such saliency relates to the rotor saliency and reluctance-type machines are an example of this. However, the three torque components are alignment torque (from the stator coil and rotor pole flux linkage), reluctance torque (from the stator coil flux and the rotor iron path), and cogging torque (from the rotor pole flux and the stator iron path), so the saliency of the stator is an equally important consideration:

$$T = \underbrace{Ni\frac{d\phi}{d\theta}}_{align.} + \underbrace{\frac{1}{2}i^2\frac{dL}{d\theta}}_{rel.} - \underbrace{\frac{1}{2}\phi^2\frac{d\mathcal{R}}{d\theta}}_{cog.} \tag{9.1}$$

9.1.1 Tooth Tips and Slot Closures

Salient poles are formed by stator teeth and slots. The shapes of stator slots are commonly categorised "open slot", "semi-closed slot", or "closed slot", shown in Figure 9.1. Assuming saturation is avoided, the stator slot opening impacts on the airgap permeance waveform and rotor surface losses.

Table 9.1: Open and closed slot dimensions. Slot bottoms may be rounded rather than square.



A fully open slot has a slot opening width equivalent to the slot width $w_{so} = w_s$. The conductors fill the slot area $A_s = w_s d_s$, less any area taken up by slot insulation or wedge materials. The conductors are largely exposed to the airgap field and eddy currents arising from alternating flux are observed. If the slot aspect ratio results in a shallow slot, or the teeth experience saturation, the excitation flux entering the slot can enter the bottom of the slot into the core rather than the side of the tooth.

The dimensions labelled on the semi-closed slot are the widths of the slot and slot opening, w_s and w_{so}, and the depths of the slot, slot taper and slot opening, d_s, d_{st} and d_{so}. The conductors are exposed to less alternating flux than those in open slots, as the pole shoe is sized to accommodate the excitation flux without saturating. For manufacturing, the minimum slot opening width is larger than the conductor diameter for ease of conductor insertion into the slots.

The fully closed slot structure prevents any excitation flux passing through the slot, provided there is no saturation, but there is a problem of short circuit flux from the coil. The level of short circuited flux is not linear with load due to the iron material $B-H$ curve. With wider slots, the tooth–tooth leakage reduces. The conductors in a closed slot structure may be exposed to negligible alternating flux, minimising eddy currents.

9.1.2 Slot and Tooth Geometries

The main options for slot and tooth geometry are (i) constant w_s with r, or (ii) constant w_t with r, as illustrated in Figure 9.1.

$$A_t(\text{Const Tooth}) = w_t(r_o - r_i) \tag{9.2}$$

$$A_t(\text{Const Slot}) = (r_o - r_i)\left(\frac{\pi}{Q}(r_o + r_i) - w_s\right) \tag{9.3}$$

Slot and tooth widths are equivalent at the inner radius $w_{s_i}(r_i) \equiv w_{s_ii}(r_i)$ and $w_{t_i}(r_i) \equiv w_{t_ii}(r_i)$. Constant w_s with r has been employed here as constant w_t with r is usually employed only where manufacturing reasons dictate. The slot leakage of constant w_t is more complex.

9.1.3 Slot Leakage Due to Coil Flux

With semi closed slots, the balance is made between protecting the conductors from exposure to the full excitation flux by giving the flux a path for coil linkage, and avoiding short-circuiting the excitation flux with tooth–tooth leakage. The coil current induces a leakage field across the slot. The field intensity in the slot is shown on the left in Figure 9.2, varying approximately linearly with the slot depth:

$$H(z) = \frac{(2N)\,i}{w_s}\frac{z}{d_s} \tag{9.4}$$

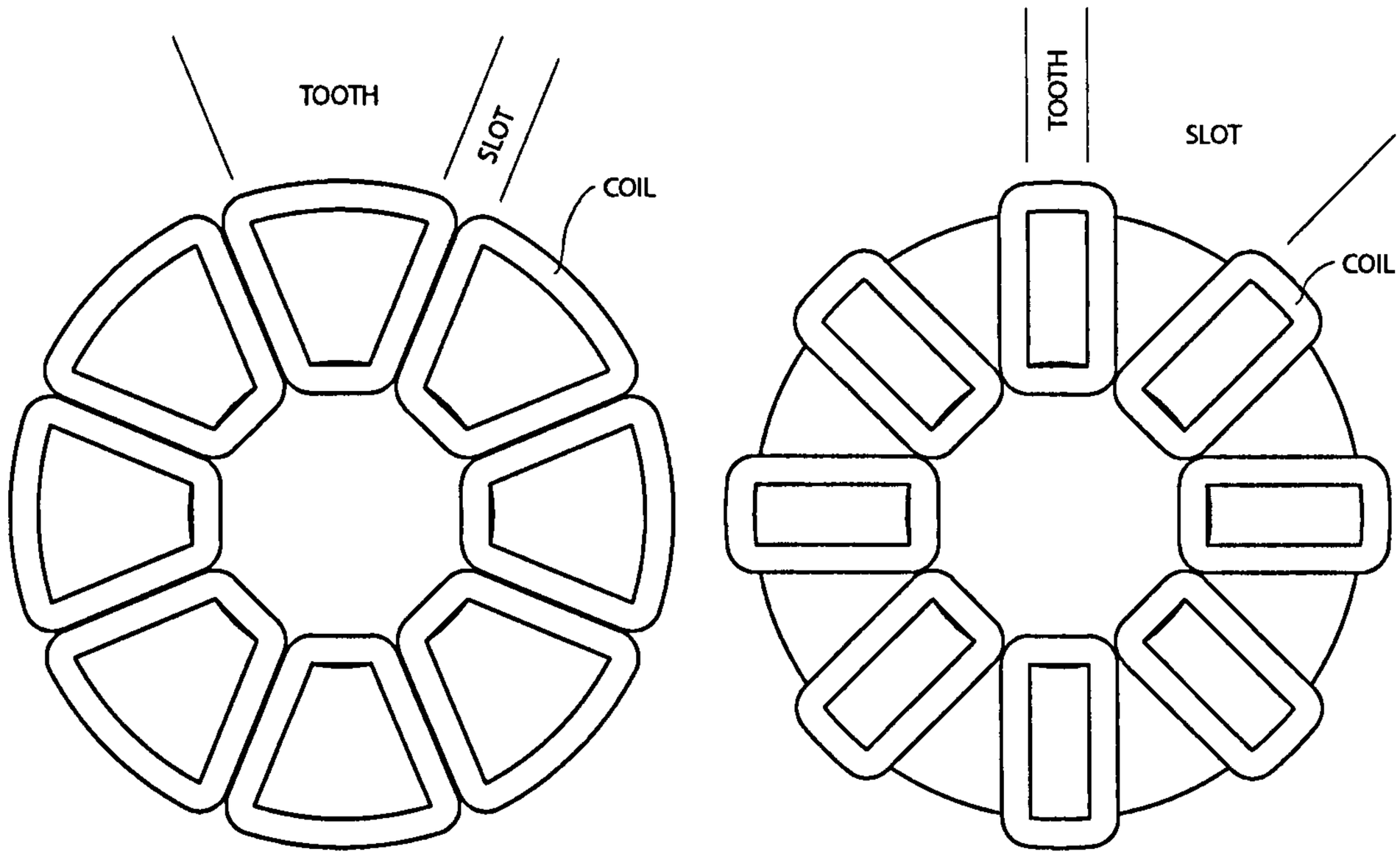


Figure 9.1: Teeth cross section and slot areas for constant $w_s(r)$ or $w_t(r)$, with 2 coils/slot concentrated coils.

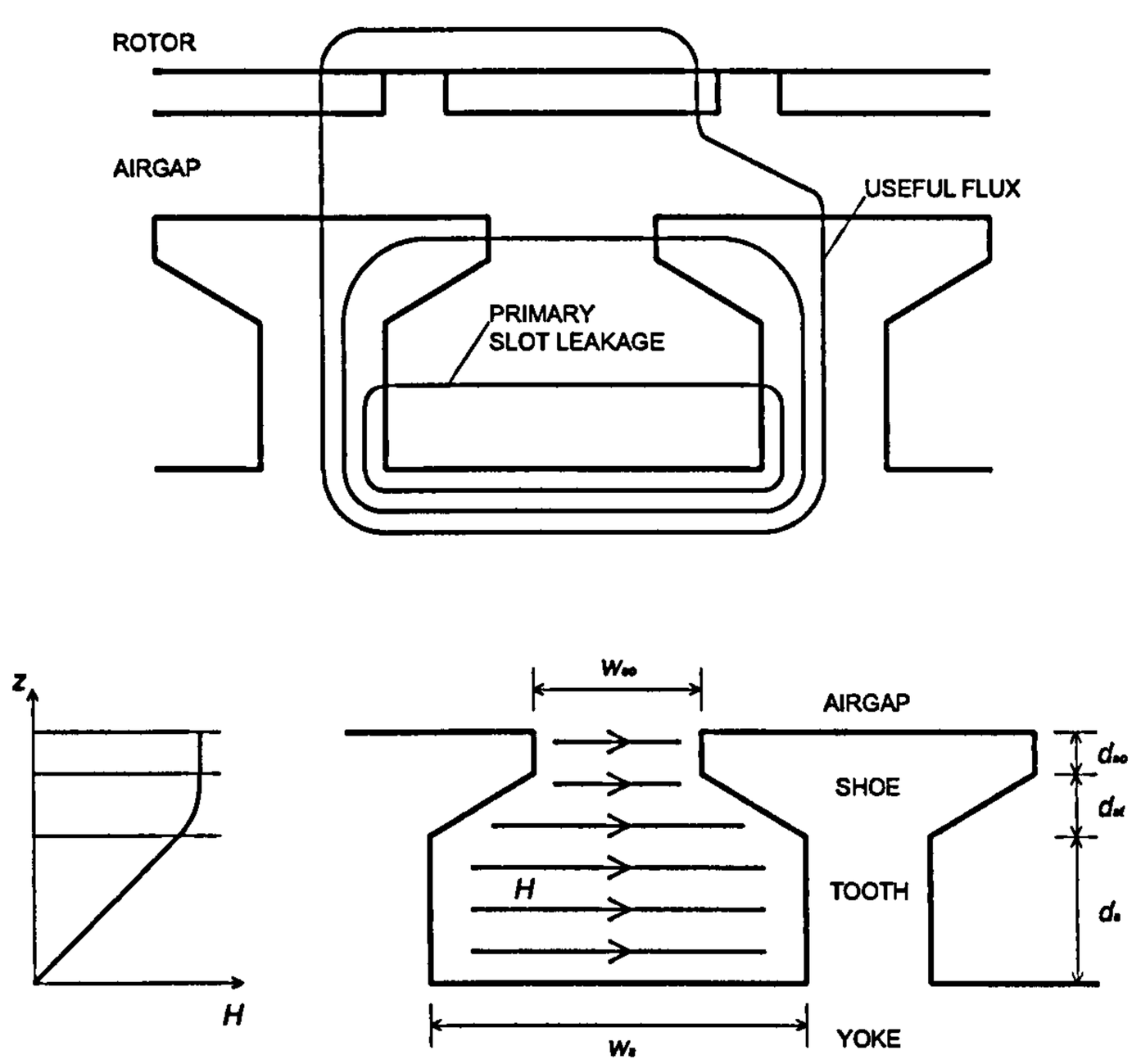


Figure 9.2: Useful and leakage coil flux paths, and slot magnetic field.

Using $\frac{1}{2}Li^2 = \int_V \frac{1}{2}\mu H^2 dV$ with a volume integral over the slot provides the inductance which matches the relationship $L_{ca} = N^2/\mathcal{R}$. The uniform distribution of the winding within the slot means the effective permeance is one third of the

normal slot permeance.

The shoe area inductance can also be approximated by $N^2/\mathcal{R}$ as the field intensity remains constant with all current already enclosed within the integral. With Q slots in a full pitch winding, this gives a slot leakage inductance of the winding proportional to the winding current.

The bottom of the slot may have filleted corners with radius r_{sf}. Similarly, the tapered slot region may be filleted.

9.1.4 Slot Leakage Due to PM Flux

Sen [1997] describes the difference between flux distribution on opposite sides of the airgap as accounted for by the "differential leakage". The fundamental components of the load mmf and flux linkage are balanced, as the machine is synchronous; yet the harmonic components are not balanced. The differential leakage therefore describes the ratio of the sum of the leakage fluxes and the fundamental flux linkage.

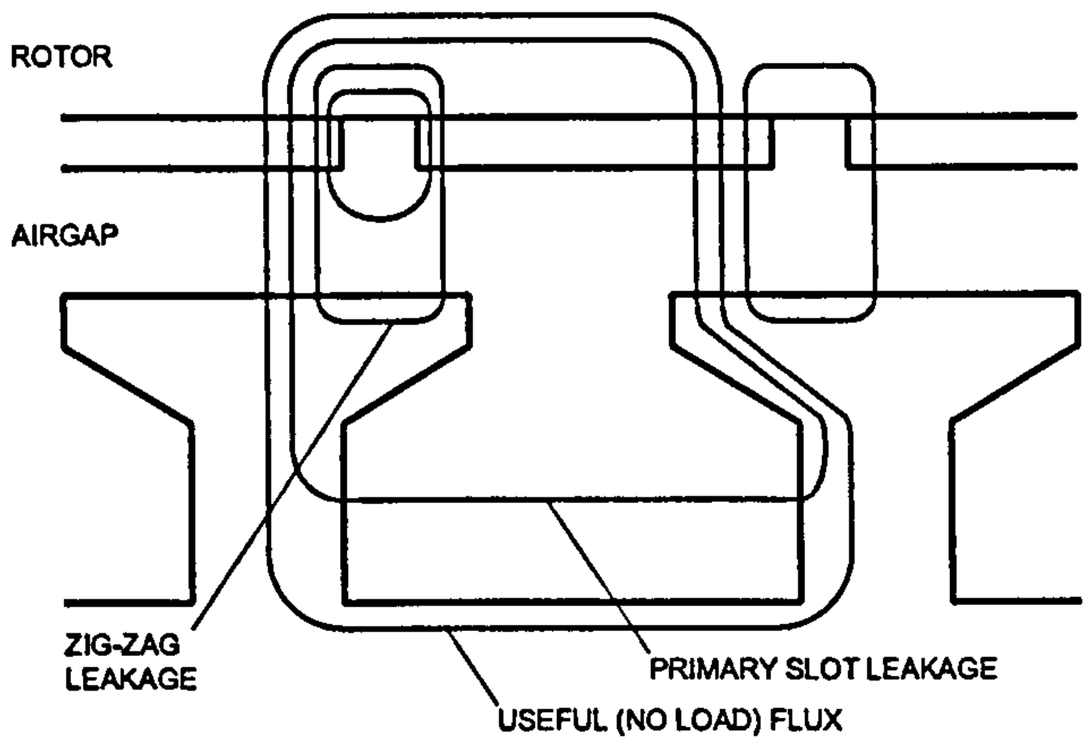


Figure 9.3: Useful and leakage paths for PM flux.

The two components of differential leakage are zigzag, shown in Figure 9.3 (along with short circuit leakage in the shoe region) associated with slots per pole and slot harmonics $2kQ/p \pm 1$, and belt associated with the winding distribution in phase belt harmonics $6k \pm 1$. Where $q < 1$, zigzag leakage on one side of the machine is zero, as it depends on the number of slots per pole but is independent of the coil pitch, while belt leakage is independent of the number of slots per pole but depends on the coil pitch.

9.2 Airgap Permeance Function

The airgap permeance function Λ describes the airgap reluctance with respect to the rotor position, which affects the main flux path circuit reluctance $d\mathcal{R}/d\theta$.

The slotless core airgap winding considered in Chapter 7 had a constant value for permeance with respect to rotor position and time.

The salient slotted stator has a non-zero Λ function, indicating the presence of cogging torque and various surface losses.

9.2.1 Carter Coefficient

A simple modification to airgap flux density with the Carter Coefficient k_{c1} takes into account possible fringing due to slots, without requiring a full airgap flux density analysis, and provides effective airgap $g' = k_{c1}g$ [Carter, 1926]:

$$k_{c1} = \left[1 - \frac{1}{\frac{\tau_s}{w_s o}\left(5\frac{g}{w_{so}} + 1\right)}\right]^{-1} \tag{9.5}$$

where τ_s and $w_s o$ are the stator slot pitch and slot opening width.

Fuller versions of this coefficient are available, and further airgap functions incorporating the Carter factor to obtain an airgap B_z function have been provided by, for example, Cavagnino, Cristino, Lazzari, Profumo and Tenconi [2000].

9.2.2 Effect of Slotting on Excitation Field

A unit area magnetic potential between a non-salient rotor and stator gives a constant airgap flux density of $B_g = \mu_0/g$. The permeance per unit area airgap is $\Lambda_0 = \mu_0/g_0$. For a non-salient rotor and salient stator the flux density varies as shown in Figure 9.4. The reluctance of the main flux path increases when the rotor is aligned with slot openings. This arises from a constant magnetic potential yet the effective airgap becomes longer, as described by the Carter factor, which increases the reluctance of the local flux path.

The mmf of the PM poles is assumed constant, which relates the flux to the permeance by $\mathcal{F} = \phi\mathcal{R}$.

Slots introduce a harmonic function variation in the airgap flux density waveform, where the fundamental period is $\Lambda_1 = 2p\pi/6pq = \pi/3q$. The fundamental period of the mmf is $\mathcal{F}_1 = \frac{2\pi}{\pi/3q} = 6q$.

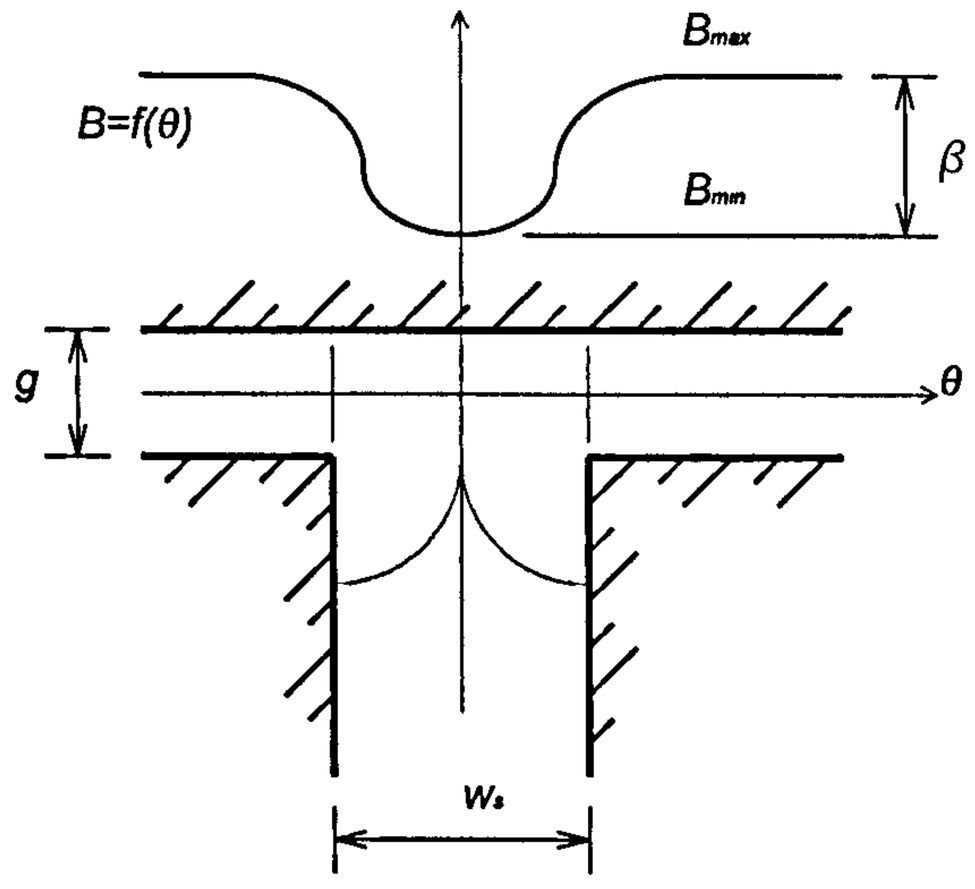


Figure 9.4: Airgap flux density pulse due to a slot.

9.2.3 Permeance Variation

The airgap length gives the airgap reluctance, but over slot openings this length increases, following the straight line – arc representation, shown in Figure 9.4. The new length becomes $g + \pi w_{so}/4$. The proportional variation in reluctance is described by $\pi w_{so}/(4g)$, so is minimised by reducing w_{so} or increasing g. A narrower slot opening reduces the flux variation, so shoes are useful to reduce the variation in the permeance function and the related cogging torque. By increasing g, the magnet length must be increased proportionally to maintain the required permeance coefficient for airgap flux density and motor performance.

9.2.4 Airgap Permeance Harmonics

Slots create pulsations in the main flux due to stator–rotor position and leakage flux. The permeance function is:

$$\Lambda_1(\theta) = \frac{\mu_0}{g_1(\theta)} \leqslant \Lambda_0 = \frac{\mu_0}{g_0} \tag{9.6}$$

so the airgap has changed from tooth to slot by $g_1(\theta) - g_0$.

9.2.5 Slot Field

Incorporating the permeance coefficient, the magnetic field energy of the slot opening becomes $\frac{1}{2}\mu_0 N_s^2 I^2 L \Lambda_1$, where $\Lambda_1 = h_1/b_1$ is the "specific permeance coefficient". For square slots this is defined by h_1/b_1, but other shapes are defined by further relations

provided by Luomi [1994].

$$\Lambda_1 = \frac{h_4}{3b_2} + \frac{h_3}{b_2} + \frac{h_1}{b_1} + \frac{h_2}{b_2 - b_1} \ln\left(\frac{b_2}{b_1}\right) \tag{9.7}$$

9.3 Losses

9.3.1 Eddy Current Losses from Slot Leakage

As a result of slot leakage, eddy currents flow in a direction to oppose the change of flux, as shown in Figure 9.5. In this case, at the top of the conductor nearest the slot opening, eddy currents add to the main current, and at the bottom they subtract from it. This is repeated for each conductor in the slot, yet they suffer different eddy current losses according to the position in the slot [Hanselman and Peake, 1995].

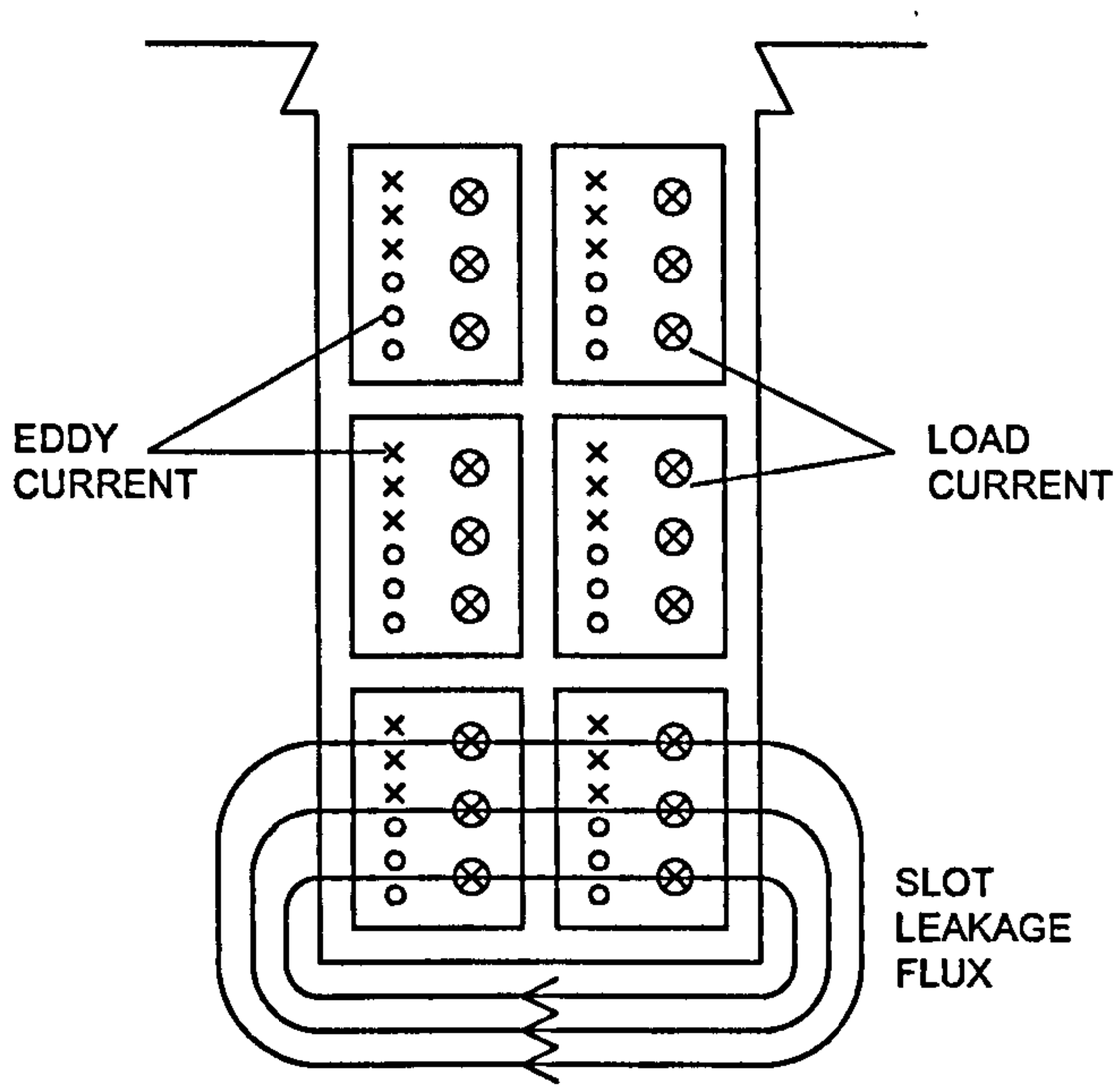


Figure 9.5: Conductor eddy currents from slot leakage.

The skin effect for rectangular conductors in slots is given by [Magnussen, 2004]:

$$\varphi(b'_c) = b'_c \frac{\sinh 2b'_c + \sin b'_c}{\cosh 2b'_c + \cos b'_c} \tag{9.8}$$

where $b'_c = \alpha_{b_c} b_c$ is the "reduced conductor height" using:

$$\alpha_{b_c} = \sqrt{\frac{nd_c}{w_s} \pi \mu_0 \mu_r f \sigma_{elec}} = \sqrt{\frac{nd_c}{w_s} \frac{1}{\delta_p}} \tag{9.9}$$

with n conductors in m layers per slot, of conductor width d_c.

The internal proximity effect due to neighbouring conductors of the same coil is:

$$\psi(b'_c) = 2b'_c \frac{\sinh b'_c + \sin b'_c}{\cosh b'_c + \cos b'_c} \tag{9.10}$$

giving a combined:

$$k_{T_p} = \varphi(\zeta) + \frac{I_u(I_u + I_p)}{I_p^2}\psi(\zeta) = \varphi(b'_c) + \frac{m^2 - 1}{3}\psi(b'_c) \tag{9.11}$$

where I_u is the total current in the layer of conductors and I_p is the total phase current. For low losses, $b'_c < 1$ gives $k_T = 1 + (m^2 - 0.2)b'^4_c/9$.

The modified expression describing active length and end winding loss becomes:

$$P_w^{loss} = 3\left[\underbrace{k_T \frac{l_{slot}}{l_c}}_{\text{in_slot}} + \underbrace{k_{T_{air}}\left(1 - \frac{l_{slot}}{l_c}\right)}_{\text{in_air}}\right] R_{dc} I^2 \tag{9.12}$$

9.3.2 No-Load Surface Losses

The variation of the airgap flux density causes similar proportional variation in the full flux path circuit, including in the magnets and rotor iron. This flux density variation in the rotor conductive materials induces eddy currents.

Losses arising due to large permeance function variations with slotting are no-load loss. (Losses due to the airgap leakage flux from stator mmf harmonics are on-load losses.) These cause pulsations in airgap flux, causing eddy currents in the stator and rotor cores, described as "surface losses". In the case of a laminated steel core, the lamination size and quality of machining determine the level of losses, as these cause lamination eddy currents and short circuits between neighbouring laminations.

By considering the airgap flux density made up of harmonic fields, with first order harmonics equal to $(Q \pm 2p)/2$, these losses may be evaluated. Harmonics are due to the permeance variation and on-load due to the stepped stator mmf wave. Both are based on the pole number and electrical speed, with losses proportional to the square of the vector sum. The approximation using the first harmonics is:

$$P_{surface} = 2\left(\frac{\pi(r_o^2 - r_i^2)\tau_s}{16}\right)(0.333 + 6.47)\left(\frac{\pi}{4}\right)^2\left(\frac{64.52 B_{g_ave}}{100}\right)^2 k_{pf} C_2 \tag{9.13}$$

where B_{g_ave} is the average airgap flux density, C_2 is the loss coefficient for PM or

iron, and $k_{pf} = (\frac{2\Delta B_g}{2-2\Delta B_g})^2$ where ΔB_g is the amplitude of the flux pulsation, assumed to be sinusoidal. A longer airgap length encourages a more sinusoidal airgap flux density waveform, as there is greater flux fringing. The variation in B_m is therefore less, which reduces the stray surface losses [Sebastian and Slemon, 1989].

PM pole surface losses are eddy current loss. Eddy currents in PM poles are reduced by using multi-piece poles. This does not impact on cogging torque, but multiple smaller pieces have a smaller individual width. In Radial Flux machines, multi-piece poles have been used in both the circumferential [Kabasawa and Takahashi, 2005] and axial [Ede et al., 2004] directions.

Electrically non-conductive bonded magnets are also used. With poles made up of multiple, insulated PM pieces, rather than one piece per pole, assembly issues may arise.

9.3.3 On-Load Surface Losses

The ratio of the stator mmf harmonic to the permeance variation harmonic is:

$$\frac{mmf \text{ harmonic}}{\text{permeance harmonic}} = \frac{2(2-2dB_g)}{2dB_g\left(2\frac{Q}{2p}\pm 1\right)}\left(\frac{I_1}{I_0}\right) \tag{9.14}$$

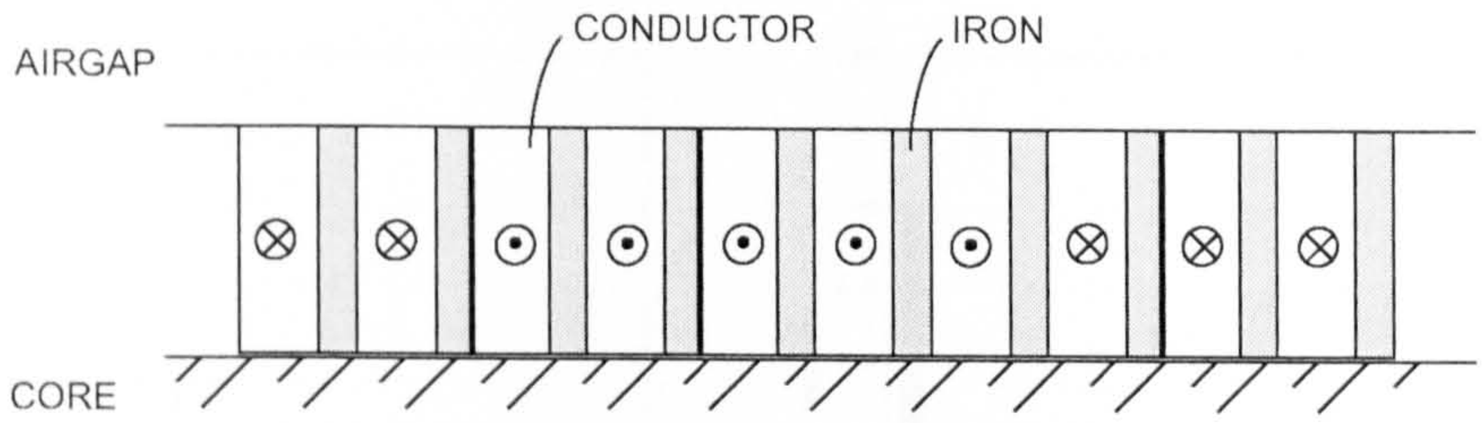
where I_1 and I_0 are the stator on-load and no-load currents. B_g harmonics from stator mmf, with winding arrangement dictating harmonics (i.e. coil pitch and phase belt) are not included here.

9.4 Integrated Teeth Winding

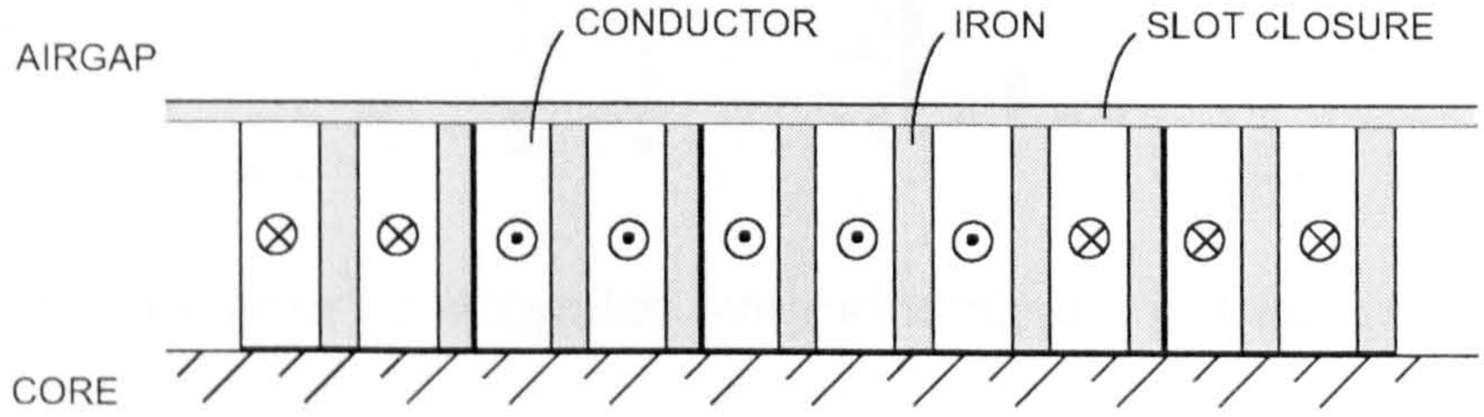
A possible adaptation of the proposed airgap winding is to sandwich the flat conductors with iron, creating small integrated teeth. This reduces the magnetic airgap length, increasing the airgap flux density, and the conductors are no longer fully exposed to the alternating excitation field. Two options for the inclusion of iron are shown in Figure 9.6.

By sandwiching individual turns, conductors may only be connected in series to form the coils. Otherwise, connection in parallel results in circulating currents due to the phase difference of the induced emf per conductor. Therefore, the coil inducced emf is the vector sum of the conductor induced emfs.

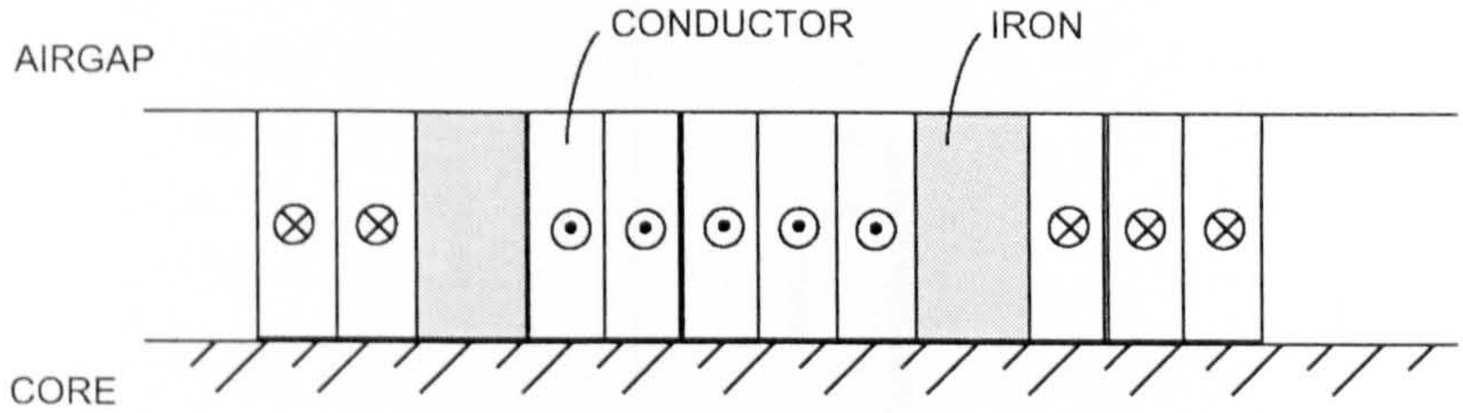
By sandwiching the coils, both parallel and series conductor connections are available, which resembles the open slot stator structure.



(a) Sandwiched individual turns.



(b) Sandwiched individual turns with slot closure.



(c) Sandwiched coils.

Figure 9.6: 2D view of integrated teeth.

The attractiveness of the integrated teeth winding arises from the manufacture possibilities, in particular using compacted powder iron [Fletcher, R., 2001]. The integrated teeth material may be a different iron from the core material. This allows use of electrical steel and compacted iron powder. By this way, the teeth can be compacted around the conductors as a final manufacturing process.

9.4.1 Stator mmf

Referring to Figures 7.16 and 7.17 of the proposed interleaved concentrated coil for an airgap winding, the harmonic components were significant. The integrated teeth winding offers a stronger stator field with the possibility of lower harmonic magnitudes. Figure 9.7 illustrates the harmonic components of the B_s waveform at airgap positions 1 mm and 3.5 mm from the stator surface. These are lower than those of the proposed interleaved coil.

Figures 9.8, 9.9 and 9.10 illustrate equivalent harmonic components of the B_s waveform at airgap positions 1 mm and 3.5 mm from the stator surface, where the

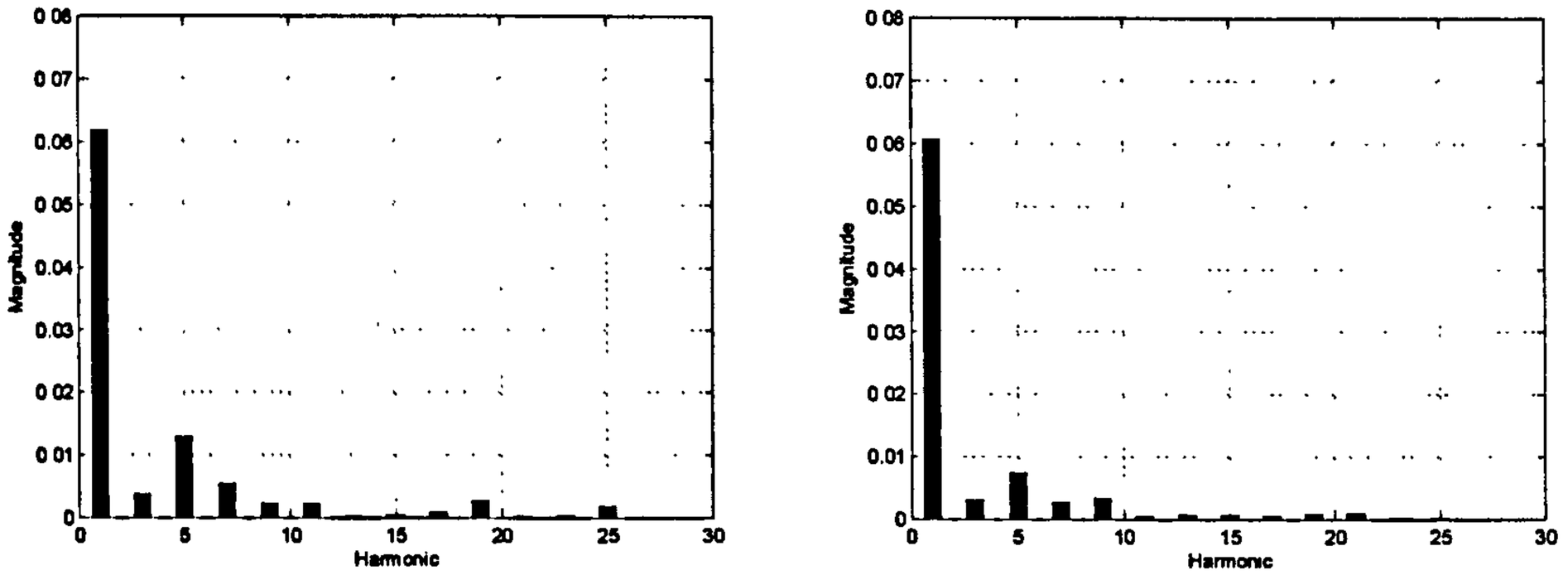


Figure 9.7: B_s waveform for integrated teeth winding at $z = 1$ mm and $z = 3.5$ mm airgap positions.

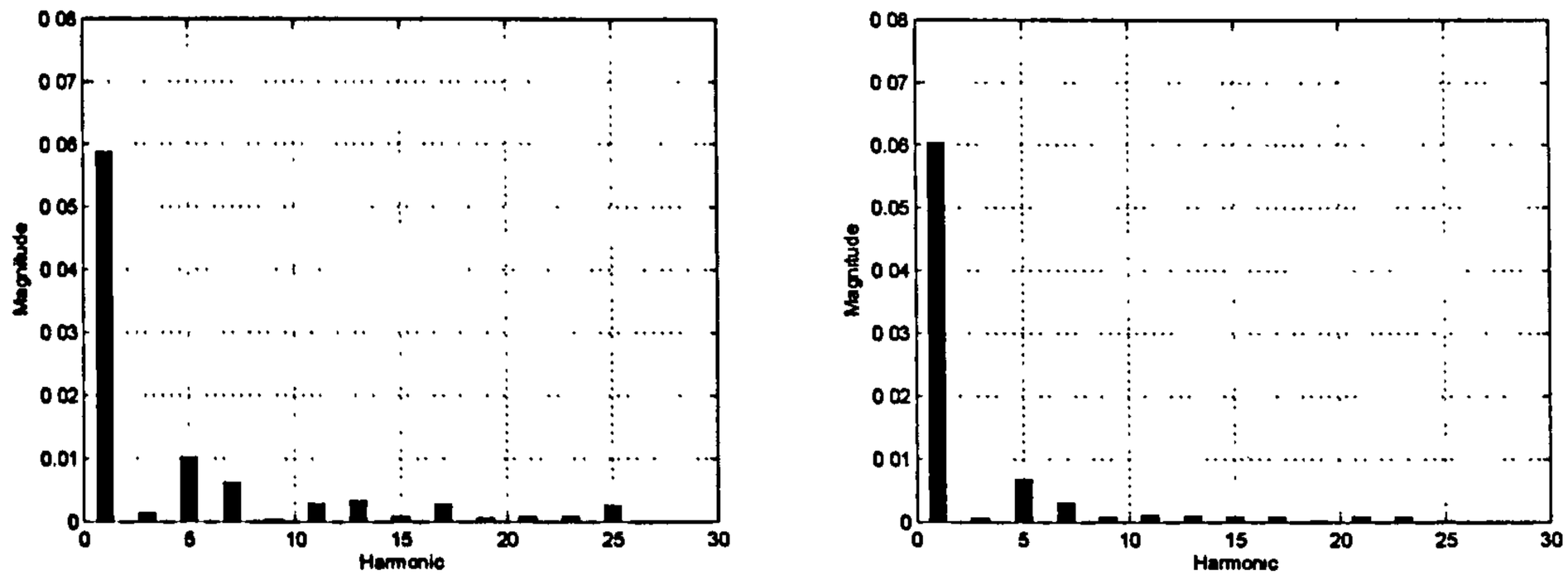
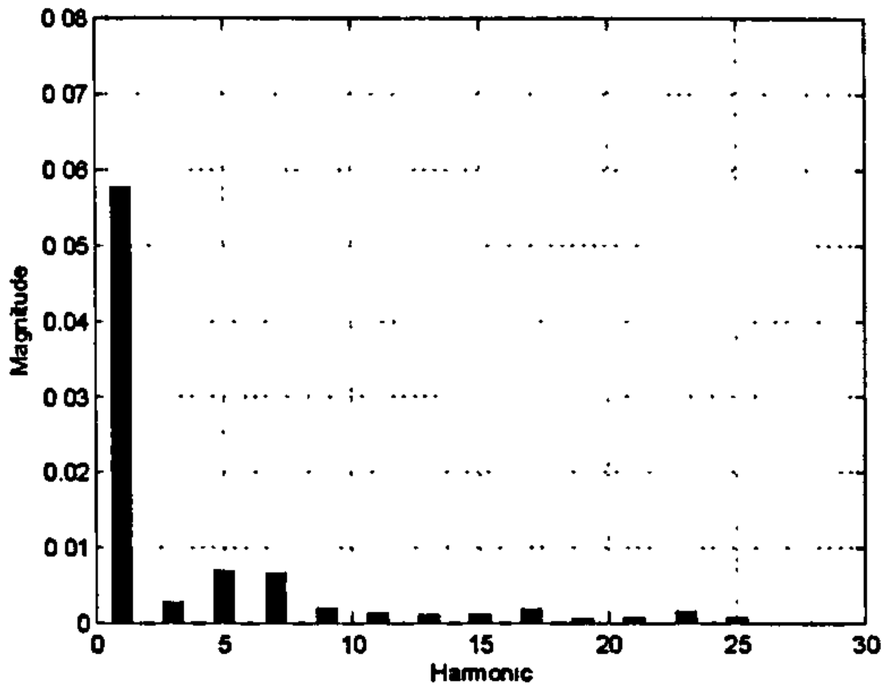


Figure 9.8: B_s waveform for integrated teeth winding with 0.1 mm slot closure at $z = 1$ mm and $z = 3.5$ mm airgap positions.

integrated teeth winding has slot closures with 0.1 mm, 0.5 mm and 1.0 mm depths. The slot closure reduces the harmonic components without reducing the fundamental harmonic. The 0.5 mm depth slot closure produces the lowest harmonics, indicating that reducing saturation is not required.

9.5 Summary

The description of cored stator harmonics and the conductor losses allows an evaluation of the copper losses from the harmonics present in the excitation. The analysis carries over conductor analysis methodology, which was built up in earlier chapters on slotless machines, to slotted machines, which are far more commonly employed. Meanwhile, it is useful to consider the harmonics in the airgap permeance function when designing the slotted core, as these contribute to the power loss mechanisms,



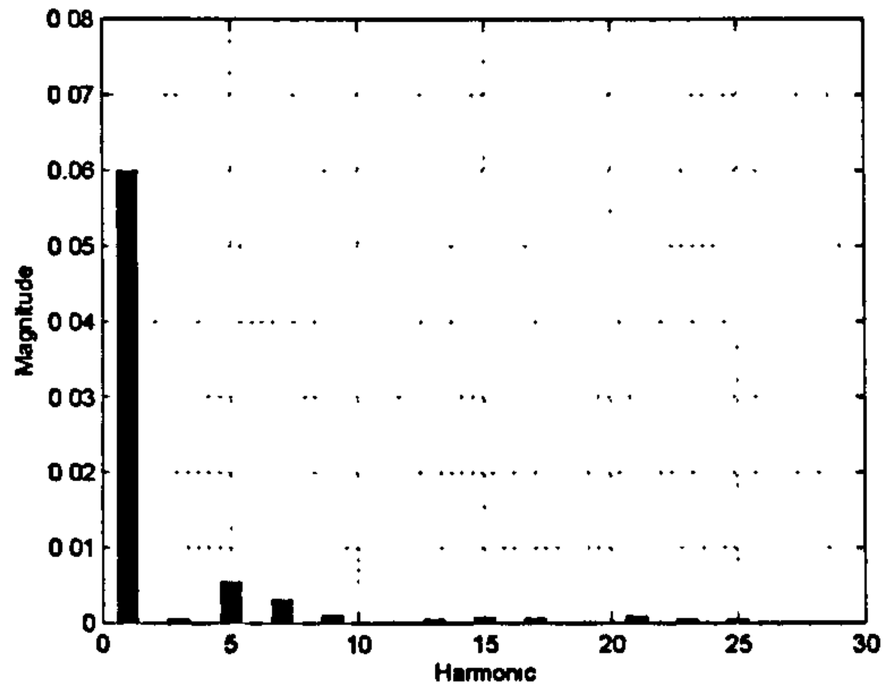
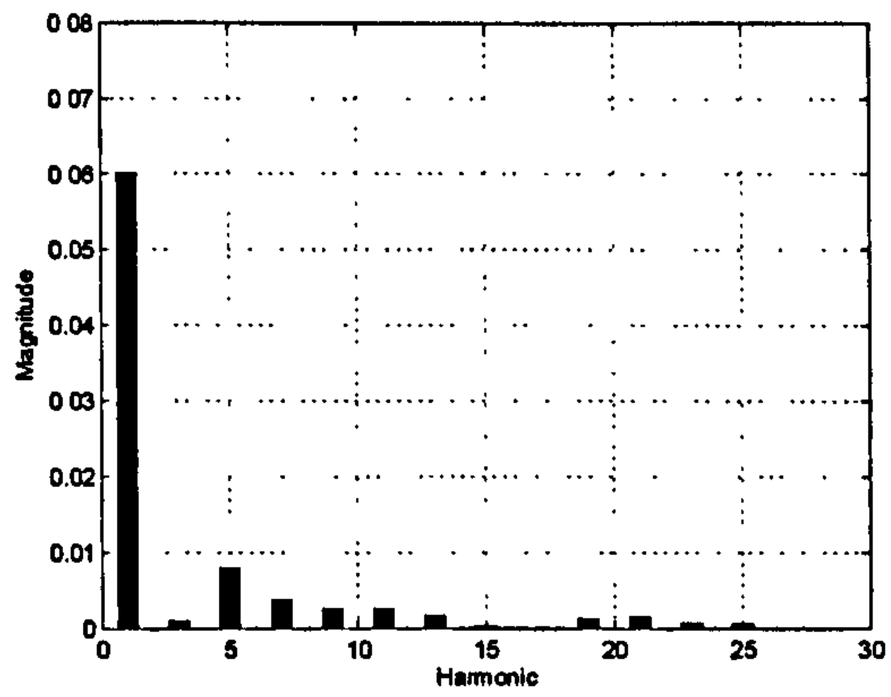


Figure 9.9: B_s waveform for integrated teeth winding with 0.5 mm slot closure at $z = 1$ mm and $z = 3.5$ mm airgap positions.



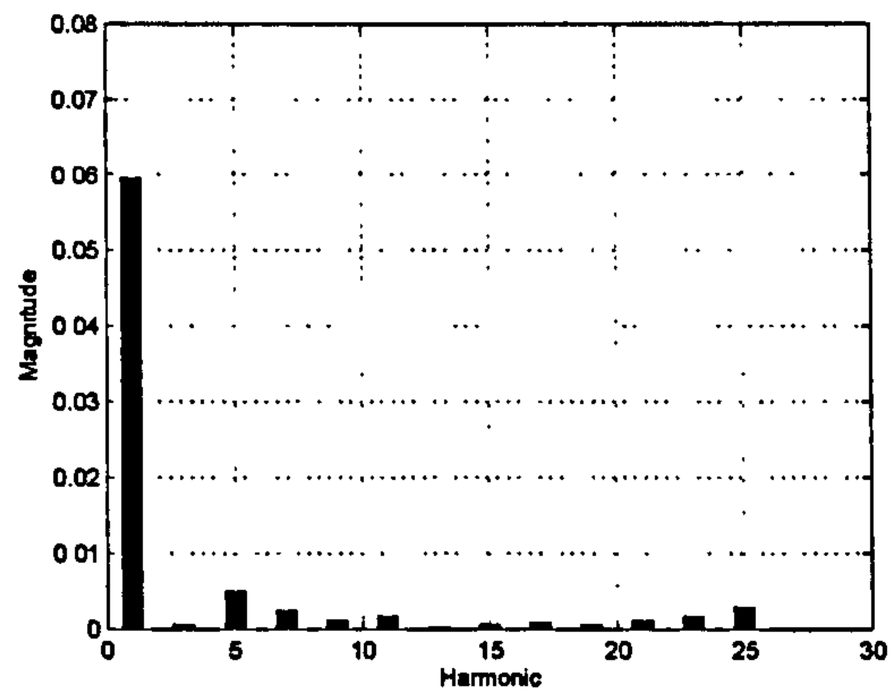


Figure 9.10: B_s waveform for integrated teeth winding with 1.0 mm slot closure at $z = 1$ mm and $z = 3.5$ mm airgap positions.

most notably the rotor surface losses experienced in the previous chapter.

This analysis has not investigated the issue of iron losses. Using the permeance function, it may be seen that the desired excitation field waveform is modified by the core shape to achieve a sinusoidal flux density in the iron and therefore less losses, considering the total loss.

Chapter 10

Conclusions and Future Work

The research aims given in Section 1.9 outlined an intention to build on the advantages offered by Axial Flux PMSM machines in HEV powertrains.

10.1 Relative to Research Objectives

The Axial Flux machine has not been explored for use in HEV powertrains, other than as a wheel motor. Through previous work and the machine design work reported here, it has been demonstrated that the Axial Flux machine can have advantageous performance characteristics and space envelope for use in powertrain applications.

Derivation of design equations and manipulation into a program for initial Axial Flux machine parameter selection

Chapter 4 outlined theoretical relations, which describe the operation of the Axial Flux PMSM machine. Versions of these for Radial Flux machines are widely available. However, derivation of these for Axial Flux machines in a generic format, which can allow design optimisation on many parameters, has been undertaken here. The AFMPC programs have been created to derive the initial machine parameters, both geometric and electromagnetic, from the required performance and material data. Further versions of the AFMPC programs calculate the machine performance from a geometric description and operating conditions. Importantly, this now enables the use of a parametric analytical model describing the machine in a complete hybrid powertrain model, whose performance is calculated over defined vehicle drive cycles.

Analytical model of airgap fields and machine performance for sizing

The equivalent magnetic circuit modelling method offers flexibility in that a simple model can be employed for the main flux circuit, with a leakage coefficient, or all main and leakage flux circuits can be modelled individually. The equivalent magnetic circuit model derived here and introduced in Chapter 5 enables machine performance prediction under on-load and no-load conditions, but, more importantly, the detailed model of the airgap reluctance provides a computationally inexpensive analysis of the airgap field to higher accuracy than given by the general expressions used in the AFMPC programs. With this method, further analysis of the power loss components adds valuable detail to the initial design optimisation process.

Consideration of individual power loss sources according to electromagnetic design aspects, for which harmonics are an important focus

Machine design details have been proposed and systematically examined. These were shaped poles in Chapter 6, interleaved concentrated coils in Chapter 7 and integrated teeth in Chapter 9. In each case, the examination has been of conductor losses, or machine characteristics which contribute to conductor losses. In the case of the Permanent Magnet Synchronous Machine with an ideal sinusoidal waveform, it is harmonic components in the excitation field and therefore induced emf, which are an unnecessary source of conductor losses, in particular eddy currents. The shaped poles were shown to offer slight improvement in the airgap field, but only offer ease of manufacture over the Halbach array. However, the detailed investigation of conductor selection and concentrated coil designs for airgap windings illustrated the attractive copper fill factor when using flat wire. Using flat wire in integrated teeth windings is also attractive, if slot closures are employed to manage the harmonic components of the reactive field.

Analytical and empirical model of HEV electric powertrain to evaluate efficiency and help achieve maximum efficiency of individual components

A 7.5 tonne Commercial Vehicle performing urban deliveries is the candidate vehicle for a hybrid electric powertrain. The hybrid configuration employs an electric drive with an Axial Flux integrated motor generator and a battery pack. Chapter 2 described the analysis of this electric drive including battery pack, accounting for the individual power loss aspects, such as battery Ohmic heating and management, switching devices and machine loss components. Analysing loss components on an individual basis is particularly useful, as it highlights the loss factors which dominate

in different operating conditions. By comparing the component duty cycles, i.e. time spent operating under particular conditions, which are derived from a typical vehicle drive cycle, the desired characteristics become apparent and can be related to the performance.

Demonstrate superior performance of Axial Flux machine in powertrain applications

Axial Flux machine designs have been proposed for two case study applications. These are an IMG, with a wide range of operating conditions under normal working circumstances, and a Generator, with a small selection of operating points depending on power demand. The design of these machines has been tailored for integration with existing powertrain components, such as physically with the engine, clutch and transmission, and electrically with the selected drive and battery. The manufacture of parts for these machines, and initial test results for the IMG, have been documented, but delays during manufacture mean the machines have not been demonstrated in their proposed applications. However, other characteristics, such as space envelope and operating efficiency have been demonstrated as superior to the Radial Flux alternatives.

10.2 Further Work

In the first instance, the outstanding assembly and integration of the electric machines for the case study hybrid powertrains requires completion.

Further research on machine electromagnetics, and in particular Axial Flux PMSM machines, should include:

- slot closures for machines with low pole numbers
- magnet skew and magnet pitch variation with respect to the radial position

Design investigations on other PMSM factors should include:

- end windings located closer to the stator core, reducing the diameter of the machine envelope
- integration of the cooling system into the active volume (rather than the standard airgap and core mounting plates)

Research on HEV powertrain components should include:

- use of optimised mechanical gears to move the motor operation to a lower speed, higher torque, and to limit the need for extended field weakening operation

- use of DC:DC voltage converters to raise the machine voltage and avoid using field weakening for higher speed operation, investigating the inefficiency of field weakening (considering the $d-$axis current) or inefficiency of the DC:DC voltage converter

Research on HEVs using existing electric drive components should include:

- combined machine, inverter and battery control for integrated energy management, with for example battery pulse charging from drive harmonics

Bibliography

Advanced DC Motors Inc. [2004].
*http://www.adcmotors.com/

Amaratunga, G., Acarnley, P. and McLaren, P. [1985], 'Optimum Magnetic Circuit Configuration for Permanent Magnet Aerospace Generators', *IEEE Transactions on Aerospace and Electronics Systems* **121**(2), 230–254.

Anderson, S. [n.d.], PhD thesis, Lund University of Technology, Sweden.

Anpalahan, P., Walker, A., Tsakok, S. and Lampérth, M. [2004], Axial Flux Machine Stator Construction with Concentrated Windings, *in* '16th International Conference on Electrical Machines', Lodz, Poland.

Arkadan, A., Vyas, R., Vaidya, J. and Shah, M. [1992], 'Effect of Toothless Stator Design on Core and Stator Conductors Eddy Current Losses in Permanent Magnet Generators', *IEEE Transactions on Energy Conversion* **7**(1), 231–237.

Atallah, K. and Howe, D. [1998], 'The Application of Halbach Cylinders to Brushless AC Servo Motors', *IEEE Transactions on Magnetics* **34**(4), 2060 –2062.

Atallah, K., Zhu, Z., Howe, D. and Birch, T. [1998], 'Armature Reaction Field and Winding Inductances of Slotless Permanent-Magnet Brushless Machines', *IEEE Transactions on Magnetics* **34**(5), 3737–3744.

Automotive World [2004].
*http://www.awknowledge.com/WCV/

Aydin, M., Huang, S. and Lipo, T. [2001*a*], Design and 3D Electromagnetic Field Analysis of Non-slotted and Slotted TORUS Type Axial Flux Surface Mounted Disc Machines, *in* 'Proceedings of IEEE International Conference on Electrical Machines and Drives', Boston, pp. 645–651.

Aydin, M., Huang, S. and Lipo, T. [2001*b*], Optimum Design and 3d Finite Element Analysis of Nonslotted and Slotted Internal Rotor Type Axial Flux PM Disc Machines, *in* 'Proceedings of IEEE Power Engineering Society Summer Meeting', Vol. 3, pp. 1409–1416.

Bäckström, T. [1996], Integrated Energy Transducer Drive for Hybrid Electric Vehicles, PhD thesis, Royal Institute of Technology, Sweden.

Barakat, G., El-Azzouzi, J. and Dakyo, B. [2002], Analytical Modeling of the Cogging Torque of an Axial Flux Permanent Magnet Synchronous Machine, *in* 'Proceedings of INTERMAG International Magnetics Conference', p. 392.

Bauder, R., Hoffmann, H., Stähle, H. and Pölzl, H.-W. [1997], Der neue audi v6-turbodieselmotor mit direkteinspritzung und vierventiltechnologie; konstruktion und mechanik,, *in* 'Internationales Wiener Motorensymposium'.

Benoudjit, A., Guettafi, A. and Nait Saït, N. [2000], 'Axial Flux Induction Motor for On-Wheel Drive Propulsion System', *Electric Machines and Power Systems* pp. 1107–1125.

BMW V8 [2002], *MTZ* p. 802.

Bolton, H., Liu, Y. and Mallinson, N. [1986], 'Investigation into a Class of Brushless DC Motor with Quasisquare Wave Voltages and Currents', *IEE Proceedings B* **133**(2), 103–111.

Boules, N. [1987], Design Optimisation of Permanent Magnet DC Machines, *in* 'Proceedings of IAS Annual Meeting, 22nd IEEE Industry Applications Conference IAS'87.', pp. 27–34.

Braunschweig Bus Drive Cycle [n.d.].

Brown, A., Ross, J., Nichols, K. and Penny, M. [2000], 'Simulation of Magneto-electronic systems using Kirchoffian Networks', *Sensors and Actuators* **81**, 346–350.

Campbell, P. [1974], 'Principles of a Permanent-Magnet Axial-Field D.C. Machine', *Proceedings of IEE* **121**(12), 1489–1494.

Campbell, P. [1975], 'The Magnetic Circuit of an Axial Field D.C. Electrical Machine', *IEEE Transactions on Magnetics* **11**(5), 1541–1543.

Caricchi, F., Crescimbini, F., Giulii Capponi, F. and Solero, L. [2001*a*], Permanent-Magnet, Direct-Drive, Starter/Alternator Machine with Weakened Flux Linkage for Constant-Power Operation over Extremely Wide Speed Range, *in* 'Proceedings of IAS Annual Meeting, 36th IEEE Industry Applications Conference IAS'01.', Vol. 3, pp. 1626–1633.

Caricchi, F., Crescimbini, F., Giulii Capponi, F. and Solero, L. [2001*b*], 'Permanent-Magnet, Direct-Drive, Starter/Alternator Machine with Weakened Flux Linkage for Constant-Power Operation over Extremely Wide Speed Range', *IEEE Transactions on Industry Applications* pp. 1626–1633.

Caricchi, F., Crescimbini, F., Honorati, O., Di Napoli, A. and Santini, E. [1996], 'Compact Wheel Direct Drive for EVs', *IEEE Industry Applications Magazine* pp. 25–32.

Caricchi, F., Crescimbini, F., Honorati, O., Lo Bianco, G. and Santini, E. [1998], 'Performance of Core-less Winding Axial-flux PM Generator with Power Output at 400 hz 3000 rpm', *IEEE Transactions on Industry Applications* **34**(6), 1263–1269.

Caricchi, F., Crescimbini, F., Mezzetti, F. and Santini, E. [1996], 'Multistage Axial Flux PM Machine for Wheel Direct Drive', *IEEE Transactions on Industry Applications* **32**(4), 882–888.

Caricchi, F., Crescimbini, F., Santini, E. and Santucci, C. [1997], Influence of the Radial Variation of the Magnet Pitch in Slotless Permanent Magnet Axial Flux Motors, *in* 'Proceedings of IAS Annual Meeting, 32nd IEEE Industry Applications Conference IAS'97.', pp. 18–23.

Caricchi, F. e. a. [1996], 'Compact Wheel Direct Drive for EVs', *IEEE Transactions on Industry Applications* .

Carter [1926], 'Magnetic Field of Dynamo Electric Machine', *IEE Transactions* .

Cavagnino, A., Cristino, M., Lazzari, M., Profumo, F. and Tenconi, A. [2000], A Simple Method to Predict the Induced EMF Waveform and the d-axis and q-axis Inductances of an Axial Flux Interior PM Synchronous Motor, *in* 'IEEE ...', pp. 208–214.

Cavagnino, A., Lazzari, M., Profumo, F. and Tenconi, A. [1999], Axial Flux Interior PM Synchronous Motor: Parameters Identification and Steady-State Performance Measurements, *in* 'IEEE ...', pp. 2552–2559.

Cavagnino, A., Lazzari, M., Profumo, F. and Tenconi, A. [2000], 'Axial Flux Interior PM Synchronous Motor: Parameters Identification and Steady-State Performance Measurements', *IEEE Transactions on Industry Applications* **36**(6), 1581–1588.

Cavagnino, A., Lazzari, M., Profumo, F. and Tenconi, A. [2001], A Comparison between the Axial Flux and the Radial Flux Structures for PM Synchronous Motors, *in* 'IEEE ...', pp. 1611–1618.

Cavagnino, A., Lazzari, M., Profumo, F. and Tenconi, A. [2002], 'A Comparison between the Axial Flux and the Radial Flux Structures for PM Synchronous Motors', *IEEE Transactions on Industry Applications* **38**(6), 1517–1524.

Chan, C. [1987], 'Axial-field Electrical Machines - Design and Applications', *IEEE Transactions on Energy Conversion* **2**(2), 294–300.

Chen, Y., Zhu, Z. and Howe, D. [1999], 'Slotless Brushless Permanent Magnet Machines: Influence of Design Parameters', *IEEE Transactions on Energy Conversion* **14**(3), 686–691.

Cho, C., Fussell, B. and Hung, J. [1993], Detent Torque and Axial Force Effects in a Dual Air-gap Axial-field Brushless PM Motor, *in* 'Proceedings of INTERMAG International Magnetics Conference', pp. CC–08.

Cirani, M. [1999], Permanent Magnet Synchronous Machine using the Torus Concept for Traction Application, Master's thesis, Royal Institute of Technology, Sweden.

Clarke, D. (Microcore) [2004]. Microcore Ltd.

Coles, P. [2003-4], MIHPOW internal report, Technical report, U of Bath.

Coles, P., Rodger, D., Hill-Cottingham, R., Lai, H., Lamperth, M. and Walker, A. [2004], Design and Analysis of an Axial Flux Permanent Magnet Machine, *in* 'Proceedings of IEE International Conference on Power Electronics, Machines and Drives, PEMD'04', Vol. 2, pp. 840–843.

Şimşir, N. and Ertan, H. [1999], A Comparison of Torque Capabilities of Axial Flux and Radial Flux Type of Brushless DC (BLDC) Drives for Wide Speed Range Applications, *in* 'Proceedings of IEEE International Conference on Power Electronics and Drive Systems PEDS'99', Hong Kong, pp. 719–724.

Di Napoli, A., Honorati, O., Santini, E. and Solero, L. [2000], 'The use of Soft Magnetic Materials for Improving Flux Weakening Capabilities of Axial Flux PM Machines', *IEEE ...* .

Dickeson, R. [2005], Commercial Vehicle News, SMMT.
*http://www.smmt.co.uk

Dubois, M., Polinder, H. and Ferreira, J. [2001], 'Comparison of Generator Topologies for Direct-Drive Wind Turbines', *IEEE* .

Dwyer, W. (Raser Technologies) [2003]. Technologies Inc.

Eastham, J., Balchin, X., Betzer, T., Lai, H. and Gair, S. [1995], Disc Motor with Reduced Unspring Mass for Direct EV Wheel Drive, *in* 'IEEE ...'.

Eastham, J. and Evans, P. [1978], 'Novel Disc-Motor Designs', *IEE Proceedings* **125**(5), 416. Correspondence.

Eaton Corporation [2004].

Ede, J., Atallah, K., Jewell, G., Wang, J. and Howe, D. [2004], Effect of Axial Segmentation of Permanent Magnets on Rotor Loss of Modular Brushless Machines, *in* 'Proceedings of IAS Annual Meeting, 39th IEEE Industry Applications Conference IAS'04', Vol. 3, pp. 1703–1708.

El-Hasan, T., Luk, P., Bhinder, F. and Ebaid, M. [2000], 'Modular Design of High-Speed Permanent-Magnet Axial-Flux Generators', *IEEE Transactions on Magnetics* **36**(5), 3558–3561.

Electric Vehicle Technologies [2004].
*http://www.evtworld.com/

Elmissiry, M. and Chari, S. [1992], 'Dynamic Performance of a Permanent Magnet, Axial Flux, Toroidal Stator, Brushless D.C. Motor', *IEEE* pp. 400–403.

Enova Systems [2004].
*http://www.enovasystems.com/

FIGE Drive Cycle [n.d.].

Fletcher, R. [2001], Electronically Commutated Electrical Machine. GB 2358523.

Ford [2005].
*http://www.ford.com/

ForesightVehicle Project: MIHPOW [2005].
*http://www.foresightvehicle.org.uk/

Furlani, E. [1992], 'A Method for Predicting the Field in Permanent-Magnet Axial-Field Motors', *IEEE Transactions on Magnetics* **28**(5), 2061–2066.

Furlani, E. [1994], 'Computing the Field in Permanent-Magnet Axial-Field Motors', *IEEE Transactions on Magnetics* **30**(5), 3660–3663.

Furlani, E. and Knewtson, M. [1997], 'A Three-Dimensional Field Solution for Permanent-Magnet Axial-Field Motors', *IEEE Transactions on Magnetics* **33**(3), 2322–2325.

Gair, S. and Yang, S. [1990], 'Transient Force Calculations on a Permanent Magnet Powder Metallurgical Cored Machine', *IEEE Transactions on Magnetics* **26**(2), 1054–1057.

Geetha, S. and Platt, D. [1992], Axial Flux Permanent Magnet Servo Motor with Sixteen Poles, *in* 'Proceedings of IAS Annual Meeting, 27th IEEE Industry Applications Conference IAS'92.', pp. 286–291.

General Motors [2004].
*http://www.gm.com/company/gmability/edu_k-12/9-12/fc_energy/hybrid_pht.html

Hammond, P. [1997], *Electromagnetism for Engineers: an Introductory Course*, 4 edn, Oxford: Pergamon.

Hanitsch, R., Belmans, R. and Stephan, R. [1994], 'Small Axial Flux Motor with Permanent Magnet Excitation and Etched Airgap Winding', *IEEE Transactions on Magnetics* **30**(2), 592–594.

Hanselman, D. C. [1998], *Brushless Permanent Magnet Motor Design*, 1st edn, Writers' Collective.

Hanselman, D. C. [2003], *Brushless Permanent Magnet Motor Design*, 2nd edn, Writers' Collective.

Hanselman, D. and Peake, W. [1995], 'Eddy-current Effects in Slot-bound Conductors', *IEE Proceedings Electric Power Applications* **142**(2), 131–136.

Hernandez-Aramburo, C. [2003], Losses in Inverter Driven Induction Motors, PhD thesis, Imperial College of Science, Technology and Medicine, UK.

Hill-Cottingham, R., Coles, P., Eastham, J., Profumo, F., Tenconi, A. and Gianolio, G. [2001], Multi-disc Axial Flux Stratospheric Aircraft Propeller Drive, *in* 'Proceedings of IAS Annual Meeting, 36th IEEE Industry Applications Conference IAS'01.', pp. 1634–1639.

Hill-Cottingham, R., Coles, P., Eastham, J., Profumo, F., Tenconi, A., Gianolio, G. and Cerchio, M. [2002], Plastic Structure Multi-Disc Axial Flux PM Motor, *in* 'Proceedings of IAS Annual Meeting, 37th IEEE Industry Applications Conference IAS'02.', pp. 1274–1280.

Högänas AB [2004], Soft Magnetic Composite.

Honda [2001], Honda Insight HEV.
*http://www.honda.com

Hredzak, B., Gair, S. and Eastham, J. [1996*a*], 'Elimination of Torque Pulsations in a Direct Drive EV Wheel Motor', *IEEE Transactions on Magnetics* **32**(5), 50105012.

Hredzak, B., Gair, S. and Eastham, J. [1996*b*], Variable Structure Control of a Disc Motor with Lateral Rotor Movement, *in* 'Proceedings of IEE Power Electronics and Variable Speed Drives', pp. 197–202.

Huang, S., Luo, J., Leonardi, F. and Lipo, T. A. [1999], 'A Comparison of Power Density for Axial Flux Machines based on General Purpose Sizing Equations', *IEEE Transactions on Energy Conversion* 14(2), 185–192.

Husain, I. [2003], *Electric and Hybrid Vehicles Design Fundamentals*, CRC Press.

Infolytica Corporation [2002], Magnet v.6.
*http://www.infolytica.com/fr/ coolstuff/ex0048/

ISE Corp. [2004].
*http://www.isecorp.com/

Iveco [2003], 4-cyl tector.

Jang, G. and Yoon, J. [1999], Three Dimensional Analysis of Magnetic Force and Torque in a BLDC Motor due to the Axial Variation of Yoke and Pole, *in* 'Proceedings of INTERMAG International Magnetics Conference', p. AF04.

Jang, G., Yoon, J., Ro, K., Park, N. and Jang, S. [1997], Performance of a Brushless DC Motor due to the Axial Geometry of the Permanent Magnet, *in* 'Proceedings of INTERMAG International Magnetics Conference', pp. BC–08.

Jensen, C., Profumo, F. and Lipo, T. [1992], 'A Low-Loss Permanent-Magnet Brushless dc Motor Utilizing Tape Wound Amorphous Iron', *IEEE Transactions on Industry Applications* **28**(3), 646651.

Kabasawa, A. and Takahashi, K. [2005], Development of the IMA Motor for the V6 Hybrid Midsize Sedan, *in* 'SAE 2005 World Congress & Exhibition'.

Krawczyk, A. and Tegopoulos, J. [1993], *Numerical Modelling of Eddy Currents*, Oxford: Clarendon Press.

Lammeraner, J. and Stafl, M. [1966], *Eddy Currents*.

Lampérth, M. [2000], Mechanical and Electrical Loses of PM Electric Machines, PhD thesis, Imperial College of Science, Technology and Medicine, UK.

Lewis, C. [2002], The Advanced Induction Motor, *in* 'Proceedings of IEEE Power Engineering Society Summer Meeting', Vol. 1, pp. 250–253.

Light Engineering Inc. [2003], Gensmart.
*http://www.lightengineering.com/

Lovat, H., Ramdenand, V. and Mecrow, B. [1998], 'Design an In-wheel Motor for Solar-powered Electric Vehicle', *IEE Proceedings B* **145**(5), 402–408.

Luomi, J. [1994], Magnetic Field Calculations, PhD thesis, Chalmers University of Technology, Sweden.

Lynch Motor Co. Ltd. [2001], Comparison of Brushed and Brushless Motors, Market technical assessment.

MacKenzie, J. and Walsh, M. [1990], *Driving Forces : Motor Vehicle Trends and their Implications for Global Warming, Energy Strategies, and Transportation Planning*, World Resources Institute.

Madlena, M., Gair, S., Canova, A. and Profumo, F. [1996], Torque Control of a BDC Axial Flux Drive Motor with Open and Closed Slot Configuration, *in* 'IEEE', pp. 837–843.

Magnussen, F. [2004], PhD thesis, Royal Institute of Technology, Sweden.

Magnussen, F. and Sadarangani, C. [2003], Winding Factors and Joule Losses of Permanent Magnet Machines with Concentrated Windings, *in* 'Proceedings of IEEE International Electric Machines and Drives Conference IEMDC'03', Vol. 1, pp. 333–339.

Marquis, I. [2004], title, Master's thesis, Imperial College of Science, Technology and Medicine, United Kindom.

Mbidi, D., van der Westhuizen, K., Wang, R., Kamper, M. and Blom, J. [2000], Mechanical Design Considerations of a Double Stage Axial-Flux PM Machine, *in* 'Proceedings of IAS Annual Meeting, 35th IEEE Industry Applications Conference IAS'00.', pp. 198–201.

Meeker, D. [2002], Femm: Finite element method magnetics.

Mercedes 400 V8 CDI [2004].
*http://www.hs-elektronik.com/datenblatt-e/mercedes-g400cdi-250ps-560nm.html

Millbrook Proving Ground Ltd. [1996], Mltb: Millbrook London transport Bus Drive Cycle.

Millner, A. [1994], Multi-Hundred Horsepower Permanent Magnet Brushless Disc Motors, *in* 'Proceedings of 9th Annual IEEE Applied Power Electronics Conference and Exposition, APEC94', pp. 351–355.

Nafisi, A. and Campbell, P. [1985], 'Composite Iron Powder Materials for the Armature of Axial-Field Permanent Magnet Machines', *IEEE Transactions on Magnetics* **21**(5), 1753–1755.

Nasar, S. and Unnewehr, L. [1984], *Electromechanics and Electric Machines*, 2nd edn, John Wiley and Sons (WIE).

Nipp, E. [1995], Extending the Field-Weakening Range of Surface Mounted Permanent-Magnet Motors, *in* 'Proceedings of PowerTech, Electric Machines and Drives', Stockholm, pp. 408–413.

Ofori-Tenkorrang, J. and Lang, J. [1995], A Comparative Analysis of Torque Production in Halbach and Conventional Surface-Mounted Permanent-Magnet Synchronous Motors, *in* 'Proceedings of IAS Annual Meeting, 30th IEEE Industry Applications Conference IAS'95.', Vol. 1, pp. 657–663.

Orange County Bus Drive Cycle [n.d.].

Parviainen, A., Pyrhönen, J. and Niemelä, M. [2001], Axial Flux Interior Permanent Magnet Synchronous Motor with Sinusoidally Shaped Magnets, *in* 'Proceedings of 10th International Symposium on Electromagnetic Fields in Electrical Engineering, ISEF', Cracow, Poland.

Patterson, D. [1996], 'Recent Advances in the Design and Construction of Axial Flux Permanent Magnet Machines', *IEEE Proceedings of Australia* . Centre for Energy Studies, Northern Territory University.

Penton [2005], Bearings Machine Design.
*http://www.bearings.machinedesign.com/

Perm Motor GmbH [2003], AC Synchronous Disc Motors with Permanent-Magnets; Generators. data sheet.
*http://www.perm-motor.de/home_e.html

Petro, J., Coonen, J. and Wasson, K. [2005], Small Motor Efficiency: A Growing Opportunity.
*http://www.novatorque.com/

Phillips, T. [2004], 'What Does High Efficiency Really Mean', *Drives and Controls* p. 36. WEG Electric Motors (UK).

Platt, D. [1989], 'Permanent Magnet Synchronous Motor with Axial Field Geometry', *IEEE Transactions on Magnetics* **25**(4), 3076–3079.

Powell, B., Bailey, K. and Cikanek, S. F. R. L. [1998], 'Dynamic Modeling and Control of Hybrid Electric Vehicle Powertrain Systems', *IEEE Transactions on Control Systems* .

Profumo, F., Tenconi, A., Zhang, Z. and Cavagnino, A. [1998], Novel Axial Flux Interior PM Synchronous Motor Realized with Powdered Soft Magnetic Materials, *in* 'IEEE', pp. 152–158.

Profumo, F., Tenconi, A., Zhang, Z. and Cavagnino, A. [2000], 'Design and Realization of a Novel Axial Flux Interior PM Synchronous Motor for Wheel-Motors Applications', *Electric Machines and Power Systems* **28**, 637649.

Profumo, F., Zhang, Z. and Tenconi, A. [1997], 'Axial Flux Machines Drives: A New Viable Solution for Electric Cars', *IEEE Transactions on Industrial Electronics* 44(1), 39–45.

Pullen, K. [1991], The Design and Development of a Small Gas Turbine and High Speed Generator, PhD thesis, Imperial College of Science, Technology and Medicine, UK.

Qu, R., Aydin, M. and Lipo, T. [2003], Performance Comparison of Dual-rotor Radial-flux and Axial-flux Permanent-magnet BLDC Machines, *in* 'Proceedings of IEEE International Electric Machines and Drives Conference IEMDC'03', Vol. 3, pp. 1948–1954.

Rahman, Z., Peyghaleh, M. and Matin, K. [2004], A Novel Coil Winding Technique Applicable to Multiple Strand Concentrated Wound Electric Motors for Low Voltage-High Torque Applications, *in* 'Conference Record of IEEE International Symposium on Electrical Insulation', pp. 8–11.

Romero-Hernandez, S. [2001], Windage Losses on Enclosed Rotating Discs with Superimposed Flow, PhD thesis, Imperial College of Science, Technology and Medicine, UK.

Roters, H. C. [1941], *Electromagnetic Devices*, John Wiley and Sons Inc., New York.

Rottenkolber, P. [2000], 'V 10 tdi: Leistungskrsus, kfz-betrieb', *Vogel Verlag* (2).

Sadarangani, C. [2000], *Electrical Machines - Design and Analysis of Induction and Permanent Magnet Motors*, KTH Högskoletryckeriet.

Saft [2003], Nickel-Metal Hydride Cell for the Automotive Industry. HV 4/5 SF. Data sheet.

Sahin, F., Tuckey, A. and Vandenput, A. [2001], Design, Development and Testing of a High-Speed Axial-Flux Permanent-Magnet Machine, *in* 'Proceedings of IAS Annual Meeting, 36th IEEE Industry Applications Conference IAS'01.', pp. 1640–1647.

Sebastian and Slemon, G. [1989], 'Transient Modeling of Performance of Variable Speed PM Motors', *IEEE Transactions on Industry Applications* **25**(1), 101–107.

Sen, P. [1997], *Principles of Electric Machines and Power Electronics*, 2nd edn, Wiley.

Shah, S., Wilkins, S., Walker, A. and Lampérth [2004], Battery pack size.

Shurflo Co. [2000], Axial Airgap Brushless DC Motor in both Salient and Non-salient Configurations, *in* 'Proceedings of SMMA Technical Conference'.

Sitapati, K. and Krishnan, R. [2001], 'Performance Comparisons of Radial and Axial Field, Permanent-Magnet, Brushless Machines', *IEEE Transactions on Industry Applications* **37**(5), 1219–1226.

Spooner, E. and Chalmers, B. [1990], TORUS - a Toroidal Stator, Permanent-Magnet Machine for Small-scale Power Generation, *in* 'Proceedings of International Conference on Electric Machines', MIT, USA, pp. 1053–1058.

Spooner, E. and Chalmers, B. [1992*a*], 'Toroidally-wound, Slotless, Axial-flux, Permanent-Magnet Generator', *IEE Proceedings B* **139**, 497–506.

Spooner, E. and Chalmers, B. [1992*b*], '"TORUS": A Slotless, Toroidal-stator, Permanent-Magnet Generator', *IEE Proceedings B* **139**(6), 497–506.

Stoll, R. L. [1974], *The Analysis of Eddy Currents*, Oxford: Clarendon Press.

Sullivan, C. [2001], 'Computationally Efficient Winding Loss Calculation with Multiple Windings, Arbitrary Waveforms, and Two-Dimensional or Three-Dimensional Field Geometry', *IEEE Transactions on Power Electronics* **16**(1), 142–150.

Swarowski [1995], *Calculus.*

Swindel, M. (Brook Compton) [2003], Rotating Electrical Machines, Axial Airgap Motors. data sheet.

Takano, H., Itoh, T., Mori, K., Sakuta, K. and Hirasa, T. [1992], 'Optimum Values for Magnet and Armature Winding Thickness for Axial-Field Permanent Magnet Brushless dc Motors', *IEEE Transactions on Industry Applications* **28**(2), 350–357.

Toshiba [1997], GTR module Si N channel IGBT MG300Q1Us51. Data sheet.

Toyota [2004].
*http://www.toyota.com/vehicles/2005/prius/key_features/hybrid_syn_drive.html

Turbo Genset Co. [2002], Core Technology.
*http://www.turbogenset.com

U. of Bath [1996], Mega v.6.

U. of Eindhoven [2001], Axial Flux PM Machine - Integrated Flywheel on Periphery. Electromechanics and Power Electronics Section.

U.K. DEFRA [2001], Climate Change United Kingdom Programme. report.

U.K. DTI National Statistics [2004*a*], Census 2001. report.
*http://www.statistics.gov.uk/census2001/

U.K. DTI National Statistics [2004*b*], Energy Consumption in the United Kingdom, orig. july 2002. report.

Unique Mobility [2002], Power Products.
*http://www.uqm.com/PowerProducts/index.html

U.S. DoE [2005], Fuel Economy.
*http://www.fueleconomy.gov/

Van Tichelen, P. and Peeters, E. [2003], Design of a new Axial Flux Permanent Magnet Generator for Hybrid Electric Vehicles, *in* 'Proceedings of 58th IEEE Vehicular Technology Conference VTC '03', pp. 3192–3196.

Visual Computing Systems Corp. [1997], Interlocking Segmented Coil Array. WO 97/44880.

Walker, A. [1999], title, Master's thesis, Imperial College of Science, Technology and Medicine, United Kindom.

Walker, A. [2002], Low Speed Generator Stator Design. Internal report.

Walker, A. [2003*a*], Analysis of Excitation Field of Surface-Mounted PM Poles giving Limited No-load Losses, *in* 'Proceedings of Int Conf on Electrical Drives and Power Electronics', Slovak Republic.

Walker, A. [2003*b*], Electric Motors and Generators in Hybrid-Electric Powertrains, *in* 'SAE Technical Paper Series 2003-01-2313, Proceedings of SAE International Future Transportation Technology Conference, FTT03', Society of Automotive Engineers, USA.

Walker, A. [2003*c*], Electric Traction System Design for a Hybrid Delivery Vehicle, *in* 'SAE Technical Paper Series 2003-01-3381, Proceedings of SAE International Truck and Bus Conference, T&B03', Society of Automotive Engineers, USA.

Walker, A. [2003*d*], Electrical System for a Hybrid Heavy Commercial Vehicle, *in* 'Proceedings of 20th Electric Vehicle Symposium', Long Beach.

Walker, A. [2003*e*], Permanent Magnet Excitation Field with Minimum Spatial-Harmonics, *in* 'Proceedings of 6th Int Symp on Electric and Magnetic Fields', Germany.

Walker, A. and Anpalahan, P. [2005], title, *in* 'Proceedings of 21st Electric Vehicle Symposium', AVERE, Monaco.

Walker, A., Lampérth, M. and Shah, S. [n.d.].

Wallace, R., Lipo, T., Morán, L. and Tapia, J. [1997], Design and Construction of a Permanent Magnet Axial Flux Synchronous Generator, *in* 'IEEE', pp. 4.1–4.3.

Wang, R. and Kamper, A. [2002], Evaluation of Eddy Current Losses in Axial Flux Permanent Magnet (AFPM) Machine with an Ironless Stator, *in* 'Proceedings of IAS Annual Meeting, 37th IEEE Industry Applications Conference IAS'02.', pp. 1289–1294.

Weart, S. [2003], *The Discovery of Global Warming*, Harvard Univ Press.

Weh, H. and Boules, N. [1980], 'Field Analysis for a High-Power, High-Speed Permanent Magnet Synchronous Machine of the Disc Construction Type', *Electric Machine and Electromagnetic* **5**, 25–37.

Weh, H., Hoffman, H. and Landroth, J. [1988], New Permanent Magnet Excited Synchronous Machine with High Efficiency at Low Speeds, *in* 'Proceedings of International Conference on Electric Machines', Italy, pp. 35–40.

West Midlands Joint Data Team [2001], Air Quality in the West Midlands, Technical report.

Wilkins [2002], Technical report.

Wrightbus [2004], Double Deck Products Gemini.
*http://www.wrightbus.com/bus_produc_dd.htm

Yang, Y.-P. and Chuang, D.-S. [2005], Optimal Design and Control of a Wheel Motor for Electric Passenger Cars, *in* 'SAE Technical Paper Series 2005-01-0282, World Congress & Exhibition'.

Yang, Y.-P., Luh, Y.-P. and Lee, C.-M. [2002], 'A Novel Design of Optimal Phase Current Waveform for an Electric Vehicle Wheel Motor', *Electric Power Components and Systems* **30**, 705–721.

Zhang, Z., Profumo, F., Tenconi, A. and Santamaria, M. [1997], 'Analysis and Experimental Validation of Performance of an Axial Flux Permanent Magnet Brushless DC Motor with Powder Iron Metallurgy Cores', *IEEE Transactions on Magnetics* **33**(5), 4194–4196.

Zhilichev, Y. [1998], 'Three-Dimensional Analytical Model of Permanent Magnet Axial Flux Machine', *IEEE Transactions on Magnetics* **34**(6), 3897–3901.

Zhu, Z. and Howe, D. [1992], 'Analytical Prediction of Coging Torque in Radial Field...', *IEEE Transactions on Magnetics* .

Ziegler, G., Hummel, K. and Krieger, K. [1997], 'Common rail einspritzsystem fr pkw-dieselmotoren', *Aachener Kolloquium* .

Appendix A

Theoretical Relations for Axial Flux Machines

A.1 Radial and Axial Machine Torque

Using the airgap magnetic shear stress σ_g for the electromagnetic force of rotor and stator interaction provides the torque according to the machine geometry of both Axial and Radial Flux machine topologies, given in Figure A.1.

An element of the rotor surface of a Radial Flux machine experiences a shear stress σ_g, giving a torque of:

$$dT_{Radial} = dA.r_g.\sigma_g = r_g d\theta dl.r_g.\sigma_g \tag{A.1}$$

which, over the airgap surface, becomes:

$$T_{Radial} = \int_{\theta=0}^{2\pi} \int_{l=0}^{l} r_g d\theta dl.r_g.\sigma_g = 2\pi r_g^2 l \sigma_g \tag{A.2}$$

A similar element of the rotor surface of an Axial Flux machine results in the torque:

$$dT_{Axial} = dA.r.\sigma_g = r d\theta dr.r.\sigma_g \tag{A.3}$$

which, over the airgap surface, becomes:

$$T_{Axial} = \int_{r=r_i}^{r_o} \int_{\theta=0}^{2\pi} r d\theta dr.r.\sigma_g = \frac{2\pi}{3}\left(r_o^3 - r_i^3\right)\sigma_g \tag{A.4}$$

Thus, with equivalent airgap shear stress:

$$T_{Axial} = \frac{(r_o^3 - r_i^3)}{3r_g^2 l} T_{Radial} \tag{A.5}$$

However, an equivalent airgap magnetic shear stress is unlikely as it is a function of the radial position in an Axial Flux machine.

Along the active length (in the radial direction), there is variation in the slot pitch, as investigated by Caricchi et al. [1997]. Furthermore, a single moment arm length cannot be used for the active area should such an approximation be required. Often, when a single length is required to provide an approximation of the torque for sizing, the inside radius is used, underestimating the true moment arm length, but compensating for the reduced airgap magnetic shear stress as r increases.

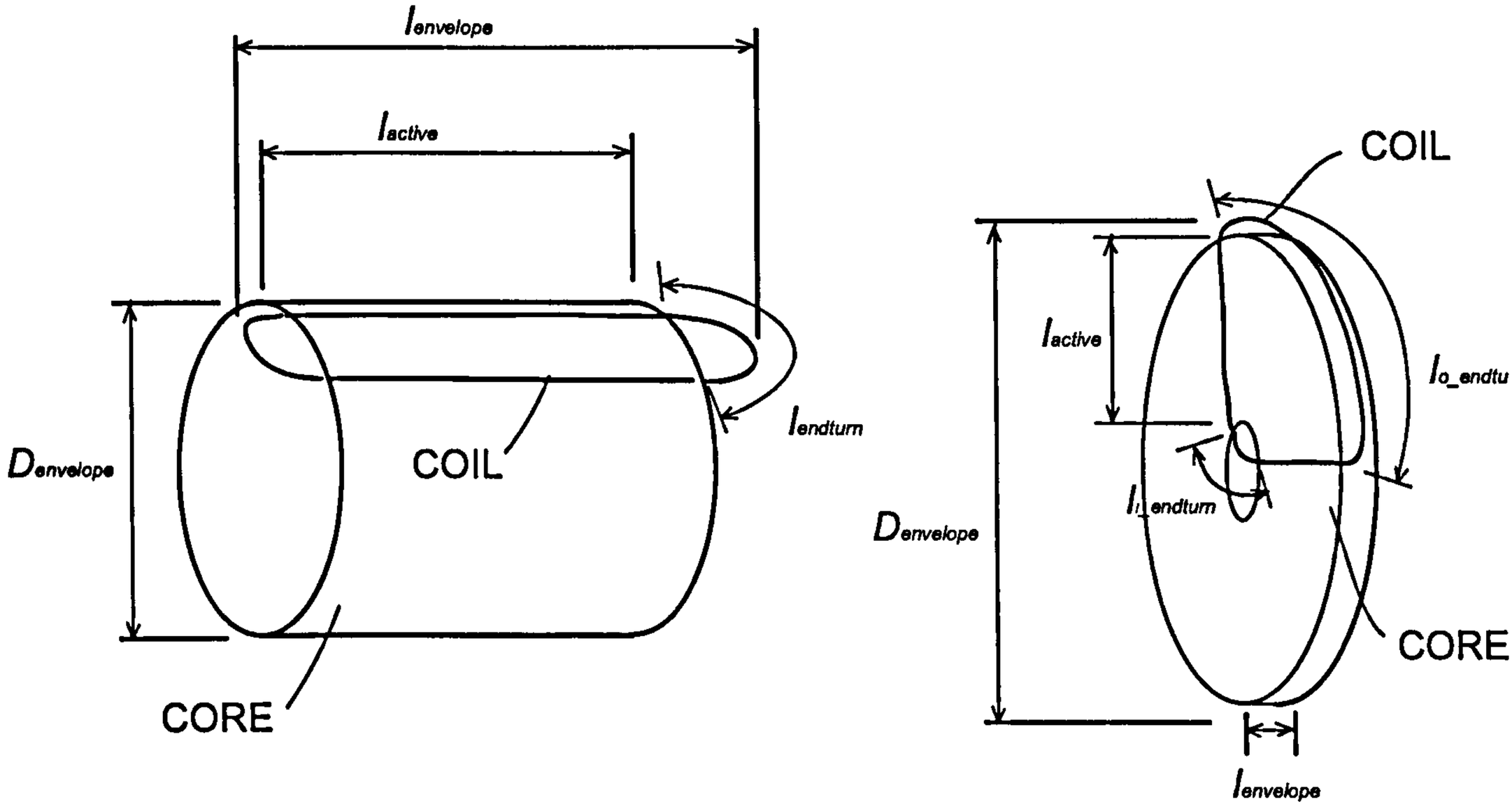


Figure A.1: Radial and Axial Flux machine topologies [Chan, 1987, orig.].

A.1.1 Airgap Shear Stress Calculation

The airgap magnetic shear stress of an Axial Flux machine is given by Equation (A.4) with knowledge of the torque and active area dimensions. Values for σ_g of up to 200 kN/m^2 for TFM and 350 kN/m^2 for HTS have been reported [Weh et al., 1988; Lewis, 2002].

Table A.1: Airgap magnetic shear stress values for selected machines [Lewis, 2002].

Motor	σ_g [kN/m^2]
Standard large induction motor	13
High performance 1500 rpm induction motor	13
Alsthom Low speed advanced induction (mill) motor (1992)	45
Alsthom Low speed advanced induction (naval prop.) motor (1997)	76
Alsthom Low speed advanced induction (naval prop.) motor (2002)	100
Selected PM motor	120
Low speed HTS motor	340

A.2 Y–connected BLDC Torque Calculation

The force expressions for BLDC machines given in Section 4.3.3 come from:

$$F = B_g S(r) \cdot A_{active} \simeq B_g S(r) \cdot \pi \left(r_o^2 - r_i^2\right) \tag{A.6}$$

where B_g is airgap flux density and $S(r)$ is the stator current loading, given by:

$$S(r) \simeq \frac{m n_s q \frac{2p}{2} I}{2\pi r} = \frac{mpqn_s I}{2\pi r} \tag{A.7}$$

With only $(m-1)/m$ phases conducting current, only this proportion of the machine active area is actively producing force.

$$F_\phi \simeq B_g pqn_s I \frac{(r_o^2 - r_i^2)}{r} \tag{A.8}$$

$$T_\phi = F_\phi \cdot r \simeq B_g pqn_s I \left(r_o^2 - r_i^2\right) \tag{A.9}$$

$$T_{tot} \simeq (m-1) B_g pqn_s I \left(r_o^2 - r_i^2\right) \tag{A.10}$$

A.3 PMSM Back *emf* Calculation

The expression given in Section 4.1.5 uses the rate of change of flux linkage, assuming all airgap flux links with the coil.

$$e = \frac{d\Psi}{dt} = \frac{d\theta_{el}}{dt}\frac{d\Psi}{d\theta_{el}} = \omega_{el}\frac{d\Psi}{d\theta_{el}} = p\omega_{mech}\frac{d\Psi}{d\theta_{el}} = p\omega_{mech}\frac{2N\phi_g}{\pi} \tag{A.11}$$

where ω_{mech} is mechanical speed in radM/s. Airgap flux for sector magnets can be given by:

$$\phi_g = B_m A_m = B_g \frac{\pi(r_o^2 - r_i^2)}{2p} k_{ppitch} \tag{A.12}$$

giving an amplitude of e of:

$$|e| = E = p\omega_{mech}\frac{2N}{\pi}\left(B_g\frac{\pi(r_o^2 - r_i^2)}{2p}k_{ppitch}\right) = 2NB_g(r_o^2 - r_i^2)k_{ppitch}\omega_{mech} \quad (A.13)$$

which agrees with the Blv law.

A.4 Motor Constant Calculation

The motor constant K_m in Section 4.4 assumes that the length of end turns and the active length are approximately equivalent (i.e. each 50% of the total conductor length):

$$K_M = \frac{2NB_g(r_o^2 - r_i^2)k_{ppitch}i}{\sqrt{I^2\,(2R_{slot})\,Q}} = \frac{2NB_g(r_o^2 - r_i^2)k_{ppitch}}{\sqrt{2\rho_{elec}(r_o - r_i)NQ/A_{Cu}}} = \frac{B_g(r_o + r_i)}{\sqrt{\rho_{elec}}}\frac{\sqrt{V_{Cu}}}{Q}\frac{\tau_m}{\tau_p} \quad (A.14)$$

where A_{Cu} and V_{Cu} are cross-sectional area and total volume of the copper given by $V_{Cu} = V_{Cu}(\text{slot}) + V_{Cu}(\text{endwind}) = 2NQ(r_o - r_i)A_{Cu}$.

A.5 Concentrated Coil Winding Dimensions

A.5.1 End Turn Length

Simplifications for the endturn dimensions at the inner and outer radii are shown in Figure A.2. τ_{c1} is for a winding with 1 coil/slot, while τ_{c2} is for one with 2 coils/slot.

$$l_{endturn_o} = \left(\pi 2r_o \tan\frac{\tau_s}{2}\right)\left(\frac{2\pi}{\pi + \tau_s}\right) = \left(\pi 2r_o \tan\frac{2\pi}{2Q}\right)\left(\frac{2\pi}{\pi + \frac{2\pi}{Q}}\right) = \ldots$$

$$= \left(r_o \tan\frac{\pi}{Q}\right)\left(\frac{4\pi}{1 + \frac{2}{Q}}\right) \quad (A.15)$$

$$l_{endturn_i} = \left(\pi 2r_i \tan\frac{\tau_s}{2}\right)\left(\frac{2\pi}{\pi - \tau_s}\right) \quad (A.16)$$

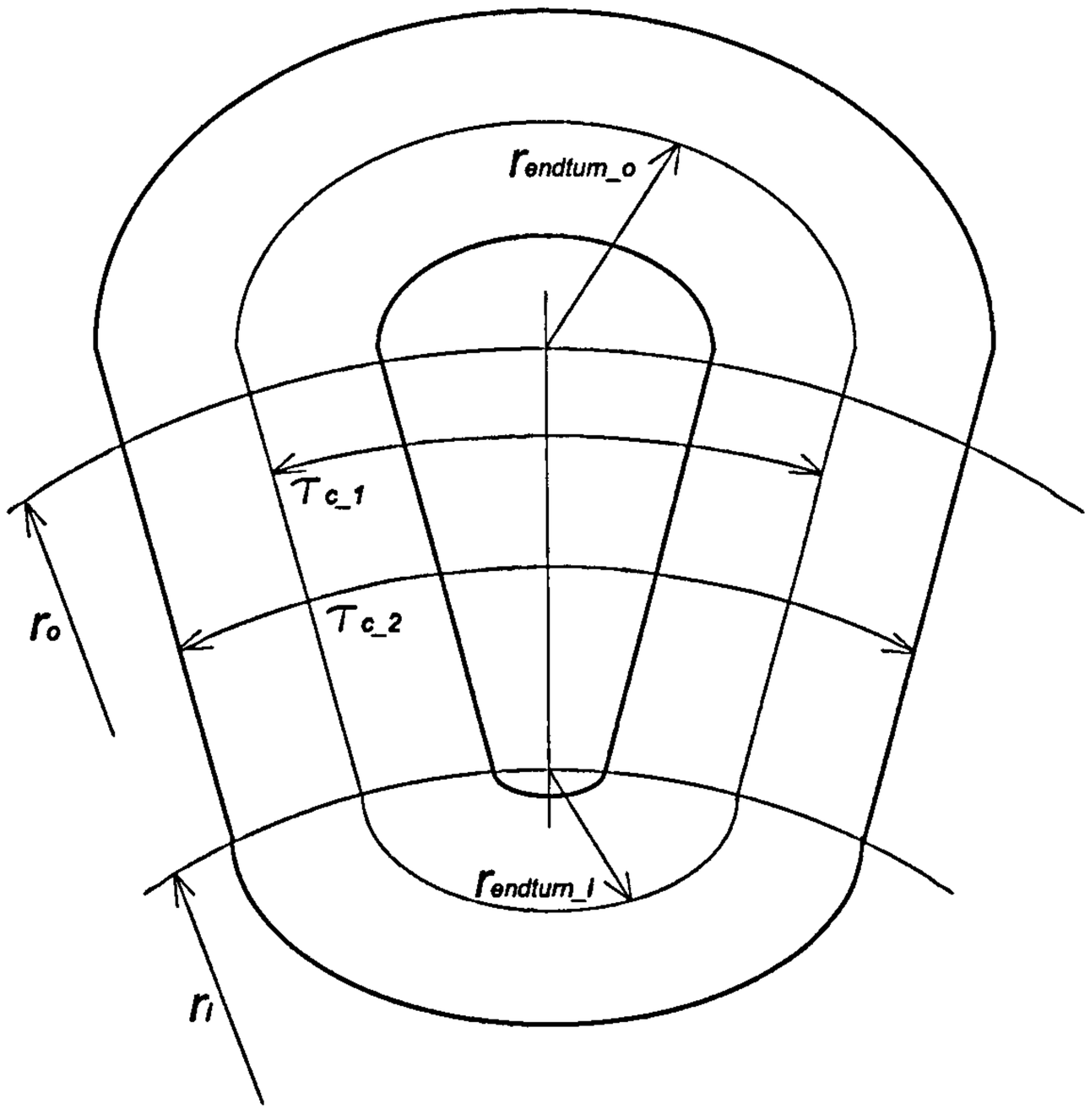


Figure A.2: End turn geometry for concentrated coils.

A.6 Skew

The cogging torque is often controlled by skewing the rotor, which also controls harmonics and reduces losses. This changes the phase of the pulsations in the permeance functions at different positions of the active length. Figure A.3(a) illustrates the unskewed arrangement and Figure A.3(b) illustrates the standard skewed arrangement. The force F is reduced by skewing, as it occurs over a wider greater electrical angle (accounted for by the "skew factor" k_{skew}) and because the force direction is no longer tangential (accounted for by $\sin(\alpha_{skew})$).

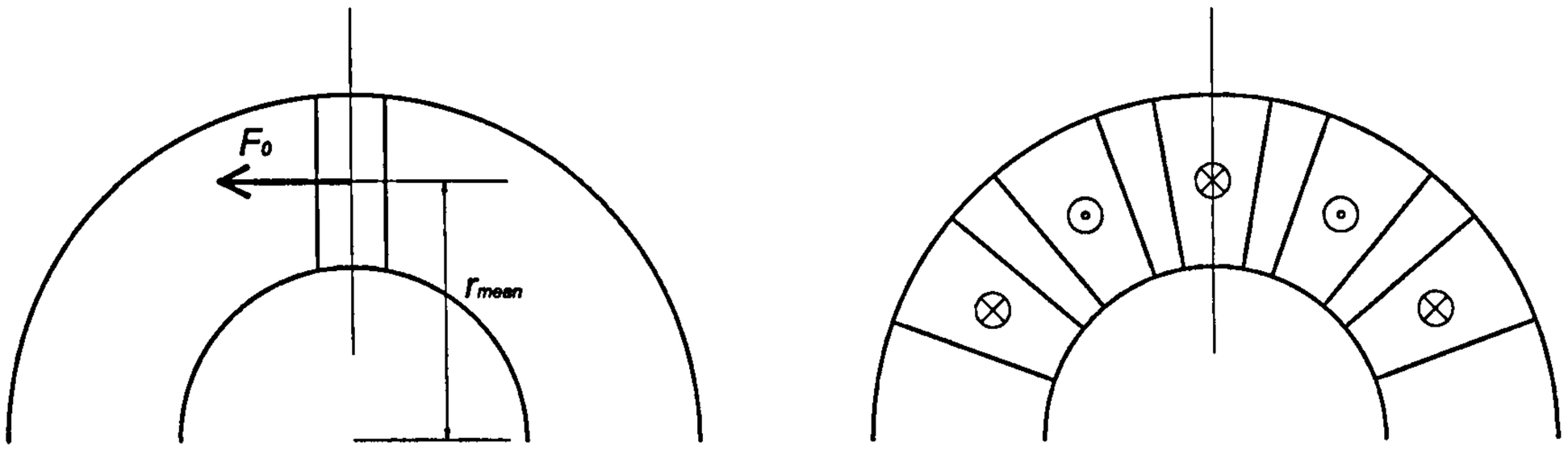
Current Source Inverter fed machines do not benefit in this way, as there is not the symmetrical multi-phase currents due to the steering bridge only feeding selected phases.

A.6.1 Skewed Rotor and Stator

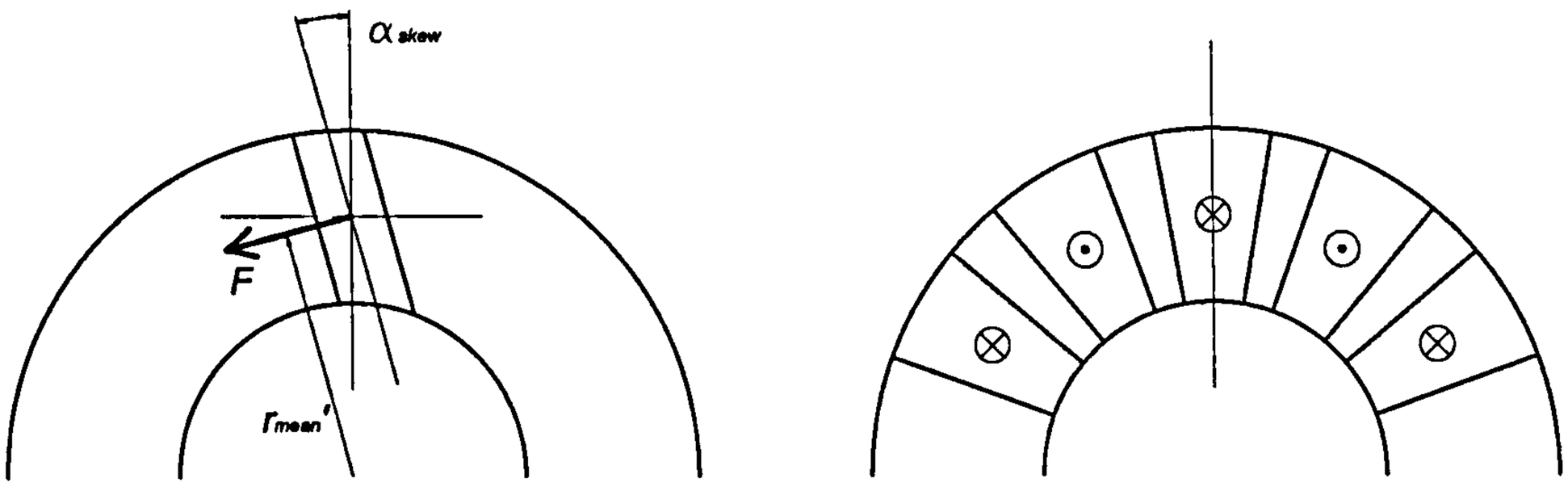
As the skew angle describes the angle between stator and rotor, it is irrespective of which item is skewed, and an alternative technique is to skew the stator, which is as common in Radial Flux machine design. This has practically the same effect as the difference in angle between pole and slot is the desired result.

However, it is possible to skew both the rotor and stator by half the skew angle

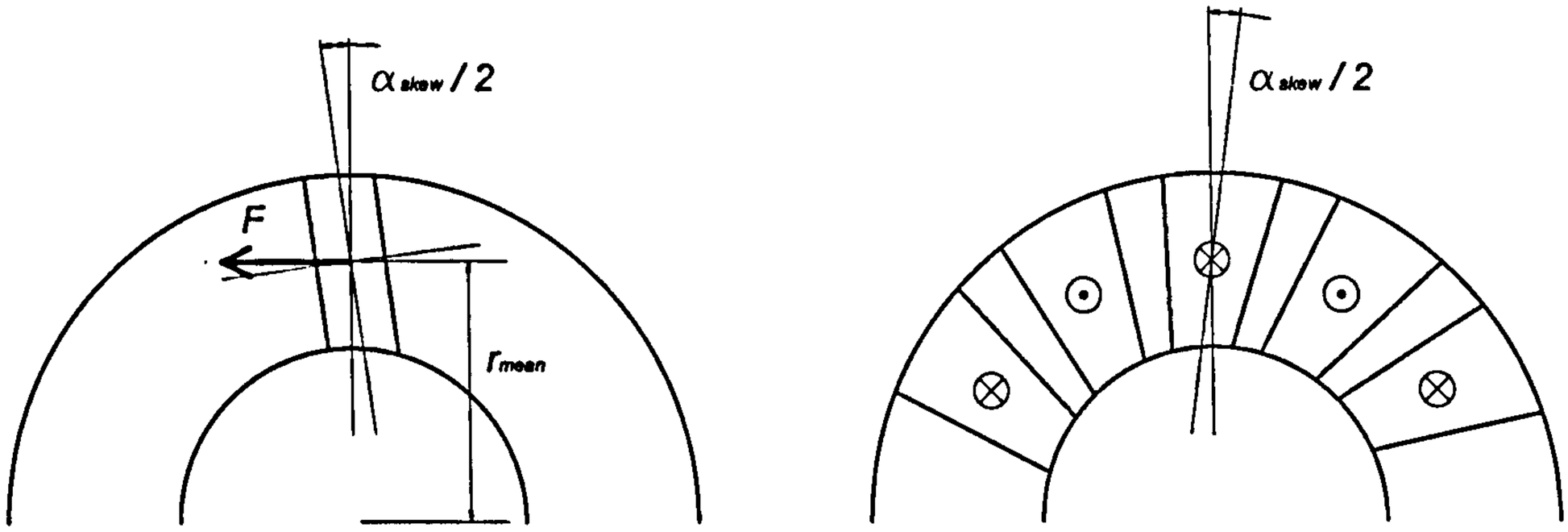
each, as shown in Figure A.3(c), which ensures the force remains tangential and maximises torque. The manufacture with winding coils into skewed slots is more complex with larger machines.



(a) Unskewed stator slot and unskewed sector shape poles. Force vector F_0.



(b) Skewed stator and unskewed poles. $F = k_{skew} \sin(\alpha_{skew}) F_0$.



(c) Skewed stator and skewed poles. $F = k_{skew} F_0$.

Figure A.3: Force vectors for skew angle between rotor and stator.

Further skewed slot designs include curved slots with both a forward or backward sweep.

A.6.2 Skew and Pole Pitch

Typically, the skew is one slot pitch to remove the fundamental component of cogging torque. The loss of torque is significant with low number of slots per pole per phase.

In addition to the variable of skew angle, the Axial machine has a variable for rotor magnet pitch which is not available to the Radial Flux machine.

Aydin et al. [2001*b*] and Nipp [1995] performed optimisation of the rotor pole skew to minimise the cogging torque.

It is not appropriate to skew one slot pitch if this is large in comparison with the active length [Boules, 1987]. While $\alpha_{skew} = \tau_s$ is appropriate to remove the fundamental cogging torque harmonics, a different value may be selected to provide the minimum overall cogging torque.

A.6.3 Skewed Slot Geometry

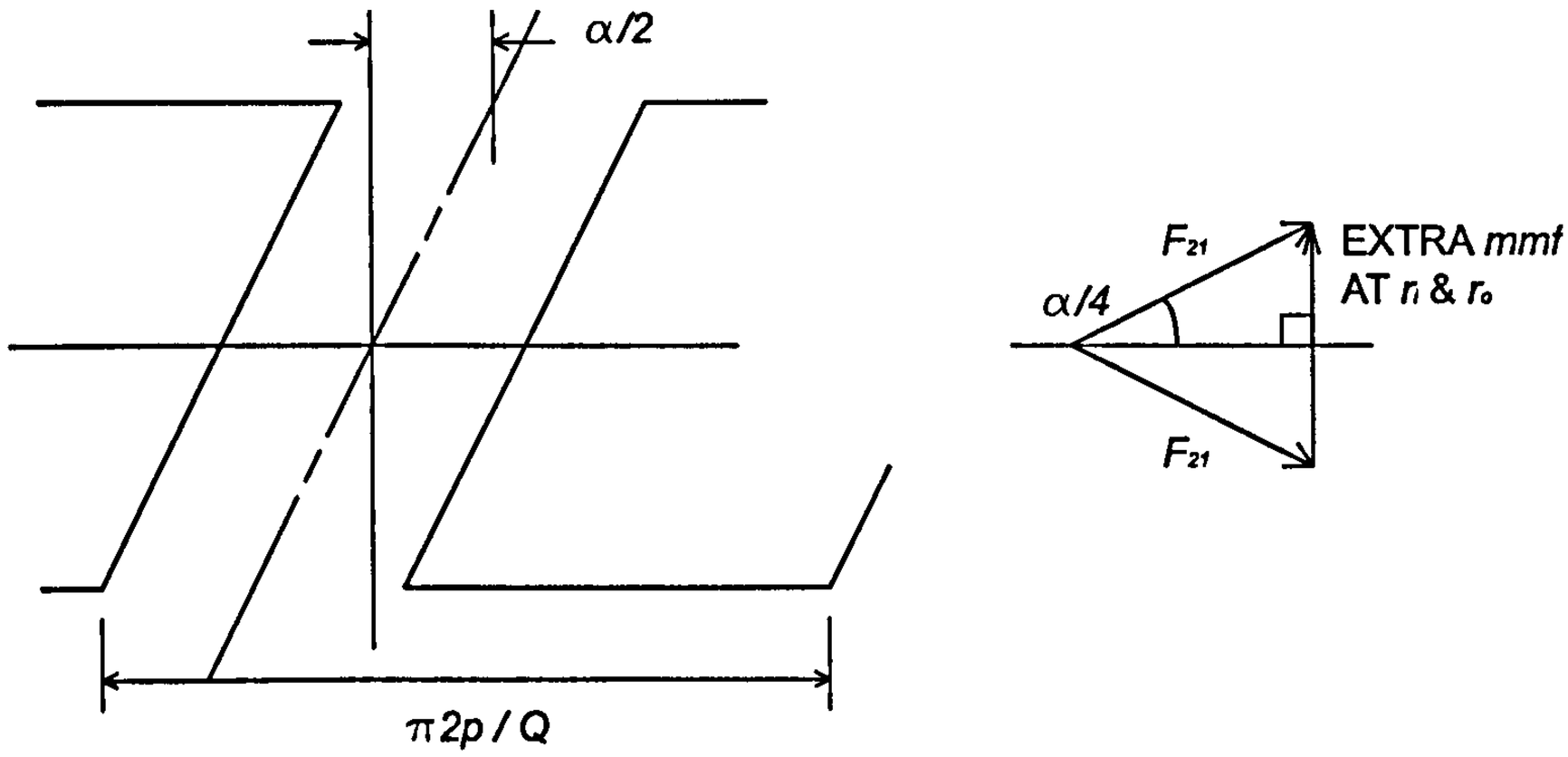


Figure A.4: geometry of skewed slot

One slot skewed by angle α, as seen in Figure A.4, has a "fractional skew" of $\sigma_{\text{frac skew}} = \alpha Q/\pi 2p$. Each end of slot is displaced by $\alpha/2$, and the extra mmf resulting at r_o and r_i is:

$$2\mathcal{F}_{21} \sin\frac{\alpha}{4} = 2\mathcal{F}_{21} \sin\frac{\sigma\pi 2p}{4Q} \tag{A.17}$$

where $\mathcal{F}$ is the rotor mmf referred to stator. The extra mmf at r_i and r_o referred to the no-load magnetising mmf, with a small angle α is:

$$\frac{\text{skew } mmf}{\text{fundamental } mmf} = \frac{\sigma\pi 2p}{2Q}\frac{\mathcal{F}_{21}}{\mathcal{F}_0} \tag{A.18}$$

where $\mathcal{F}_0$ is the magnetising mmf. In Radial Flux machines, the extra mmf and B_g increase linearly with distance from the centre, so the loss due to skew at a distance from centre is proportional to the square of the distance, making an average loss

over the length one third of that at the core ends:

$$P_{\text{skew}} = \frac{1}{3}\left(\frac{\sigma\pi 2p}{2Q}\right)^2\left(\frac{\mathcal{F}_{21}}{\mathcal{F}_0}\right)^2 x \quad (\text{no}-\text{load Fe loss}) \tag{A.19}$$

For $q \geqslant 3$, this power loss is negligible [Sadarangani, 2000].

Appendix B

Equivalent Magnetic Circuit Model Terms

B.1 Reluctances and Fluxes

Primary flux path rotor and stator steel areas are modelled as reluctances $\mathcal{R}_{fer}$ and $\mathcal{R}_{fes}$. Magnets are modelled as a flux source ϕ_0 representing remnant flux and magnet reluctance $\mathcal{R}_m$, with flux source direction determining polarity. The airgap is modelled as reluctance $\mathcal{R}_g$.

Areas of leakage and fringing fluxes are modelled as reluctances $\mathcal{R}_l$ and $\mathcal{R}_f$. Therefore, the circuit fluxes of interest are the total magnet flux ϕ_{0+PM}, the airgap flux ϕ_g and leakage fluxes ϕ_l.

Reluctances $R_{g,m,Fe}$ for the airgap, magnet and iron return are defined by material permeability, cross-sectional area and path length.

Flux sources ϕ_0 for the magnet poles are defined by remnant flux density and cross-sectional area. ϕ_0 is not the total flux in the magnet piece, as the total flux in the circuit and magnet reluctance must be considered.

B.2 Solution Matrices

By applying Kirchhoff's Voltage law, the equivalent circuit may be analysed without simplification, and the unknown flux found through any part of the flux path:

$$[\mathcal{F}] = [\mathcal{R}]\,[\Phi] \quad \rightarrow \quad [\Phi] = [\mathcal{R}]^{-1}\,[\mathcal{F}] \tag{B.1}$$

B.2.1 3D Model Fringing Fluxes

The 3D version of this model for airgap flux due to coil mmf includes terms for the fringing $\mathcal{R}_{1,2,3,4}$. The matrices for this circuit are:

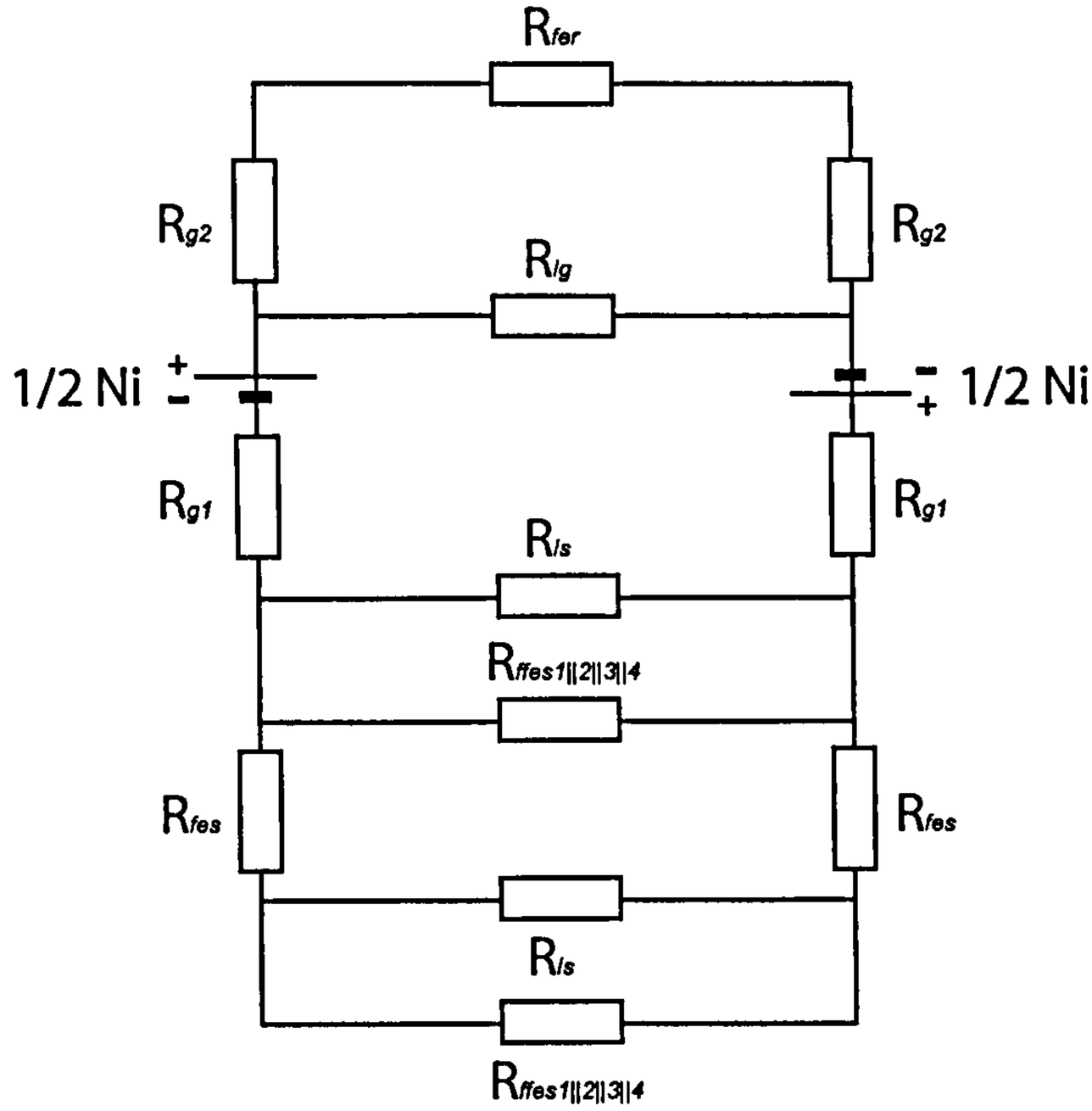


Figure B.1: Flux by current in windings for 3D model.

$$[\mathcal{R}] = \begin{bmatrix} \mathcal{R}_{0101} & -\mathcal{R}_{lg} & 0 \\ -\mathcal{R}_{lg} & \mathcal{R}_{0202} & -\mathcal{R}_{ls}||\mathcal{R}_{ffes1||2||3||4} \\ 0 & -2\mathcal{R}_{ls}||\mathcal{R}_{ffes1||2||3||4} & \mathcal{R}_{0303} \end{bmatrix}, \quad [\mathcal{F}] = \begin{bmatrix} 0 \\ -Ni \\ 0 \end{bmatrix}$$

where:

$$\mathcal{R}_{0101} = 2\mathcal{R}_{g2} + \mathcal{R}_{ffer1||2||3||4} + \mathcal{R}_{lg}$$

$$\mathcal{R}_{0202} = 2\mathcal{R}_{g1} + \mathcal{R}_{lg} + \mathcal{R}_{ls}||\mathcal{R}_{ffes1||2||3||4}$$

$$\mathcal{R}_{0303} = 2\mathcal{R}_{fes} + \mathcal{R}_{ls}||\mathcal{R}_{ffes1||2||3||4}$$

and useful ϕ_g which interacts with magnets is $\left[\Phi_{(1)}\right]$.

B.2.2 Permanent Magnets

The PM material demagnetises when the operating point (on the $B-H$ curve) passes the knee point. The position of the knee point varies with temperature, making the magnet more sensitive to demagnetisation at higher temperature. The demagnetising (or reverse) flux is calculated [Anderson, n.d.].

The current angle β is varied from $-\pi/3$ to $+\pi/3$, and connecting say three phases together by Y, the currents $i_a + i_b + i_c = 0$.

$$i_a = \hat{I}\cos(\theta);\;\; i_b = \hat{I}\cos(\theta - \frac{2\pi}{3});\;\; i_c = \hat{I}\cos(\theta - \frac{4\pi}{3})$$

which with the full pitch winding gives a maximum stator mmf across four magnets of $\mathcal{F}_{max_4PM} = 2N\hat{I}$ and maximum mmf across individual magnets of $\mathcal{F}_{max_PM} = N\hat{I}/2$.

With $\mathcal{F}_c = h_m H_c$, the magnet height h_m can be found by:

$$\begin{aligned}
\sum \mathcal{F} = 0 \;\; &= \;\; h_m H_c - A_m B_m \frac{h_m}{\mu_r \mu_0 A_m} - A_m B_m \frac{g}{\mu_0 A_m} - N\hat{I} \\
&= \quad \downarrow \\
h_m \;\; &= \;\; \frac{N\hat{I} + B_m \dfrac{g}{\mu_0}}{H_c - \dfrac{B_m}{\mu_r \mu_0}} \\
h_{m_min} \;\; &= \;\; \frac{k_{demag} N\hat{I} + B_{m_min} \dfrac{g}{\mu_0}}{H_c - \dfrac{B_{m_min}}{\mu_r \mu_0}}
\end{aligned} \tag{B.2}$$

where k_{demag} is a preferred operating margin or safety factor to demagnetisation, and B_{m_min} is the minimum tolerable magnet flux density.

Using Equation (B.2) with a value for current of peak phase current, phase-phase short circuit current, phase-ground short circuit current, and any other fault condition of interest, it is possible to calculate the sufficient magnet height to avoid demagnetising.

B.2.3 Nonlinear Magnetic Materials

Geetha and Platt [1992] calculated the machine performance under low current with an equivalent magnetic circuit. In order to include saturation under high current, the reluctance values were modified according to non-linear $B-H$ relations. The common way to incorporate this is place a limit on ϕ_{fe} which forces greater leakage

when this limit is exceeded.

B.3 3D Equivalent Magnetic Circuit Model

B.3.1 Solution Matrices

In the 3D model shown in Figure 5.1, the position of the rotor with respect to the stator does not affect the flux generated by the magnets and the flux generated by current in the coils, so airgap flux can be found. However, the rotor position is required in order to obtain flux linkage, and therefore back emf and torque as presented in Chapter 4. Assuming the aligned position, the current can be obtained and the resulting ϕ_g calculated.

For the 3D equivalent magnetic circuit model of a double airgap machine with airgap winding introduced in Section 5.1, the matrices $[\mathcal{R}]$ and $[\mathcal{F}]$ are constructed as:

$$[\mathcal{F}] = \begin{bmatrix} 0 & 0 & 2Ni & -2Ni & -\phi_0 R_m & -\phi_0 R_m & \phi_0 R_m & \phi_0 R_m & 0 & 0 \end{bmatrix}^T$$

$$[\mathcal{R}] = \begin{bmatrix}
\mathcal{R}_{0101} & -2\mathcal{R}_{fes} & \mathcal{R}_{0103} & 0 & 0 & 0 & 0 & 0 & 0 & 0 \\
-2\mathcal{R}_{fes} & \mathcal{R}_{0202} & 0 & \mathcal{R}_{0204} & -\mathcal{R}_{lg1} & 0 & 0 & 0 & 0 & 0 \\
\mathcal{R}_{0301} & 0 & \mathcal{R}_{0303} & \mathcal{R}_{0304} & -\mathcal{R}_{lg1} & -\mathcal{R}_{lg1} & 0 & 0 & 0 & 0 \\
0 & \mathcal{R}_{0402} & \mathcal{R}_{0403} & \mathcal{R}_{0404} & 0 & 0 & -\mathcal{R}_{lg1} & -\mathcal{R}_{lg1} & 0 & 0 \\
0 & 0 & -\mathcal{R}_{lg1} & 0 & \mathcal{R}_{0505} & -\mathcal{R}_{lg2} & 0 & -\mathcal{R}_m & \mathcal{R}_{0509} & 0 \\
0 & 0 & -\mathcal{R}_{lg1} & 0 & -\mathcal{R}_{gl2} & \mathcal{R}_{0606} & -\mathcal{R}_m & 0 & \mathcal{R}_{0609} & 0 \\
0 & 0 & 0 & -\mathcal{R}_{lg1} & 0 & -\mathcal{R}_m & \mathcal{R}_{0707} & -\mathcal{R}_{lg2} & 0 & \mathcal{R}_{0710} \\
0 & 0 & 0 & -\mathcal{R}_{lg1} & -\mathcal{R}_m & 0 & -\mathcal{R}_{lg2} & \mathcal{R}_{0808} & 0 & \mathcal{R}_{0810} \\
0 & 0 & 0 & 0 & \mathcal{R}_{0905} & \mathcal{R}_{0906} & 0 & 0 & \mathcal{R}_{0909} & 0 \\
0 & 0 & 0 & 0 & 0 & 0 & \mathcal{R}_{1007} & \mathcal{R}_{1008} & 0 & \mathcal{R}_{1010}
\end{bmatrix}$$

where

$$\mathcal{R}_{0101} = 2\mathcal{R}_{fes} + 2\frac{\mathcal{R}_{ls}\mathcal{R}_{ffes1234}}{\mathcal{R}_{ls} + \mathcal{R}_{ffes1234}}$$

$$\mathcal{R}_{0103} = -2\frac{\mathcal{R}_{ls}\mathcal{R}_{ffes1234}}{\mathcal{R}_{ls} + \mathcal{R}_{ffes1234}}$$

$$\mathcal{R}_{0202} = 2\mathcal{R}_{fes} + 2\frac{\mathcal{R}_{ls}\mathcal{R}_{ffes1234}}{\mathcal{R}_{ls} + \mathcal{R}_{ffes1234}}$$

$$\mathcal{R}_{0204} = -2\frac{\mathcal{R}_{ls}\mathcal{R}_{ffes1234}}{\mathcal{R}_{ls} + \mathcal{R}_{ffes1234}}$$

$$\mathcal{R}_{0301} = -\frac{\mathcal{R}_{ls}\mathcal{R}_{ffes1234}}{\mathcal{R}_{ls} + \mathcal{R}_{ffes1234}}$$

$$\mathcal{R}_{0303} = 2\frac{\mathcal{R}_{lg3}\mathcal{R}_{g1}}{\mathcal{R}_{lg3} + (g + \frac{h_c}{2})\mathcal{R}_{g1}} + 2\frac{\mathcal{R}_{lg3}\mathcal{R}_{g2}}{\mathcal{R}_{lg3} + (g + \frac{h_c}{2})\mathcal{R}_{g2}} + 2\mathcal{R}_{lg1} + \frac{\mathcal{R}_{ls}\mathcal{R}_{ffes1234}}{\mathcal{R}_{ls} + \mathcal{R}_{ffes1234}}$$

$$\mathcal{R}_{0304} = -2\frac{\mathcal{R}_{lg3}\mathcal{R}_{g1}}{\mathcal{R}_{lg3} + (g + \frac{h_c}{2})\mathcal{R}_{g1}} - 2\frac{\mathcal{R}_{lg3}\mathcal{R}_{g2}}{\mathcal{R}_{lg3} + (g + \frac{h_c}{2})\mathcal{R}_{g2}}$$

$$\mathcal{R}_{0402} = -\frac{\mathcal{R}_{ls}\mathcal{R}_{ffes1234}}{\mathcal{R}_{ls} + \mathcal{R}_{ffes1234}}$$

$$\mathcal{R}_{0403} = -2\frac{\mathcal{R}_{lg3}\mathcal{R} + g1}{\mathcal{R}_{lg3} + (g + \frac{h_c}{2})\mathcal{R}_{g1}} - 2\frac{\mathcal{R}_{lg3}\mathcal{R}_{g2}}{\mathcal{R}_{lg3} + (g + \frac{h_c}{2})\mathcal{R}_{g2}}$$

$$\mathcal{R}_{0404} = 2\frac{\mathcal{R}_{lg3}\mathcal{R}_{g1}}{\mathcal{R}_{lg3} + (g + \frac{h_c}{2})\mathcal{R}_{g1}} + 2\frac{\mathcal{R}_{lg3}\mathcal{R}_{g2}}{\mathcal{R}_{lg3} + (g + \frac{h_c}{2})\mathcal{R}_{g2}} + 2\mathcal{R}_{lg1} + \frac{\mathcal{R}_{ls}\mathcal{R}_{ffes1234}}{\mathcal{R}_{ls} + \mathcal{R}_{ffes1234}}$$

$$\mathcal{R}_{0505} = \mathcal{R}_m + \frac{\mathcal{R}_{fer1}\mathcal{R}_{ffer5678}}{\mathcal{R}_{fer1} + \mathcal{R}_{ffer5678}} + \mathcal{R}_{lg2} + \mathcal{R}_{gl1}$$

$$\mathcal{R}_{0509} = -\frac{\mathcal{R}_{fer1}\mathcal{R}_{ffer5678}}{\mathcal{R}_{fer1} + \mathcal{R}_{ffer5678}}$$

$$\mathcal{R}_{0606} = \mathcal{R}_{lg2} + \frac{\mathcal{R}_{fer2}\mathcal{R}_{ffer5678}}{\mathcal{R}_{fer2} + \mathcal{R}_{ffer5678}} + \mathcal{R}_m + \mathcal{R}_{lg1}$$

$$\mathcal{R}_{0609} = -\frac{\mathcal{R}_{fer2}\mathcal{R}_{ffer5678}}{\mathcal{R}_{fer2} + \mathcal{R}_{ffer5678}}$$

$$\mathcal{R}_{0707} = \mathcal{R}_m + \frac{\mathcal{R}_{fer1}\mathcal{R}_{ffer5678}}{\mathcal{R}_{fer1} + \mathcal{R}_{ffer5678}} + \mathcal{R}_{lg2} + \mathcal{R}_{lg1}$$

$$\mathcal{R}_{0710} = -\frac{\mathcal{R}_{fer1}\mathcal{R}_{ffer5678}}{\mathcal{R}_{fer1} + \mathcal{R}_{ffer5678}}$$

$$\mathcal{R}_{0808} = \mathcal{R}_{lg2} + \frac{\mathcal{R}_{fer2}\mathcal{R}_{ffer5678}}{\mathcal{R}_{fer2} + \mathcal{R}_{ffer5678}} + \mathcal{R}_m + \mathcal{R}_{lg1}$$

$$\mathcal{R}_{0810} = -\frac{\mathcal{R}_{fer2}\mathcal{R}_{ffer5678}}{\mathcal{R}_{fer2} + \mathcal{R}_{ffer5678}}$$

$$\mathcal{R}_{0905} = -\frac{\mathcal{R}_{fer1}\mathcal{R}_{ffer5678}}{\mathcal{R}_{fer1} + \mathcal{R}_{ffer5678}}$$

$$\mathcal{R}_{0906} = -\frac{\mathcal{R}_{fer2}\mathcal{R}_{ffer5678}}{\mathcal{R}_{fer2} + \mathcal{R}_{ffer5678}}$$

$$\mathcal{R}_{0909} = \mathcal{R}_{ffer1234} + \frac{\mathcal{R}_{fer2}\mathcal{R}_{ffer5678}}{\mathcal{R}_{fer2} + \mathcal{R}_{ffer5678}} + \frac{\mathcal{R}_{fer1}\mathcal{R}_{ffer5678}}{\mathcal{R}_{fer1} + \mathcal{R}_{ffer5678}}$$

$$\mathcal{R}_{1007} = -\frac{\mathcal{R}_{fer1}\mathcal{R}_{ffer5678}}{\mathcal{R}_{fer1} + \mathcal{R}_{ffer5678}}$$

$$\mathcal{R}_{1008} = -\frac{\mathcal{R}_{fer2}\mathcal{R}_{ffer5677}}{\mathcal{R}_{fer2} + \mathcal{R}_{ffer5678}}$$

$$\mathcal{R}_{1010} = \mathcal{R}_{ffer1234} + \frac{\mathcal{R}_{fer2}\mathcal{R}_{ffer5678}}{\mathcal{R}_{fer2} + \mathcal{R}_{ffer5678}} + \frac{\mathcal{R}_{fer1}\mathcal{R}_{ffer5678}}{\mathcal{R}_{fer1} + \mathcal{R}_{ffer5678}}$$

B.3.2 Reluctance Values

The parametric relations describing each reluctance are derived from the permeance relations:

$$\mathcal{R}_{ffer1} = \frac{\pi}{\mu_0\mu_{r(air)}(r_o - r_i)\ln(2k_{ppitch})}$$

$$\mathcal{R}_{ffer2} = \frac{8p}{\mu_0\mu_{r(air)}\pi r_o k_{ppitch}}$$

$$\mathcal{R}_{ffer3} = \frac{\pi}{\mu_0\mu_{r(air)}h_{fer}\ln(2k_{ppitch})}$$

$$\mathcal{R}_{ffer4} = \frac{8p}{\mu_0\mu_{r(air)}\pi r_o k_{ppitch}}$$

$$\mathcal{R}_{ffer5} = \frac{\pi}{\mu_0\mu_{r(air)}(r_o - r_i)\ln(2k_{ppitch})}$$

$$\mathcal{R}_{ffer6} = \frac{2p}{\mu_0\mu_{r(air)}\pi r_o k_{ppitch}}$$

$$\mathcal{R}_{ffer7} = \frac{\pi}{4\mu_0\mu_{r(air)}h_{fer}\ln(2k_{ppitch})}$$

$$\mathcal{R}_{ffer8} = \frac{4p}{\mu_0\mu_{r(air)}\pi r_o k_{ppitch}}$$

$$\mathcal{R}_{lg3} = \frac{7.47p}{\mu_0\mu_{r(air)}2\pi r_o k_{ppitch}}$$

$$\mathcal{R}_{fer2} = \frac{\pi}{\mu_0\mu_{r(air)}(r_o - r_i)\ln\left(1 + \frac{\pi h_{fer}}{\pi\frac{(r_o+r_i)}{2p} - h_{fes}}\right)}$$

$$\mathcal{R}_m = \frac{h_m}{\mu_0\mu_{r(PM)}(r_o - r_i)w_{mech_r_mean}}$$

$$\mathcal{R}_{g2} = \left(g + \frac{h_c}{2}\right)\frac{1}{\mu_0\mu_{r(air)}(w_{mech_r_mean} + g)(r_o - r_i)}$$

$$\mathcal{R}_{lg1} = \frac{\pi}{\mu_0 \mu_{r(air)}(r_o - r_i)\ln\left[1 + \frac{\pi(g+h_c)2p}{2(1-k_{ppitch})\pi(r_o+r_i)}\right]}$$

$$\mathcal{R}_{g1} = \frac{h_c}{2\mu_0 \mu_{r(air)}(w_{mech_r_mean} + g)(r_o - r_i)}$$

$$\mathcal{R}_{lfes1} = \frac{\pi}{\mu_0 \mu_{r(air)} h_{fes} \ln(2k_{ppitch})}$$

$$\mathcal{R}_{lfes2} = \frac{\delta p}{\mu_0 \mu_{r(air)} \pi r_o k_{ppitch}}$$

$$\mathcal{R}_{lfes3} = \frac{\pi}{\mu_0 \mu_{r(air)} h_{fes} \ln(2k_{ppitch})}$$

$$\mathcal{R}_{lfes4} = \frac{\delta p}{\mu_0 \mu_{r(air)} \pi r_i k_{ppitch}}$$

$$\mathcal{R}_{ls} = \frac{\pi}{\mu_0 \mu_{r(Fe)}(r_o - r_i)\ln\left[1 + \frac{\pi h_{fes}}{2\left[\frac{\pi(r_o+r_i)}{2p} - w_{mech_r_mean} - g\right]}\right]}$$

$$\mathcal{R}_{fes} = \frac{h_{fes}}{\mu_0 \mu_{r(Fe)} \pi (w_{mech_r_mean} + g)(r_o - r_i)}$$

B.4 Stator Leakage Paths

Chapter 9 considers the slotted cored stator where the winding is placed in slots.

B.4.1 Leakage across Stator Slots

Roters [1941] describes the total leakage flux ϕ_l between two stator teeth, which are wound with $N/2$ turns coils per unit length, up to point x from the core yoke as:

$$\phi_l(x) = \int_0^x \frac{\mathcal{F}_x}{\mathcal{R}'_l} dx = \frac{NI}{\mathcal{R}'_l} \int_0^x x dx = \frac{NIx^2}{2\mathcal{R}'_l} \tag{B.3}$$

where $\mathcal{R}'_l$ is the direct leakage reluctance per unit length, so for $x = h$:

$$\phi_l(x = h) = \phi_l = \frac{NIh^2}{2\mathcal{R}'_l} = \frac{h}{2\mathcal{R}'_l} \times NIh \tag{B.4}$$

This assumes that the teeth extend much longer than the pole faces to neglect distortion by the pole faces. The *mmf* across the yoke end of the leakage path is zero, while at the pole face it is NIh, with a uniform variation between the values at these points. The relation gives a leakage flux of the total excitation *mmf* of both poles divided by double the total reluctance between the pole cores. In the

saturated case, the reluctance drop is accounted for by a "reluctance factor".

B.4.2 Flux Linkage of Leakage across Stator Slots

Flux ϕ is the main flux across the airgap from the core teeth faces. With small ϕ_l there is near constant ϕ along the tooth, and the reluctance drop in the tooth is estimated by assuming a uniform flux of $\phi + \frac{2}{3}\phi_l$ along the length, by the following:

$$\mathcal{F}_t(x) = \int_0^x H_t dx = \int_0^x \frac{\phi}{\mu_t S} dx = \frac{1}{\mu_t S} \int_0^x \left(\phi + \phi_l - \frac{NIx^2}{2\mathcal{R}_l'} \right) dx \tag{B.5}$$

where $\mathcal{F}$ is the *mmf*, giving:

$$\mathcal{F}_t(x) = \frac{1}{\mu_t S} \left(\phi x + \phi_l x - \frac{NIx^3}{6\mathcal{R}_l'} \right) \tag{B.6}$$

so for $x = h$:

$$\mathcal{F}_t(x = h) = \frac{\phi + \frac{2}{3}\phi_l}{\mu_t S} h \tag{B.7}$$

The total flux linkage from the leakage flux, ψ_h, is:

$$\psi_h(x = h) = \int_0^h Nx \cdot \frac{\mathcal{F}(x)}{\mathcal{R}_l'} dx = \frac{IN^2}{\mathcal{R}_l'} \int_0^h x^2 dx = \frac{N^2 I H^3}{3\mathcal{R}_l'} = \frac{2}{3}\Phi_l N h \tag{B.8}$$

Appendix C

Test Rig & Manufacturing Jigs

C.1 Airgap Conductor Test Rig

Figure C.1 shows the testrig used to measure and investigate excitation fields from various magnet arrays, and to investigate eddy currents arising in conductors of different geometries. This is a modified version of that used in Lampérth [2000].

C.2 Excitation Field Measurement

A Hirst Gauss probe, with proprietary data logging software, was employed to obtain the airgap field measurements.

C.3 Coil Winding Jigs

Figures C.2 and C.3 illustrate the coil winding jigs and formers.

C.4 Iron Core Jigs

The core teeth were manufactured in compacted insulated iron powder (SMC 550 [Högänas AB, 2004]) from blocks size Ø80 x 50 mm. Two teeth were machined from each block with the radii for the inside and outside of the active area applied.

The milling of the slots required additional support behind the material to prevent it breaking out, as is common in climb milling used to achieve a superior finish.

Figure C.4 shows the slitting device constructed to achieve a laminated strip width of 8 mm for the slotless Generator. An 8 mm width has previously been too narrow.

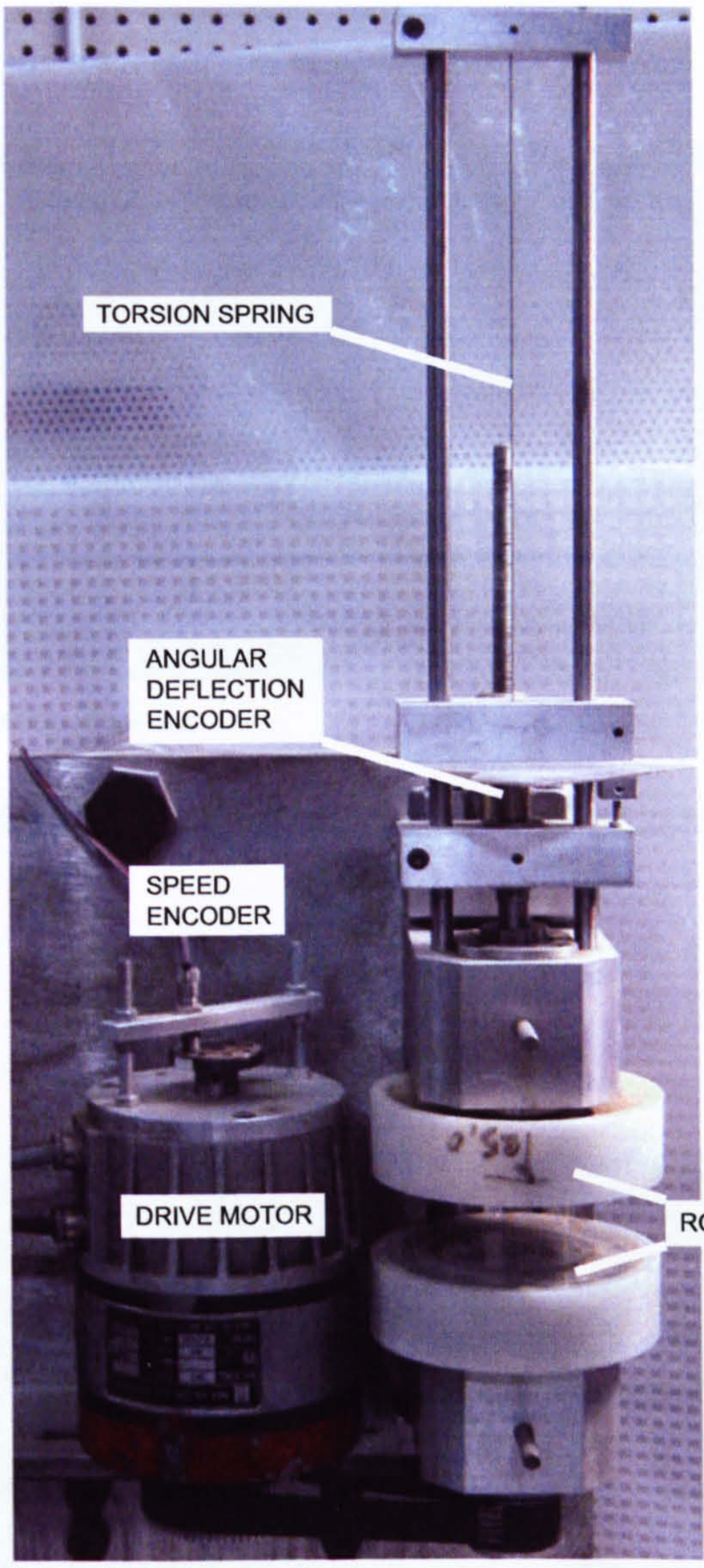


Figure C.1: Test rig

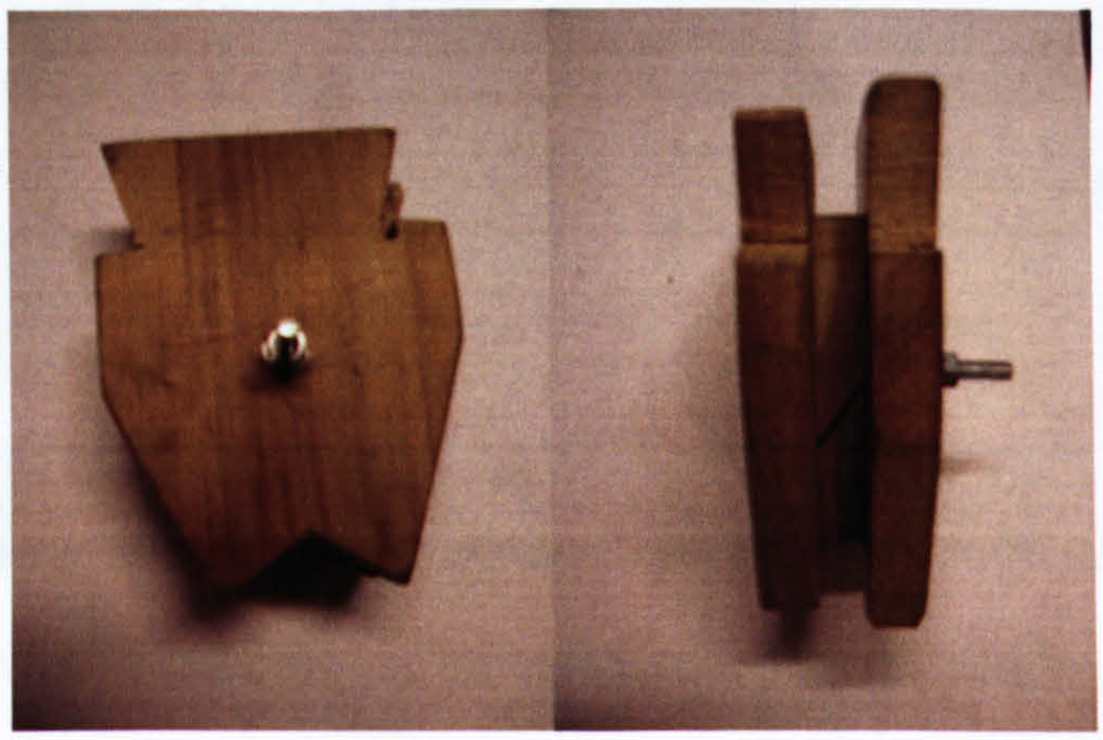
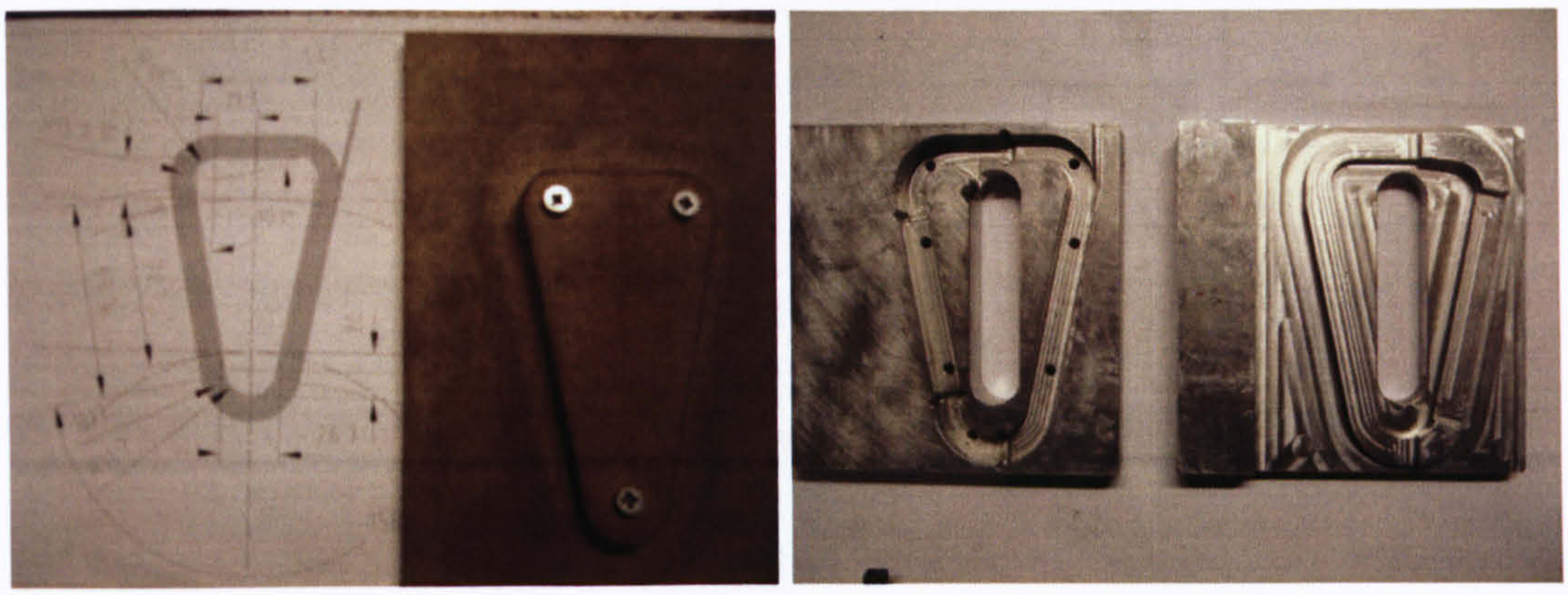


Figure C.2: 9-slot concentrated coil winding jigs.



(a) Coil jig with drawing

(b) Coil former

Figure C.3: Airgap winding manufacture jigs.

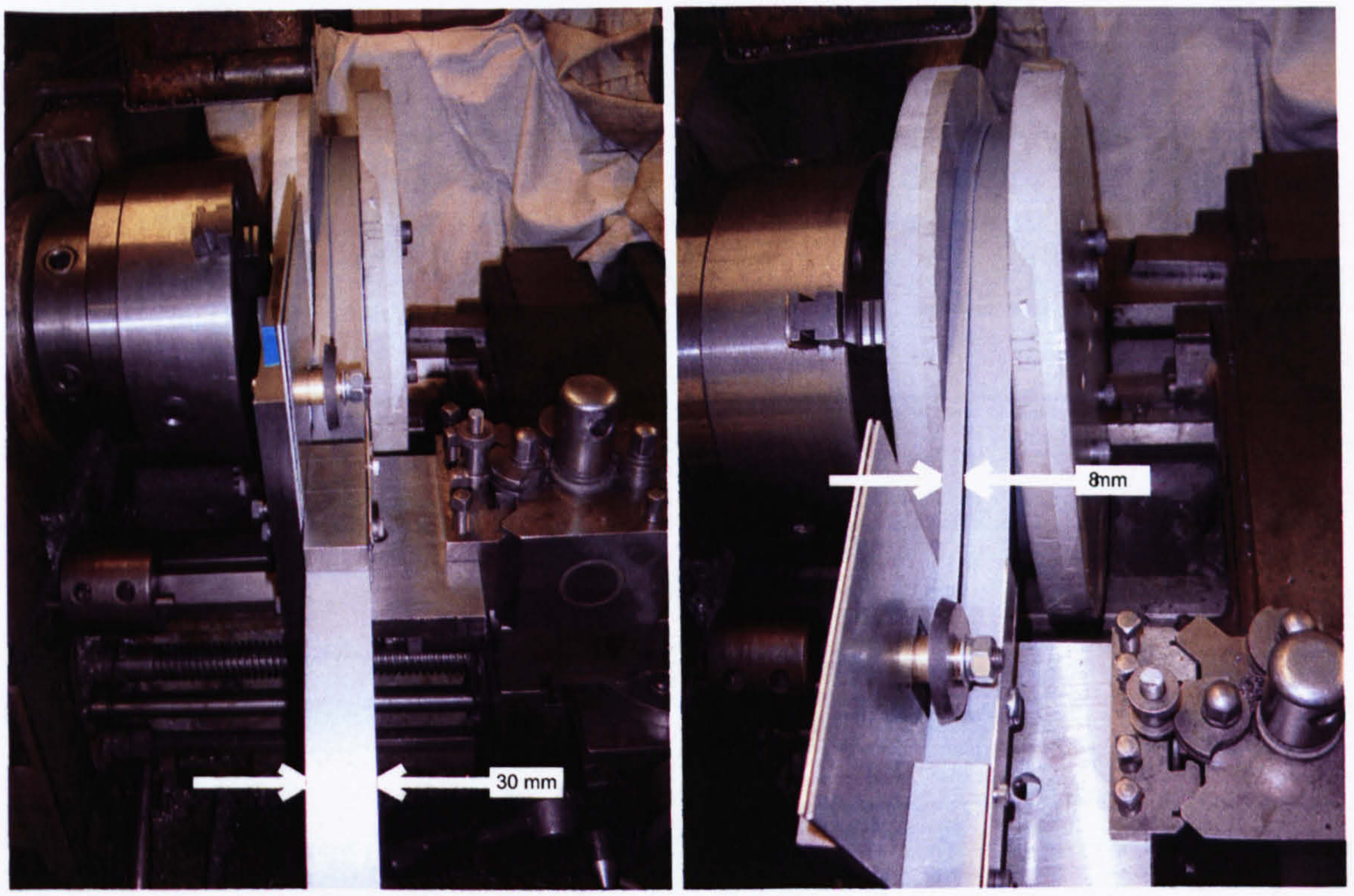


Figure C.4: Slitting jig for laminated airgap winding core.